Deep-time reconstructions of Earth's surface environments and elevations

Satyam Pratap Singh

A thesis submitted to fulfil the requirements of the degree of
Doctor of Philosophy

THE UNIVERSITY OF
SYDNEY

School of Geosciences
Faculty of Science
The University of Sydney
Australia
2026

Supervisor: A/Prof. Maria Seton

Co-Supervisor: Dr. Sabin Zahirovic

Co-Supervisor: Dr. Nicky M. Wright

Statement of Originality

This is to certify that the content of this thesis is my own work. This thesis has not been submitted for any other degree or purpose.

I certify that the intellectual content of this thesis is the product of my own work, and that all assistance received in preparing this thesis and all sources have been acknowledged.

Satyam Pratap Singh
May 25, 2026

Acknowledgements

I would like to begin by expressing my gratitude through the timeless Sanskrit verse:

Guru Brahmā, Guru Viṣṇu,
Guru Devo Maheśvaraḥ;
Guru Sākṣāt Parabrahma,
Tasmai Śrī Gurave Namaḥ.

A teacher is Brahmā, the creator;
A teacher is Viṣṇu, the preserver;
A teacher is Maheśvara (Śiva), the transformer;
A teacher is verily the Supreme Reality.
Unto that revered teacher, I offer my salutations.

This verse reflects the profound role of a teacher as the one who creates, sustains, and transforms knowledge, and ultimately embodies the pursuit of truth. It captures my deep respect for the mentors who have guided my intellectual and personal journey throughout this Ph.D. My deepest gratitude goes to my supervisors, **A/Prof. Maria Seton**, **Dr. Sabin Zahirovic**, and **Dr. Nicky M. Wright**, each of whom has shaped my development in invaluable ways. Maria has been a constant source of inspiration, encouraging me to tackle challenging questions while giving me the freedom to explore bold ideas. Nicky has played a crucial role in sharpening my scientific reasoning and helping me cultivate clarity, rigour, and effective communication in my work. Sabin's guidance, motivation, and broad perspective have been instrumental in supporting my growth into a well-rounded researcher. I am deeply grateful for their time, trust, and unwavering support.

I would also like to thank my friends **Utpal Singh** and **Sudhir**, whose contributions were central to the development of several computational frameworks used in this thesis. Their collaboration, insight, and enthusiasm made this work stronger, and their friendship made the journey far more enjoyable.

My heartfelt thanks extend to my colleagues and officemates—**Jono, Tom, Addi, and Joe**—for their support, camaraderie, and the many conversations and shared moments that helped me feel at home in a foreign country.

I am grateful to the **University of Sydney** and **EarthByte Group** for providing the computational facilities, intellectual environment, and institutional support that made this research possible. I also acknowledge the **BHP STELLAR Project** for funding this research, without which this work would not have been possible.

Finally, I owe my deepest gratitude to my **parents**, my **grandmother**, and my **wife, Aditi**, whose unwavering love, strength, and belief in me sustained every step of this journey.

Their sacrifices, patience, and support have been the foundation upon which this thesis stands.

Authorship Attribution Statement

This thesis is based on the following three research articles, which collectively form the central body of original work:

Article 1: *Singh, S. P., Zahirovic, S., Seton, M., Wright, N. M., Atwood, N., Belgarde, C., Mallard, C., Alfonso, C. P., & Ibrahim, Y. (2025). Optimised Mesozoic Rifting Model of the Central Gulf of Mexico Basin. International Geology Review — in review.*
I conceptualised and designed this study in collaboration with the listed co-authors, performed the data compilation, analysis, and modelling, produced all figures and tables, and wrote the initial and revised drafts of the manuscript.

Article 2: *Singh, S. P., Seton, M., Zahirovic, S., Wright, N. M., Atwood, N., & Fay, C. (2025). Topographic Diversity in Subduction-Related Mountains Driven by Plate Tectonics and Mantle Dynamics. Earth and Planetary Science Letters — in review.*
I developed the methodology and study framework with input from co-authors, conducted all analyses, created the visualisations, and prepared the manuscript drafts.

Article 3: *Singh, S. P., Seton, M., Zahirovic, S., Wright, N. M., & Williams, S. (2025). Deep Learning Reconstructs Global Active Margin Paleotopography Since the Mesozoic from Plate Kinematics and Mantle Dynamics. Submitted: PNAS Nexus.*
I designed the research, carried out machine-learning modeling, integrated multiple datasets, produced all figures and tables, and drafted the manuscript.

Permission from corresponding authors has been obtained for inclusion of published or in-review material in all cases where I am not the corresponding author.

Satyam Pratap Singh
May 25, 2026

As principal supervisor for this candidature, I confirm that the above authorship attribution statements are accurate and faithfully reflect the contributions to each publication and to the relevant sections of this dissertation.

A/Prof. Maria Seton
May 25, 2026

Generative AI Attribution Statement

During the preparation of this thesis, the author used generative AI tools for text editing purposes. Specifically:

- **ChatGPT** and **Perplexity** were used for minor text editing, including grammar correction, and clarity enhancement in chapters 1 and 5. All outputs generated by these tools were reviewed and revised by the author to maintain accuracy, scientific integrity, and alignment with the thesis content.

The author takes full responsibility for all content submitted in this thesis and confirms that the work is their own. All use of generative AI was consistent with the University of Sydney's guidelines and policies for responsible AI use in research.

Abstract

Reconstructing Earth's ancient surface topography in deep geological time represents an interdisciplinary challenge that demands the synthesis of plate tectonic reconstructions, geodynamic simulations, paleoclimate simulation, and advanced computational methodologies. This thesis makes significant progress toward understanding how Earth's surface elevations have evolved through geologic time by pioneering an integrated computational framework that bridges geological observations with numerical models for paleotopographic reconstruction.

An important aspect of this investigation is the development of a novel optimised deformable plate tectonic reconstruction that incorporates time-evolving, spatially focused deforming meshes within rift zones, as applied to the Gulf of Mexico. The approach applies exponentially varying strain localization toward rift axes—implemented through pyGPlates—within existing plate reconstructions. As applied to the GoM case study, I have found that through fast and systematic optimization across 32,400 mesh configurations calibrated against geophysically derived present-day crustal-thickness models, the optimized deformable mesh reduced the root-mean-square error (RMSE) from 14.8 km (uniform deformation model) to 5.6 km relative to the GEMMA crustal-thickness model. The workflow simultaneously models tectonic subsidence arising from both lithospheric stretching and thermal subsidence during rifting, yielding quantitative predictions of subsidence histories. The prediction illuminates key depositional enigmas, including approximately 1.5 km of subsidence preceding Yucatán Block drift during the Sinemurian (193–183 Ma) that facilitated red-bed accumulation through paleodrainage networks, and the southward migration of red-bed deposition beneath Jurassic salt formations, which explains a perplexing 40 Myr stratigraphic hiatus. Differential subsidence patterns also elucidate the pronounced westward deflection of Cenomanian–Turonian (100.5–89.8 Ma) clastic depositional systems, providing quantitative constraints on basin-asymmetry evolution.

Transitioning to active margins, where mountain building reflects the complex interplay among plate kinematics, mantle dynamics, and climate-modulated surface processes, this thesis introduces a spatiotemporal data-mining ecosystem anchored in an Explainable Artificial Intelligence (XAI) framework. The Python Deep Time Data Mining (pyDTDM) computational library—developed to integrate heterogeneous, multi-gigabyte datasets spanning plate reconstructions, global mantle convection simulations, and paleoclimate model outputs—enables systematic interrogation of topographic drivers across present-day subduction zones. Employing an XAI model trained on modern active-margin topography (ETOPO) sampled at 0.1° global resolution, the framework quantifies the nonlinear contributions of subduction flux, trench-migration dynamics, upper-mantle temperature fields, vertical mantle-flow patterns, and long-term precipitation to elevation variability. Shape

functions extracted from the XAI model reveal that subduction flux is the dominant orogenic driver, with trench-advance episodes intensifying crustal thickening and topographic expression, whereas trench retreat correlates with orogenic collapse. Mantle-temperature anomalies and upwelling flows exert secondary but significant influences, while long-term precipitation modulates erosional denudation over Myr-scale timescales.

Leveraging insights from the XAI analysis, the thesis advances a deep neural-network architecture capable of reconstructing active-margin paleotopography throughout the Mesozoic and Cenozoic at 1 Myr temporal resolution. Trained on present-day ETOPO elevation data as the target variable, and using temporally resolved plate-kinematic parameters, mantle-convection fields from global CitcomS simulations, and a paleoclimate-informed parameter, namely the time a region spent within the equatorial humid belt, as inputs, the network successfully predicts paleoelevation patterns. These predictions are validated against independent igneous rock geochemical ratio–based paleoelevation estimates and established regional reconstructions. Application to global active margins resurrects previously unrecognized orogenic episodes, most notably revealing the East Asian Cordillera, which reached elevations exceeding 3 km during the mid-Cretaceous, driven by Izanagi Plate subduction, before undergoing episodic collapse linked to slab-rollback and ridge-subduction events. The model's reconstruction of Andean paleotopography exhibits strong coherence with existing regional studies, capturing major uplift phases during the Paleogene and Miocene.

The computational infrastructure developed in this thesis embodies the principles of reproducibility and open science, with the pyDTDM libraries, deformable-plate reconstruction workflows, and the Kalpa open-source geospatial-analysis platform disseminated under GPL and LGPL licenses to facilitate community adoption. The Kalpa platform specifically addresses long-standing barriers to artificial-intelligence adoption in geosciences by integrating machine-learning capabilities with native handling of raster, vector, and volumetric geospatial formats—including GeoTIFF, NetCDF, shapefiles, and point-cloud data—while emphasizing reproducible workflows and visualization optimized for deep-time reconstructions.

This body of work confronts key limitations transparently, acknowledging uncertainties that propagate from plate-reconstruction model selection, the scarcity of independent paleoelevation validation proxies, and simplifying assumptions regarding depth-dependent lithospheric stretching and climate–topography feedbacks. Nevertheless, the integrated methodological paradigm established here represents a transformative advance in deep-time Earth-system science. By harmonising geological modelling, machine-learning scalability, and physical interpretability within unified computational frameworks, this work not only generates reconstructions of ancient landscapes but also delivers an XAI-based framework that quantifies the relative importance of individual tectonic, mantle, and climatic drivers and provides first-order insights into associated uncertainties in model predictions. Broader implications extend to mineral-systems exploration by leveraging paleotopographic controls on exhumation and preservation potential, paleoclimate modelling that requires realistic boundary conditions for ancient atmospheric circulation, biodiversity-evolution studies examining orographic barriers to dispersal, and a deeper understanding of how deep-Earth dynamics sculpt planetary surfaces across geological time.

Contents

Chapter 1

Introduction

The Earth's surface has changed substantially over geological time owing to intricate interactions among plate tectonics, mantle convection, and climate-influenced surface processes (Clark, 2007; Yuan et al., 2024; Wolf et al., 2022). Variations in surface elevation are crucial for understanding the evolution of a planet's interconnected spheres, including the lithosphere, biosphere, and atmosphere (Boschman and Condamine, 2022; Igea and Tanentzap, 2021; Rahbek et al., 2019; Spicer, 2017). For example, topographic uplift at convergent margins, driven by plate tectonics and mantle convection, can force moisture-laden winds from the ocean to shed their moisture when encountering topographic barriers, resulting in high precipitation on the windward side and low precipitation on the leeward side (Evenstar et al., 2023; Lang et al., 2020). This topography-climate coupling strongly influences regional climate and ecosystems (Evenstar et al., 2023; Körner, 2004; Rahbek et al., 2019; Willett, 1999). Conversely, subsidence during continental rifting can create extensive inundated areas, forming new basins and depositional environments that sustain marine life (Hips, 2022; Leleu et al., 2016) and influence the accumulation of natural resources such as sedimentary copper deposits (Hitzman et al., 2005, 2010). Additionally, uplift in active margins, particularly in equatorial humid regions, can enhance silicate weathering, drawing down atmospheric carbon dioxide and contributing to long-term global cooling (Macdonald et al., 2019).

Deep-time surface reconstructions offer crucial insights into the geological evolution of the planet by enabling the mapping, modelling, and interpretation of Earth's surface conditions over millions to hundreds of millions of years (Mills et al., 2019; Müller et al., 2019; Scotese, 2021). This thesis examines deep-time surface reconstructions, which not only document the migration, reconfiguration and evolution of continents and ocean basins but also elucidate the underlying physical mechanisms driving the surface elevation changes. This thesis specifically focuses on reconstructing the evolution of tectonic subsidence in passive rift margins, which have long been known to be caused by lithospheric stretching and thermal subsidence (McKenzie, 1978; Le Pichon and Sibuet, 1981), using the Gulf of Mexico (GoM) as a case study. Second, I investigated how different plate kinematics, geodynamics, and climate parameters influence the present-day topography of mountain belts at active margins, which were then used to reconstruct deep-time surface elevations of global active margins since the Mesozoic. In this thesis, paleotopography is used specifically for the reconstructed vertical elevation of the Earth surface above sea level. Paleoelevation refers to the reconstructed vertical position of a point on Earth's surface rela-

tive to sea level and, as such, encompasses both paleotopography and paleobathymetry. Paleoenvironment refers to reconstructed depositional and geomorphic settings, such as shallow-marine shelves, deep-marine basins, fluvial plains, or high-elevation orogenic belts, inferred from geological, sedimentological, and geomorphological evidence. In this thesis, the terms paleoelevation and paleotopography are frequently used interchangeably when describing reconstructed landscapes and their vertical elevation.

The thesis aims to create advanced computational frameworks and software tools that make deep-time reconstruction simple, scalable, and reproducible. By utilising massive amounts of geological data and models, such as plate tectonic reconstructions and mantle convection models, using the novel tools and frameworks described in this thesis, I aim to demonstrate that deep-time reconstruction can digitally reproduce paleoelevation. This can help us better understand large-scale Earth system processes, such as past climate patterns, biodiversity evolution, and the geographical distribution of natural resources across geological times.

This thesis systematically addresses the following three overarching research questions:

RQ1: What are the primary physical factors influencing elevation changes in continental rift and active margins over geological timescales?

RQ2: How can geological data and models be used to accurately reconstruct paleotopography?

RQ3: What are the broader implications of these reconstructions for interpreting the paleoenvironments?

Table 1.1: Chapter-wise Themes, Key Contributions, and Research Questions Addressed

Chapter	**Theme**	**Key Contributions**	**Research Questions Addressed**
2	Passive Margins	Optimized deformable plate models for crustal thickness and tectonic subsidence; Application to Mesozoic depositional history in the central GoM basin	RQ1, RQ2, RQ3
3	Topographic Diversity at Present Day Active Margins	Novel Explainable AI framework for quantification of tectonic, mantle, and climate drivers on topography	RQ1
4	Mesozoic Active Margins	Deep learning model for reconstructing active margins	RQ2, RQ3

1.1 Existing Approaches for Reconstructing Earth's Surface Elevation

Over decades, several approaches have been developed in geoscience disciplines to reconstruct and understand the evolution of paleotopography over deep-time. For simplicity, these approaches can be classified into two categories: process-driven and data-driven models.

1.1.1 Data-Driven Models

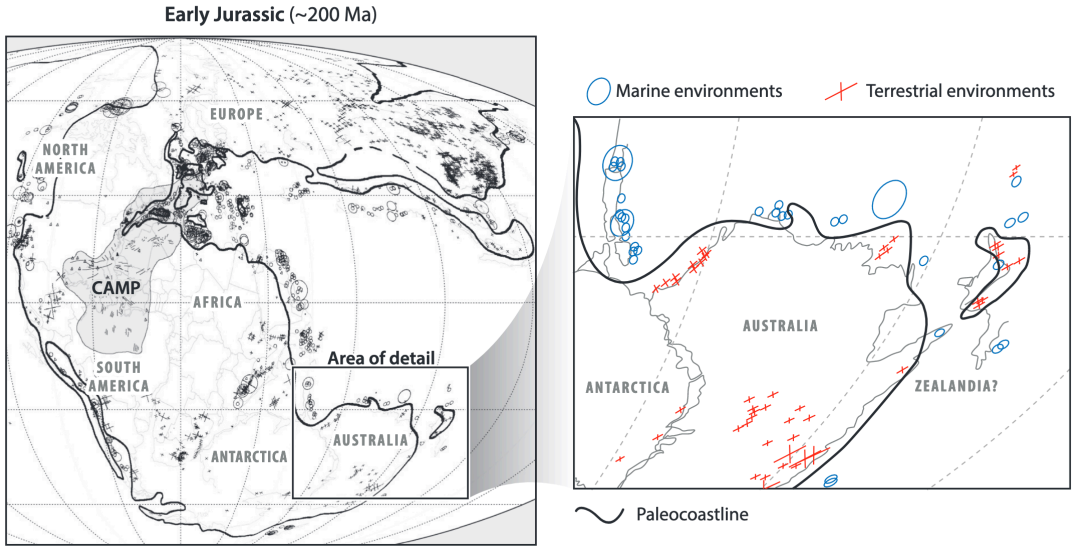

Figure 1.1: **Example of a data-driven paleogeographic reconstruction.** This map of the Early Jurassic (~200 Ma) illustrates the synthesis of kinematic models with geological observations to define surface environments. The black lines indicate mapped paleocoastlines derived from geologic data, while the symbols represent specific data points (with size inversely proportional to age dating precision). The gray-shaded region marks the Central Atlantic Magmatic Province (CAMP). This approach exemplifies the reconstruction of Earth's surface features by integrating plate reconstruction software (e.g., GPlates) with vast geological datasets such as the Paleobiology Database. Figure adapted from Scotese (2021).

Data-driven models use various statistical and/or empirical methods to reconstruct paleotopography from observational data (Boschman, 2021; Poblete et al., 2021; Scotese, 2021). These methods provide information for paleotopography modelling from various observational datasets, including lithofacies, stable-isotope paleoaltimetry, low-temperature thermochronology, sedimentary records, geochemical signatures, and fossil assemblages (Badgeley et al., 2022; Boschman, 2021; Li and Garzione, 2017; Li, 2021; Liu et al., 2024; Kuhlemann, 2007; Poblete et al., 2021; Rowley et al., 2001). For example, global paleotopography reconstruction relies on proxy-based inferences, in which geological indicators such as lithofacies distributions delineate ancient highlands, lowlands, and marine environments (e.g., Figure 1.1, Table 1.2); for instance, evaporites indicate arid basins, whereas conglomerates indicate proximal mountainous sources (Scotese, 2021; Ziengler et al., 1985). Similarly, for ocean basin reconstruction, empirical age-depth correlations

derived from thermal subsidence curves are used to reconstruct bathymetric evolution (Wright et al., 2020; Parsons and Sclater, 1977). Other heuristic approaches, such as Vérard et al. (2015), utilize statistical models to match present-day topography to distinct geological domains and then allocate elevations to passive margins or collisional zones in deep-time.

Advancements between 2022 and 2025 considerably improved data-driven capabilities through enhanced tools and web-based platforms (Aminov et al., 2023; Liu et al., 2024; Zeng et al., 2025; Zhou et al., 2025). For example, data-driven machine learning approaches have enabled the reconstruction of paleocrustal thickness near active margins using geochemical proxies, which can then be translated to paleoelevation using simple isostatic relations (Liu et al., 2024; Zhou et al., 2025). Additionally, recent studies have used integrated detrital zircon U-Pb geochronology, calcite U-Pb dating, and stable/clumped isotope analyses to refine paleoelevation and paleo-drainage reconstructions (Zeng et al., 2025). Furthermore, software such as the Terra Antiqua tool facilitates data-driven reconstruction (Aminov et al., 2023). Terra Antiqua provides an open-source QGIS plugin that is compatible with GPlates. It can process proxy data, including paleofacies, fossils, and paleoelevation proxies, using physically informed algorithms to estimate land-sea distributions and hypsometry (Aminov et al., 2023). These techniques generate user-friendly maps, addressing the reproducibility concerns inherent in classic lithofacies-based paleotopography models.

Despite these advancements, data-driven approaches face significant limitations. Because data-driven models rely primarily on proxy data, which are limited in both space and time, reconstruction becomes difficult in environments such as eroded active margins, where data may be lost (Botsyun et al., 2020; Garzione et al., 2000; Rowley and Garzione, 2007). Moreover, due to assumptions of modern-day isotope lapse rates and erosion, or atmospheric overprints, interpolation biases and elevation errors can often reach 1–3 km (Badgeley et al., 2022; Ehlers and Poulsen, 2009; Hartley et al., 2007; Mulch, 2016). Stable-isotope paleoaltimetry and low-temperature thermochronology, such as apatite fission-track analysis, provide localized insights but are often episodic and climatically sensitive. These characteristics can undermine modern deep-time analogues. Furthermore, due to spatiotemporal data sampling and preservation limitations, we can only obtain snapshots of Earth's topography at sparse time steps.

1.1.2 Process-Driven Models

Process-driven approaches model Earth's surface evolution using numerical models governed by physical equations, providing tools for explaining elevation changes by coupling plate tectonics, deep Earth dynamics (e.g., mantle convection), and surface processes (e.g., erosion and deposition) (Lu et al., 2024; Wolf et al., 2022; Yuan et al., 2024). Geodynamic models, such as CitcomS, use viscous mantle flow to calculate dynamic topography, taking into account characteristics such as viscosity contrasts and slab geometries (Bower et al., 2015; Tan et al., 2006; Zhong and Gurnis, 1995). Similarly, coupled landscape-geodynamic frameworks advance this by simulating feedback, such as tectonic uplift driving erosion, which alters isostatic rebound and sediment routing (e.g., Figure 1.2)(Wolf et al., 2022; Yuan et al., 2024). For example, in subduction zones, models simulate overriding plate deformation and precipitation–erosion interactions, revealing topographic asymmetry (Lu et al., 2024; Schellart, 2017).

Table 1.2: **Correlation between elevation, depositional environments, and geological evidence.** This classification scheme serves as a foundational framework for assigning paleotopography and bathymetry in data-driven global reconstructions. It links specific elevation/depth bins to depositional environments and their corresponding preservation in the geological record (e.g., lithology and metamorphic grade). Adapted from Scotese (2021).

Elevation (m)	**Environment(s)**	**Geological Evidence**
	Continental / Topographic Highs	
10,000 to 4,000	Collisional mountains	High-temperature, high-pressure metamorphics
4,000 to 2,000	Andean-type mountains	Andesites/granodiorites in a continental setting
2,000 to 1,000	Island arc volcanoes	Andesites/granodiorites in a marine setting
	Intracontinental rift shoulders	Adjacent fanglomerates
1,000 to 200	Rift valley	Basalts, lake deposits in grabens
	Some forearc ridges	Tectonic mélanges
	Transitional / Coastal	
200 to 0 (Sea Level)	Coastal plains	Alluvial complexes, lower river systems, major floodplain complexes
	Delta tops	Swamps and channel sands
	Marine / Bathymetric Lows	
0 to −50	Inner shelves	Heterogeneous marine sediments
	Reef-dammed shelves	Bahamian-type carbonates
	Delta fronts	Topset silts and sands
−50 to −200	Outer shelves	Fine sediments, most bioproductites
	Some epeiric basins	Fine clastics or carbonates
	Pro-deltas	Foreset silts and proximal turbidites
−200 to −4,000	Continental slope/rise	Slump/contourite facies
	Mid-ocean ridges	Oceanic crust (< 60 Myr old)
	Pro-delta fans	Bottomset clays and distal turbidites
−4,000 to −6,000	Ocean floors	Pelagic sequences on oceanic crust
−6,000 to −12,000	Ocean trenches	Turbidites on pelagic sequences

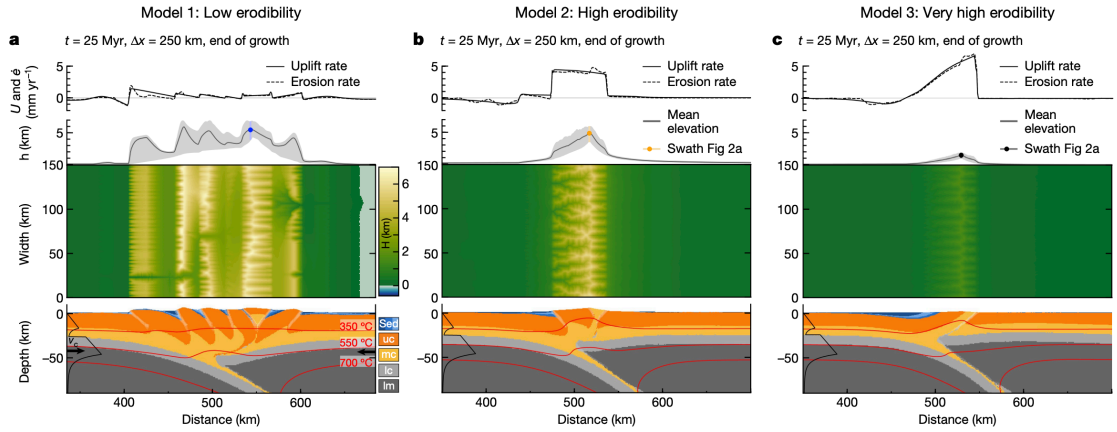

Figure 1.2: **Coupled thermo-mechanical and landscape evolution modeling.** Unlike purely data-driven methods, process-driven approaches simulate surface topography by coupling deep-Earth dynamics with surface processes. Panels (a–c) display model snapshots at the end of shortening for three different convergence scenarios. From bottom to top, each column shows: the crustal/mantle material distribution (sed: sediments; uc/mc/lc: upper/middle/lower crust; lm: lithospheric mantle) with temperature contours; the resulting map-view landscape; and the swath elevation profile with uplift (U) and erosion rates ($\dot{e}$). This demonstrates how tectonic boundary conditions (Δx: convergence magnitude; v_c: convergence rate) directly control the evolution of orogenic topography. Modified from Wolf et al. (2022).

Process-driven models provide a robust framework for studying the drivers and evolution of topography in various tectonic settings; however, they are not computationally designed to reconstruct deep-time paleotopography and are therefore seldom used for global reconstructions. These models also do not incorporate direct proxies into their frameworks. Furthermore, because they are computationally intensive and require appropriate initial conditions, model parameters, and boundary-condition setups, it is challenging to match observed topography by fine-tuning the initial or boundary conditions or model parameters (Bower et al., 2015; Wolf et al., 2022).

1.2 Uniting Process- and Data-Driven Methods for Deep-Time Surface Reconstruction

In this thesis, I develop novel hybrid approaches that integrate data-driven models with the deep mechanistic insights afforded by process-based modelling for paleotopographic reconstructions, thereby overcoming several limitations of either methodology. At its core is a scaffold of plate tectonic reconstructions, which provides both the kinematic architecture and quantitative attributes required for subsequent modelling stages. Plate-tectonic reconstructions are more than static inputs; they actively shape geodynamic simulations and serve as boundary conditions—for example, in modelling passive rift evolution or deep-time mantle evolution using physics–based numerical models as well as supplying input parameters for machine learning models of active margins to understand drivers and reconstruct paleotopography. Our hybrid methodologies cross disciplinary boundaries by orchestrating the fusion of data, numerical model outputs, and algorithms within a unified workflow, resulting in internally coherent and constrained reconstructions with the flex-

ibility to adapt across spatial scales and geological epochs. The outcome is a modelling paradigm that continuously cross-validates physical constraints while respecting empirical signals, thereby increasing credibility and interpretability.

1.2.1 Plate-Tectonic Reconstruction as the Backbone

A common thread running across all chapters of this thesis is the use of plate-tectonic reconstructions that systematically chronicle the shifting configuration and movement of lithospheric plates and their boundaries over geological time (Müller et al., 2019; Seton et al., 2012; Zahirovic et al., 2022). This methodological backbone delineates not only the spatial and temporal occurrence of major boundary types (subduction zones, rift systems, and transform faults) but also maps the progressive assembly and dispersal of continents and the development of ocean basins. In addition to classic rigid plate models, this study investigated deformable plate reconstructions, which allow for the calculation of the temporal evolution of distributed strain rates and stretching factors within deforming boundaries (King and Welford, 2022; Müller et al., 2019). Additionally, from these time-resolved plate reconstruction models, a comprehensive ensemble of kinematic parameters is extracted: absolute and relative plate velocities, trench migration rates, convergence rate, and oceanic lithosphere ages are a subset of the data-driven metrics derived from this extensive foundation. These kinematic quantities have dual and complementary roles. On the one hand, they serve as key boundary and forcing conditions for forward-oriented numerical models of tectonic subsidence and mantle convection. Concurrently, they are distilled into predictive features for machine learning and data-driven frameworks, providing mechanistic inputs required to infer present and past surface elevations along with other geodynamic and climatic factors. In workflows focused on passive rift margins reconstruction, these inputs control tectonic subsidence and basin evolution; in active-margin contexts, they act as critical dynamic links connecting subduction mechanics and mantle flow regimes to the episodic growth and collapse of mountain belts.

1.2.2 Deformable Plate Reconstruction and Subsidence Modelling at Passive Margins

Within the context of passive rift margins, this thesis introduces an innovative class of deformable plate models strategically designed to capture focused extension near the rift axis, characterized by exponentially increasing stretching, rather than the conventional assumption of uniform deformation across the margin. Instead of diffusing extension evenly, these models localize strain to reflect realistic tectonic processes, better mirroring the natural evolution observed in rifted basins (Bott, 1992; Brune et al., 2017; Ebinger et al., 2017). The strain rate, derived from plate reconstructions, serves as a dynamic boundary condition for a continuously deforming computational mesh. This mesh framework was used to simulate the temporal evolution of crustal thickness and solve the governing equations associated with tectonic subsidence (Le Pichon and Sibuet, 1981; McKenzie, 1978). Model optimization was achieved by calibrating the mesh parameters against present-day geophysical datasets, notably the present-day crustal thickness model (Laske et al., 2013; Reguzzoni and Sampietro, 2015). Such calibration ensures that subsidence histories are firmly anchored in observational data while maintaining dynamic consistency with regional tectonics. The implementation of this methodology is demonstrated through its application to the central GoM Basin, which is elaborated in Chapter 2. The resulting

tectonic subsidence curves serve a dual role: they furnish robust quantitative constraints on pre-salt accommodation space, illuminate intervals of missing stratigraphy, and expose basin asymmetry, which is a critical diagnostic for process-based reconstructions of passive-margin paleotopography.

1.2.3 Deep-Time Data Mining Framework for Active Margin Reconstruction

Modelling mountain topography in active margins poses substantial challenges owing to feedbacks among mantle dynamics, plate tectonics, and climate-driven surface processes (Champagnac et al., 2012; Clark, 2007; Wolf et al., 2022; Yuan et al., 2024). Although physically rigorous, numerical modelling approaches often become unwieldy when extrapolated to regional or global scales. Computational demands are escalating, and parameter uncertainty can undermine practical applicability, particularly for deep-time reconstructions spanning millions of years. In response to these complexities, this thesis uses data mining to systematically unravel the physical controls of elevation change in active margins. The initial approach is rooted in explainable artificial intelligence (XAI) (Konstantinov and Utkin, 2021; Lou et al., 2013), in which large-scale spatiotemporal datasets curated from plate reconstructions (Zahirovic et al., 2022), global mantle convection (Bower et al., 2015; Tan et al., 2006; Zhong and Gurnis, 1995) and paleoclimate simulations (Li et al., 2022) are mined using interpretable machine-learning methods. Within this framework, physically meaningful parameters such as subduction volume rate, trench migration rate, upper mantle temperature, vertical flow fields and paleoprecipitation were statistically cross-referenced with present-day mountain belt elevations at active margins. The XAI model is designed to illuminate the complex web of tectonic, mantle, and climatic drivers underpinning topographic diversity. Nonlinear response functions (also called shape functions) reveal how incremental changes in each parameter propagate through the Earth system to impact surface elevation. This interpretability makes the approach particularly powerful for addressing "how" and "why" questions—unpacking the origins and mechanisms underlying mountain diversity across tectonic regimes.

To transition from interpretability to comprehensive spatiotemporal prediction, this study advances a parallel deep learning architecture. Building on insights gleaned from XAI, a neural network was configured to assimilate the full suite of plate- and mantle-derived predictors, alongside targeted climate proxies, i.e., the residence time in equatorial humid belts, to reconstruct active margin paleotopography. This network was initially trained on modern elevation (Amante and Eakins, 2009) sampled globally along active margins, mapping the intricate relationships between kinematic, geodynamic, and climatic inputs. Once validated, temporally resolved plate reconstruction and mantle convection data were injected as time-dependent stimuli, enabling the network to generate paleoelevation predictions across the full extent of the Mesozoic and Cenozoic eras at 1 Myr intervals. The model outputs were vetted against independent established regional reconstructions (Boschman, 2021), paleoelevation proxies, and geochemistry-derived paleoelevation estimates (Liu et al., 2024; Zhou et al., 2025), demonstrating the capacity to recover well-documented uplift episodes and sensitivity to previously unrecognized orogenic events. This hybrid, physics-informed, data-driven paradigm represents a methodological advance that enables robust, scalable, and dynamically consistent reconstructions of Earth's evolving topography in regions defined by complex tectonic process.

Chapter 2

Article 1: A Crustal Thickness Evolution Model for the Mesozoic Central Gulf of Mexico

A Crustal Thickness Evolution Model for the Mesozoic Central Gulf of Mexico

Satyam Pratap Singh[1], Sabin Zahirovic[1], Maria Seton[1], Nicky M. Wright[1], Nicholas Atwood[2], Catherine Belgarde[2], Claire Mallard[1,2], Christopher Alphonso[1], Youseph Ibrahim[1, 3]

[1]EarthByte Group, School of Geosciences, The University of Sydney, NSW 2006, Australia

[2] BHP Minerals Service Co, Tucson, Arizona 85704, USA

[3] Now at Department of Geology and Geophysics, Texas A&M University, TX 77840, United States

Corresponding author: Satyam Pratap Singh (satyampratap.singh@sydney.edu.au)

Highlights:

- We introduce a crustal thickness evolution model for the Gulf of Mexico (GoM) using lithospheric deformation in an existing plate tectonic reconstruction.
- The 40 Myr gap in the GoM's Mesozoic strata is due to rapid subsidence, shifting red bed deposition beneath the Jurassic salt formations.
- An increase in tectonic subsidence from the eastern to western GoM may explain the strong westward deflection of the Cenomanian-Turonian clastic depositional systems.

Key Words:

Crustal Thickness Modelling, GPlates, Gulf of Mexico, Tectonic Subsidence, Red beds

Abstract

The Gulf of Mexico (GoM) is one of the most extensively studied offshore regions; however, its Mesozoic evolution remains uncertain. The thick sedimentary cover and Jurassic salt canopy hinder geophysical imaging and complicate our understanding of the Mesozoic depositional history and crustal architecture. This study introduces a new crustal thickness evolution model for the GoM using time-evolving focused deformation along the rift, where the stretching factors evolve to increase exponentially seaward to the point of continental rupture and ocean crust formation. Our model, which uses an existing rigid plate reconstruction, calculates tectonic subsidence (TS) through time and accounts for crustal stretching and thermal subsidence. The model predictions can be used to explain the depositional history of the pre-salt section and crustal architecture of the GoM Basin. Our model produced a predicted present-day crustal thickness with a root mean square error of 5.6 km with the GEMMA crustal thickness model, a

significant reduction from the 14.8 km error produced by conventional uniform deformation models. The resultant TS of ~1.5 km before the Yucatán Block drifted in the Sinemurian provides routes for red bed deposition through the paleo-drainage systems of the northern GoM as successor basin infilling. The model explains ~40 Myrs of missing sedimentary strata, which we attribute to rapid subsidence in the central GoM, causing a southward shift in red bed deposition, which is presently located beneath the Jurassic salt formations. Furthermore, the model demonstrates that the increased TS towards the western GoM may have resulted in the westward deflection of Cenomanian-Turonian deposits. Our model offers a robust framework for understanding the evolution of global passive rift margins.

1. Introduction

The Gulf of Mexico (GoM) is a geologically complex basin, with its Mesozoic evolution obscured by thick sedimentary cover and pervasive salt tectonics (e.g. Filina et al. 2022). Although advanced 3D seismic reflection data, including on-bottom nodal surveys, provide a means of seeing through the cover, the availability of these datasets for the region is limited because much of it is proprietary. Furthermore, the complex interplay between thick sedimentary layers and widespread mobile salts makes it difficult to conduct detailed seismic imaging and investigate pre-salt structures (e.g. Christeson et al. 2014; Eddy et al. 2014, 2018; Van Avendonk et al. 2015). In addition to seismic data, magnetic data provide a valuable tool for investigating subsurface structures, as they are generally not affected by the presence of sediments and can provide crucial insights into the geological features underlying the sedimentary cover (e.g. García-Reyes and Dyment 2022; Pindell et al. 2016). Despite these technological advances, the absence of drilling samples and complex geological conditions make the reconstruction of the geological evolution of the GoM challenging.

Based on available geophysical data, such as gravity, magnetic anomalies, and geological constraints, numerous tectonic models have been proposed for the formation of the GoM (e.g. Pindell et al. 2016; Nguyen and Mann 2016; Garcia-Reyes and Dyment 2022). Although these models generally agree on a broader framework for the GoM formation, including the initiation of rifting after the Ouachita-Marathon orogeny (which formed from the collision of Laurentia with Gondwana) in the Late Paleozoic and the completion of seafloor spreading by the mid-Early Cretaceous, they vary in several key aspects (e.g. Escalona et al. 2021; García-Reyes and Dyment 2022; Marton and Buffler 1994; Minguez et al. 2020; Nguyen and Mann 2016; Pindell and Kennan 2009). These include the interpretations of Triassic red bed deposition, the timing of continental rifting initiation, the relationship of salt deposition to oceanic crust formation, the mode of breakup, and the pre-rift fit of crustal blocks in the GoM (e.g. Filina et al. 2022). For example, the conventional model for red bed formation suggests deposition in rift grabens during the initial rifting phase (Salvador 1991; Figure 1). However, such a rift-graben structural architecture is not widely observed in 2D or 3D seismic sections across the GoM Basin, suggesting the need for an alternative model for red bed deposition (Milliken 1988; Nicholas and Waddell 1989; Snedden and Galloway 2019). Further complicating the understanding of red bed deposition is the ~40 Myrs hiatus in deposition between Triassic red beds and the overlying Jurassic Louann salt in the northern GoM (e.g. Dickinson et al. 2010; Umbarger 2018; Wiley

2017). In a broader sense, certain regions along the Yucatán margin and eastern GoM Basin (Figures 1 and 2) exhibit thick pre-salt deposits, as evident in reflection seismic sections (e.g., Williams-Rojas et al. 2012; Horn et al. 2016; O'Reilly et al. 2017). However, a precise model for their formation and whether they truly represent red bed deposits remains uncertain because of the challenges posed by the thick sedimentary cover, which impedes drilling efforts.

Seismic refraction and reflection data suggest a significant amount of deformation of the GoM crust throughout its evolution (e.g. Christeson et al. 2014; Eddy et al. 2014; Izquierdo-Llavall et al. 2022; Pindell et al. 2014; Snedden and Galloway 2019). Gravity inversion of crustal thickness (Alvey et al. 2018) reveals a substantial area of thin crust remains within the present-day GoM region. Competing models propose that this thin crust resulted from either hyperextension and mantle exhumation (e.g. Minguez et al. 2020; Pindell et al. 2014), formation of oceanic crust preceding primary seafloor spreading (e.g. Lundin and Doré 2017), or magmatically modified continental crust (Filina and Beutel 2022). The presence of seaward-dipping reflectors (SDRs) in seismic data from the eastern GoM (e.g. Filina et al. 2022) has been proposed as evidence for a magma-rich (volcanic) passive margin. Magma-rich margins form during rifting with abundant magmatism, characterized by basalt flows, dike intrusions, and the development of SDRs. In contrast, magma-poor margins involve minimal volcanic input during rifting, leading to crustal thinning, hyperextension, and the exhumation of mantle rocks directly to the seafloor (e.g. Péron-Pinvidic et al. 2008; Pérez-Gussinye 2013). This is observed in the central to north-eastern GoM and along parts of the Yucatán margin (e.g. Izquierdo-Llavall et al. 2022), where mantle exhumation reflects a tectonic regime dominated by mechanical stretching rather than magmatic accretion. This juxtaposition underscores the unresolved debate regarding the tectonic evolution of the GoM.

Traditional plate tectonic reconstruction models (e.g. Bird et al. 2005; Eddy et al. 2014; García-Reyes and Dyment 2022; Hudec and Norton 2019; Kneller and Johnson 2011; Lundin and Doré 2017; Marton and Buffler 1994; Minguez et al. 2020; Nguyen and Mann 2016; Pindell et al. 2021; Snedden and Galloway 2019), by definition, consider tectonic plates as rigid bodies that limit their ability to account for the complex deformation of the continental crust observed in the GoM. Deformable plate tectonic models address this limitation by incorporating strain rate and crustal deformation modelling along plate boundaries (Gurnis et al. 2018; Müller et al. 2019; King and Welford 2022) into existing rigid plate reconstructions. A key innovation in these models is the use of a deforming mesh, a triangulated topological network that enables the calculation of strain rates, stretching and shortening factors, and crustal thickness through space and time in the deforming regions. However, most existing deformable plate models (e.g. King and Welford 2022; Müller et al. 2019; Nguyen et al. 2022) assume uniform stretching factors, which conflicts with seismic observations of localized, high-stretching factors near rift axes (e.g. Christeson et al. 2014; Mann 2014). This limitation can introduce edge effects around rigid continental blocks, leading to discrepancies between the modelled and observed crustal thickness (King and Welford 2022). To address these challenges, we integrated a new type of deforming mesh into existing rigid plate reconstructions (Kneller and Johnson 2011; Pindell et al. 2021) using pyGPlates, a Python library for GPlates (Gurnis et al. 2018; Müller et al. 2018), without creating a new reconstruction. Unlike previous models, we employed a deforming mesh that concentrated the strain rates toward the rift axis, enhancing strain localization (Section 3.3). Our focused deformation approach improves the alignment of modelled crustal thickness variations

from thicker continental margins to thinner rifted regions. By evaluating 32,400 deforming mesh configurations and optimizing the results by adjusting the deforming mesh parameters to minimize the difference between the predicted and observed present-day crustal thickness (e.g. GEMMA model; Reguzzoni and Sampietro 2015), our approach provides a robust framework for reconstructing the complex tectonic history of the GoM. Furthermore, our model allows us to calculate tectonic subsidence, which refers to the gradual sinking of the Earth's crust owing to plate tectonic processes. Our tectonic subsidence model accounts for lithospheric stretching and thermal evolution, which are key factors controlling the accommodation space for sediment deposition during the early stages of basin formation (Xie and Heller 2009). By integrating realistic strain distributions into existing rigid plate reconstruction, our work advances the understanding of GoM evolution and offers an improved framework for interpreting tectonic subsidence history.

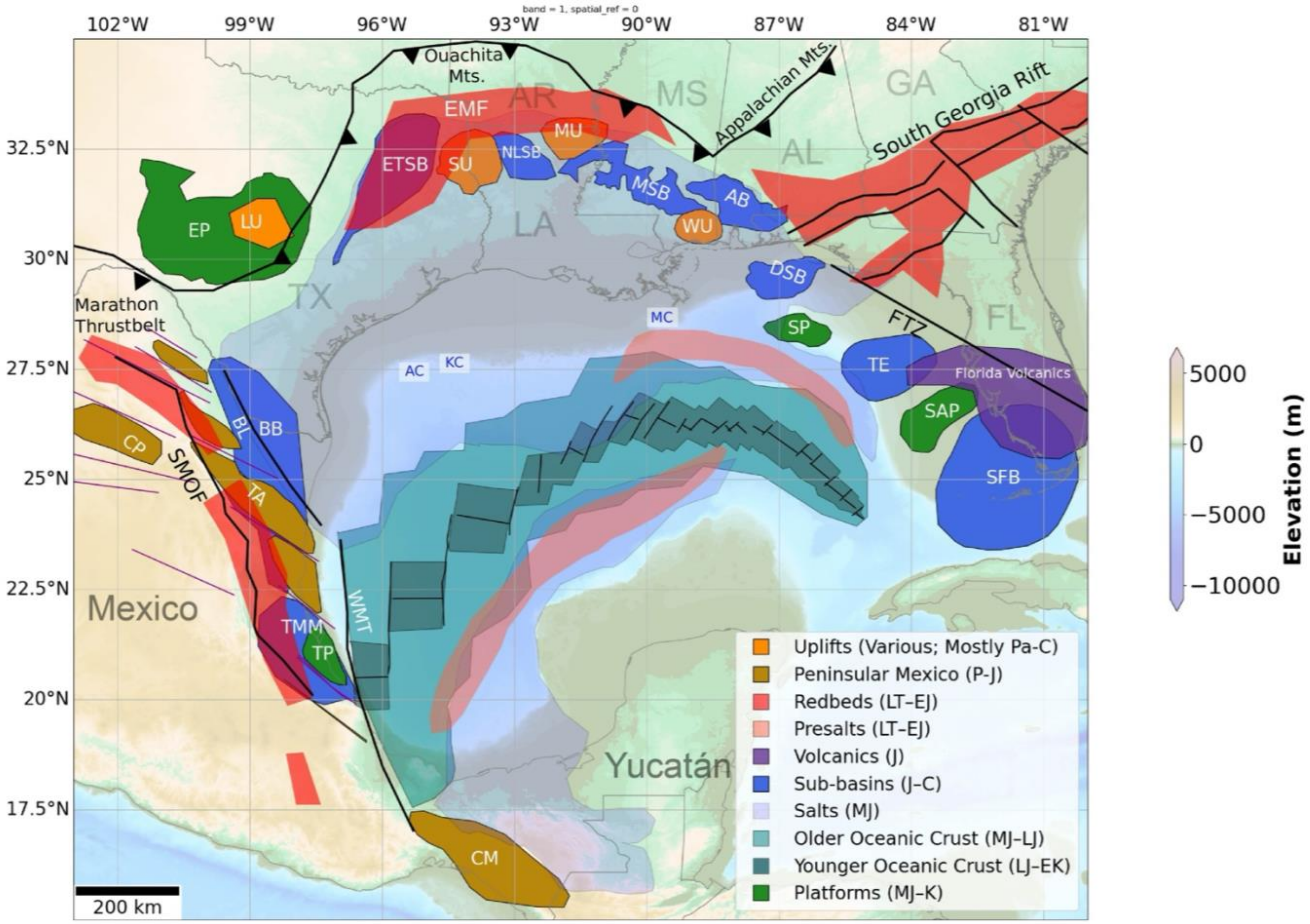

Figure 1: Tectonic elements of the Gulf of Mexico Basin.

The ages listed below are approximate onset ages, representing the first formation or the main initial tectono-stratigraphic phase. Many elements have multiphase histories; detailed local stratigraphy and multiphase histories are cited in the text and referenced literature.

Abbreviations and approximate onset ages (when the feature or its primary tectono-stratigraphic phase first formed): AB, Alabama Basin (Middle Jurassic); AC, Alaminos Canyon (Late Pleistocene–Holocene incision); BB, Burgos Basin (Tertiary: onset Paleocene, main fill Paleocene–Miocene); BL, Burgos Lineament (Mesozoic basement/lineament — Jurassic origin); CM, Chiapas Massif (crystalline basement — Neoproterozoic to Permian); CP, Coahuila Platform (Early Cretaceous carbonate platform, Barremian–Albian); DSB, DeSoto Salt Basin (Middle Jurassic salt province; Louann-type salt deposition); EP, Edwards Platform (Early Cretaceous, Aptian–Albian carbonate platform); ETSB, East Texas Salt Basin (Middle Jurassic salt province); EMF, Eagle Mills Formation (Early Mesozoic syn-rift; Late Triassic–Early Jurassic); FTZ, Florida Transfer Zone (Jurassic rift/transfer related to Gulf opening); KC, Keathley Canyon (Late Neogene–Quaternary incision / canyon evolution with major development in the Pliocene–Pleistocene); LU, Llano Uplift (Precambrian crystalline basement — Mesoproterozoic Grenville-age crust); MC, Mississippi Canyon (Late Pleistocene–Holocene incision and modern canyon); MSB, Mississippi (Interior) Salt Basin (Middle Jurassic salt basin and surrounding depocenter; Louann-age salt initiation); MU, Monroe Uplift (Paleozoic basement element with uplift expression beginning in the Mesozoic and marked reactivation in the Cretaceous–Paleogene); NLSB, North Louisiana Salt Basin (Middle Jurassic salt province); SAP, Sarasota Platform (Florida Platform element with Neogene–Pliocene surface deposits; major Neogene platform accretion); SFB, South Florida Basin (platform initiation during Mesozoic rifting with sustained carbonate growth through the Cretaceous and Cenozoic); SMOF, Sierra Madre Oriental Fault (principal contractional deformation Late Cretaceous–Paleogene); SP, Southern Plateau (Late Jurassic to Early Cretaceous); SU, Sabine Uplift (Triassic–Jurassic mid-rift high origin; later reactivation Cretaceous–Eocene); TA, Tamaulipas Arch (positive arch related to rift/transform margin — Late Jurassic–Early Cretaceous onset); TE, Tampa Embayment (Triassic–Jurassic rift trough / embayment initiation); TMM, Tampico–Misantla–Magiscatzin (basin framework began with Jurassic rifting; major carbonate/platform growth in the Early–Middle Cretaceous); TP, Tuxpan Platform (initiation in Mesozoic with reef/platform growth pronounced in the Albian–Cenomanian); WU, Wiggins Uplift (Paleozoic basement element; relict uplift active during Triassic–Jurassic rifting and influential during Late Jurassic sedimentation); WMT, Western Margin Transform (Jurassic continent–ocean transform associated with Gulf opening). The figure was modified from Snedden and Galloway (2019). The purple lines represent an en echelon fault array from Pindell et al. (2021) that influenced the motion of Peninsular Eastern Mexico during GoM rifting. CM and oceanic crust data were interpreted from Pindell et al. (2021). The pre-salt basins were based on Filina et al. (2022). Ages in figure are abbreviated as follows: Pa, Paleozoic; C, Cenozoic; P, Permian; J, Jurassic; EJ, Early Jurassic; MJ, Middle Jurassic; LJ, Late Jurassic; K, Cretaceous; EK, Early Cretaceous; LK, Late Cretaceous. The US states are abbreviated as TX (Texas), LA (Louisiana), AR (Arkansas), MS (Mississippi), AL (Alabama), and GA (Georgia). The color scale on the right indicates the elevation and bathymetry (in meters) of the underlying background map.

2 Geological History

2.1 Rifting Initiation and Early Magmatism

During the Late Triassic, the Yucatán region was connected to the North American plate, with its northern boundary marked by the Ouachita Mountains and its western boundary demarcated by the Burgos lineament (BL; Pindell et al. 2021; Snedden and Galloway 2019). Continental crustal extension commenced with rift development in eastern North America and back-arc rifting in Mexico (Izquierdo-Llavall et al. 2022; Pindell 1985). The exact timing of rift initiation is difficult to constrain given the limited well controls located in the northern GoM Basin and Mexico and the absence of magnetic isochrons (García-Reyes and Dyment 2022). Nevertheless, most models suggest that rifting started in the Late Triassic to Early Jurassic (~240–190 Ma; e.g. Kneller and Johnson 2011; Pindell and Dewey 1982; Pindell 1985). The rift formation in eastern North America overlapped with a period of intense magmatic activity known as the Central Atlantic Magmatic Province (CAMP). Large quantities of lava, dykes, and sills have been mapped, dating to around 200 Ma, marking a peak in CAMP magmatism (Marzoli et al. 2018). The extension between the Yucatán Block and North America was relatively minor during this time, indicating distinct tectonic behavior compared to rift development in other areas such as the South Georgia Rift (SGR; Pindell et al. 2021; Snedden and Galloway 2019).

2.2 Red bed deposition

After the initiation of rifting and magmatism, the northern and eastmost regions of the GoM, as well as eastern Mexico, witnessed the deposition of distinctive sedimentary units comprising red to greenish-grey shales, white and locally red-colored sandstones, and dolomites, collectively forming the Eagle Mills Formation (Figure 1; Salvador 1991; Snedden and Galloway 2019). Although the formation is considered to be Triassic (Carnian; 237–228.4 Ma) based on limited fossil evidence (Scott et al. 1961; Wood and Benson 2000), its precise age remains uncertain. Traditionally, these red beds were thought to have been deposited within grabens formed during the early Pangea rifting, aligned with the Triassic SGR (Salvador 1991). However, the re-evaluation of older seismic data has cast doubt on the presence of extensive graben systems (Milliken 1988; Nicholas and Waddell 1989; Snedden and Galloway 2019), suggesting that minimal stretching occurred and that the red beds may represent successor basin deposits resulting from accommodation created by post-orogenic subsidence following the Ouachita-Marathon orogeny (Snedden and Galloway 2019).

2.3 Pre-salt sedimentary basins

The U-Pb analyses of well data samples from the northern GoM revealed that the youngest depositional age of the red beds extended only until ~200 Ma, followed by a significant hiatus until the deposition of post-rift salt at 169-170 Ma (Dickinson et al. 2010; Pindell et al. 2021; Umbarger 2018; Wiley 2017). However, the cause of this significant stratal gap remains unclear.

Multiple seismic surveys have identified thick pre-salt sediments along the northern Yucatán margin and eastern GoM (e.g. Horn et al. 2016; O'Reilly et al. 2017; Van Avendonk et al. 2015; Williams-Rojas et al. 2012), although debates persist regarding their exact presence and thickness, particularly in the western GoM, where imaging is complicated by extensive overlying salt. Despite these observations, the precise formation processes of these pre-salt sediments remain elusive owing to the challenges associated with drilling through thick sedimentary layers.

2.4 Rift-to-Drift transition and crustal extension

Existing plate reconstruction models propose that the Yucatán Block underwent anticlockwise rotation during the Early and Middle Jurassic (~200 to ~164 Ma) as it transitioned from the rift to the drift phase, followed by seafloor spreading (e.g. Pindell et al. 2021; Nguyen and Mann 2016). This rift-to-drift transition is associated with various basement features on the easternmost side of the GoM Basin, including the Florida Transfer Zone (FTZ; Marton and Buffler 1994; Pindell et al. 2021; Pindell and Kennan 2009). Evidence of increased Mesozoic extension is indicated by early Mesozoic volcanism in the area south of the FTZ (Figure 1). However, the deformation distribution during this transition remains poorly understood (Marton and Buffler 1994; Pindell et al. 2021). Moreover, the northern GoM Basin is marked by a series of elevated basement blocks associated with thick and less extended continental crust, whereas deep basins containing thick salt accumulations are interspersed between them, characterized by thinner and more extended continental crust (e.g. Buffler and Sawyer 1985; Marton and Buffler 1994). One prominent feature is the Sabine Uplift, interpreted as a mid-rift high—an elevated, fault-bounded block of thicker continental crust that formed between diverging rift basins during the Triassic rifting phase of the GoM (Figure 1; Adams 2007). Geophysical data confirm the Sabine Uplift as a block of thick crust, with deep wells recovering Late Paleozoic sediments and Mississippian volcanic rocks (Marton and Buffler 1994). These Mesozoic-uplifted areas experienced subsequent phases of reactivation and further uplift during the mid-to-late Cretaceous and Paleocene-Eocene (Adams 2007). Although some studies suggest that the Sabine Uplift could have been influenced by a transform fault system, possibly the Saltillo–St. Lawrence Shear System (Adams 2007), the precise mechanism and specific bounding faults remain uncertain. Further investigations are required to fully constrain the role of faulting in uplift and to definitively identify the bounding-transform fault. Variations in crustal stretching and the presence of elevated blocks and deep basins in different regions of the GoM highlight the complex and heterogeneous nature of the rift-to-drift transition.

2.5 SDRs and associated magnetic anomalies

Reflection and refraction seismic data analysis in the north-eastern (e.g. Eddy et al. 2014; Hudec et al. 2013; Imbert 2005; Kneller and Johnson 2011; Liu et al. 2019; Lundin and Doré 2017; Rowan 2014) and southern parts of the GoM Basin, along the Yucatán margin (e.g. Filina and Hartford 2021; Hudec and Norton 2019; O'Reilly et al. 2017; Steier and Mann 2019; Williams-Rojas et al. 2012), have revealed the presence of seaward-dipping reflections known as SDRs (Figure 2b). While some studies have suggested that these SDR complexes exhibit significant deformation and are formed due to intense magmatic activity, probably during the CAMP magmatism event (Filina and Beutel 2022), others have suggested a magma-poor origin for these

SDRs (Curry et al. 2018; Minguez et al. 2020). For instance, Minguez et al. (2020) suggested that these reflectors may be syn-rift volcanic fills. Notably, these SDRs align with prominent magnetic anomalies, such as the Florida magnetic anomalies (FMA; Figure 2), suggesting a close association with rift-related magmatism (e.g. Mjelde et al. 2008; Talwani et al. 1995). Alternatively, for a magma-poor model, such a magnetic signature can also be explained by intrusions in the lower part of a horst-like crustal block (i.e., the Southern Plateau; Figure 1; Minguez et al. 2020). Nevertheless, magnetic anomalies exhibit distinct characteristics, such as long wavelengths and rounded or oblate shapes. One particularly noteworthy magnetic high running north-south off the western Yucatán shelf margin is the Campeche magnetic anomaly (CMA; Figure 2). The CMA shares similarities in shape and intensity with prominent Houston magnetic anomalies (HMA; Figure 2) and the FMA found along the northern continental margin of the GoM (Pindell et al. 2016). Deep seismic data suggest that the CMA (Goswami et al. 2016) and FMA (Imbert and Philippe 2005) are likely associated with volcanic flows formed within the syn-rift sections of rift basins. However, owing to their significant burial depths, it remains challenging to determine whether they are SDRs related to magmatic activity. A similar origin has been proposed for the HMA (Mickus et al. 2009). Furthermore, the Yucatán magnetic anomaly (Figure 2; YMA) in the southern GoM Basin also coincides with the interpreted SDRs observed in seismic images (Steier and Mann 2019; Filina et al. 2022). The identification of SDRs and their association with magnetic anomalies provides crucial insights into the magmatic processes and tectonic evolution of the GoM.

2.6. Seafloor spreading

The transition from rifting to the seafloor spreading phase in the GoM is closely linked to the mid-Jurassic basin evolution, marked by the widespread deposition of the Louann Salt. Strontium isotope data constrain the salt deposition event to the Bajocian (~170–169 Ma; Pindell et al. 2021), placing it near the transition from continental rifting to oceanic spreading. Although salt deposition provides a key chronological marker, the precise timing and nature of the underlying crust remain debatable (e.g. Filina et al. 2022). Various models have been proposed that rely on geological and geophysical observations to determine the timing and nature of seafloor spreading (e.g. Anderson and Schmidt 1983; Escalona et al. 2021; García-Reyes and Dyment 2022; Marton and Buffler 1994; Minguez et al. 2020; Nguyen and Mann 2016; Pindell and Kennan 2009; Pindell 1985).

Satellite-derived gravity data have advanced the understanding of the oceanic domain of the GoM, enabling the interpretation of Extinct Spreading Centres (ESC) offset by a series of curvilinear fracture zones (e.g. Minguez et al. 2020; Sandwell et al. 2014). Additionally, the magnetic data revealed the presence of an Extinct Spreading Ridge Anomaly (ESRA; Figure 2b). The extinct ridge and continent-ocean boundary (COB) distribution in the eastern GoM indicates structural asymmetry in the basin (Figures 1 and 2b). Hudec et al. (2013) proposed that this asymmetry resulted from an asymmetrical basin opening, whereas Filina et al. (2020) suggested that it could be explained by ridge propagation in the eastern basin. Another model proposes that mantle exhumation followed by symmetrical oceanic spreading could account for the observed asymmetry (Minguez et al. 2020). This interpretation is based on minor magnetic anomalies and their conjugates, known as En Echelon Anomalies (EEA), in the eastern GoM (Figure 2b;

Minguez et al. 2020). The EEA were modelled as a serpentinized exhumed mantle surrounding the oceanic crust rather than as direct evidence of seafloor spreading (Minguez et al. 2020). Support for the mantle exhumation model also comes from seismic data in the eastern GoM, which reveal ridge-like basement highs (Pindell et al. 2014). These features have been interpreted as a mechanical boundary between the crust and mantle that facilitates mantle exhumation (Pindell et al. 2014). The basement highs correlate with the EEA magnetic anomalies and are bordered by the outer trough, which exhibits basement deepening of approximately 2 km adjacent to the inferred oceanic crust (Figure 2b).

A recent regional magnetic anomaly map shows a symmetrical pattern of east-west oriented conjugate intermediate-wavelength magnetic anomalies, aligned with the EEA in the eastern GoM (García-Reyes and Dyment 2022). This pattern has been interpreted as evidence of seafloor spreading, although the location of the interpreted extinct spreading center differs from that of other models, aligning instead with the symmetry axis of the basin's conjugate magnetic anomalies. In the western GoM, the BAHA High (Figure 2b), a subsurface basement high, exhibited a structural relief of approximately 3 km, as observed in the seismic data. Notably, the associated magnetic anomaly signature was less distinct in this region (Figure 2). The origin of the BAHA High remains debatable. Some interpretations suggest that it represents older oceanic crust formed during an early stage of spreading, while others propose that it is a hyperextended continental crust or exhumed mantle (Hudec and Norton 2019; Pindell et al. 2021; Hudec et al. 2019). This complexity highlights the intricate evolution of the crustal architecture during the development of the GoM Basin.

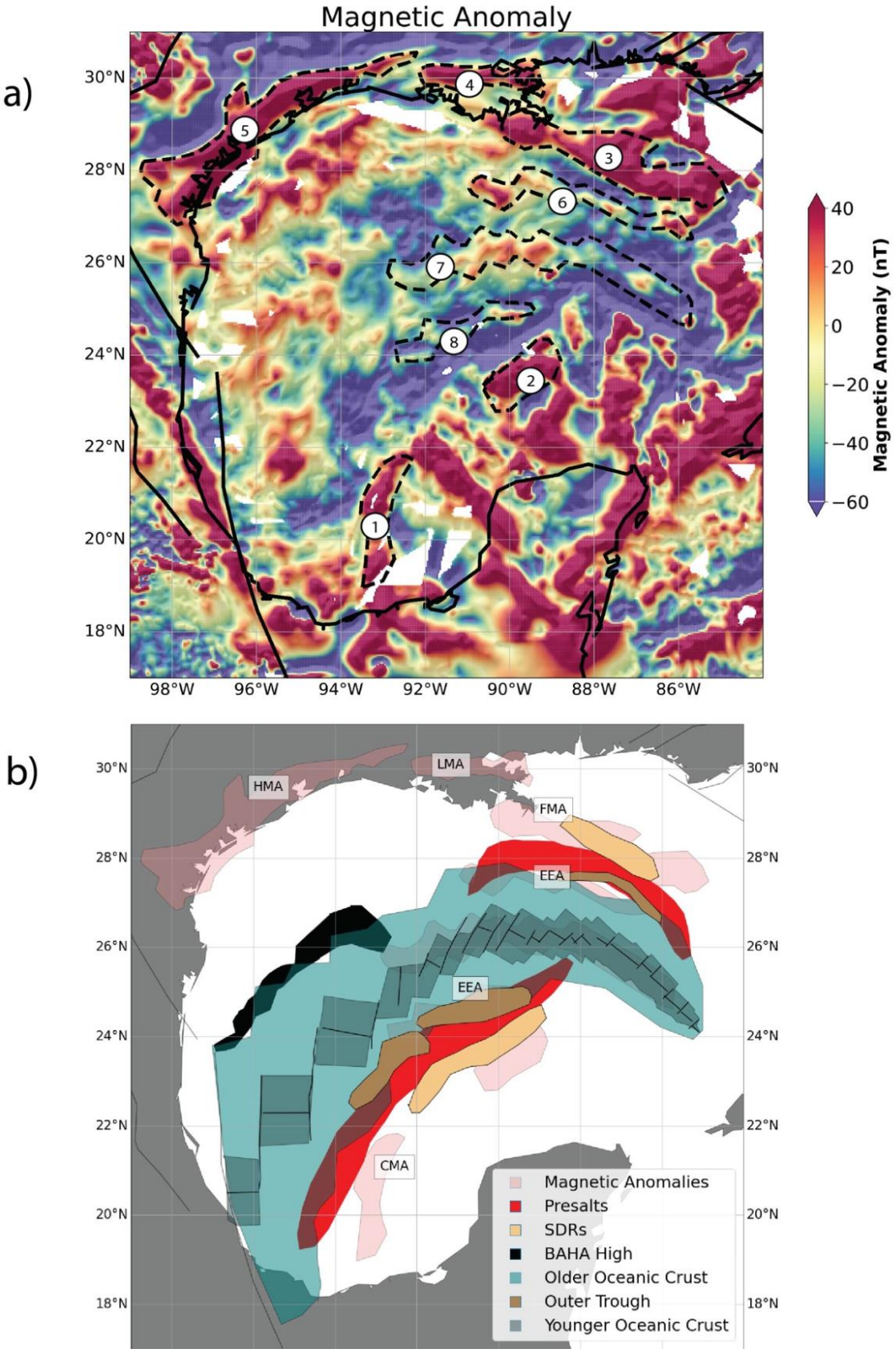
a)
Magnetic Anomaly
30°N
28°N
26°N
24°N
22°N
20°N
18°N
98°W
96°W
94°W
92°W
90°W
88°W
86°W
1
2
3
4
5
6
7
8
40
20
0
−20
−40
−60
Magnetic Anomaly (nT)
b)
HMA
LMA
FMA
EEA
EEA
CMA
Magnetic Anomalies
Presalts
SDRs
BAHA High
Older Oceanic Crust
Outer Trough
Younger Oceanic Crust

Figure 2. a) Magnetic anomaly map of the region (Meyer et al. 2017) showing important magnetic highs): (1) Campeche magnetic anomaly (CMA), (2) Yucatán magnetic anomaly (YMA), (3) Florida magnetic anomaly (FMA), (4) Louisiana magnetic anomaly (LMA), (5) Houston Magnetic Anomaly (HMA), (6) and (8) En Echelon anomalies (EEA), and (7) Extinct Spreading Ridge Anomaly (ESRA). b) An illustration of the important geophysical interpretations in the region compiled from different sources. The presence of SDRs aligned with significant magnetic anomalies suggests a strong association with rift-related magmatism in the eastern GoM. HMA, LMA, and CMA are all characterized by similar long-wavelength, rounded, or oblate-shaped anomaly patterns. The HMA and CMA likely indicate volcanic flows formed within the syn-rift sections of rift basins (see text), although confirming their nature is challenging because of their considerable burial depths. Seismic reflection data have revealed the presence of ridge-like basement highs, interpreted as a mechanical boundary between the crust and mantle, facilitating mantle exhumation (Minguez et al. 2020; Pindell et al. 2014). These basement highs correlate well with the set of EEA anomalies. Moreover, these basement highs are bordered by the outer trough, which exhibits a deepening of the basement by 2 km adjacent to the inferred oceanic crust. The BAHA high, a subsurface basement high located in the western GoM, exhibits a structural relief of approximately 3 km, as observed in the seismic data. Notably, the magnetic anomaly signature associated with this feature is less distinct in this area. The origin of the BAHA high is still debated, with some initial interpretations suggesting that it is older oceanic crust formed during an early stage of spreading, while others propose a hyperextended continental crust or exhumed mantle (Hudec and Norton 2019; Hudec et al. 2019; Pindell et al. 2021). The interpretation of older and younger oceanic crust is based on Pindell et al. (2021), which was used as the input rigid plate model for modelling deformation in this study.

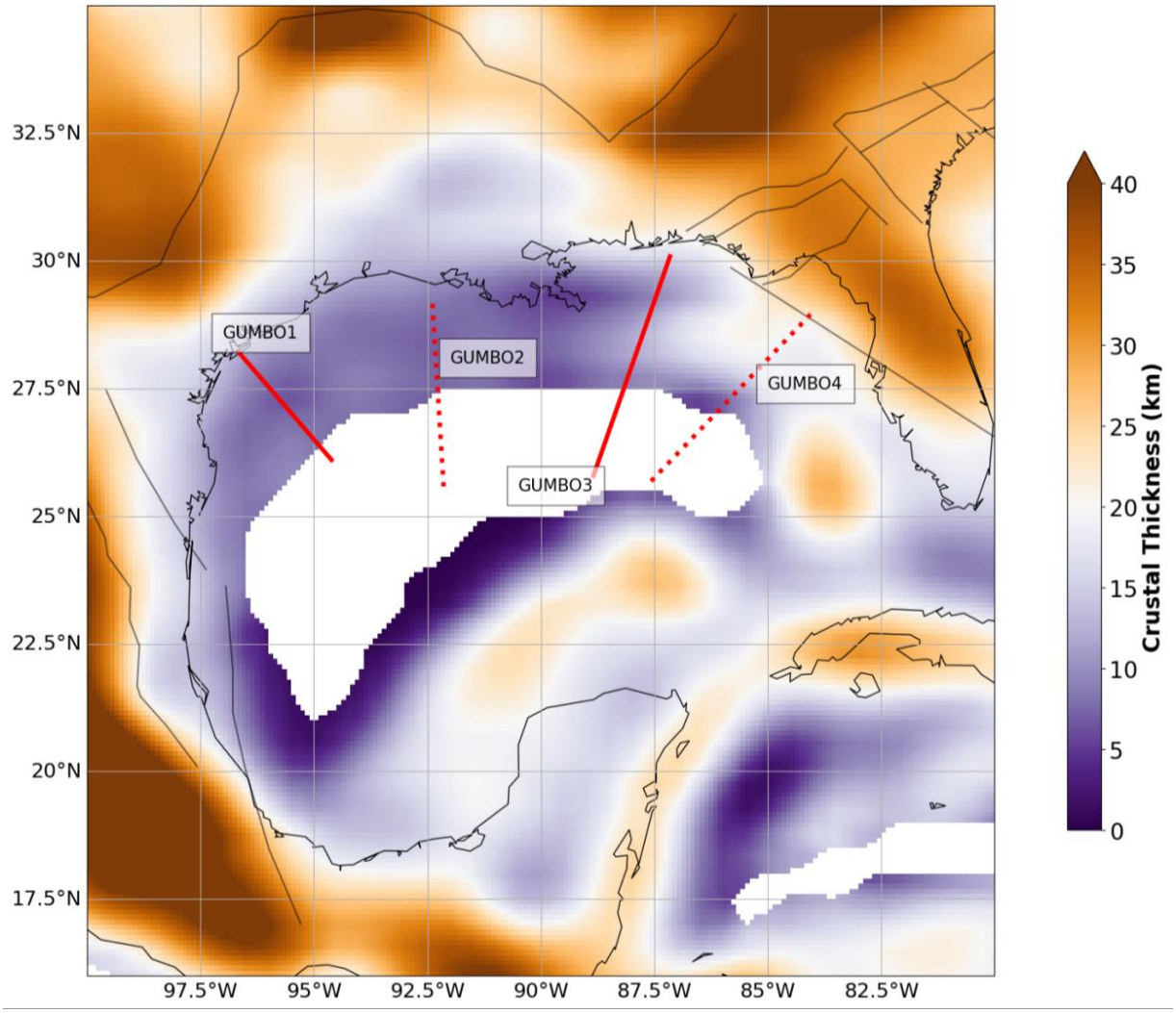

Figure 3. The GEMMA crustal thickness model (Reguzzoni and Sampietro 2015) was smoothed and up-sampled at a 0.1° resolution for plotting. Optimization was performed on the original 0.5° grid (see Section 3.4 and Supplementary Figure S2 for details). The profiles of the GUMBO experiments referred to in this study are depicted as red solid and dashed lines (Christeson et al. 2014; Eddy et al. 2018, 2014; Van Avendonk et al. 015). A schematic evolution of the GoM is presented along the red solid lines in Figure 10, whereas the red dashed lines are discussed in the text but not illustrated. GUMBO1 lies along the western GoM, whereas GUMBO3 and GUMBO4 lie along the eastern GoM. GUMBO2 lies in the central GoM.

3. Methodology

Our study developed a new approach to model lithospheric deformation within rift zones by integrating a new type of deforming mesh into existing rigid plate tectonic reconstructions using pyGPlates (Gurnis et al. 2018; Müller et al. 2018; more details in the Supplementary Information). We implemented a deforming mesh characterized by an exponentially increasing strain rate toward the rift axis, controlled by mesh parameters (Section 3.3), which we refer to as focused deformation. This approach enhances strain localization by capturing the transition from a highly stretched crust near the rift axes to a less deformed crust toward the continental margins, improving the agreement with the observed variations in the present-day crustal thickness of the GoM Basin.

Our workflow builds upon existing plate motion models for key tectonic blocks, including North America, Yucatán, and South America (Section 3.1). These rotations serve as boundary conditions for the forward modelling of deformation within a geologically defined deformable mesh at the start of the rifting. By expressing the relative motion and velocities of the triangulated nodes within the mesh as finite rotations, we calculated the strain rates associated with rifting (Appendix A; Müller et al. 2019). Our approach further enabled the reconstruction of finite strain histories at specific locations within the mesh, allowing the calculation of crustal stretching, thinning, and thickness changes over time (Appendix B). Our framework automatically selects the optimal deformation mesh by iteratively comparing the modelled crustal thickness at present with a geophysically derived crustal thickness (e.g. Reguzzoni and Sampietro 2015) model to minimize misfit, a process we refer to as optimization (more details in Section 3.4). Thus, we assume that by minimizing the misfit, we can gain insight into the evolution of crustal architecture throughout the rift-to-drift phases of the GoM.

The temporal evolution of lithospheric deformation and thermal cooling was used to estimate tectonic subsidence, which is defined as the component of subsidence driven by lithospheric stretching and thermal re-equilibration (McKenzie 1978; Jarvis and McKenzie 1980; Xie and Heller 2009). This excludes sediment loading, which contributes to the total subsidence. Although our workflow also accounts for sediment and salt loading by incorporating sediment thickness estimates and isostatic adjustments (Appendix D), our primary focus is on understanding tectonic processes during rifting and early basin formation, when tectonic subsidence dominates. During the Late Triassic–Middle Jurassic, sedimentation was low, especially in the central GoM, owing to the development of carbonate platforms (Figure 1; Snedden et al. 2016; Sweet et al. 2022). Even in northern GoM regions with high sediment input, backstripping shows that 50–60% of the Jurassic subsidence was tectonic (Li 2006). Accordingly, sediment loading is addressed in the Supplementary Information (Appendix D). Despite uncertainties in this interval due to salt cover and limited control (Filina et al. 2022), our model reconstructs deformation and subsidence histories to shed light on this poorly understood phase of GoM tectonic evolution.

3.1 Rationale for Using the Rigid Plate Tectonic Reconstruction Framework

The Carnian age (~237–228.4 Ma) of the Eagle Mills Formation suggests that rifting may have been initiated during the Late Triassic (Scott et al. 1961; Wood and Benson 2000). To account for this, it is critical that our model incorporates finite rotations of the Yucatán Block, which reflect its position at the time. Unfortunately, most GoM plate reconstruction models (e.g. Escalona et al. 2021; Filina and Beutel 2022; García-Reyes and Dyment 2022; Minguez et al. 2020; Nguyen and Mann 2016; Nguyen et al. 2022; Pindell and Kennan 2009) only mention minor extensions prior to CAMP without quantifying the amount of extension or providing explicit finite rotations for the Yucatán Block. This can be a significant limitation because lithospheric deformation during the syn-rift phase may directly affect the crustal thickness and tectonic subsidence. In contrast, Kneller and Johnson's (2011) reconstruction offers a model indicating that the extension began in the Carnian. Therefore, we adopted their plate reconstruction model for the pre-rift position at 230 Ma. Kneller and Johnson's (2011) reconstruction model integrated gravity and magnetic data, bedrock geology, seismic reflection and refraction profiles, receiver function studies, isostatic crustal thickness models, and well data to constrain a deforming model for the Central Atlantic and a rigid plate model for the GoM. Because Kneller and Johnson's (2011) model does not explicitly provide rotation parameters, we estimated the pre-rift Euler rotation of the Yucatán Block using georeferencing techniques. However, Kneller and Johnson (2011) proposed seafloor spreading in the Late Aalenian (~176 Ma) with Callovian salt deposition (~161–163 Ma). With the salt now identified as Bajocian rather than Callovian–early Oxfordian (Pindell et al. 2021) — potentially up to 9 Myrs older — the timing of the rift-drift transition is also likely different, suggesting a need to adjust the plate tectonic reconstruction accordingly. Therefore, to model the rift-to-drift transition, we adopted the recently published plate reconstruction model of Pindell et al. (2021). This model was selected because it offers an updated, internally consistent synthesis of the Permo-Triassic assembly and Mesozoic evolution of the GoM. Notably, Pindell et al. (2021) integrated multiple lines of evidence, including magnetic data and new geochronological constraints (e.g. the Bajocian age for salt deposition determined using $^{87}Sr/^{86}Sr$ isotopes). Pindell et al. (2021) documented the transition from continental rifting to oceanic spreading, with a distinct syn-drift shift in the pole of rotation at approximately 150 Ma. Moreover, its detailed kinematic framework along the inferred deformation region (such as the Burgos Lineament, Peninsular Mexico, FTZ, and Ouachita–Marathon belt) is useful in defining the boundaries of our deformation mesh (see Section 3.2), which is not available in other published models. Although we used the Pindell et al. (2021) model from 195 Ma onward, it acknowledges that syn-rift lithospheric extension in the GoM region spanned from the Late Triassic (Carnian) to approximately Bajocian time, with total Triassic extension magnitudes (100–150 km) roughly consistent with those produced by the Kneller and Johnson (2011) model prior to 195 Ma. Thus, the Late Triassic extension in our modelling framework aligns with Kneller and Johnson's reconstructions, followed by the updated synthesis of Pindell et al. (2021) for the subsequent evolution. For the motion of the South American block, we used the Müller et al. (2019) model, which incorporates the rotation of Heine et al. (2013). However, there is a slight discrepancy between Pindell et al. (2021) and Heine et al. (2013), with the former suggesting a slightly tighter fit for the eastern Equatorial Atlantic and a slightly looser fit for the western Equatorial Atlantic.

3.2 Defining Deformation Zone

To capture lithospheric deformation during the rifting of the GoM Basin, we defined an initial deforming mesh on the Yucatán and North American blocks, delineating the extended and unextended regions as they existed at the onset of rifting, approximately 230 Ma. The extent of deformation landward from the passive margin was determined by the unstretched continental crust limit (UCCL; Nemčok 2016), which marks the transition from an unextended to thinned continental lithosphere. The northern boundary aligns with the Ouachita-Marathon thrust belt (e.g. Dickinson et al. 2010; Snedden and Galloway 2019), representing the boundary between the unextended North American continental lithosphere and the rifted margin (Figures 1 and 3). The eastern boundary of our deformation zone is defined by the Burgos Lineament and the Western Margin Transform (Figure 1). The southern boundary is defined by the Yucatán Block, although the Chiapas Block was excluded because it did not become part of the Yucatán until the Valanginian (Pindell et al. 2021). Within our mesh, regions such as the Sabine and Monroe Uplifts (Figure 1) were treated as rigid, non-deforming blocks. These uplifts, interpreted as Triassic mid-rift, high-standing fault-bounded blocks composed of thicker continental crust (Adams 2007; Salvador 1991; Snedden and Galloway 2019), were incorporated as fixed nodes in the model. This approach prevents unrealistic deformation patterns in areas dominated by brittle faulting and high-frequency variations in crustal thickness, which cannot be captured by our model.

While deformation extended across broader regions (purple region in Figure 6), such as eastern Mexico, the Florida-Bahamas platform, and the Yucatán Block itself, we focused our mesh on the northern and central GoM Basin. This decision reflects the primary goal of our study, which is to model deformation in the region directly contributing to syn-rift subsidence and crustal thinning in the central GoM. For areas outside this focus, such as eastern Mexico, we applied a uniform deformation mesh derived from previous models (e.g. Müller et al. 2019; Pindell et al. 2021). We acknowledge that deformation beyond the designed mesh likely influences the overall kinematic evolution of the GoM. This does not imply that the excluded regions did not undergo deformation or that these motions did not affect the deformation in the GoM. These factors have already been accounted for in the base rigid plate reconstruction model (Pindell et al. 2021). This means that we avoided modelling the strain rate and crustal thickness evolution in regions where the deformation was too complex to be modelled by either uniform or focused deformation. Moreover, the boundaries between rigid and deforming regions introduce potential uncertainties in crustal thickness and tectonic subsidence estimates. We did not attempt to optimize these boundaries explicitly. Future studies may refine these boundaries by incorporating additional seismic, well, and gravity data to improve the resolution of the deformation mesh and crustal thickness calculations.

3.3 Focused Deformation Modelling

Conventional deforming meshes typically assume uniform thinning throughout the deforming mesh when calculating crustal thickness and tectonic subsidence (Figure 4a; Müller et al. 2019). However, this assumption is not valid for many geological scenarios. Seismic imaging of passive margins such as the GoM and around the globe has consistently shown that the unextended continental crust tends to be thicker, and as we move towards the rift axis, the crustal thickness decreases (Huerta and Harry 2012; Christeson et al. 2014; Mann 2014; Mann 2022). Moreover, differential subsidence patterns are commonly observed in basins during the rifting and breakup phases, resulting in enhanced subsidence towards the seaward side of the hinge zone (Xie and Heller 2009). This is because of the focused extensional strain distribution, which can be attributed to brittle and ductile weakening processes (e.g. Brune et al. 2023). For instance, lithospheric necking can cause localized thinning via a large-scale thermal weakening process that transforms the originally cold and strong lithosphere into a hotter and weaker mantle (e.g Chenin et al. 2018). Variations in crustal strength and viscosity can also lead to uneven deformation, resulting in focused deformation (Bott 1992; Ebinger et al. 2017). To capture these complexities, numerical models that incorporate nonuniform thinning and variable strain distributions are necessary. To address this, we defined a new, focused deforming mesh for the GoM (Figure 4a). In the focused deforming mesh, the strain rate evolves over time to progressively concentrate toward the rift axis until continental rupture occurs and oceanic crust forms (Figure 4a). This is accomplished by introducing additional points within the deforming network and assigning velocities to these points such that the strain rate increases exponentially along the stretching direction from the unstretched edge of the rift toward its center (Figures 4b and c). This behavior is governed by three key parameters:

- **Exponential Stretching Coefficient (C):** This coefficient controls the spatial variation in the strain rate across the rift profile. The strain rate increases exponentially from the unstretched edge (x=0) toward the rift axis (x=1), following the equation

$$\dot{\varepsilon}(x) = \dot{\varepsilon_0} \cdot e^{cx} \cdot \frac{c}{(e^c - 1)}$$

  where $\dot{\varepsilon_0}$ is the strain rate of the unsubdivided mesh, C is the rate of exponential increase, and x is the normalized distance (0 at the unstretched edge and 1 at the rift axis). For example, C=1.0 results in strain rates at the unstretched edge (x=0) being 58% of $\dot{\varepsilon_0}$, while rates at the rift axis (x=1) are 158% of $\dot{\varepsilon_0}$.

- **Strain Rate Resolution:** This parameter determines how closely the mesh must match the exponential strain rate profile across the rift. This sets a tolerance for the extent to which the strain rate can deviate from the ideal exponential curve before further subdivision of the mesh. For example, if the strain rate resolution was set to 4×10^{-17} s^{-1}, the mesh was refined until the strain rate differences between adjacent elements were smaller than this value. This ensured that the strain rate distribution was physically accurate and matched the exponential profile required by the model.

- **Rift Edge Length Threshold:** This parameter sets the minimum length (in degrees) for the rift edges in the mesh. Edges shorter than this threshold were not further subdivided, regardless of the strain rate resolution. This prevents excessive refinement, which could lead to computational inefficiency or an unnecessarily high resolution in areas where it is not required (Figure 4b and c). This ensures that the mesh remains computationally manageable by limiting the number of subdivisions in regions where further refinement would not significantly improve the accuracy.

Together, these parameters balance the need for physical accuracy in the strain-rate distribution with the computational efficiency in mesh refinement. This approach replicates the observed crustal thinning patterns at passive margins (e.g. Chenin et al. 2018), where the strain localizes into narrow zones (e.g. Tetreault and Buiter 2018).

3.4 Mesh Parameter Optimisation

The strain rate within the deforming mesh, combined with the initial crustal thickness at the start of rift initiation, was used to model the crustal thickness using the mass conservation equation (Appendix B). However, the optimal values for the key deformation parameters, that is, the exponential stretching coefficient, strain rate resolution, rift edge length threshold, and initial crustal thickness, are not known a priori (Table 1). To determine these values, we performed a systematic optimization, which, in this context, refers to a parametric search aimed at minimizing the difference between our model's output and independent observations. Specifically, we computed the present-day crustal thickness using our forward model implemented in pyGPlates and then compared these results with independent geophysical datasets, including the GEMMA model (Figure 3; Reguzzoni and Sampietro 2015), CRUST1.0 model (Laske et al. 2013), and crustal thickness estimates from GUMBO seismic lines (Filina 2019; Van Avendonk et al. 2015). The model parameters were adjusted over 32,400 different combinations by varying the exponential stretching coefficient, rift edge length threshold, strain rate resolution, and initial crustal thickness, with the goal of minimizing the root mean square error (RMSE) between the calculated crustal thickness (at 0 Ma) and the values provided by these reference models. The RMSE serves as a quantitative metric of model accuracy because it penalizes large deviations more than smaller deviations, ensuring that models with significant mismatches receive higher error scores. This approach offers a comprehensive assessment of model performance. Although we optimized the model against both GEMMA and CRUST1.0 (Supplementary Figures S2–S4, Supplementary Animations), we prefer the GEMMA model because it incorporates constraints from CRUST2.0 (Bassin et al. 2000) along with GOCE-derived gravity data, which includes uncertainty estimates (~3 km) that are particularly relevant for our study area (Supplementary Figures S5). In comparison, CRUST1.0 provided thickness estimates that differed by 10–15 km from the GEMMA and GUMBO seismic data. Because GEMMA and the GUMBO seismic profiles show strong mutual agreement, the large discrepancy in CRUST1.0 suggests it is less representative of the crustal architecture in this specific region. Consequently, we selected GEMMA as the primary reference because it provides a more robust consensus between satellite gravity data and localized seismic observations, supported by quantifiable uncertainty estimates.

3.5 Limitations and Assumptions

Although our methodology provides a robust framework, certain limitations must be acknowledged. Our study employed one of several available plate reconstructions as a boundary condition for numerical modelling. This study focused on a single reconstruction owing to the extensive number of model runs performed to systematically sample the parameter space. Exploring alternative reconstructions could further clarify the influence of the boundary conditions on the model outputs. With the availability of new open-source plate reconstructions, future studies should incorporate these datasets to evaluate their impacts. In this study, we assumed that the crustal and mantle densities were constant. In reality, lateral and vertical variations in density occur because of compositional differences and metamorphic transformations, particularly in rifted and extended crustal areas. However, incorporating these complexities requires additional constraints that are not available on a basin-wide scale. Moreover, in our study, we assumed that the degree of thinning (β) was approximately the same for both the crust and **sub-crustal lithospheric mantle (together comprising the lithosphere)** in the GoM. We acknowledge that more complex scenarios involving depth-dependent stretching or simple shear could yield slightly different outcomes, which is an avenue worth exploring in future studies. Additionally, our model does not explicitly include the effects of orogenic loading or mantle-driven dynamic topography. These factors became particularly significant in the Cretaceous–Neogene but were less influential during the Jurassic when tectonic subsidence dominated. Future studies should incorporate these factors to further improve the model.

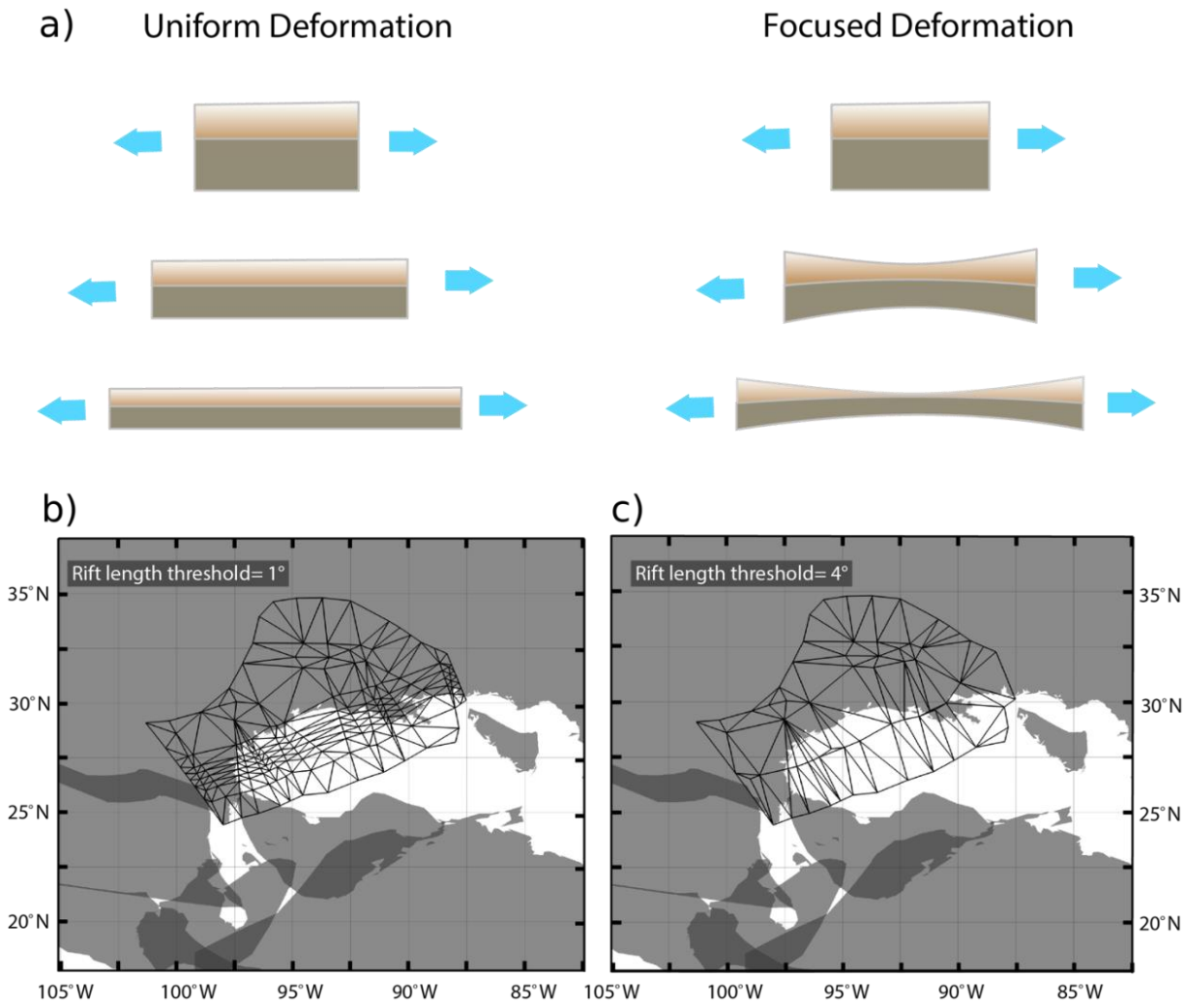

Figure 4. a) Model showing the difference between uniform and focused deformation, where the top layer represents the crust and the bottom layer represents the lithospheric mantle. **b-c**) Deformation topology network (black mesh) used in this study and comparison of parameters showing how the rift edge length threshold is used to divide the strain rate in the deformation mesh. Panel b) has a rift edge length threshold value of 1°, whereas c) has a rift edge length threshold value of 4°. The strain rate resolution parameter guides the decision on when to subdivide the network (perpendicular to the rift direction) to match the exponential curve within a certain tolerance, thereby controlling the strain rate perpendicular to the rift. The rift edge length threshold parameter further controls the division of the topological network. The minimum possible element length of the topological network cannot be less than this parameter, thereby governing the non-uniform spatial variation of the strain rate. The grey blocks refer to reconstructed present-day coastlines, which overlap in the regions of tighter pre-Pangea fit. The north-eastern South America has also undergone significant deformation due to north Andean Rifting in the mid-Jurassic. However, these regions were outside the scope of this study.

Table 1. Parameters used in this study to generate our optimized deforming model. The crustal density values for our model were derived from the density calculations of GUMBO1 and GUMB02, as detailed by Filina (2019). Similarly, the water density was referenced from Smith and Sandwell (1997), whereas the mantle density was obtained from Mooney and Kaban (2010). For this study, we assumed a standard lithospheric thickness of 125 km, which is consistent with the thickness estimate derived from the shear wave velocity model within the unstretched region (131 ± 28 km; Ho et al. 2016).

Parameters	**Values**
Initial Crustal Thickness (H_i)	Optimized constant
Lithospheric Thickness (L)	125 km
Density of Crust (ρ_c)	2800 kg/m^3
Density of Mantle (ρ_m)	3330 kg/m^3
Density of water (ρ_w)	1030 kg/m^3
Exponent Stretching Factor (C)	Optimized constant
Rift Edge Length Threshold	Optimized constant
Strain Rate Resolution	Optimized constant
Thermal Expansion coefficient (α)	3.28e-5 $^oC^{-1}$
Thermal Diffusivity	8.04e-7 m^2/s

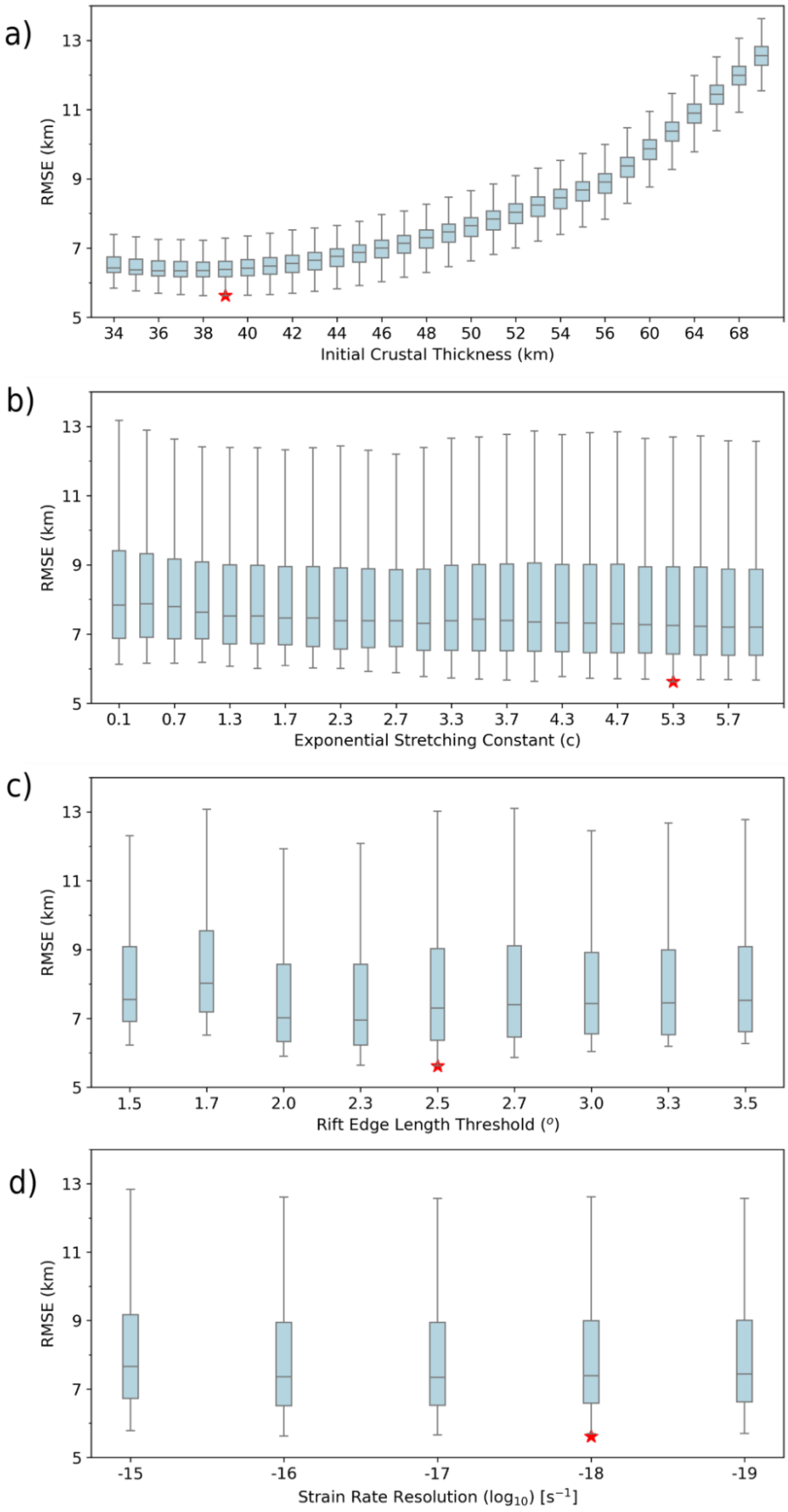
a)
RMSE (km)
Initial Crustal Thickness (km)
b)
RMSE (km)
Exponential Stretching Constant (c)
c)
RMSE (km)
Rift Edge Length Threshold (°)
d)
RMSE (km)
Strain Rate Resolution (log10) [s−1]

Figure 5. Our optimization of 32,400 different focused deforming mesh configurations yielded the following results: a) the initial crustal thickness at the start of the model, b) the exponential stretching coefficient, c) the rift edge length threshold, and d) the strain rate resolution. RMSE, calculated between crustal thickness estimates at 0 Ma and the known GEMMA crustal thickness model (Reguzzoni and Sampietro 2015), was used as the performance metric. The red star marks the minimum RMSE value found during the simultaneous optimization of the initial crustal thickness and the focused deformation mesh parameters defined in Section 3.3.

4 Results

4.1. Optimisation

Through our optimization across 32,400 configurations, we identified the specific parameter combination that produced the lowest overall error (the global minimum in misfit). This optimal model yielded an RMSE of 5.6 km when compared with the GEMMA model (Reguzzoni and Sampietro 2015), with an exponential stretching coefficient of 5.3, and an estimated initial crustal thickness prior to GoM stretching of 39 km (Figure 5). Notably, the rift edge length threshold and strain rate resolution parameters, which are crucial for achieving the closest match, consistently fell within the ranges of 2.25–2.75° and 10^{-16} to 10^{-17} s^{-1}, respectively. The uniform deformation model from Müller et al. (2019) for the GoM produced an RMSE of 14.8 km when compared with the GEMMA crustal thickness model (Reguzzoni and Sampietro 2015), demonstrating that our focused deformation model outperformed it by nearly 2.5 times in estimating the crustal thickness. The crustal thickness estimates based on UCCL suggest a thickness of 38.4 ± 3.0 km for unstretched crust (e.g. Huerta and Harry 2012; Kaban et al. 2014; Nguyen et al. 2022; Reguzzoni and Sampietro 2015), which closely aligns with the optimised value of initial crustal thickness obtained from the model. This suggests that a highly thickened crust inherited from the Ouachita Orogeny is unlikely, given our initial crustal thickness estimate of 39 km, which is thinner than what would typically result from an orogenic event. This may imply that pre-rifting thinning occurred between the Ouachita Orogeny and the start of our model at 230 Ma, driven by processes such as post-orogenic collapse, thermal relaxation, or far-field tectonic stress during the Permo-Triassic period. Additionally, our model agreed with the GUMBO crustal thickness estimates, particularly in the eastern and western GoM regions, with an absolute error of ~1.5 km (Supplementary Figures S2 and S3). The RMSE produced by our crustal thickness model when compared to GUMBO1 and GUMBO2 is 1.53 km and 1.58 km, respectively (Supplementary Figure S2). However, the RMSE for GUMBO3 was slightly higher at 7.83 km, suggesting that complex deformation may have influenced crust thickness in the eastern GoM. Notably, a mismatch of approximately 3 km in the estimates of the Moho depth from seismic reflection and refraction (Eddy et al. 2014) along GUMBO3 could be another reason for the higher RMSE.

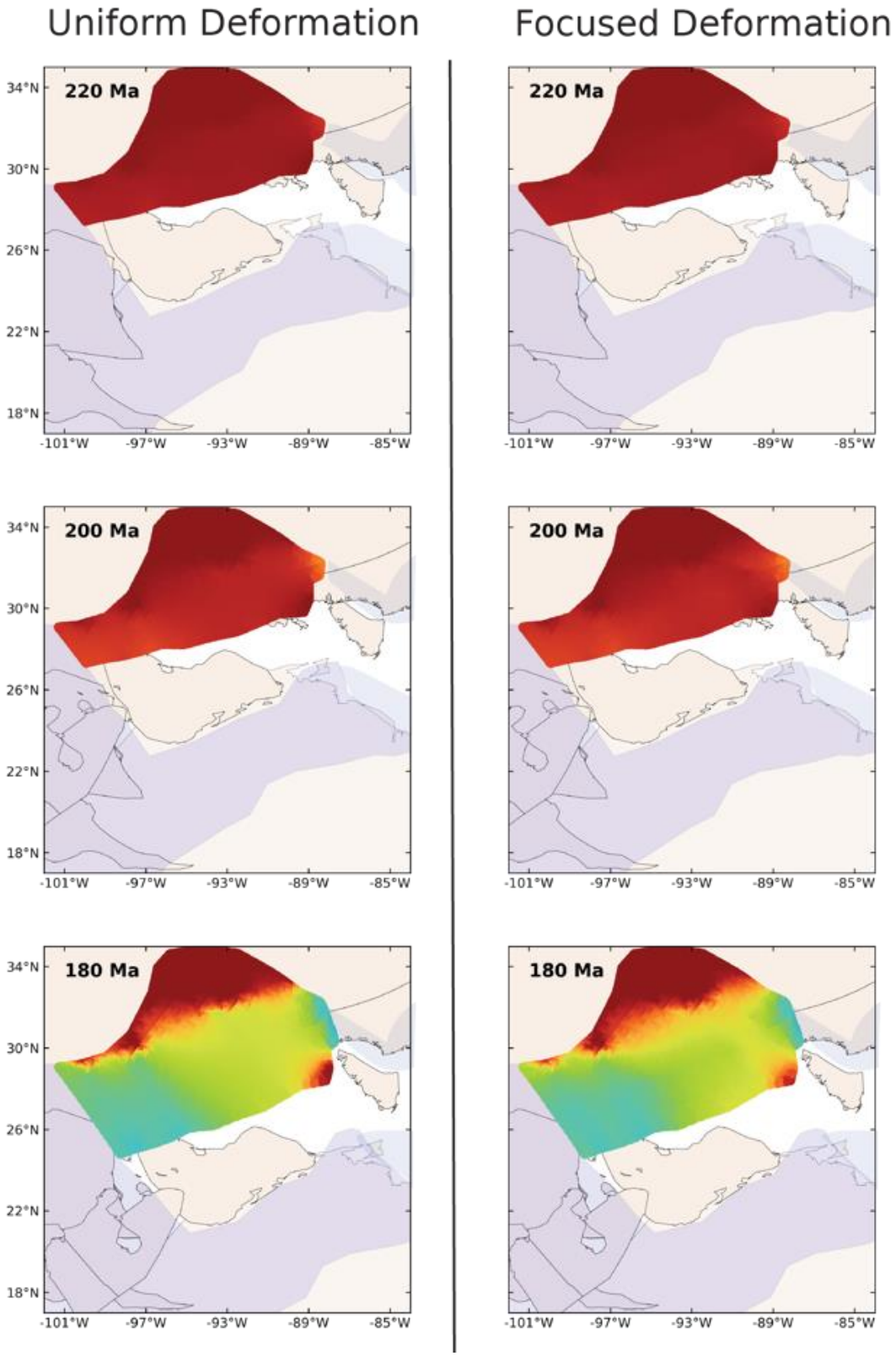
Uniform Deformation
Focused Deformation
220 Ma
200 Ma
180 Ma
34°N
30°N
26°N
22°N
18°N
-101°W
-97°W
-93°W
-89°W
-85°W

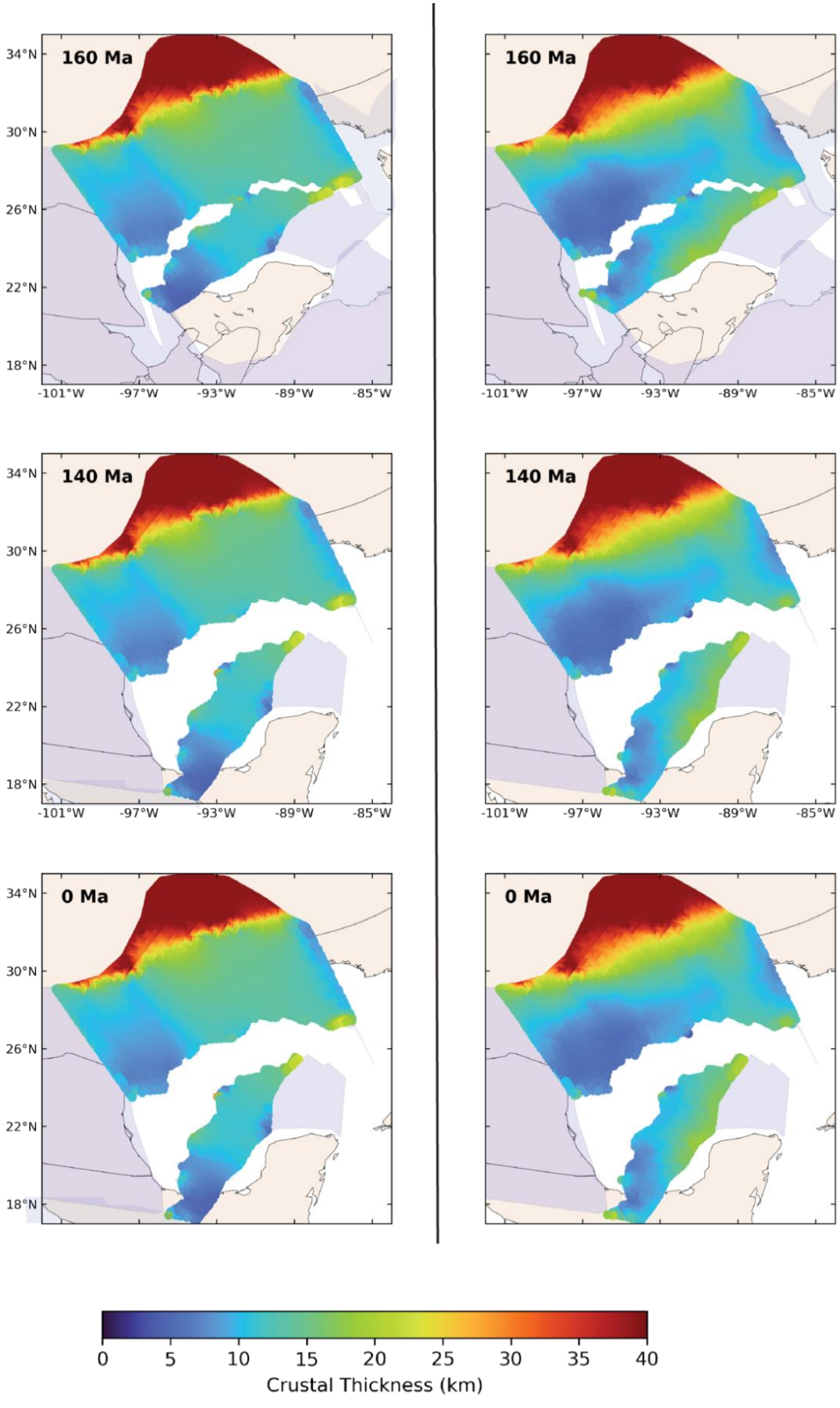
160 Ma
160 Ma
140 Ma
140 Ma
0 Ma
0 Ma
34°N
30°N
26°N
22°N
18°N
-101°W
-97°W
-93°W
-89°W
-85°W
0
5
10
15
20
25
30
35
40
Crustal Thickness (km)

Figure 6. Comparison of crustal thicknesses between our uniform deformation model and the focused deformation model applied to the rigid plate reconstruction model described in Section 3.1. The purple colored region demonstrates the entire deformed continental crust in the region, but our modelling focused only on the central GoM. The thin outlines visible beneath the colored models represent reconstructed present-day coastlines provided for geographic reference. During the early evolution from 230 to 190 Ma, the crustal thickness showed spatial similarities in both the uniform and focused deformation scenarios. However, from ~190 to ~175 Ma, a region of focused stretching emerges in the central GoM (see 180 Ma). Notably, there is a significant disparity in crustal thickness estimation between the focused and uniform deformation models after the rifting event at ~160 Ma.

4.2 Evolution of stretching factor, crustal thickness, and tectonic subsidence

4.2.1 Early Triassic-Sinemurian (~230 to 190 Ma)

During the initial phase, the extension was relatively uniform along the north-south direction, characterized by minimal stretching ($\beta = 1.1$) and crustal thinning (Figure 6). The gradual stretching process resulted in the development of low strain rates ($6 \times 10^{-16} – 4.0 \times 10^{-16}\ s^{-1}$) evenly distributed across the region. However, tectonic subsidence calculations revealed lateral variations in the east-west direction, leading to the creation of accommodation for the deposition of Triassic sediments (Figures 7 and 8). The western GoM exhibited approximately 1.5 km of tectonic subsidence, which gradually decreased towards the central GoM (Figure 8a). The eastern GoM region adjacent to the SGR showed a similar subsidence value (~1.2 km).

4.2.2 Pliensbachian-Toarcian (~190 to ~175 Ma)

During this phase, our model indicates rapid tectonic subsidence of 3–5 km between North America and Yucatán (Figures 7 and 8b). However, the stretching zone exhibited spatial variability (Figure 9). As the Yucatán Block drifted southward, the strain rate within the deformation zone increased from $4.0 \times 10^{-16}\ s^{-1}$ to $1.7 \times 10^{-15}\ s^{-1}$, resulting in more focused deformation in the region between blocks. Our model allows for the adjustment of the deformation mesh, concentrating the extension within the necking region. Notably, our results highlight the development of a focused stretching zone that propagates from the western to the eastern region of the GoM (Figure 9c and d). In contrast, the uniform deformation model failed to capture this focused thinning region, particularly in the central and eastern GoM (see snapshots 180 Ma and 160 Ma in Figure 6).

We found that rapid tectonic subsidence initiated in a wider zone in the western GoM and a narrower zone in the central and eastern GoM during the Pliensbachian (~185 Ma) and then propagated to create a wider central and western GoM by the Bajocian (~170 Ma). Tectonic subsidence reached approximately 4-5 km in the western GoM and 2-3 km in the eastern GoM, revealing lateral variations in accommodation within the GoM prior to its opening (Figure 8b). However, our model indicates that this heightened subsidence was confined to the region of focused stretching rather than being uniformly distributed across the basin. We observed significant stretching, with the β value transitioning from 1.1 at the start of the Early Jurassic to a value greater than 4 by the end of the Early Jurassic, resulting in substantial crustal thinning

(Figure 9). Overall, stretching occurred over a wider zone in the western GoM region than in the central and eastern regions. Our crustal thickness calculation demonstrates that during the Pliensbachian period, the western GoM experienced considerable thinning, with an average thickness of 17 km, while the central and eastern regions of the GoM thinned to an average thickness of 26 km (Figure 6).

4.2.3 Middle-Late Jurassic (~175 Ma to ~145 Ma)

During the Toarcian to Callovian period, the western GoM experienced substantial thinning due to intensified extension caused by the anticlockwise rotation of the Yucatán Block. Consequently, the average crustal thickness in this region decreased to less than 10 km. Furthermore, the western GoM exhibited higher tectonic subsidence than the eastern region (Figure 7). Although the extension in the western GoM ceased in the Callovian (~166 Ma), it persisted into the Early Oxfordian (~162 Ma) in the eastern GoM, albeit at a reduced rate (Figures 9 and 10). Our model indicates that the zone of focused stretching propagated from west to east prior to the onset of seafloor spreading. However, our deformation model revealed a stepwise opening process with the onset of the seafloor spreading. It commenced in the Bathonian in the western GoM, followed by spreading in the central GoM during the Callovian, and eventually reaching the eastern GoM by the Oxfordian. Notably, an intriguing observation from our model is that seafloor spreading occurred south of the focused stretching region, suggesting a possible rift jump. Additionally, the spreading center exhibited asymmetry in both the eastern and western GoM with respect to the focused stretching zone. However, in the central GoM, the spreading center is in close proximity to the focused stretching region.

4.2.4 Cretaceous

During the Cretaceous, the GoM experienced lithospheric cooling and entered a phase dominated by thermal subsidence (Figure 8), creating ample space for the deposition of thick sedimentary layers and further sediment loading subsidence. Following the extensional phase, gradual conductive cooling of the lithosphere occurred, leading to increased density in both the crust and mantle. The basin underwent gradual subsidence to maintain isostatic equilibrium. Throughout the Cretaceous, the GoM was characterized by passive tectonic conditions in most areas, with occasional localized interruptions caused by factors such as igneous activity and thermal uplift in the eastern Texas region surrounding the Sabine Uplift (Adams 2007; Snedden and Galloway 2019). Although these factors significantly influence the local tectonic subsidence of the basin, they cannot be accounted for in our model. For instance, the Southern Arkansas Uplift in the mid-Cretaceous may have locally influenced subsidence by up to 3 km (Snedden and Galloway 2019).

5 Discussion

5.1. Initial rifting and red bed deposition

During the initial rifting phase prior to the anticlockwise rotation of the Yucatán Block, our model indicates ~1.5 km of subsidence, which would have created accommodation for the deposition of red bed sediments. However, our tectonic subsidence calculation suggests that the estimated thickness of the red bed sediments from our model in the northern GoM is slightly lower than the inferred thickness (Milliken 1988). This observation may imply that the deposition of red beds filled pre-existing accommodation spaces rather than being deposited directly within a newly formed graben. It is important to note that our tectonic subsidence calculation relies on stretching constrained by Yucatán motion, and we have limited constraints on the internal deformation of the Yucatán Block and the position of the mid-rift high. Moreover, our model may not be able to capture high-frequency, high-amplitude changes in stratal thicknesses caused by brittle deformation, which can also be responsible for the thicker red beds in northern GoM. Nonetheless, our model offers valuable insights into how sediments may have been routed southward from the Ouachita-Marathon region.

The initial tectonic subsidence of ~1.5 km in the eastern and western parts of the GoM between 230 and 190 Ma before the drifting stage suggests that sediment deposition routes were bifurcated to the east and west within the narrow extensional zone between Yucatán and North America. This is further supported by the presence of interior drainage systems extending across various North American basement source terranes, as evidenced by the diverse U-Pb age spectra from pre-salt wells (e.g. Frederick et al. 2020; Snedden and Galloway 2019). Detrital zircon data from 16 wells show the existence of three distinct paleo-drainage systems in the northern GoM (Frederick et al. 2020), which aligns well with the potential depocenters in our model (Figure 8). These reconstructions suggest that a western paleo-drainage system extended from the highlands of Central Texas to the submarine Potosi Fan on the western margin of the Laurentia. Detrital zircon ages from the Eagle Mills sediments in this region suggest tributary sources from the East Mexico Arc, Yucatán/Maya, and Marathon-Ouachita provinces, encompassing a range of detrital zircon ages (Frederick et al. 2020). The south-western sediment source was characterized by peri-Gondwanan detrital zircon ages from the late Paleozoic accreted basement and/or successor basins, whereas the south-eastern fluvial networks originated from traditional North American basement provinces, including Grenville, Mid-Continent, and Yavapai-Mazatzal. The southern paleo-drainage system in the north-central GoM region bifurcated around the uplifted terranes of Sabine and Monroe (Figure 8). The eastern paleo-drainage system exhibited a regional southward flow, with pre-salt detrital provenance data predominantly indicating local Gondwanan/peri-Gondwanan sources, such as the proximal Suwannee terrane and Osceola Granite complex (Frederick et al. 2020).

Our model suggests that these paleo-drainage systems likely served as sources of basin fill in the GoM (Figure 8). The creation of accommodation in the western GoM facilitated the deposition of red bed sediments from the western paleo-drainage system and the western branch of the bifurcated southern paleo-drainage routes. Similarly, tectonic subsidence in the eastern GoM region would have provided accommodation for sedimentation in the eastern branch of the southern and eastern paleo-drainage systems.

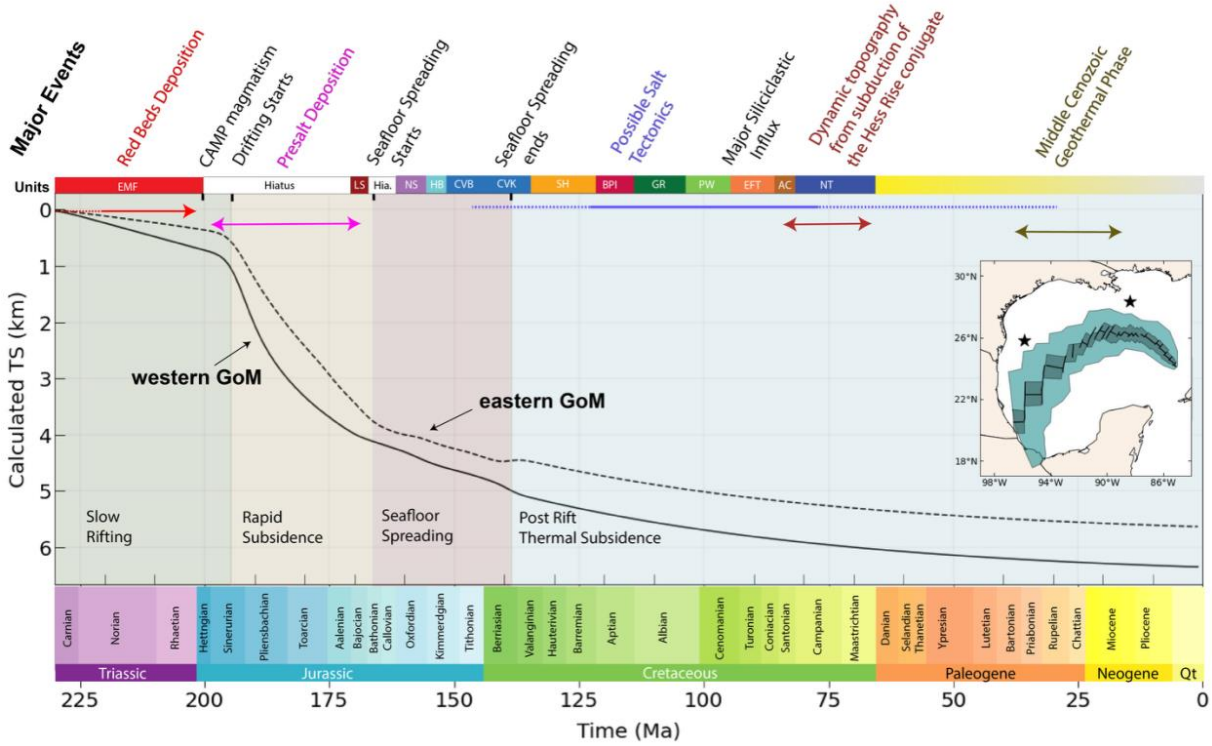

Figure 7. Tectonic subsidence calculation from the model. Four stages can be used to describe the tectonic evolution of the GoM Basin. Slow rifting Phase: In this phase, there is a small tectonic subsidence, creating accommodation for infilling the GoM Basin with red beds. Rapid Subsidence Phase: Following the rift-drift transition, rapid subsidence occurs, resulting in 3-4 km of subsidence. This led to the deposition of the pre-salt strata. Seafloor Spreading Phase: Louann Salt was already deposited. First, the western GoM opened, followed by the opening of the eastern GoM. Post-Rift Thermal Subsidence Phase: The last stage is marked by the conductive cooling of the lithosphere, resulting in gradual tectonic subsidence. The difference in tectonic subsidence between the western and eastern GoM further increases. Most of the later secondary tectonic activity (major events in color) would have influenced tectonic subsidence and has not been accounted for in this study. Abbreviations of depositional sequences from Snedden and Galloway (2019): EMF, Eagle Mills Formation; LS, Louann Salt; NS, Norphlet-Smackover Formations; HB, Haynesville-Buckner Formations; CVB, Cotton Valley-Bossier; CVK, Cotton Valley-Knowles; SH, Sligo-Hosston; BPI, Bexar-Pine Island; GR, Glen Rose; PW, Paluxy–Washita; EFT, Eagle Ford-Tuscaloosa; AC, Austin Chalk; and NT, Navarro-Taylor.

5.2 Rapid subsidence and pre-salt deposition

The ~40 Myr hiatus between the syn-rift red beds of the Eagle Mills Formation and the overlying Middle Jurassic Louann Salt poses an important conundrum. Because the Eagle Mills Formation is deeply buried, detrital zircon analyses from its regional stratigraphic equivalents—specifically the Wood River Formation of the South Florida Basin and the Dockum Group north of the Ouachita-Marathon orogenic belt—are used to constrain this timeline. These equivalent units yield maximum depositional ages of approximately 235–195 Ma (Wiley 2017) and 234–200 Ma

(Umbarger 2018), respectively. This confirms a substantial age gap between the cessation of these Late Triassic–Early Jurassic red bed sequences and the onset of the Louann Salt (Dickinson et al. 2010). Limited exposure of early Mesozoic outcrops south of the Ouachita Mountains and only a few drilled wells below the autochthonous Louann Salt in the onshore USA make the geological record in the western GoM soon after the Permian unclear (Snedden and Galloway 2019). For example, there is a 90 Myr gap between the Permian strata and the earliest fully marine Upper Smackover strata formed during the middle Mesozoic drift and cooling phase of the GoM Basin in west Texas (Snedden and Galloway 2019).

Our model suggests that the onset of the Yucatán rotation triggered a sudden increase in tectonic subsidence (Figure 7), creating ample accommodation for sedimentation before marine incursion. The region of high tectonic subsidence shifted further south near the Yucatán margin, implying approximately 4-5 km of tectonic subsidence in the focused stretching zone and suggesting the presence of a thick pre-salt sedimentary layer. This aligns with the current understanding of a pre-salt sedimentary basin, as mapped by seismic and potential field data (e.g. Filina 2019), indicating continuous deposition. Our model suggests a wider region for pre-salt deposition in the western GoM than in the eastern GoM, with higher tectonic subsidence values near the Yucatán margin, indicating thicker sediment in that area. We propose that the sudden increase in accommodation in the southern GoM, close to Yucatán, facilitated the deposition of sediments from the north-central GoM into the present-day pre-salt sedimentary basin. While rifting and red bed deposition continued uninterrupted until salt deposition, the primary zone of deformation gradually shifted southward toward the Yucatán margin. This region, which is now buried beneath the salt canopy, remains poorly imaged and lacks comprehensive penetration. Consequently, the western paleo-drainage and the western branch of the southern paleo-drainage actively filled the newly created accommodation and bypassed the previous basin located to the north (Figure 8), potentially explaining the large hiatus between the red beds and the beginning of the Louann Salt in the northern GoM.

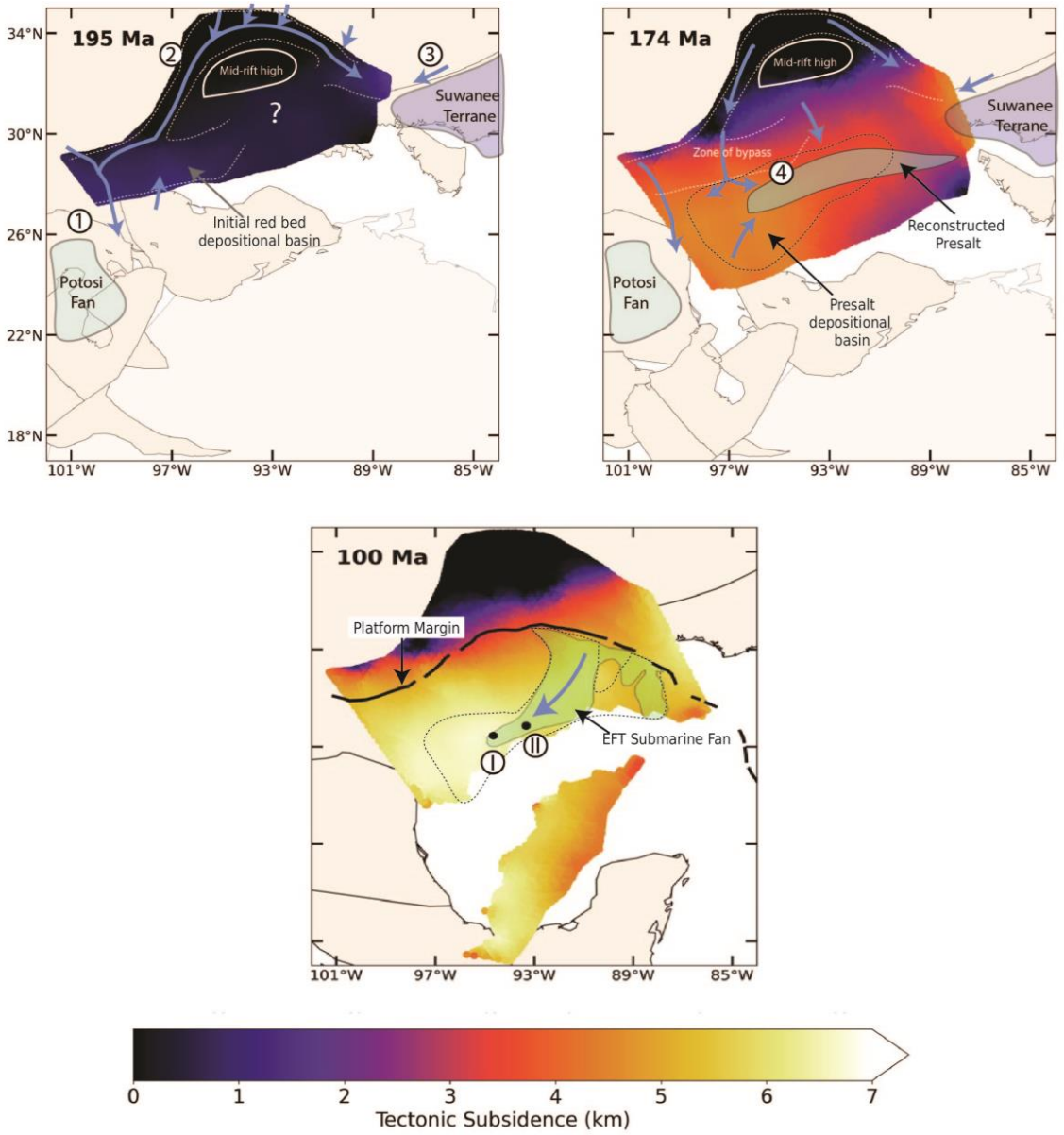

Figure 8. A successor basin fill model showing that a large area in the central GoM may have been filled with red bed sedimentation. Sediment routing was based on an analysis of key wells and their detrital zircon geochronology, which revealed the direction of sediment routing trends (Snedden and Galloway 2019). 1) Western paleo-drainage systems. 2) The southern paleo-drainage systems bifurcated around the mid-rift high into two branches: the eastern and western branches. 3) Eastern paleo-drainage systems. Our model shows tectonic subsidence along these paleo-drainages (top left panel). Our model shows the development of rapid tectonic subsidence in a focused region (4; top right panel). Proposed model and sediment routing for pre-salt deposition based on our tectonic subsidence calculation. This region is wider in the western GoM; however, it becomes narrower towards the east. We propose that sedimentation was a continuous process in the GoM. However, owing to the creation of accommodation during rapid subsidence, red bed deposition shifted further south near the Yucatán margin. Moreover, the

western paleo-drainage, as well as the western branch of the southern paleo-drainage, would have been a major source of these sediments. This tectonic subsidence signature may have exerted a long-lived sediment routing control into post-salt Cretaceous clastic systems, as illustrated by the abrupt westward deflection of Cenomanian-Turonian submarine fans (bottom middle panel). These systems originated from the southern Louisiana platform margin (northern sediment source) and extended towards the Tiber (II) and BAHA II (I) well locations in the western GoM (Snedden et al. 2016; Sweet et al. 2022). However, well data are limited further west in the deep waters of the GoM. However, our model suggests that these submarine fans may have extended even farther west, beyond the range of current well penetration, owing to increasing differential subsidence towards the west.

5.3 Evolution of Rifting

Determining the precise type of crust in the GoM has been challenging because of the lack of wells penetrating the crustal basement. Moreover, the extent and timing of magmatism and/or mantle exhumation remain topics of debate for the GoM (e.g. Filina et al. 2022; Minguez et al. 2020). The extent of magmatism during the rifting stage is influenced by several factors, including mantle temperature, extension rates, mantle composition, preceding rift history, and the presence or absence of hot active upwelling of the asthenosphere (e.g. Armitage et al. 2010; Tetreault and Buiter 2018; Tugend et al. 2020; White and McKenzie 1989). Among these factors, mantle temperature is considered the most crucial because it governs the onset of decompression melting (Tugend et al. 2020). Elevated mantle temperatures increase the magma supply, resulting in higher volumes of magmatism at magma-rich margins (e.g. White and McKenzie 1989). The rate of lithospheric extension during breakup is another critical factor that significantly influences magma supply (Armitage et al. 2010). Magma-rich margins tend to form under conditions in which plate separation occurs at a faster pace than in magma-poor margins (e.g. Lundin et al. 2014). Mantle composition also plays a role in the volume of melt produced, with more primitive and volatile-rich mantles generating greater amounts of melt (Cannat et al. 2008). Therefore, the level of magmatism observed at the rift margin and within the GoM depends on the complex interactions between these parameters. Our model provides valuable insights into the temporal and lateral variations in magmatism throughout GoM evolution. Based on the stretching factor, crustal thickness, and extension rate evolution derived from our model, we propose a two-phase development of the crustal architecture of the GoM.

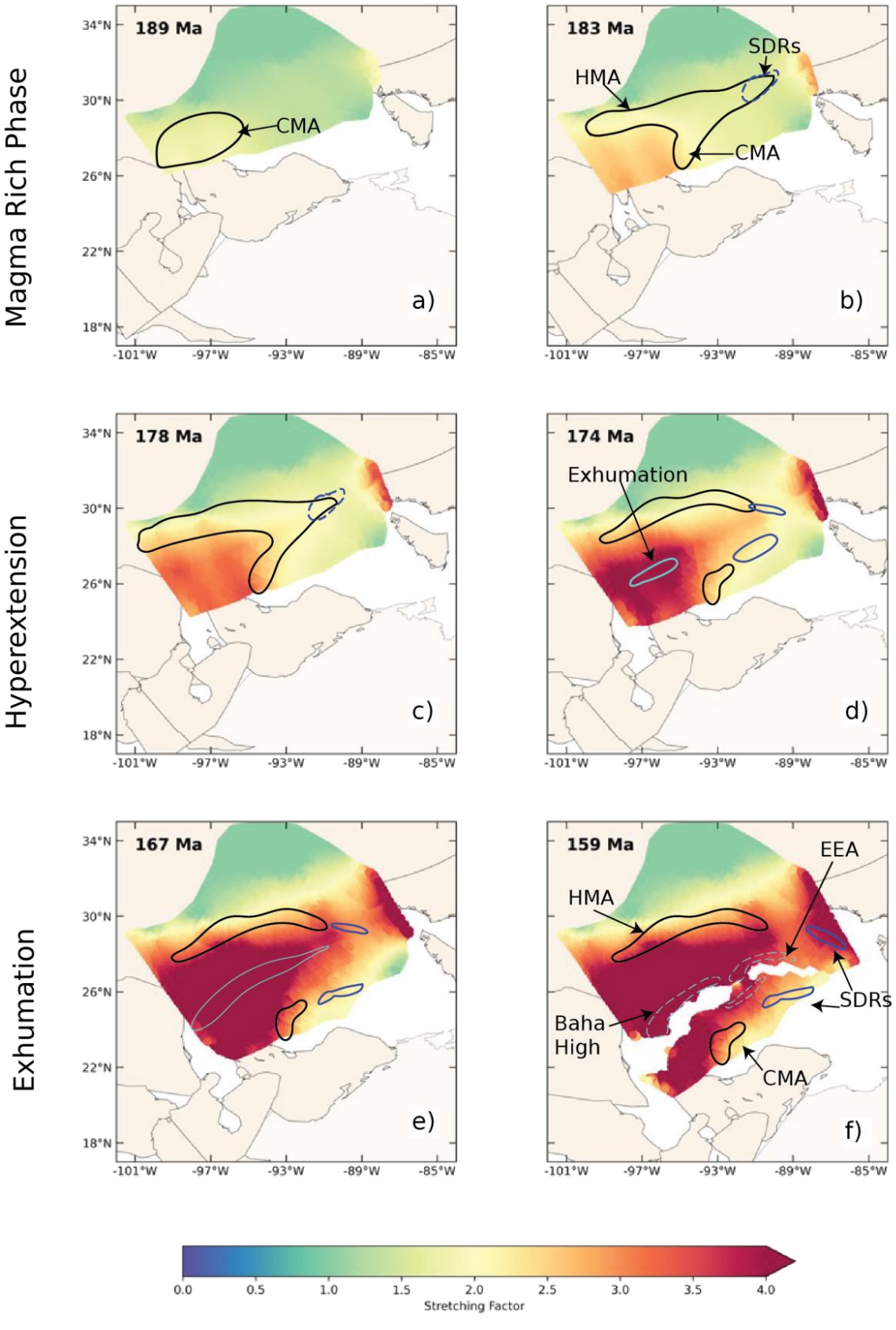
Magma Rich Phase
Hyperextension
Exhumation
189 Ma
CMA
a)
183 Ma
SDRs
HMA
CMA
b)
178 Ma
c)
174 Ma
Exhumation
d)
167 Ma
e)
159 Ma
EEA
HMA
SDRs
Baha
High
CMA
f)
34°N
30°N
26°N
22°N
18°N
-101°W
-97°W
-93°W
-89°W
-85°W
0.0
0.5
1.0
1.5
2.0
2.5
3.0
3.5
4.0
Stretching Factor

Figure 9. a) Formation of CMA aligns well with crustal thinning, suggesting rift-related volcanism. b) Formation of HMA, LMA, and SDRs. c) Hyperextension began in the western GoM. d) Hyperextension propagated to the eastern GoM and separation of CMA and HMA. HMA, CMA, and SDR underwent deformation owing to the motion of the Florida and Yucatán Blocks. Exhumation may have started in the western GoM, leading to the formation of the BAHA high. e) Seafloor spreading began Exhumation in the eastern GoM, resulting in the EEA. f) SDR undergoes deformation owing to the motion of the Florida Block. Symmetric and Conjugate EEA were separated in the central GoM. However, further west, the EEA was asymmetric and tapered out. Magnetic anomalies and SDRs are shown in black and blue, respectively. The solid light blue polygon represents the location of possible exhumation. Dashed light blue polygons represent reconstructed BAHA high and EEA anomalies, respectively. Beige polygons represent present-day coastlines reconstructed to a specific time.

5.3.1 Phase 1: Magmatism

The transition from rifting to seafloor spreading in passive rift margins occurs when the crustal stretching factor reaches 3–5 (Davis and Kusznir 2004; McKenzie 1978; Reston 2009), allowing magma to suddenly breach through the crust (Dewey and Bird 1970). However, some volcanic activity may occur in passive rift margins prior to breakup when the stretching factor exceeds ~2 (Le Pichon and Sibuet 1981). Our model revealed a link between crustal thinning and the formation of the HMA, CMA, and LMA in the western GoM, as well as the positioning of the SDRs in the eastern GoM. The CMA in the western GoM formed near the Yucatán margin during the Sinemurian period (Figure 9a). As deformation progressed, the region stretched, leading to the formation of the HMA (Figure 9b). Deep seismic data imply that the CMA (Goswami et al. 2016) and FMA (Imbert and Philippe 2005) are probably related to volcanic flows within the syn-rift regions of the rift basins. The occurrence of the HMA in the western GoM during the Sinemurian may also be linked to magmatic activity, similar to that of the CMA. In the eastern GoM, the SDRs observed off the Yucatán margin coincide with the YMA (e.g. Steier and Mann 2019; Filina and Hartford 2021; Filina and Beutel 2022). The refraction velocity model (Eddy et al. 2014) indicates that the same region where the SDRs were interpreted in the FMA exhibits a high-velocity lower crust and Moho associated with the intrusions. Liu et al. (2019) modelled SDRs reflections with high magnetic susceptibilities and densities, which fit well with potential field data. Some studies have proposed that SDRs may represent syn-rift volcanic fills (e.g., Minguez et al. 2020). Others consider the HMA and YMA to be COBs marked by SDR successions (e.g. Lundin and Doré 2017). The stretching factor values ($\beta \approx 2$) associated with these anomalies suggest that they may not be COBs, as these values are low for oceanic crust formation (Figures 9a and b).

One possible explanation for the formation of these SDRs and magnetic anomalies is their proximity to the CAMP event in eastern North America (e.g. Filina and Beutel 2022). The elevated subcontinental mantle temperature during the CAMP event would have led to increased decompressional melt generation, resulting in magmatism and lower-crustal intrusion (Figure 10). However, the extent of this magmatism was limited because of the relatively short duration of the CAMP event. A similar process has been proposed to explain rifting in the north-western Indian Ocean, where the presence of the Deccan Traps, located 1000 km away from the rift zone,

created a thermal anomaly that triggered igneous intrusion along the Gopi Rift (Armitage et al. 2010). However, this thermal anomaly was eventually depleted, leading to the formation of a magma-poor Laxmi Ridge margin (Armitage et al. 2010). The production and emplacement of magma during the formation of the GoM may have varied laterally, which could explain the presence of SDRs along the eastern GoM owing to its proximity to the CAMP event. Alternatively, the HMA may also be related to SDRs, but owing to its depth and thick salt cover, it remains challenging to determine the presence of SDR patterns in seismic sections. Another plausible reason for the reduced occurrence of magmatic SDRs in the western GoM could be the hindered melt extraction caused by the greater lithospheric thickness in that region (e.g. Izquierdo-Llavall et al. 2022; Nguyen et al. 2022). Furthermore, our model indicates that because of the motion of the Florida Bahamas and Yucatán Blocks, these SDRs would have experienced significant deformation and later separated from each other as a result of seafloor spreading, resulting in their present-day locations (Figures 9 and 10).

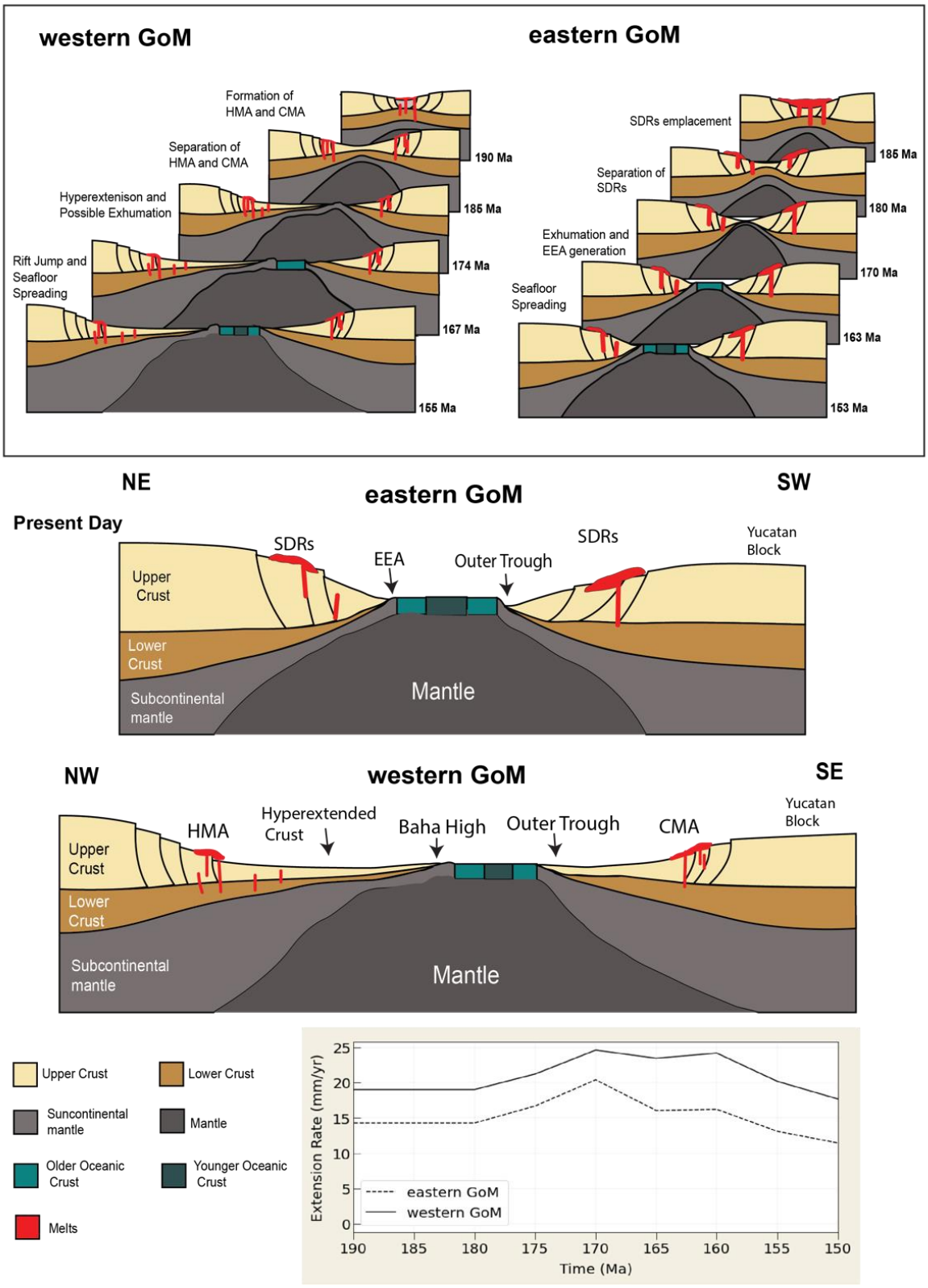
western GoM
eastern GoM
Formation of HMA and CMA
Separation of HMA and CMA
Hyperextenison and Possible Exhumation
Rift Jump and Seafloor Spreading
190 Ma
185 Ma
174 Ma
167 Ma
155 Ma
SDRs emplacement
Separation of SDRs
Exhumation and EEA generation
Seafloor Spreading
185 Ma
180 Ma
170 Ma
163 Ma
153 Ma
NE
eastern GoM
SW
Present Day
SDRs
EEA
Outer Trough
SDRs
Yucatan Block
Upper Crust
Lower Crust
Subcontinental mantle
Mantle
NW
western GoM
SE
HMA
Hyperextended Crust
Baha High
Outer Trough
CMA
Yucatan Block
Upper Crust
Lower Crust
Subcontinental mantle
Mantle
Upper Crust
Lower Crust
Suncontinental mantle
Mantle
Older Oceanic Crust
Younger Oceanic Crust
Melts
Extension Rate (mm/yr)
25
20
15
10
5
0
eastern GoM
western GoM
190
185
180
175
170
165
160
155
150
Time (Ma)

Figure 10. Summary of the evolution of GoM crustal architecture. Our model suggests that the Mesozoic evolution of the eastern and western GoM Basins—approximately along profiles GUMBO1 and GUMBO3 (Figure 3; note that the figures are schematic and not to scale)—began as a magma-rich margin. During the Pliensbachian age, magmatic intrusions and extrusions occurred, resulting in the formation of the HMA, CMA, and LMA in the western GoM, as well as SDRs in the eastern GoM. The elevated subcontinental mantle temperature during the CAMP event likely caused increased decompressional melt generation, leading to magmatism and lower-crustal intrusions. However, this magmatism was short-lived. The subsequent Toarcian development indicates a magma-poor origin, characterized by hyperextension and potential mantle exhumation. The rate of extension plays a significant role in shaping crustal architecture. Higher extension rates (>20 mm/yr) facilitate rapid mantle upwelling, resulting in exhumation. As the extension rate is higher farther from the pole of rotation, the western GoM underwent more thinning and wider hyperextension than the eastern GoM.

5.3.2 Phase 2: Hyperextension and Exhumation

The magma-rich rifting phase in the GoM was relatively brief because of the short-lived CAMP event. Following the transition from rift to drift, our results indicate a wider region of thinned crust in the western GoM, indicating hyperextension (Figure 9c and d). However, this region narrows as we move towards the central and eastern GoM. A higher stretching factor (β>3–5) is required for the formation of the oceanic crust, and these values are at the lower limit for magma-rich margins. However, our calculations suggest that if this were the case in the GoM, the formation of the oceanic crust would have commenced sooner and further north than currently estimated based on the ESRA (Figure 2). New tectonic models for GoM evolution based on the interpretation of the new magnetic anomaly map have proposed a fossil spreading center that differs from previous studies, which lies in the north (García-Reyes and Dyment 2022) and coincides with the wide region of high stretching factor (β >3) predicted by our model. The estimated COBs and symmetrical patterns of intermediate-wavelength magnetic anomalies matched our model predictions in the western GoM. However, our optimized model produces a very wide zone of deformation in the western GoM rather than a narrow zone, which is primarily observed in the case of hyperextension (Reston 2009). Our analysis revealed a β value of 4 in the wider western GoM Basin during the Early Toarcian, whereas the eastern GoM exhibited a β value of 1.5 within a narrow zone. However, by the Late Aalenian–Early Bajocian, the eastern GoM shows a β value of approximately 4, whereas the western GoM reaches approximately 5.2. This may suggest that rift propagation occurred from west to east, gradually 'unzipping' this hyperextended crust (Figure 9). The unzipping process was triggered by the anticlockwise rotation of the Yucatán Block around the rotation pole located in the Florida Strait (Pindell et al. 2021). An alternate explanation that posits the eastern part as a continental rift and the western part as an early stage of seafloor spreading could also be true (e.g. Filina and Beutel 2022; García-Reyes and Dyment 2022). However, this alternate model presents challenges because the large deformation zone, high stretching factors ($\beta \geq 4$), and elevated extension rates of our optimized model are more consistent with hyperextension and possible exhumation, as described in other models (e.g Pindell et al. 2016; Minguez et al. 2020). This discrepancy could also be attributed to the choice of base rigid plate tectonic reconstruction, which defines the motion of the continental block and, consequently, controls the rate of extension.

Notably, the extension rate plays a significant role in shaping the crustal architecture of an extended continental crust, and its distance from the rotation pole affects this extension rate (Lundin et al. 014). Closer to the rotation pole, the linear rate of plate extension is relatively small, resulting in a proximal margin characterized by limited extension, where the brittle-ductile transition remains in the crust and brittle deformation occurs along high-angle faults (e.g. Colletta et al. 1988). As we move farther away, deformation progresses into a thinning phase, where complete embrittlement of the crust, fault penetration, and mantle serpentinization are likely (e.g. Lundin et al. 2014). Mantle exhumation was predicted at an even greater distance from the pole. Eventually, the pole of rotation becomes so distant that the linear half-spreading rate exceeds the critical velocity for melting (e.g. Bonatti 1985; Chu and Gordon 1998). A similar explanation can be applied to the GoM to understand its crustal architecture. In the western GoM, which is located further away from the rotation pole, some studies have proposed a phase of seafloor spreading (e.g. Filina and Beutel 2022; García-Reyes and Dyment 2022), whereas others have indicated thinning and wider hyperextension of the continental crust with an exposed upper mantle (e.g. Pindell et al. 2016; Van Avendonk et al. 2015). Additionally, analog rock property-based modelling of the EEA suggests the presence of a narrower zone of exhumed serpentinized mantle along the eastern GoM (e.g. Minguez et al. 2020). Recent seismic reflection profiles also indicate segments of the exhumed mantle along the Yucatán margin (Izquierdo-Llavall et al. 2022). These observations, along with the extension rate derived from our model, suggest that by the end of the Early Jurassic, the western GoM experienced a prolonged period of hyperextension, possibly followed by mantle exhumation prior to the seafloor spreading (Figure 10). Moreover, numerical models have demonstrated that extension rates exceeding 20 mm/yr facilitate rapid upwelling of the mantle, leading to an increase in the lower crust temperature, ductile deformation, and a decrease in viscosity (e.g. Tetreault and Buiter 2018). Such high extension rates cause the strain in the mantle to decouple from the crust, creating a pathway for exhumation and generating a counterflow in the mantle.

Although our model cannot account for uplift due to the mantle exhumation process, the extension rate calculations from our model can be useful for understanding the evolution of the hyperextension phase. Our extension rate calculations suggest that the western GoM experienced a high extension rate (>20 mm/yr) around the Middle Toarcian (~177 Ma). However, during the same period, the eastern GoM exhibited a lower extension rate (Figure 10). Nevertheless, by the Late Aalenian (~171 Ma), the eastern GoM underwent a high extension rate conducive to exhumation, resulting in the formation of a symmetric and conjugate EEA. In the western GoM, the magnetic anomaly pattern and seismic results are less clear, but the presence of the BAHA high along areas of high extension rates suggests hyperextension and possible mantle exhumation from the Middle to Late Toarcian. Furthermore, with a shift in the extension rate from high to moderate, a rift jump likely occurred, with a more pronounced effect in the wider western GoM compared to the narrower eastern GoM. For a rift jump to occur, Tetreault and Buiter (2018) proposed that a region must be sufficiently wide for mantle upwelling to reach a depth at which it interacts with the ductile lower crust. The deflection of strain by the ductile crustal layers towards the edge of the rift can then shift the upwelling to the edge of the rift, abandoning the original rift (e.g. Brune et al. 2017; Naliboff and Buiter 2015). This scenario may have occurred in the western GoM because of its wider zone of extension, resulting in a rift jump and the final margin structure characterized by a narrow margin (Yucatán) and the other with a wider, more hyperextended crust (north-western GoM). As seafloor spreading initiated in the

western GoM, the eastern GoM experienced extension within a narrower zone, which likely prevented the complete decoupling of the lower crust and resulted in a more symmetrical exhumation pattern.

5.3.3 Post-Rift Thermal Subsidence

The Early Cretaceous was characterized by seafloor spreading, followed by gradual lithospheric cooling, which resulted in slower thermal subsidence following lithospheric stretching and thinning (Figure 7). Prior to seafloor spreading, the earliest basin-wide deposits in the GoM Basin were the Louann Salt (Pindell et al. 2021). Subsequently, the Oxfordian Norphlet and Smackover Formations (NS sequence) were deposited over these evaporites, resulting in salt-detached raft blocks in a region outlined by the Florida Escarpment, centered on the western DeSoto Canyon and the eastern Mississippi Canyon (Snedden and Galloway 2019). The reconstruction of these blocks indicates a southwest direction of rafting by gravity gliding with NS as pre-kinematic sequences and Haynesville-Buckner (HVB), Cotton Valley-Bossier (CVB), and Cotton Valley-Knowles (CVK) synkinematic sequences deposited roughly at the same time as seafloor spreading (Pilcher et al. 2014; Snedden and Galloway 2019). Our model suggests that the increased tectonic subsidence towards the rifting zone, as well as the increasing tectonic subsidence from east to west (Figure 7), can explain the formation of a seaward paleo-slope, allowing gravity gliding of raft blocks in the southwest direction.

Our findings suggest a slow increase in tectonic subsidence during the Mid-Cretaceous. However, most of this period was dominated by carbonates, resulting in the formation of an extensive platform-margin reef system in the northern GoM, which served as an effective barrier preventing siliciclastic sediment from reaching the deep GoM Basin, where high tectonic subsidence occurred (Snedden and Galloway 2019). This was followed by the Cenomanian-Turonian interval, when local tectonics and drainage expansion allowed siliciclastic sediments to reach the deeper parts of the basin (Snedden and Galloway 2019). This is evident from the presence of Eagle Ford-Tuscaloosa (EFT) sandstones, which span from the southern Louisiana platform margin to the deepwater of the Keathley Canyon and Alaminos Canyon (Snedden et al. 2016; Sweet et al. 2022). Down-dip deep-water depositional system equivalent sediments have been discovered in several wells as far west as the BAHA II and Tiber wells (Figure 8). Mapping of these depositional patterns through deep-water wells of the GoM Basin suggests a possible significant westward deflection (Snedden et al. 2016). Our model suggests that this westward deflection might be influenced by differential tectonic subsidence in an east-to-west direction and indicates that the initial tectonic subsidence generated by rifting can have long-term consequences for depositional systems, altering their orientation long after rifting ceases. Although there is limited deep-well control in the western GoM, our model suggests that the Cenomanian and earlier Albian submarine fans may have experienced a similar deflection further into the western GoM Basin (Figure 8).

5.4 Model Gaps and Uncertainties

Our model provides a new perspective on the evolution of the GoM, encompassing rift development and the evolution of the GoM crust architecture through an optimized deformation

model. It offers insights into tectonic subsidence during the early phase of GoM opening, shedding light on the creation of accommodations for the deposition of red beds and pre-salt sediments before seafloor spreading. However, several sources of uncertainty remain. For instance, sediments from nearby regions have accumulated in the GoM over millions of years, significantly deepening the basin and influencing total subsidence (Supplementary Figure S1; Snedden and Galloway 2019). Relatively thin Early Mesozoic sediments have a limited effect on accommodation space compared to thick Cenozoic sediments, especially in the central GoM. For instance, for a 4-7 km thick pre-salt in the subsided part of the basin by the end of the GoM opening phase, the resulting contribution of sediment deposition after stretching should be approximately 1–1.5 km. This is considerably less than the 4-6 km subsidence in the deeper GoM owing to tectonic subsidence. However, quantifying the role of these Early Mesozoic sediments over time is challenging because of the lack of available seismic imaging in the deeper GoM Basins. Nevertheless, our model can be used as an input parameter for landscape evolution models (Salles et al. 2018) to understand the consequences of sedimentary loading and basin formation.

The presence of vast Louann salt deposits and accompanying anhydrites, which were covered by sedimentary rocks, created extensive salt tectonics, making precise estimation of the overall tectonic subsidence value difficult (Ventress et al. 1989). The dynamic effect of the descending Farallon slab in the Late Cretaceous into western North America also influenced tectonic subsidence by an estimated 2–3 km in the western GoM (Spasojevic and Gurnis 2012; Wang et al. 2017). These locally significant elements were eliminated from the estimation of tectonic subsidence. Our study primarily focused on the early rifting phases and the creation of accommodation spaces in the GoM. We acknowledge that salt mobilization during the Cenozoic redistributed surface loads and modified crustal structures, potentially affecting the subsidence patterns. Incorporating this Cretaceous–present salt redistribution would require detailed forward modelling of salt flow and crustal response, which is beyond the scope of the current study but remains an important consideration for future work.

Our model captures the first-order controls of tectonic subsidence during the Mesozoic; however, a detailed analysis of the salt deformation dynamics is beyond the scope of this study. Given the complex interplay between salt withdrawal, sediment loading, and subsequent faulting, we recognize the need for future work dedicated to examining how salt tectonics affect subsidence patterns across different regions of the basin, particularly the observed asymmetry between the western and eastern GoM. Moreover, there is considerable ambiguity regarding present-day crustal thickness models. For instance, models such as GEMMA, which are based on the inversion of satellite gravity, are highly dependent on the density of the sedimentary cover. These models may be even more uncertain in regions of the GoM with heterogeneous salt coverage. Additionally, these crustal thickness models inherently have uncertainties that can influence crustal thickness estimates. Furthermore, the use of different crustal thickness models for our optimization may have resulted in varying crustal thickness calculations (Supplementary Figure S3).

Overall, in scenarios where estimating tectonic subsidence from back-stripped data is challenging owing to limited sedimentation during the early phase of rifting, our optimized

model, constrained by known back-stripped tectonic subsidence or other geophysical data, is a valuable tool.

6 Conclusion

Our research introduces an optimized and focused deformation model for reconstructing the Mesozoic history of the GoM using existing plate tectonic reconstructions. Our results reveal that initial tectonic subsidence occurred in the eastern and western regions of the northern GoM during the Late Triassic, indicating the infilling of the northern GoM-centered successor basin along three distinct paleo-drainage systems. Furthermore, our model demonstrates that a rapid increase in tectonic subsidence near Yucatán in the southern GoM likely led to sediment deposition in the present-day basin, largely bypassing the previous successor basin in the north. The hiatus between the Triassic Red beds and Bajocian salts in the northern GoM can thus be attributed to this southward shift in the depocenter.

Our model supports a hybrid origin for the GoM, characterized by an initial phase of magma-rich evolution and a transition into magma-poor margins, exhibiting temporal variability in magmatism. HMA, LMA, and CMA coincided with crustal thinning in the western GoM, suggesting a magma-rich origin for this margin. However, our model also indicated prolonged hyperextension prior to seafloor spreading during the Pliensbachian-Toarcian. Through focused deformation, we demonstrate the propagation of the rift through the unzipping of hyperextended crust from west to east, explaining the distinct crustal architecture observed in the GoM Basin. The stretching factor and extension rate calculations derived from our model suggest that the western GoM exhibits a wider hyperextended crust with potential mantle exhumation, which likely occurred during the Middle Toarcian period. In contrast, the eastern GoM displayed narrower and more symmetric mantle exhumation during the Late Aalenian-Early Bajocian. Our model further shows that the westward deflection of the Cenomanian-Turonian submarine fan resulted from the inherited increasing differential tectonic subsidence from the eastern to the western GoM. Our study establishes a robust framework for understanding the complex tectonic history of the early GoM Basin and provides valuable insights that lay the groundwork for future research on the evolution of passive rift margins worldwide.

Funding

This work was supported by BHP through the STELLAR industry collaboration and by the Australian Research Council under Grant [DE210100084] (to Sabin Zahirovic) and Grant [DP200100966] (to Maria Seton).

Disclosure statement

The authors declare that they have no known financial or personal relationships that could influence the work reported in this study.

Data Availability Statement

The model was created by open-source software pyGPlates (Müller et al., 2018). Reconstruction model files and workflows available from 10.5281/zenodo.10587769.

Author Contributions Statement

Satyam Pratap Singh led the numerical modelling, data analysis, figure preparation, visualization, and manuscript writing. Sabin Zahirovic contributed to the research concept, manuscript revision, and supervision. Maria Seton assisted with the supervision, interpretation of results, project administration, and funding acquisition. Nicky M. Wright contributed to data compilation, figure preparation, visualization, validation, and critical revisions. Nicholas Atwood and Catherine Belgarde were involved in validation, interpretation, and manuscript revisions. Claire Mallard contributed to the methodology development, interpretation, and manuscript review. Christopher Alphonso and Youseph Ibrahim assisted with numerical modelling, data visualization, software support, and manuscript refinement.

Acknowledgements

The authors thank the BHP STELLAR industry collaborators for their support and contribution. The development of pyGPlates and GPlates was supported by the Australian National Collaborative Research Infrastructure Strategy (NCRIS) program, Australia.

References

Adams RL. 2007. Abstract: Basement Tectonics and the Origin of the Sabine Uplift. Houston Geological Society Bulletin [Internet]. [accessed 2023 Apr 18] 49(9):19–19. http://archives.datapages.com/data/HGS/vol49/no09/19.htm

Alvey A, Kusznir NJ, Roberts A. 2018. Regional Crustal Structure of the Gulf of Mexico From Gravity Inversion [Internet]. In: Denver, CO; [accessed 2024 Jun 17]. https://www.searchanddiscovery.com/abstracts/html/2015/90216ace/abstracts/2092755.html

Anderson TH, Schmidt VA. 1983. The evolution of Middle America and the Gulf of Mexico–Caribbean Sea region during Mesozoic time. Geol Soc America Bull [Internet]. [accessed 2023 Jan 16] 94(8):941. https://doi.org/10.1130/0016-7606(1983)94<941:TEOMAA>2.0.CO;2

Armitage JJ, Collier JS, Minshull TA. 2010. The importance of rift history for volcanic margin formation. Nature [Internet]. [accessed 2023 Apr 11] 465(7300):913–917. https://doi.org/10.1038/nature09063

Bird DE, Burke K, Hall SA, Casey JF. 2005. Gulf of Mexico tectonic history: Hotspot tracks, crustal boundaries, and early salt distribution. AAPG Bulletin [Internet]. [accessed 2024 Jun 17] 89(3):311–328. https://doi.org/10.1306/10280404026

Bonatti E. 1985. Punctiform initiation of seafloor spreading in the Red Sea during transition from a continental to an oceanic rift. Nature [Internet]. [accessed 2023 Apr 13] 316(6023):33–37. https://doi.org/10.1038/316033a0

Bott MHP. 1992. The stress regime associated with continental break-up. Geological Society, London, Special Publications [Internet]. [accessed 2023 Jun 19] 68(1):125–136. https://doi.org/10.1144/GSL.SP.1992.068.01.08

Brune S, Heine C, Clift PD, Pérez-Gussinyé M. 2017. Rifted margin architecture and crustal rheology: Reviewing Iberia-Newfoundland, Central South Atlantic, and South China Sea. Marine and Petroleum Geology [Internet]. [accessed 2023 Jun 19] 79:257–281. https://doi.org/10.1016/j.marpetgeo.2016.10.018

Brune S, Kolawole F, Olive J-A, Stamps DS, Buck WR, Buiter SJH, Furman T, Shillington DJ. 2023. Geodynamics of continental rift initiation and evolution. Nat Rev Earth Environ [Internet]. [accessed 2023 Apr 11]:1–19. https://doi.org/10.1038/s43017-023-00391-3

Buffler RT, Sawyer DS. 1985. Distribution of Crust and Early History, Gulf of Mexico Basin [Internet]. [accessed 2024 Jun 17] 35. https://archives.datapages.com/data/gcags/data/035/035001/0333.htm

Cannat M, Sauter D, Bezos A, Meyzen C, Humler E, Le Rigoleur M. 2008. Spreading rate, spreading obliquity, and melt supply at the ultraslow spreading Southwest Indian Ridge. Geochemistry, Geophysics, Geosystems [Internet]. [accessed 2023 Apr 13] 9(4). https://doi.org/10.1029/2007GC001676

Chenin P, Schmalholz SM, Manatschal G, Karner GD. 2018. Necking of the Lithosphere: A Reappraisal of Basic Concepts With Thermo-Mechanical Numerical Modeling. Journal of Geophysical Research: Solid Earth [Internet]. [accessed 2023 Jun 19] 123(6):5279–5299. https://doi.org/10.1029/2017JB014155

Christeson GL, Van Avendonk HJA, Norton IO, Snedden JW, Eddy DR, Karner GD, Johnson CA. 2014. Deep crustal structure in the eastern Gulf of Mexico. Journal of Geophysical Research: Solid Earth [Internet]. [accessed 2023 Jan 16] 119(9):6782–6801. https://doi.org/10.1002/2014JB011045

Chu D, Gordon RG. 1998. Current plate motions across the Red Sea. Geophysical Journal International [Internet]. [accessed 2023 Apr 13] 135(2):313–328. https://doi.org/10.1046/j.1365-246X.1998.00658.x

Colletta B, Le Quellec P, Letouzey J, Moretti I. 1988. Longitudinal evolution of the Suez rift structure (Egypt). Tectonophysics [Internet]. [accessed 2023 Apr 13] 153(1):221–233. https://doi.org/10.1016/0040-1951(88)90017-0

Curry MAE, Peel FJ, Hudec MR, Norton IO. 2018. Extensional models for the development of passive-margin salt basins, with application to the Gulf of Mexico. Basin Research [Internet]. [accessed 2024 Jun 18] 30(6):1180–1199. https://doi.org/10.1111/bre.12299

Davis M, Kusznir N. 2004. 4. Depth-Dependent Lithospheric Stretching at Rifted Continental Margins. In: 4 Depth-Dependent Lithospheric Stretching at Rifted Continental Margins [Internet]. [place unknown]: Columbia University Press; [accessed 2024 Jul 8]; p. 92–137. https://doi.org/10.7312/karn12738-005

Dewey JF, Bird JM. 1970. Mountain belts and the new global tectonics. Journal of Geophysical Research (1896-1977) [Internet]. [accessed 2024 Jul 8] 75(14):2625–2647. https://doi.org/10.1029/JB075i014p02625

Dickinson WR, Gehrels GE, Stern RJ. 2010. Late Triassic Texas uplift preceding Jurassic opening of the Gulf of Mexico: Evidence from U-Pb ages of detrital zircons. Geosphere [Internet]. [accessed 2023 Jun 18] 6(5):641–662. https://doi.org/10.1130/GES00532.1

Ebinger CJ, Keir D, Bastow ID, Whaler K, Hammond JOS, Ayele A, Miller MS, Tiberi C, Hautot S. 2017. Crustal Structure of Active Deformation Zones in Africa: Implications for Global Crustal Processes. Tectonics [Internet]. [accessed 2023 Jun 19] 36(12):3298–3332. https://doi.org/10.1002/2017TC004526

Eddy DR, Van Avendonk HJA, Christeson GL, Norton IO. 2018. Structure and origin of the rifted margin of the northern Gulf of Mexico. Geosphere [Internet]. [accessed 2023 Apr 13] 14(4):1804–1817. https://doi.org/10.1130/GES01662.1

Eddy DR, Van Avendonk HJA, Christeson GL, Norton IO, Karner GD, Johnson CA, Snedden JW. 2014. Deep crustal structure of the northeastern Gulf of Mexico: Implications for rift evolution and seafloor spreading. Journal of Geophysical Research: Solid Earth [Internet]. [accessed 2023 Jan 16] 119(9):6802–6822. https://doi.org/10.1002/2014JB011311

Escalona A, Norton IO, Lawver LA, Gahagan L. 2021. Quantitative Plate Tectonic Reconstructions of the Caribbean Region from Jurassic to Present. Memoir 123: South America-Caribbean-Central Atlantic Plate Boundary, 2021 [Internet]. [accessed 2023 Apr 13]:239–263. https://doi.org/10.1306/13692247M1233849

Filina I. 2019. Crustal architecture of the northwestern and central Gulf of Mexico from integrated geophysical analysis. Interpretation [Internet]. [accessed 2023 Jun 19] 7(4):T899–T910. https://doi.org/10.1190/INT-2018-0258.1

Filina I, Austin J, Doré T, Johnson E, Minguez D, Norton I, Snedden J, Stern RJ. 2022. Opening of the Gulf of Mexico: What we know, what questions remain, and how we might answer them. Tectonophysics [Internet]. [accessed 2022 Oct 10] 822:229150. https://doi.org/10.1016/j.tecto.2021.229150

Filina I, Beutel E. 2022. Geological and Geophysical Constraints Guide New Tectonic Reconstruction of the Gulf of Mexico. [place unknown]. https://doi.org/10.1002/essoar.10511463.1

Filina I, Hartford L. 2021. Subsurface structures along western Yucatan from integrated geophysical analysis. Marine and Petroleum Geology [Internet]. [accessed 2023 Aug 21] 127:104964. https://doi.org/10.1016/j.marpetgeo.2021.104964

García-Reyes A, Dyment J. 2022a. Structure, age, and tectonic evolution of the Gulf of Mexico. Earth and Planetary Science Letters [Internet]. [accessed 2024 Jun 17] 577:117259. https://doi.org/10.1016/j.epsl.2021.117259

García-Reyes A, Dyment J. 2022b. Structure, age, and origin of the Caribbean Plate unraveled. Earth and Planetary Science Letters [Internet]. [accessed 2024 Jun 17] 571:117100. https://doi.org/10.1016/j.epsl.2021.117100

Goswami A, Hartwig A, Reuber K, Pindell J. 2016. Imaging the Pre-Salt Gulf of Mexico: Basin Classification and Comparison With Other World Class Petroleum Basins [Internet]. In: [place unknown]; [accessed 2024 Jun 18]. https://www.searchanddiscovery.com/abstracts/html/2016/90260ice/abstracts/2474591.html

Gurnis M, Yang T, Cannon J, Turner M, Williams S, Flament N, Müller RD. 2018. Global tectonic reconstructions with continuously deforming and evolving rigid plates. Computers & Geosciences [Internet]. [accessed 2022 Dec 18] 116:32–41. https://doi.org/10.1016/j.cageo.2018.04.007

Ho T, Priestley K, Debayle E. 2016. A Global Horizontal Shear Velocity Model of the Upper Mantle from multi-mode Love Wave Measurements. Geophysical Journal International. 207:ggw292. https://doi.org/10.1093/gji/ggw292

Horn BW, Goswami A, Haire E, Radovich B, McGrail A, Pindell J. 2016. Regional Interpretation Across the Entire Gulf of Mexico Basin – A New Perspective. The Houston Geological Society Bulletin [Internet]. [accessed 2023 Jan 16] 58(7):31–33. http://archives.datapages.com/data/HGS/vol58/058007/31_hgs580031.htm

Hudec MR, Dooley TP, Peel FJ, Soto JI. 2019. Controls on the evolution of passive-margin salt basins: Structure and evolution of the Salina del Bravo region, northeastern Mexico. GSA Bulletin [Internet]. [accessed 2023 Jan 16] 132(5–6):997–1012. https://doi.org/10.1130/B35283.1

Hudec MR, Norton IO. 2019. Upper Jurassic structure and evolution of the Yucatán and Campeche subbasins, southern Gulf of Mexico. AAPG Bulletin [Internet]. [accessed 2023 Jan 16] 103(5):1133–1151. https://doi.org/10.1306/11151817405

Hudec MR, Norton IO, Jackson MPA, Peel FJ. 2013. Jurassic evolution of the Gulf of Mexico salt basin. AAPG Bulletin [Internet]. [accessed 2023 May 1] 97(10):1683–1710. https://doi.org/10.1306/04011312073

Huerta AD, Harry DL. 2012. Wilson cycles, tectonic inheritance, and rifting of the North American Gulf of Mexico continental margin. Geosphere [Internet]. [accessed 2022 Aug 4] 8(2):374–385. https://doi.org/10.1130/GES00725.1

Imbert P. 2005. The Mesozoic Opening of the Gulf of Mexico: Part 1, Evidence for Oceanic Accretion During and After Salt Deposition. In: Post PJ, Rosen NC, Olson DL, Palmes SL, Lyons KT, Newton GB, editors. Petroleum Systems of Divergent Continental Margin Basins [Internet]. Vol. 25. [place unknown]: SEPM Society for Sedimentary Geology; [accessed 2024 Jun 18]; p. 0. https://doi.org/10.5724/gcs.05.25.1119

Imbert P, Philippe Y. 2005. The Mesozoic Opening of the Gulf of Mexico: Part 2, Integrating Seismic and Magnetic Data into a General Opening Model. In: [place unknown]; p. 1151–1190. https://doi.org/10.5724/gcs.05.25.1151

Izquierdo-Llavall E, Ringenbach JC, Sapin F, Rives T, Callot JP. 2022. Crustal structure and lateral variations in the Gulf of Mexico conjugate margins: From rifting to break-up. Marine and Petroleum Geology [Internet]. [accessed 2023 Apr 13] 136:105484. https://doi.org/10.1016/j.marpetgeo.2021.105484

Jarvis GT, McKenzie DP. 1980. Sedimentary basin formation with finite extension rates. Earth and Planetary Science Letters [Internet]. [accessed 2023 Jun 20] 48(1):42–52. https://doi.org/10.1016/0012-821X(80)90168-5

Kaban MK, Tesauro M, Mooney WD, Cloetingh SAPL. 2014. Density, temperature, and composition of the North American lithosphere—New insights from a joint analysis of seismic, gravity, and mineral physics data: 1. Density structure of the crust and upper mantle. Geochemistry, Geophysics, Geosystems [Internet]. [accessed 2023 Jul 22] 15(12):4781–4807. https://doi.org/10.1002/2014GC005483

King MT, Welford JK. 2022. Advances in Deformable Plate Tectonic Models: 1. Reconstructing Deformable Continental Blocks and Crustal Thicknesses Back Through Time. Geochemistry, Geophysics, Geosystems [Internet]. [accessed 2024 Jun 26] 23(6):e2022GC010372. https://doi.org/10.1029/2022GC010372

Kneller EA, Johnson CA. 2011. Plate Kinematics of the Gulf of Mexico Based on Integrated Observations from the Central and South Atlantic [Internet]. [accessed 2023 Jun 19]:283–300. http://archives.datapages.com/data/gcags/data/061/061001/283_gcags610283.htm

Laske G, Masters G, Ma Z, Pasyanos M. 2013. Update on CRUST1.0 - A 1-degree Global Model of Earth's Crust [Internet]. [accessed 2023 Sep 29]:EGU2013-2658. https://ui.adsabs.harvard.edu/abs/2013EGUGA..15.2658L

Le Pichon X, Sibuet J-C. 1981. Passive margins: A model of formation. Journal of Geophysical Research: Solid Earth [Internet]. [accessed 2023 Jan 10] 86(B5):3708–3720. https://doi.org/10.1029/JB086iB05p03708

Li P. 2006. Reconstruction of Burial History of Strata in the North Louisiana Salt Basin Area. GCAGS Transactions. 56:455–471.

Liu M, Filina I, Mann P. 2019. Crustal structure of Mesozoic rifting in the northeastern Gulf of Mexico from integration of seismic and potential fields data. Interpretation [Internet]. [accessed 2023 Apr 13] 7(4):T857–T867. https://doi.org/10.1190/INT-2018-0259.1

Lundin ER, Doré AG. 2017. The Gulf of Mexico and Canada Basin: Genetic Siblings on Either Side of North America. GSAT [Internet]. [accessed 2023 Apr 10]:4–11. https://doi.org/10.1130/GSATG274A.1

Lundin ER, Redfield TF, Péron-Pindivic G. 2014. Rifted Continental Margins: Geometric Influence on Crustal Architecture and Melting. In: Pindell J, Horn B, Rosen N, Weimer P, Dinkleman M, Lowrie A, Fillon R, Granath J, Kennan L, editors. Sedimentary Basins: Origin, Depositional Histories, and Petroleum Systems [Internet]. Vol. 33. [place unknown]: SEPM Society for Sedimentary Geology; [accessed 2023 Apr 12]; p. 0. https://doi.org/10.5724/gcs.14.33.0018

Mann P. 2014. Passive Plate Margin. In: Harff J, Meschede M, Petersen S, Thiede J, editors. Encyclopedia of Marine Geosciences [Internet]. Dordrecht: Springer Netherlands; [accessed 2024 Jan 30]; p. 1–8. https://doi.org/10.1007/978-94-007-6644-0_100-1

Mann P. 2022. Chapter 3 - Crustal structure and tectonostratigraphy of rifted-passive margins with applications for hydrocarbon exploration. In: Rotzien JR, Yeilding CA, Sears RA, Hernández-Molina FJ, Catuneanu O, editors. Deepwater Sedimentary Systems [Internet]. [place unknown]: Elsevier; [accessed 2024 Jan 30]; p. 83–117. https://doi.org/10.1016/B978-0-323-91918-0.00018-9

Marton G, Buffler RT. 1994. Jurassic Reconstruction of the Gulf of Mexico Basin. International Geology Review [Internet]. [accessed 2022 Aug 3] 36(6):545–586. https://doi.org/10.1080/00206819409465475

Marzoli A, Callegaro S, Dal Corso J, Davies JHFL, Chiaradia M, Youbi N, Bertrand H, Reisberg L, Merle R, Jourdan F. 2018. The Central Atlantic Magmatic Province (CAMP): A Review. In: Tanner LH, editor. The Late Triassic World: Earth in a Time of Transition [Internet]. Cham: Springer International Publishing; [accessed 2023 Jan 16]; p. 91–125. https://doi.org/10.1007/978-3-319-68009-5_4

McKenzie D. 1978. Some remarks on the development of sedimentary basins. Earth and Planetary Science Letters [Internet]. [accessed 2022 Jul 29] 40(1):25–32. https://doi.org/10.1016/0012-821X(78)90071-7

Meyer B, Saltus R, Chulliat A. 2017. EMAG2v3: Earth Magnetic Anomaly Grid (2-arc-minute resolution) [Internet]. [accessed 2023 Jul 21]. https://doi.org/10.7289/V5H70CVX

Mickus K, Stern RJ, Keller GR, Anthony EY. 2009. Potential field evidence for a volcanic rifted margin along the Texas Gulf Coast. Geology [Internet]. [accessed 2023 Jan 14] 37(5):387–390. https://doi.org/10.1130/G25465A.1

Milliken JV. 1988. Late Paleozoic and Early Mesozoic geologic evolution of the Arklatex Area [Thesis] [Internet]. [place unknown]: Rice University; [accessed 2023 Jan 16]. https://scholarship.rice.edu/handle/1911/13309

Minguez D, Gerald Hensel E, Johnson EAE. 2020. A fresh look at Gulf of Mexico tectonics: Testing rotations and breakup mechanisms from the perspective of seismically constrained

potential-fields modeling and plate kinematics. Interpretation [Internet]. [accessed 2022 Aug 24] 8(4):SS31–SS45. https://doi.org/10.1190/INT-2019-0256.1

Mjelde R, Breivik AJ, Raum T, Mittelstaedt E, Ito G, Faleide JI. 2008. Magmatic and tectonic evolution of the North Atlantic. Journal of the Geological Society [Internet]. [accessed 2024 Jun 18] 165(1):31–42. https://doi.org/10.1144/0016-76492007-018

Mooney WD, Kaban MK. 2010. The North American upper mantle: Density, composition, and evolution. Journal of Geophysical Research: Solid Earth [Internet]. [accessed 2025 Sep 5] 115(B12). https://doi.org/10.1029/2010JB000866

Müller RD, Zahirovic S, Williams SE, Cannon J, Seton M, Bower DJ, Tetley MG, Heine C, Le Breton E, Liu S, et al. 2019. A Global Plate Model Including Lithospheric Deformation Along Major Rifts and Orogens Since the Triassic. Tectonics [Internet]. [accessed 2022 Aug 24] 38(6):1884–1907. https://doi.org/10.1029/2018TC005462

Naliboff J, Buiter SJH. 2015. Rift reactivation and migration during multiphase extension. Earth and Planetary Science Letters [Internet]. [accessed 2023 Jun 19] 421:58–67. https://doi.org/10.1016/j.epsl.2015.03.050

Nemčok M, editor. 2016. Determination of unstretched continental, thinned continental, proto-oceanic, and oceanic crustal boundaries. In: Rifts and Passive Margins: Structural Architecture, Thermal Regimes, and Petroleum Systems [Internet]. Cambridge: Cambridge University Press; [accessed 2023 Jul 22]; p. 76–96. https://doi.org/10.1017/CBO9781139198844.004

Nguyen LC, Levander A, Niu F, Morgan J, Li G. 2022. Insights on Formation of the Gulf of Mexico by Rayleigh Surface Wave Imaging. Geochemistry, Geophysics, Geosystems [Internet]. [accessed 2023 Apr 13] 23(12):e2022GC010566. https://doi.org/10.1029/2022GC010566

Nguyen LC, Mann P. 2015. Gravity and magnetic constraints on the Jurassic opening of the oceanic Gulf of Mexico and the location and tectonic history of the Western Main transform fault along the eastern continental margin of Mexico. Interpretation [Internet]. [accessed 2023 May 24] 4(1):SC23–SC33. https://doi.org/10.1190/INT-2015-0110.1

Nguyen LC, Mann P. 2016. Gravity and magnetic constraints on the Jurassic opening of the oceanic Gulf of Mexico and the location and tectonic history of the Western Main transform fault along the eastern continental margin of Mexico. Interpretation. 4(1):SC23–SC33. https://doi.org/10.1190/INT-2015-0110.1

Nicholas RL, Waddell DE. 1989. The Ouachita system in the subsurface of Texas, Arkansas, and Louisiana. In: Hatcher RD Jr, Thomas WA, Viele GW, editors. The Appalachian-Ouachita Orogen in the United States [Internet]. Vol. F-2. [place unknown]: Geological Society of America; [accessed 2023 Jun 19]; p. 0. https://doi.org/10.1130/DNAG-GNA-F2.661

O'Reilly C, Keay J, Birch-Hawkins A, Bate D, Halliday J, TGS. 2017. Regional Play Types in the Mexican Offshore. GEO ExPro Magazine [Internet]. [accessed 2023 Feb 20]. https://archives.datapages.com/data/geo-expro-magazine/014/014004/pdfs/36.html

Pérez-Gussinye M. 2013. A tectonic model for hyperextension at magma-poor rifted margins: An example from the west iberia-newfoundland conjugate margins. Geological Society Special Publication. 369(1):403–427. https://doi.org/10.1144/SP369.19

Péron-Pinvidic G, Manatschall G, Dean SM, Minshull TA. 2008. Compressional structures on the West Iberia rifted margin: Controls on their distribution. Geological Society Special Publication. 306:169–183. https://doi.org/10.1144/SP306.8

Pilcher RS, Murphy RT, McDonough Ciosek J. 2014. Jurassic raft tectonics in the northeastern Gulf of Mexico. Interpretation [Internet]. [accessed 2023 Sep 21] 2(4):SM39–SM55. https://doi.org/10.1190/INT-2014-0058.1

Pindell J, Dewey JF. 1982. Permo-Triassic reconstruction of western Pangea and the evolution of the Gulf of Mexico/Caribbean region. Tectonics [Internet]. [accessed 2024 Jul 5] 1(2):179–211. https://doi.org/10.1029/TC001i002p00179

Pindell J, Graham R, Horn B. 2014. Rapid outer marginal collapse at the rift to drift transition of passive margin evolution, with a Gulf of Mexico case study. Basin Research [Internet]. [accessed 2022 Aug 31] 26(6):701–725. https://doi.org/10.1111/bre.12059

Pindell J, Kennan L. 2009. Tectonic evolution of the Gulf of Mexico, Caribbean and northern South America in the mantle reference frame: An update. Geological Society, London, Special Publications. 328:1–55. https://doi.org/10.1144/SP328.1

Pindell J, Miranda C. Ernesto, Alejandro C, Leopoldo H. 2016. Aeromagnetic Map Constrains Jurassic-Early Cretaceous Synrift, Break Up, and Rotational Seafloor Spreading History in the Gulf of Mexico. In: Lowery CM, Snedden JW, Rosen NC, editors. Mesozoic of the Gulf Rim and Beyond: New Progress in Science and Exploration of the Gulf of Mexico Basin [Internet]. Vol. 35. [place unknown]: SEPM Society for Sedimentary Geology; [accessed 2023 Jan 16]; p. 0. https://doi.org/10.5724/gcs.15.35.0123

Pindell J, Villagómez D, Molina-Garza R, Graham R, Weber B. 2021. A revised synthesis of the rift and drift history of the Gulf of Mexico and surrounding regions in the light of improved age dating of the Middle Jurassic salt. Geological Society, London, Special Publications [Internet]. [accessed 2022 Aug 24] 504(1):29–76. https://doi.org/10.1144/SP504-2020-43

Pindell JL. 1985. Alleghenian reconstruction and subsequent evolution of the Gulf of Mexico, Bahamas, and Proto-Caribbean. Tectonics [Internet]. [accessed 2023 Jan 16] 4(1):1–39. https://doi.org/10.1029/TC004i001p00001

Reguzzoni M, Sampietro D. 2015. GEMMA: An Earth crustal model based on GOCE satellite data. International Journal of Applied Earth Observation and Geoinformation [Internet]. [accessed 2022 Sep 12] 35:31–43. https://doi.org/10.1016/j.jag.2014.04.002

Reston TJ. 2009. The structure, evolution and symmetry of the magma-poor rifted margins of the North and Central Atlantic: A synthesis. Tectonophysics [Internet]. [accessed 2024 Jul 8] 468(1):6–27. https://doi.org/10.1016/j.tecto.2008.09.002

Rowan MG. 2014. Passive-margin salt basins: hyperextension, evaporite deposition, and salt tectonics. Basin Research [Internet]. [accessed 2023 Feb 20] 26(1):154–182. https://doi.org/10.1111/bre.12043

Salles T, Ding X, Brocard G. 2018. pyBadlands: A framework to simulate sediment transport, landscape dynamics and basin stratigraphic evolution through space and time. PloS one [Internet]. [accessed 2024 Jan 30] 13(4):e0195557. https://journals.plos.org/plosone/article?id=10.1371/journal.pone.0195557

Salvador A. 1991. Origin and development of the Gulf of Mexico basin. In: Salvador A, editor. The Gulf of Mexico Basin [Internet]. Vol. J. [place unknown]: Geological Society of America; [accessed 2023 Jan 16]; p. 0. https://doi.org/10.1130/DNAG-GNA-J.389

Sandwell D, Müller D, Smith W, Garcia E, Francis R. 2014. New global marine gravity from CryoSat-2 and Jason-1 reveals buried tectonic structure. Science. 346:65–67. https://doi.org/10.1126/science.1258213

Scott KR, Hayes WE, Fietz RP. 1961. Geology of the Eagle Mills Formation. GCAGS Transactions [Internet]. [accessed 2023 Jan 16] 11:1–14. http://archives.datapages.com/data/gcags/data/011/011001/0001.htm

Smith WHF, Sandwell DT. 1997. Global Sea Floor Topography from Satellite Altimetry and Ship Depth Soundings. Science [Internet]. [accessed 2023 Aug 21] 277(5334):1956–1962. https://doi.org/10.1126/science.277.5334.1956

Snedden J, Virdell J, Whiteaker T, Ganey-Curry P. 2016. A basin-scale perspective on Cenomanian-Turonian (Cretaceous) depositional systems, greater Gulf of Mexico (USA). Interpretation. 4:SC1–SC22. https://doi.org/10.1190/INT-2015-0082.1

Snedden JW, Galloway WE. 2019. The Gulf of Mexico Sedimentary Basin: Depositional Evolution and Petroleum Applications [Internet]. Cambridge: Cambridge University Press; [accessed 2022 Dec 18]. https://doi.org/10.1017/9781108292795

Spasojevic S, Gurnis M. 2012. Sea level and vertical motion of continents from dynamic earth models since the Late Cretaceous. AAPG Bulletin [Internet]. [accessed 2025 Aug 20] 96(11):2037–2064. https://doi.org/10.1306/03261211121

Steier A, Mann P. 2019. Late Mesozoic gravity sliding and Oxfordian hydrocarbon reservoir potential of the northern Yucatan margin. Marine and Petroleum Geology [Internet]. [accessed 2023 Apr 13] 103:681–701. https://doi.org/10.1016/j.marpetgeo.2019.03.001

Sweet ML, Phillips MP, Cunningham R, Snedden JW, Weber R. 2022. The Early Cretaceous Transition from Carbonate to Siliciclastic Deposition in the Deep Waters of the Northern Gulf of Mexico: New Insights from the Keathley Canyon 102 #1 Well. GCAGS Journal. 11:58–70.

Talwani Manik, Ewing J, Sheridan RE, Holbrook WS, Glover L. 1995. The Edge Experiment and the U.S. East Coast Magnetic Anomaly. In: Banda E, Torné M, Talwani M., editors. Rifted

Ocean-Continent Boundaries [Internet]. Dordrecht: Springer Netherlands; [accessed 2024 Jun 18]; p. 155–181. https://doi.org/10.1007/978-94-011-0043-4_9

Tetreault JL, Buiter SJH. 2018. The influence of extension rate and crustal rheology on the evolution of passive margins from rifting to break-up. Tectonophysics [Internet]. [accessed 2023 Jan 10] 746:155–172. https://doi.org/10.1016/j.tecto.2017.08.029

Tugend J, Gillard M, Manatschal G, Nirrengarten M, Harkin C, Epin M-E, Sauter D, Autin J, Kusznir N, McDermott K. 2020. Reappraisal of the magma-rich versus magma-poor rifted margin archetypes. Geological Society, London, Special Publications [Internet]. [accessed 2023 Apr 11] 476(1):23–47. https://doi.org/10.1144/SP476.9

Umbarger KF. 2018. Late Triassic North American Paleodrainage Networks and Sediment Dispersal of the Chinle Formation: A Quantitative Approach Utilizing Detrital Zircons [Thesis] [Internet]. [place unknown]: University of Kansas; [accessed 2023 Apr 13]. https://kuscholarworks.ku.edu/handle/1808/27833

Van Avendonk H, Christeson G, Norton I, Eddy D. 2015. Continental rifting and sediment infill in the northwestern Gulf of Mexico. Geology. 43. https://doi.org/10.1130/G36798.1

Ventress WPS, Bebout DG, Perkins BF, Moore CH. 1989. Gulf of Mexico Salt Tectonics, Associated Processes and Exploration Potential [Internet]. [place unknown]: SEPM Society for Sedimentary Geology; [accessed 2023 Apr 13]. https://doi.org/10.5724/gcs.89.10

Wang H, Gurnis M, Skogseid J. 2017. Rapid Cenozoic Subsidence in the Gulf of Mexico Resulting From Hess Rise Conjugate Subduction. Geophysical Research Letters [Internet]. [accessed 2022 Sep 12] 44(21):10,930-10,938. https://doi.org/10.1002/2017GL074959

White R, McKenzie D. 1989. Magmatism at rift zones: The generation of volcanic continental margins and flood basalts. Journal of Geophysical Research: Solid Earth [Internet]. [accessed 2023 Apr 11] 94(B6):7685–7729. https://doi.org/10.1029/JB094iB06p07685

Wiley KS. 2017. Provenance of Syn-rift Clastics in the Eastern Gulf of Mexico: Insight from U-Pb Detrital Zircon Geochronology and Thin Sections. Graduate Theses, Dissertations, and Problem Reports [Internet]. https://doi.org/10.33915/etd.6951

Williams-Rojas CT, Reyes-Tovar E, Miranda-Peralta L, Reyna-Martinez G, Cardenas-Alvarado A, Maldonado-Villalon R, Munoz-Bocanegra V, Lora-delaFuente C. 2012. Hydrocarbon Potential of the Deepwater Portion of the "Salina del Istmo" Province, Southeastern Gulf of Mexico, Mexico. GCAGS Transactions [Internet]. [accessed 2023 Feb 20] 61:681–684. http://archives.datapages.com/data/gcags/data/062/062001/641_gcags620641.htm

Wood G, Benson D. 2000. The North American occurrence of the algal coenobium Plaesiodictyon: Paleogeographic, paleoecologic, and biostratigraphic importance in the Triassic. Palynology. 24:9–20. https://doi.org/10.2113/0240009

Xie X, Heller PL. 2009. Plate tectonics and basin subsidence history. GSA Bulletin [Internet]. [accessed 2022 Dec 18] 121(1–2):55–64. https://doi.org/10.1130/B26398.1

Chapter 3

Article 2: Topographic Diversity in Subduction-Related Mountains Driven by Plate Tectonics and Mantle Dynamics

Topographic Diversity in Subduction-Related Mountains Driven by Plate Tectonics and Mantle Dynamics

Satyam Pratap Singh[1], Maria Seton[1], Sabin Zahirovic[1], Nicky M. Wright[1], Nicholas Atwood[2], Clement Fay[3]

[1]*EarthByte Group, School of Geosciences, The University of Sydney, NSW 2006, Australia*
[2]*BHP Minerals Service Co, Tucson, Arizona 85704, USA*
[3]*BHP Minerals Service Co, Victoria Street, London SW1E 5LB, UK*

Corresponding Author: Satyam Pratap Singh (satyampratap.singh@sydney.edu.au)

Abstract

Topography at active margins results from complex interactions among plate tectonics, mantle convection, and climate-driven surface processes. However, quantifying the relative contributions of these processes to the diverse topography of active margins remains a significant challenge. Existing geodynamic and surface process models are computationally intensive, often limiting analyses to a narrow set of parameters and regional scales. Here, we introduce a framework that integrates Explainable Artificial Intelligence (XAI) with data from global plate reconstructions, mantle convection, and paleoclimate simulations to quantify the drivers of global active margin topography. Our model predicted the present-day elevation with a root mean square error of 444 m and a coefficient of determination (R^2) of 0.77 compared to ETOPO. Subduction flux, trench migration rate, and upper mantle temperature were identified as the dominant controls on elevation. These parameters give rise to three distinct topographic regimes: (1) high subduction flux (>0.08 km^3/yr) driving elevations above 3000 m (e.g., Central Andes); (2) moderate subduction flux with trench retreat yielding low topography (<1000 m; e.g., Calabria); and (3) advancing trenches producing broad elevated terrains (>1500 m; e.g., Central Makran). Our framework offers the potential for reconstructing the paleotopography of active margins, shedding light on the distribution of Earth's mineral resources and the evolution of biodiversity.

Keywords

Active Margin; Topography; Artificial Intelligence; Plate Tectonics; Geodynamics

1. Introduction

The topography of active margins arises from the complex interplay of plate tectonics (e.g., Champagnac et al., 2012; Schellart, 2008), mantle convection (e.g., Faccenna et al., 2021; Faccenna and Becker, 2020), and climate-influenced surface processes (e.g., erosion; Willett et al., 2001; Wolf et al., 2022; Yuan et al., 2024). Subduction zones generate a wide range of topographic features, from mountain belts and volcanic arcs to forearc basins and deep-sea trenches (Faccenna et al., 2013; Royden, 1993). Although subduction-related crustal shortening is the primary mechanism for orogeny, recent studies have shown that it accounts for only a portion of the present-day elevation variability (Champagnac et al., 2012; Wolf et al., 2022; Yuan et al., 2024). Other geodynamic and climatic processes likely play a significant role (Faccenna et al., 2013; Wolf et al., 2022; Yuan et al., 2024), but quantifying their relative contributions at a global scale remains challenging. A previous global analysis suggested that shortening rates alone explain less than 25% of the variance in topographic metrics, such as mean elevation and relief (Champagnac et al., 2012). Additional tectonic variables, such as trench migration, subduction velocity, and lithospheric buoyancy, can influence overriding plate deformation and support topographic highs (Schellart and Moresi, 2013; Faccenna and Becker, 2020). At the same time, mantle convection, through its role in driving dynamic topography and influencing basal tractions on the lithosphere, can modulate long-wavelength elevation patterns (Braun, 2010; Flament et al., 2013; Hager et al., 1985). Surface processes, particularly climate-driven erosion, interact with tectonics and isostasy to modify relief, further complicating efforts to attribute causality (Clark et al., 2004; Han et al., 2024; Whipple, 2009). Coupled surface process and geodynamic numerical models, which are widely used to study topography and the interplay of plate tectonics, climate, and mantle dynamics (e.g., Lu et al., 2024; Wolf et al., 2022; Yuan et al., 2024) face several challenges. These models are computationally expensive, often regionally focused (Wolf et al., 2022; Schellart, 2017), and difficult to scale globally or apply to the deep geologic past. They are also sensitive to the initial and boundary conditions and lack flexibility in exploring a broad parameter space. Consequently, many questions about the driving forces behind active margin topography remain unresolved, particularly in regions of continuous subduction, where processes such as slab dynamics, overriding plate deformation, and precipitation-driven erosion may all contribute.

Recent advancements in Earth Sciences, driven by innovative tools and spatiotemporal data curation (Bower et al., 2015; Li et al., 2022; Müller et al., 2018; Zhong and Gurnis, 1995), have opened the field to new data mining techniques like never before. Tools such as GPlates (Müller et al., 2018) enable the reconstruction of past plate configurations and kinematics, which, when coupled with mantle convection models such as CitcomS (Bower et al., 2015; Tan et al., 2006; Zhong and Gurnis, 1995) and paleoclimate simulations (e.g., Li et al., 2022), allow for the exploration of interactions between surface processes and the deep Earth. In parallel with these strides, advancements in machine learning—particularly in interpretable Explainable Artificial Intelligence (XAI) models like the Explainable Boosting Machines (EBM)—offer new analytical capabilities to uncover previously hidden information in these datasets (Konstantinov and Utkin, 2021; Lou et al., 2013). The EBM combines the predictive power of advanced machine learning models with interpretability, providing insights into how an individual parameter influences the outcome while keeping all other parameters constant (Lou et al., 2013). Our research employs the EBM model that links a global-scale mantle convection model (Bower et al., 2015; Tan et al., 2006; Zhong and Gurnis, 1995), plate tectonic reconstruction (Zahirovic et al., 2022), and paleoclimate simulation (Li et al., 2022) to understand the elevation at active margins with subduction (Fig. 1).

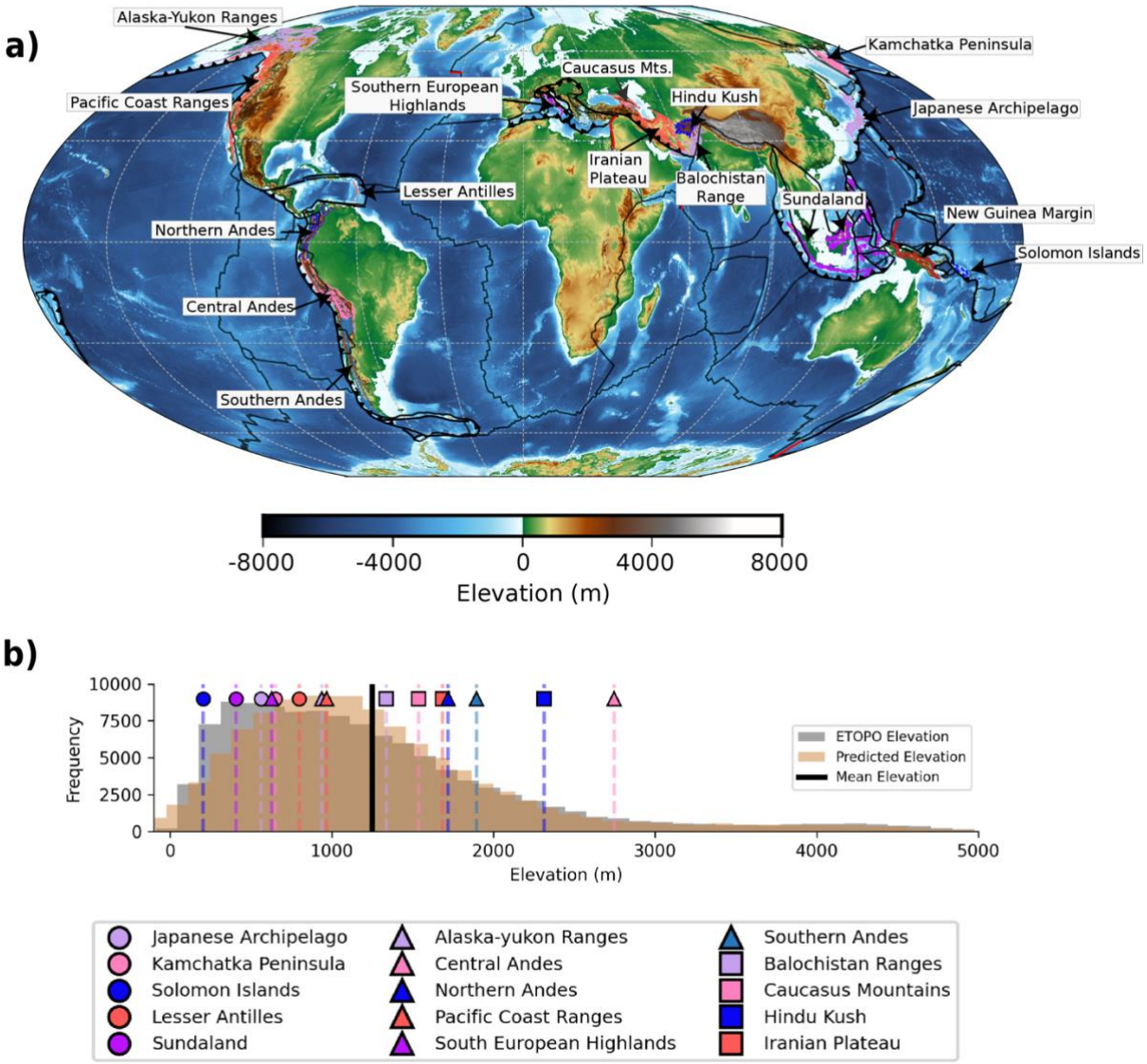

Figure 1: Global Distribution of Active Margin

a) Global active margin topography from ETOPO (Amante and Eakins, 2009). The colored polygons indicate the mountainous regions from the Global Mountain Biodiversity Assessment (GMBA) database (Snethlage et al., 2022) sampled to train our EBM model. The solid black lines represent plate boundaries. The solid black line with teeth represents the subduction zones. Colored outlines indicate the locations of individual mountain chains.**b)** Frequency distribution of elevations for the mountain chains, based on 113,359 sample points from ETOPO at 0.1° resolution. Vertical lines and symbols indicate the mean elevation of each mountain chain, according to tectonic setting: island arcs (circles), non-collisional mountains (triangles), and convergent continental margins (squares). The solid black line marks the mean elevation of all global mountains included in this study from ETOPO (Amante and Eakins, 2009).

The interpretable tree-based approach of the EBM allows us to disentangle and quantify the contributions of multiple parameters, such as plate kinematics, mantle dynamics, and paleoclimate, to the present-day active margin topography (Supplementary Table 1 and Fig. 2a). The EBM model can effectively capture nonlinear relationships and manage collinearity among variables (Konstantinov and Utkin, 2021), which are key challenges when modelling interconnected processes in geodynamics and Earth systems. Additionally, the shape functions of the EBM enable us to understand the topographic response caused by variations in a specific parameter on the topography without relying on numerous regional analog or numerical models. Furthermore, our approach allows us to examine diverse mountain ranges from different regions of the world within a single framework, a capability that has not been previously possible. By utilizing the EBM, our research aims to objectively disentangle the complex interplay between different components of plate tectonics, mantle convection, and long-term climate on diverse mountain topographies in a data-driven manner. This study provides key insights into the forces that govern active margin topography.

2. Methods

We use spatiotemporal data mining to explore and integrate our input parameters from: a plate tectonic reconstruction (see Section 2.1); a mantle convection model (see Section 2.2); and a paleo-precipitation simulation (see Section 2.3). We additionally use present-day elevation (ETOPO; Amante and Eakins, 2009) as our target parameter (see Section 2.4). For our analysis, we convert all input parameters (i.e. tectonic variables, mantle convection outputs, and paleo-precipitation) into arrays of 0.1° x 0.1° points. These points are sampled within regions defined as 'active mountains'. We classify a mountain as active if it is located within the global mountain polygons from the Global Mountain Biodiversity Assessment (GMBA; Snethlage et al., 2022) and situated on the overriding plate of a convergent margin with a resolved slab in the SLAB2 model (Hayes et al., 2018). We similarly discretize trenches (based on their geometries defined within the plate model) into 0.1° points so that we can capture the spatial variability of the plate kinematics along the entire trench length. We perform our analysis within a Python-based workflow (see the Open Research Section). These processed inputs serve as features for building the EBM model (see Section 2.5), which allows us to quantify the contributions of tectonic, mantle, and climatic processes

2.1 Plate Tectonic Reconstruction

We extract several plate kinematic parameters along convergent plate boundaries (i.e. the discretize trenches) for the past 100 Ma in 1 Myr increments based on a global plate tectonic reconstruction model (Zahirovic et al., 2022) in their no-net-rotation (NNR) reference frame. The NNR frame is chosen because it assumes zero net rotation for the lithosphere with respect to the mantle, making it ideal for isolating and analyzing lithospheric processes and plate kinematics (Torsvik et al., 2010). Specifically, we extract: (i) the convergence rate (its magnitude and both trench-orthogonal and trench-parallel components), (ii) subducting plate velocity (its magnitude and both trench-orthogonal and trench-parallel components), (iii) obliquity angle, and (iv) trench migration rate. In addition, we compute the subduction flux rate (Q), which was determined by multiplying the plate thickness (h), subducting arc length,

and convergence rate (v_c). We estimated the thickness of the subducting oceanic plate (h) using the Parsons and Sclater (1977) cooling model, which relates lithospheric thickness to seafloor age, where seafloor ages were additionally determined using the Zahirovic et al. (2022) plate reconstruction. For each point within the 0.1° × 0.1° array of active mountains at every time step, we calculated the minimum distance to the nearest discretized trench and assigned the corresponding plate kinematic parameters. Because present-day elevation reflects the cumulative response to geological processes operating over multi-million-year timescales, we used a data-driven method to optimize the choice of temporal window for incorporating plate kinematic features. The mean plate kinematic parameters were computed using an n-Myr temporal window as follows:

$$\bar{Q} = \frac{\sum_{t=0}^{n} Q^t}{n}$$

We tested temporal windows of 10, 15, 20, 25, 30, 35, 40, 45, 50, 60, 70, 80, 90, and 100 Myr to explore their sensitivity in the calculation of our kinematic parameters. As our plate reconstruction relies on a hierarchy of finite rotations derived largely in ~10 Myr intervals and we are interested in the longer-term trend, we did not explore window lengths <10 Myr. Based on this assessment (see Section 3 and Fig. S1), we adopted a 15 Myr window for our main analysis.

2.2 Mantle Convection Modelling

Global-scale mantle convection simulations for the past 410 Ma were performed using the Zahirovic et al. (2022) plate tectonic reconstruction and CitcomS, a finite element-based numerical mantle convection model that simultaneously solves for mass, momentum, and energy conditions by assuming pseudo-compressible flow (McNamara and Zhong, 2004; Moresi et al., 2014; Tan et al., 2006; Zhong et al., 2000). We further imposed constraints on the thermal structure of the lithosphere and thermal structure of slabs in the upper mantle, as used in a previous study (Bower et al., 2015). Downwellings at active margins are therefore influenced by the combination of convergence rates as well as the negative buoyancy of subducting slabs. This integration enables us to capture the overall impact of global mantle circulation on the evolution of the plate-mantle system. The reconstruction points within the mountain polygon were used to sample the present-day mean upper mantle temperature and mean vertical mantle flow velocity at depths ranging from 200 to 440 km. These depths span from the base of the lithosphere to the uppermost lower mantle and capture both recent and deep time subduction impacts on mantle dynamics. We did not use the top 200 km because it includes the enforced boundary condition in the uppermost mantle (Bower et al., 2015).

2.3 Paleoclimate Simulation

In our study, we use the paleo-precipitation output from the fully coupled paleoclimate simulations of Li et al. (2022), performed using the Community Earth System Model version 1.2.2 (CESM1.2.2), which covers the past 540 Ma. The climate simulations used paleogeographic reconstructions from the Scotese and Wright (2018) paleo-digital elevation model. Instead of specifying atmospheric CO_2 concentrations, the simulations were constrained to reproduce the reconstructed global mean surface temperatures (Li et al., 2022; Scotese, 2016), ensuring that the modelled climate remained consistent with paleoclimate estimates. A limitation of these paleoclimate simulations is that they are available only on a relatively coarse grid (0.9° × 1.25° in latitude and longitude), which may underestimate fine-scale spatial variability. To ensure consistency with the plate kinematic point array, we upsampled the precipitation fields to the same spatial grid. The annual precipitation was

calculated for each 1 Myr time step, then averaged over different temporal windows (Fig. S1), and the optimal window size was selected for our main analysis (see Section 3).

2.4 Elevation Dataset

We use present-day elevation from ETOPO (Amante and Eakins, 2009) within active mountain belts as our target data for the supervised EBM modelling. Prior to resampling ETOPO to our 0.1° x 0.1° point-array, we first applied a Gaussian filter with σ = 2 grid cells (~2 arc-min) to smooth short-wavelength variations, which ensures that only topographic variations at the scale relevant to the feature set are retained.

2.5 Explainable Boosting Machine

The EBM is a tree-based cyclic gradient boosting generalized additive model (GAM) with automatic interaction detection (Lou et al., 2013). Its structure incorporates a GAM with interactions in the following form:

$$g(E[y]) = \beta_0 + \sum \Delta_j(x_j) + \sum \Delta_{j+k}(x_j, x_k)$$

where g is the link function, y is the target parameter to be fitted (i.e. ETOPO elevation; Amante and Eakins, 2009), $E[.]$ is the expectation operation, β_0 is the bias,$\Delta_j(x_j)$is the shape function which shows the pattern of how different plate kinematics, mantle convection and paleo-precipitation parameters (x_j) are related to predicted elevation, and $\Delta_{j+k}(x_j, x_k)$ captures the interaction effects between pairs of parameters. Not all pairs need interactions, but the EBM automatically detects and includes significant interactions. The EBM compares the inputs to the target by minimizing the squared error (L2 loss) between the predicted and observed elevations (i.e. ETOPO elevation; Amante and Eakins, 2009). The EBM harnesses the power of modern machine learning techniques, such as bagging and gradient boosting. It utilizes shallow decision trees in a constrained additive framework, meaning each feature contributes through simple, visualizable functions. These shallow splits, along with optional monotonicity constraints, make the model's behavior easier to interpret compared to deeper boosted tree models (Caruana et al., 2015). The boosting machine strategy is applied in a round-robin fashion through different parameters to reduce the collinearity effect. Predictions in the EBM are the sum of the contributions from each tree in the ensemble, facilitating a clear understanding of how each parameter and interaction contributes to elevation. Furthermore, EBM employs automatic interaction detection to identify important interactions between parameters, thereby enhancing the overall interpretability.

For the training and evaluation of the EBM model, we randomly withheld 30% of the reconstruction points as a test subset and used the remaining 70% for training. This partitioning was not intended to assess predictive generalization across space, since neighboring points at 0.1° resolution may share correlated tectonic, mantle, and climate parameters. Instead, the purpose of the split was to provide a conventional error metric (RMSE) while focusing on how the model captures the relationships between these parameters and elevation. We note that this point-wise split may slightly inflate the test performance because of spatial autocorrelation, and a more robust spatial cross-validation strategy (e.g., training on a subset of orogens and validating on others) would be a useful avenue for future work.

3. Plate Kinematics and Active Margin Topography

Our model suggests that feature temporal window sizes between 10 and 30 Myr produce similar RMSE values when compared with the sampled ETOPO data (Amante and Eakins, 2009; Fig. S1). However, the RMSE increased with increasing window size. A window size of 10–30 Myr yielded a low RMSE, indicating less overfitting. We selected a 15 Myr window size for the preferred EBM model (Fig. S1). However, using other values within this range does not considerably influence the analysis, resulting in only a minimal misfit difference of ~5–10 m (Fig. S1). We initially tested a wide range of plate kinematic parameters (Fig. S2), but including all parameters produced complex shape functions that were difficult to interpret (Fig. S3). To maintain interpretability, we retained only the parameters that were mostly independent and least linearly correlated, as determined from correlation statistics (Figs. S2–S3). For example, the distance from the nearest trench edge strongly correlates with elevation owing to oroclinal bending and mantle flow (Schellart, 2017), effects already captured in our trench migration rate calculation. Retaining only the most informative parameters ensured that the model remained interpretable without compromising its essential dynamics.

Our EBM establishes a robust relationship between mountain elevation and plate kinematics, highlighting the importance of key tectonic parameters (Fig. 2c). The final EBM model achieved an RMSE of 444 m on the 30% unseen test dataset and 402 m on the 70% training dataset, compared to ETOPO. The coefficient of determination (R^2) was 0.77, indicating a moderately strong correlation between the predicted and ETOPO elevation values (Fig. 2b). These metrics indicate that our model explains 77% of the variance in the observed elevation with a relatively small error, underscoring its reliability in capturing first-order controls on topography at active margins.

Our model also provides a metric called the mean absolute score (Fig. 2c), which quantifies the average contribution of each input parameter to the elevation relative to the mean elevation of all mountains in the dataset (1250 m). For example, a mean absolute score of 363 m for subduction flux indicates that variations in subduction flux account for, on average, ~363 m of elevation across the dataset relative to the overall mean. According to the mean absolute score of our model, subduction flux and trench migration rate emerged as the most critical factors driving elevation variability, whereas the upper mantle temperature and vertical mantle flow velocity formed subordinate but important factors governing elevation. Subduction flux, which is derived from the plate tectonic reconstruction model and quantifies the volume rate of lithospheric material being subducted (see Section 2.1), has the largest influence on elevation predictions, with a mean absolute score of 363 m (Fig. 2c). Similarly, the trench migration rate, which measures the advancement or retreat of trenches over time, had a significant impact, with a mean absolute score of 237 m (Fig. 2c).

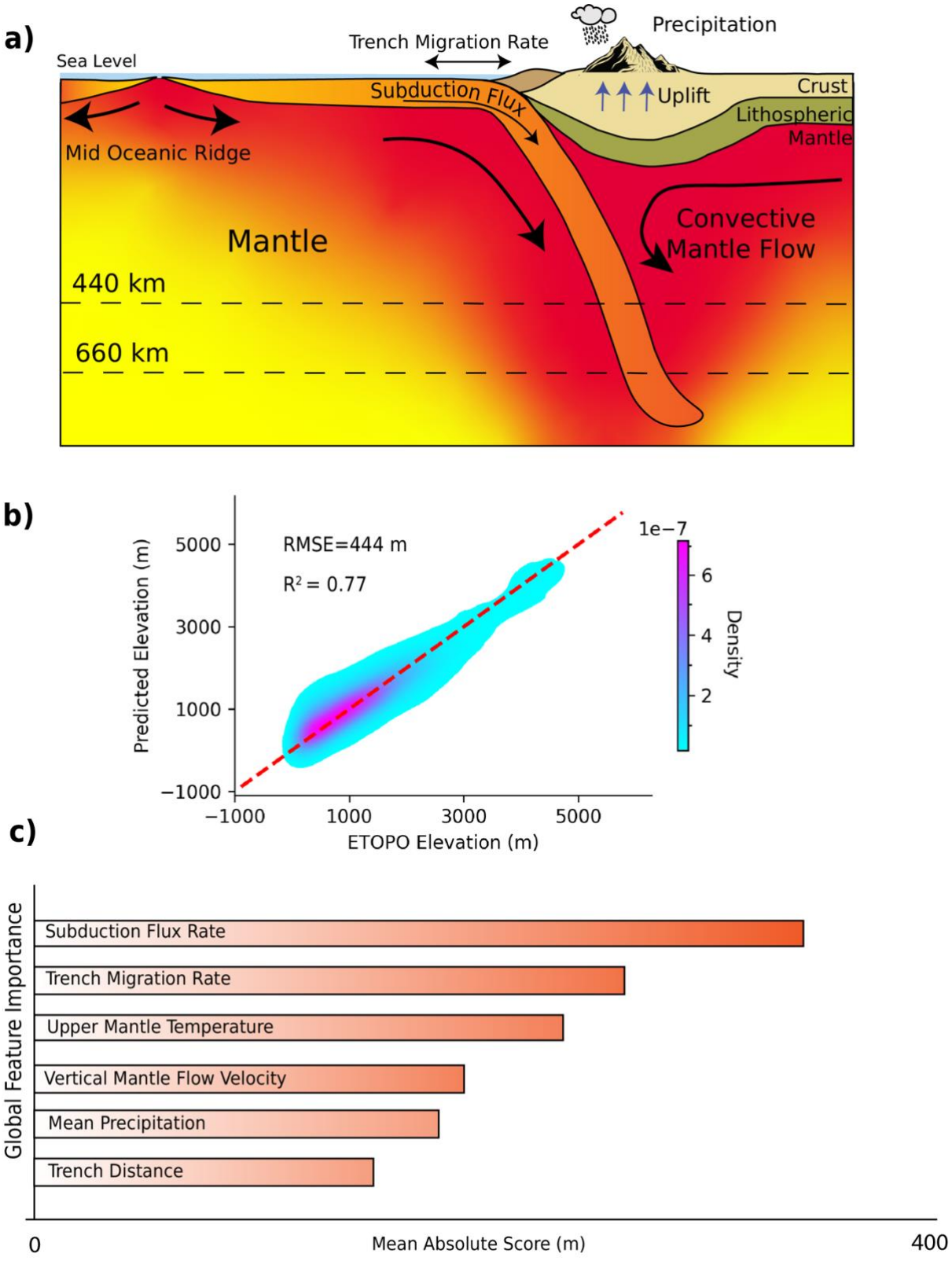

Figure 2: EBM Model Performance

a) Schematic representation of subduction-related mountains illustrating the principal factors influencing mountain topography along active margins.

b) Cross-plot comparing ETOPO (Amante and Eakins, 2009) elevation with those predicted by the EBM model, illustrating the model's performance.

c) Feature importance ranking, showcasing the top six features of our EBM model for all mountains included in this study. Higher values indicate a greater influence on the elevation prediction.

The shape function for the subduction flux illustrates how the predicted elevation responds to changes in the subduction flux, when all other parameters are held constant (Fig. 3a). The y-axis represents the additive contribution to elevation relative to the global mean elevation (1250 m), meaning positive values indicate an increase above the mean and negative values indicate a decrease. The shape function exhibited a sharp positive trend for higher subduction flux values, suggesting that subduction flux strongly enhances the topography at active margins. Unlike the mean absolute score, which summarizes the average contribution of each parameter across all mountains, the shape function captures the parameter-specific response, revealing non-linearities and interactions in the model. Very high lithospheric subduction flux rates (>0.08 km^3/yr), resulting from strong convergence rates (>8 cm/yr) and thick subducting oceanic lithosphere (>80 km), are associated with elevated topography, with predicted elevations exceeding 3000 m. For instance, in the Central Andes (e.g., Altiplano-Puna), the contribution score ranged between 1000 and 2500 m, reflecting the strong influence of high subduction flux on high elevations (Fig. 3c). This pattern aligns with a previous study showing that a thicker and older subducting lithosphere (45–50 Myrs old) is associated with a higher topography on the overriding plate (Capitanio et al., 2011). Here, the subduction flux can be interpreted as a proxy for tectonic forcing on the overriding plate. Elevation contribution decreases to the north and south of the Central Andes, which is associated with a reduction in the subduction flux driven by a decrease in the age of the subducting oceanic plate (Fig. 3c). Similarly, the shape function of the trench migration rate showed a positive correlation with the contribution score (Fig. 4c), consistent with other slab-driven trench migration models (Schellart and Moresi, 2013; Xue et al., 2022). A strong trench retreat (> 2 cm/yr), observed in regions such as the Japanese Archipelago, Calabria Mountains in Southern Europe, and the Eastern and Sredinny Ranges in the Kamchatka Peninsula, was associated with high negative contribution scores ranging from -1000 to 0 m (Fig. 4c and d). This occurs because retreating trenches linked to slab rollback lead to overriding plate extension (Schellart, 2008; Schellart and Moresi, 2013; Xue et al., 2022), significantly lowering elevation (Fig. 4d). Active margins with slow retreating or stationary trenches (0 to 2 cm/yr), such as the Northern and Southern Andes of South America or the Pacific Coast Ranges of North America, exhibit low contribution scores ranging from -500 to 500 m from trench migration (Fig. 4a and d). However, moderate to high flux (0.03–0.06 km^3/yr) from the subduction of the oceanic lithosphere may positively contribute to increasing the overall elevation of these mountains (Fig. 3a). Along the trench, variations in the contribution score at moderate to high subduction flux indicate an increase in elevation with trench distance, particularly in extensional regions farther from the trench (Fig. 3d).

Regions with low subduction flux (<0.03 km^3/yr), such as the Eastern and Central Iranian Ranges, the Balochistan Range in western Asia, and the Hellenides and Dinaric Alps in Eastern Europe, show negative contributions ranging from -1000 to 0 m owing to low convergence rates associated with the convergence of continental plates and the subduction of only small amount old, dense oceanic lithosphere (Fig. 3b). However, significant trench advance linked to slab rollover contributed positively, with scores ranging from 300 to 700 m (Fig. 4c). A strong trench advance compresses the overriding plate, creating a long-wavelength uplift and broader elevated topography (Fig. 4e).

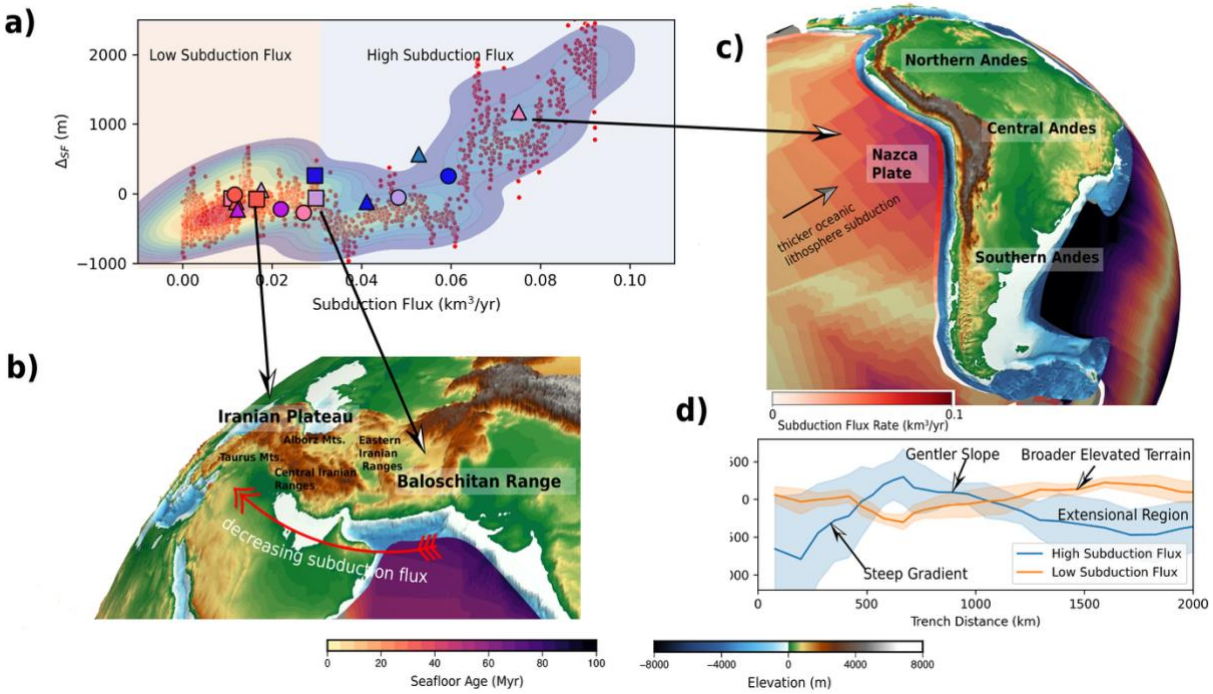

Figure 3: Role of Subduction Flux on Active Margin Topography

a) Shape function illustrating the contribution score of subduction flux to the predicted elevation. As the subduction flux increases, its contribution to topographic elevation also increases. The colormap indicates point density, with warmer colours corresponding to higher density (i.e., more data points).

b) Mountains in western Asia exhibit a lower subduction flux due to the slower convergence of the continental block and a limited supply of dense oceanic lithosphere for subduction. Consequently, these mountains displayed negative contribution scores for the subduction flux.

c) Illustration highlighting the influence of the subduction flux on Andean elevation. The thickness of the subducting lithosphere is proportional to seafloor age. In the Andes, subduction flux peaks in the central region, where the thicker Nazca Plate is being subducted, significantly contributing over 1000 m to the Central Andean elevation. Conversely, as the plate thickness decreases toward the Southern and Northern Andes, the contribution of subduction flux on elevation also diminishes.

d) Interaction plot displaying contribution scores when trench distance and subduction flux are varied while keeping other parameters constant. High subduction fluxes (>0.03 km³/yr) are associated with narrower but higher elevations, characterized by steeper slopes on the oceanward side and gentler slopes on the continental side. In contrast, a low subduction flux results in broader topographic profiles.

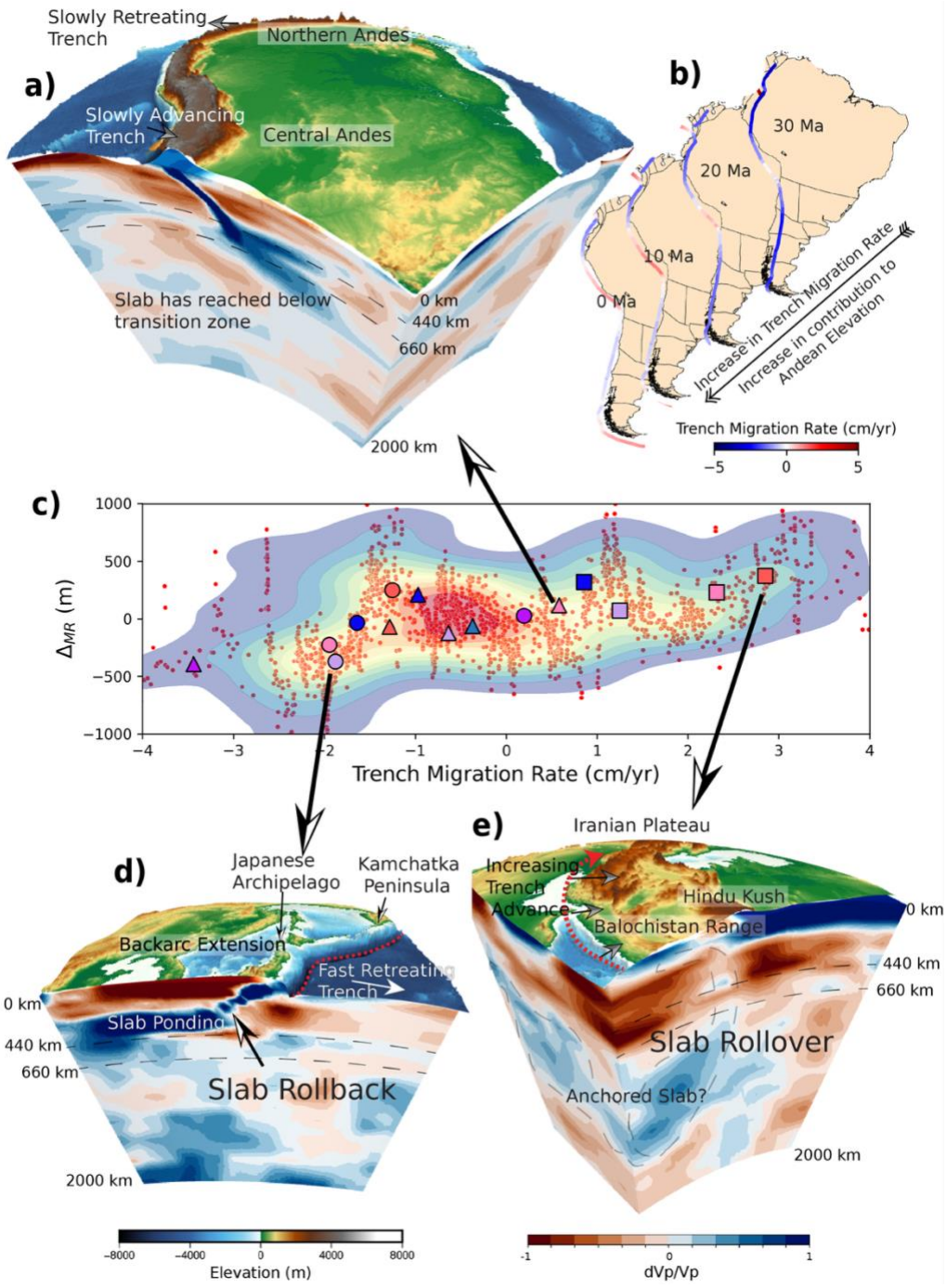

Figure 4: Role of Trench Migration Rate on Mountain Topography

a) Seismic tomography model (TX2019slab; Lu et al., 2019) illustrating the subducted slab, which has penetrated well below the transition zone in the Central Andes. **b)** Temporal evolution of the mean trench migration rates in the Andes. The trench advance rate in the Central Andes has increased over time, suggesting potential slab anchoring. In contrast, the retreat observed in the Southern and Northern Andes may have been induced by the upper mantle return flow.

c) Shape function demonstrating the contribution of the trench migration rate to the topography. Island arcs experience significant trench retreat, whereas converging continents show a notably high contribution from advancing trenches. The colour scale indicates the

density of data points in the shape function, with warmer colours representing higher density. Symbols are as defined in Fig. 1.

d) Seismic tomography model (TX2019slab; Lu et al., 2019) depicting slab ponding beneath the Japanese Archipelago. This phenomenon leads to slab rollback and trench retreat, resulting in lower elevations and evidence of back-arc extension in this region.

e) Seismic tomography model (TX2019slab; Lu et al., 2019) illustrating trench advance and rollover in the West Asian mountains. The model also revealed a portion of what may be an anchored slab responsible for the trench rollover. Although these mountains exhibit negative contribution scores from the subduction flux, they show a significantly high contribution from advancing trenches, resulting in broader elevated regions.

4. The Effect of Mantle Dynamics on Active Margin Topography

Surface topography is significantly influenced by mantle dynamics, particularly by the underlying viscous stresses, often referred to as dynamic topography (Braun, 2010; Flament et al., 2013). However, estimating present-day dynamic topography remains challenging because of the difficulty in isolating the lithospheric contribution from that of the mantle, and model-derived values are inherently approximate. To better understand the effects of mantle dynamics, we utilized a global mantle convection model (see Section 2.2) to simulate the vertical mantle flow velocity and temperature, rather than using model-predicted dynamic topography. Although this approach circumvents some of the uncertainties in dynamic topography estimation, it is important to emphasize that the mantle temperature and vertical velocity fields are subject to the assumptions and parameterizations of the underlying mantle convection model (Bower et al., 2015). Our EBM model enables us to individually assess the effects of mantle temperature and vertical flow velocity via shape functions (Fig. 5a and b), while efficiently handling collinearity.

In the mantle convection model, temperature and velocity are influenced by several factors. For example, plate velocities and trench motion affect the heat distribution and rate of upper mantle flow through different convection patterns (Faccenna et al., 2021). Mantle plumes introduce heat and drive localized upwellings (Koppers et al., 2021), whereas proximity to geological features, such as cratons, creates stable, cooler regions (Bower et al., 2015). Additionally, subduction zones influence the mantle through descending cold slabs (Bower et al., 2015; Chen et al., 2022).

The upper mantle (200–440 km) temperature and vertical component of flow contributed to the elevation predictions with mean absolute scores of 200 m and 169 m, respectively (Fig. 2c). The negative correlation between the upper mantle temperature and contribution scores suggests that a colder upper mantle has the strength to support a thicker lithosphere and, consequently, higher elevations (Fig. 5a). For instance, if we keep all the other parameters fixed, in the South American Cordillera, where the upper mantle temperature is low (~1100°C), the contribution score is up to 600 m, whereas in the Northern American Cordillera, where the temperature is higher (~1200°C), the contribution score is <300 m (Fig. 5c and d). Conversely, stronger downwelling in subduction zones, such as the Solomon Islands, exerts a pulling force that reduces the elevation (Fig. 5b). Mountains, such as the Pacific Coast Ranges of North America and Southern European Highlands, which have retreating trenches, exhibited very low sinking velocities, with contribution scores ranging

from -100 to 100 m (Fig. 5b). Regions with strong mantle upwellings tend to elevate the surface, yielding positive contribution scores of up to 500 m. For example, in North America, the Rocky Mountains and Sierra Madre Ranges (Figs.5e and f) show a significant influence from upper mantle upwellings, with thermochronology and river incision data suggesting dynamic support of up to 1 km (Karlstrom et al., 2012; Nieto-Samaniego et al., 2006).

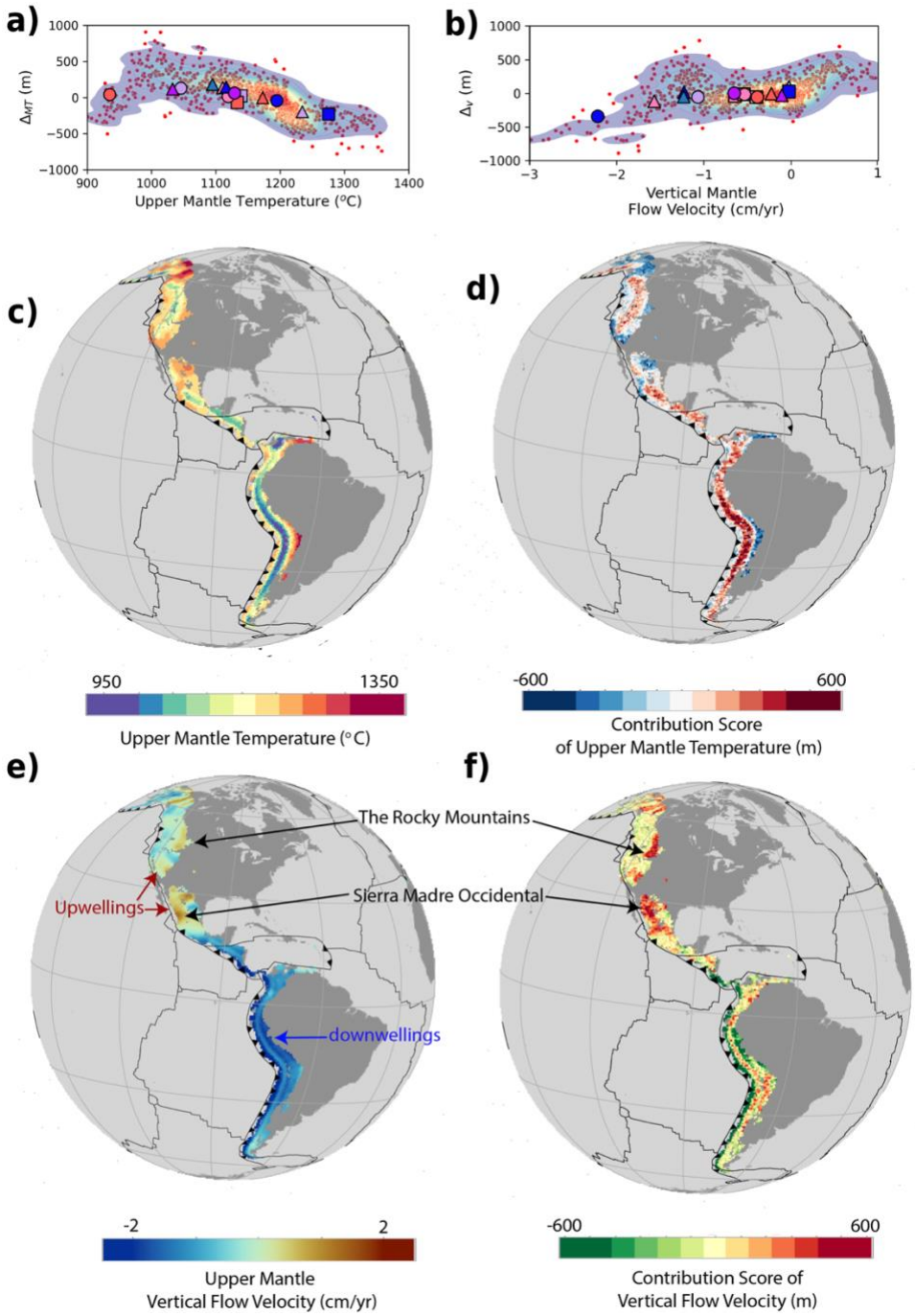

Figure 5: Mantle Dynamics and Topography

a) Shape function illustrating the inverse correlation between the upper mantle temperature and its contribution to topography, indicating that colder mantle temperatures are associated with higher topographic contributions. Warmer colors represent a higher density of data points. Symbols are as defined in Figure 1.

b) Shape function depicting the vertical flow velocity in the upper mantle, showing a positive correlation with the contribution score, suggesting that an increased flow velocity contributes to elevated topography. Warmer colors represent a higher density of data points. Symbols are as defined in Figure 1.

c) Upper mantle temperature from CitcomS output and **d)** its spatial distribution of contribution. The colder upper mantle in the Southern American Cordillera corresponds to a higher contribution to the topography.

e) Upper mantle flow velocity from CitcomS output and **f)** its contribution to elevation. Notably, the Rockies and Sierra Madre Occidental exhibited a very high contribution from upper mantle upwellings, highlighting the significant role of mantle dynamics in shaping mountain topography.

5. The Role of Long-Term Climate on Active Margin Topography

Mountainous regions are anticipated to exhibit several simultaneous responses to climate-driven increases in erosion rates, including a reduction in range width, temporary surge in sediment yield, sustained acceleration in rock uplift rates, and a decrease in the subsidence rate of surrounding basins (Leonard et al., 2023; Whipple, 2009; Whipple and Meade, 2006). These responses collectively influence topographic complexity. Examining the long-term relationship between precipitation and elevation revealed a nuanced dynamic: the contribution score tended to increase with precipitation, which is generally associated with increased erosion (Ferrier et al., 2013), causing isostatic rebound and uplift (Fig. 6a and b). However, the relationship between surface uplift and topography requires further analysis. Since we did not observe a significant correlation, this could indicate a weak or negligible link between long-term precipitation and elevation, or uncertainties in the paleoelevation inputs used to derive paleoprecipitation in the paleoclimate simulations. Recent studies employing critical taper theory and coupled geodynamic–surface process models (Wolf et al., 2022; Yuan, 2024) have demonstrated that the extent to which climate modulates mountain size, particularly height and width, depends strongly on the convergence velocity and rheology of the orogen. These factors govern the mechanical behavior of mountain belts and their sensitivity to erosional processes. While our analysis, using XAI and paleo-precipitation simulations, provides insight into long-term climate influence, it is subject to few important limitations. First, our model does not account for complex geodynamic processes, such as orogenic collapse, that contribute to critical taper equilibrium independently of climate-driven erosion. Second, a methodological inconsistency exists, as the paleoclimate models rely on the Scotese and Wright (2018) model, which has different convergence velocities from the plate reconstruction used in our analysis. Since the interplay between climate and mountain building is highly sensitive to convergence velocity, exploring these coupled effects within a consistent kinematic framework remains a crucial direction for future work. The observed weak correlation between precipitation and elevation may reflect these limitations, but may also be inherent to the complex and potentially bidirectional relationship between these variables, in which elevation and precipitation influence each other through various feedback mechanisms. Nevertheless, our results show that in regions of high precipitation,

such as the Coast Ranges in North America, closer to trenches, there is a negative contribution score (0 to -300 m), which may represent elevation loss due to sediment erosion, while adjacent areas have a positive score of 200–300 m, which may represent an elevation gain due to isostatic rebound (Fig. 6c and d). As precipitation continues to rise, increased erosion may degrade the overall topography, as observed in the high-precipitation region of Southeast Asia (Fig. 6c and d). Moreover, distinct interactions between tectonics and climate are discernible on both the oceanward and continental sides of mountains (Fig. 3d). The oceanward side, which is subjected to moisture-laden winds and high precipitation, experiences stronger erosional forces, resulting in steeper topography (Fig. 3d). In contrast, the continental side, which is characterized by gentler slopes, experiences less erosion. Active margins in different subduction settings tend to have varying pro- and retro-wedge basin depths and deposition patterns (Royden, 1993). For example, high subduction flux (> 0.03 km^3/yr) mountains have quite deep pro-wedge basins, whereas basins in low subduction flux areas are shallower (Fig. 3d).

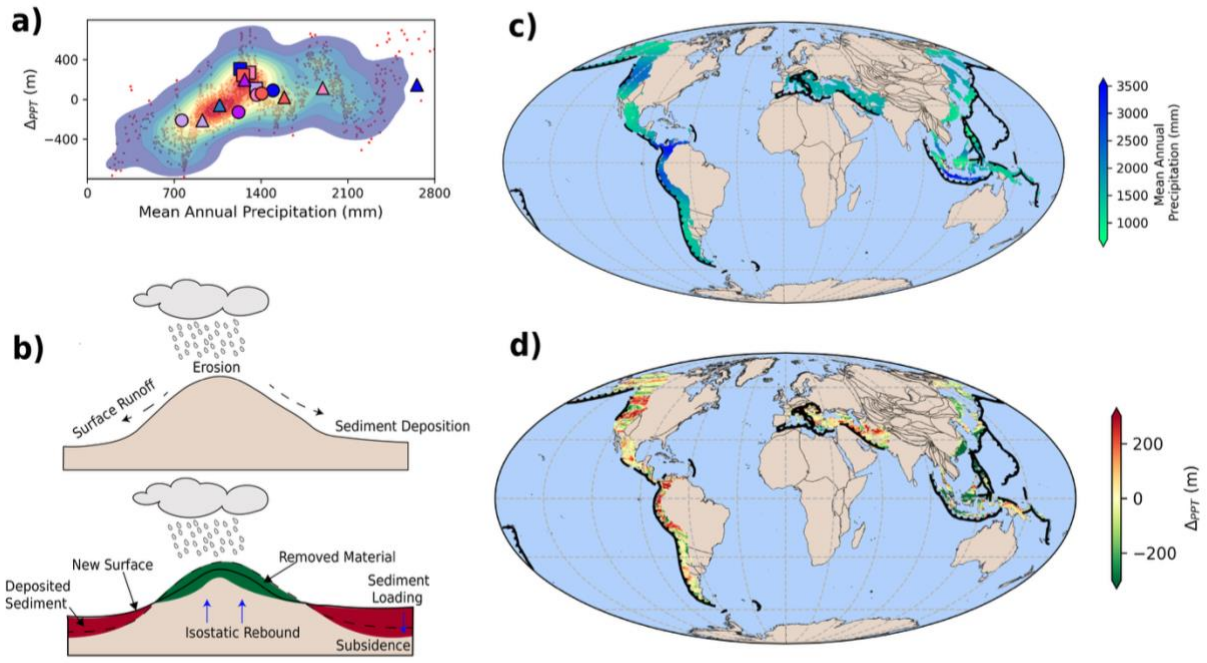

Figure 6: Influence of Long-Term Climate on Topography

a) Shape function representing global mean annual precipitation for the last 15 Myrs (Li et al., 2022), and its influence on topographic variation.

b) Illustration depicting the response of long-term climate to topography. Although erosion generally degrades topography, it can also trigger isostatic rebound, resulting in rock uplift. Conversely, significant sedimentation can increase elevation but may lead to subsidence because of sediment loading.

c) Mean annual precipitation over the past 15 Myrs (Li et al., 2022).**d)** Analysis of the response of mean paleoprecipitation to mountain topography. In regions of high precipitation, such as the Pacific Coast Ranges, areas of reduced contribution (indicated in red) near the trench which may signify erosion, whereas areas farther from the trench display higher contributions (indicated in green) associated with sediment deposition.

6. Topographic Variations in Different Subduction Settings

The classification of orogeny at active margins has traditionally been divided into collision and subduction, based on the continental or oceanic nature of the downgoing plate (Cawood et al., 2009; Dewey and Bird, 1970). However, this approach provides limited insight into geodynamic processes and associated topographic variations. Recent classification models have introduced two end-member types: (i) slab-pull orogeny, linked to subduction restricted to the upper mantle, and (ii) slab-suction orogeny, associated with large-scale mantle convection cells (Faccenna et al., 2021; Royden, 1993). While these distinctions offer a better understanding of mantle dynamics at active margins, they do not adequately explain the related topography. Our classification, based on the EBM model, introduces a new perspective on subduction-related orogeny and the associated topographies. By simply plotting the top two parameters of the EBM model, that is, the subduction flux and trench migration rate, on orthogonal axes, our analysis revealed that the topography of global active margins is naturally organized within a triangular region, with these two features explaining 48% of the vairance in the model (Fig. 7). Our diagram delineates distinct clusters corresponding to different types of topographic end-members and highlights the continuous spectrum of the dynamic processes governing these variations (Fig. 7). Our insights bridge the gap between plate tectonics, geodynamic drivers, and surface expressions, offering a comprehensive framework for interpreting subduction-driven orogenic systems.

6.1 Topographic Variation in Orogens with Retreating Trenches and Moderate Subduction Flux

In the early stages of subduction, the slab descending into the denser lower mantle may begin to accumulate in the transition zone. This accumulation can lead to slab rollback and trench retreat (Fig. 4d and 7b). Mountains formed in areas of significant trench retreat, such as the Kamchatka Peninsula, Calabria, and the Japanese Archipelago, typically develop under conditions of low-to-moderate subduction flux and exhibit minimal downgoing mantle flow, with small-scale mantle convection confined to the upper mantle (Faccenna et al., 2021). Owing to the highly mobile trench that generally migrates backward, large-scale protracted shortening is prevented (Royden, 1993). This process leads to the formation of moderately thick crustal stacks and extension of the overriding plate (Royden, 1993). Trench retreat can lower the elevation of these mountains to between 200 and 800 m. While the presence of subducting material can provide a positive contribution that may increase the elevation by 500 to 1000 m, particularly in areas close to the trench, back-arc extension is more pronounced farther from the trench (Fig. 3d). Consequently, the resulting mountains in these settings generally have elevations of less than 1 km (Fig. 3a and 4c), and their crustal thicknesses typically do not exceed 50 km (Faccenna et al., 2021).

6.2 Topography of High Subduction Flux-Driven Mountains

Mountains characterized by high subduction fluxes (>0.06 km^3/yr), such as the Central Andes, generate significant slab suction forces due to rapidly descending slabs, which can trigger large-scale mantle convection (Faccenna et al., 2021) (Fig. 7a). As the slab penetrates the more viscous lower mantle, it produces an anchoring effect that limits lateral migration (Faccenna et al., 2017; Garfunkel et al., 1986; Zhong and Gurnis, 1995). This restricted

migration, combined with a very high subduction flux, increases the compressional stress in the overriding plate, resulting in an elevation rise of 3–4 km (Fig. 3a,c and 7a). These mountains are distinguished by very thick crust (~60-70 km) and prominent high plateaus, such as the Altiplano-Puna (Beck et al., 1996). In the back-arc region, compression may arise because deeper slabs are more commonly anchored. Additionally, when slabs penetrate after ponding at the 660 km discontinuity, they can trigger large-scale symmetrically converging convection cells that draw surface plates toward the downwelling zone (Faccenna et al., 2021; Yang et al., 2016). The rapid descent of thick, fast-sinking slabs absorbs less heat from the surrounding mantle, resulting in a colder upper mantle (Fig. 5a). This colder mantle further supports the overall topography, contributing an additional ~500–600 m to the mountain elevation. Consequently, these mountains can achieve elevations greater than 4 km, despite existing in a non-collisional setting, owing to the abundant supply of rapidly converging subducting oceanic lithosphere.

6.3 Topographic Variation in Advancing Orogens

The presence of a continental block on the subducting plate can ultimately lead to collisional orogenesis, as observed in the India-Eurasia collision (van Hinsbergen, 2022; Yin and Harrison, 2000). Before the collision, the convergence rates and volume of the subducting material decrease owing to the presence of a less dense continental block, which may resist subduction (Fig. 7c). Moreover, if an old and thick subducting oceanic lithosphere is present, it exhibits high resistance to deformation and bending; consequently, such slabs can result in trench advance (Di Giuseppe et al., 2009). Much of the shortening and uplift in these mountains can be attributed to the advancing trench. A high trench advance rate combined with slab rollover can create long-wavelength topography, such as that observed in the Makran subduction zone in West Asia (Xue et al., 2022), leading to elevations >1.5 km (Fig 4c and e). These mountains typically feature wide and elevated terrain. In such mountains, slab pull forces are likely minimal because of episodes of slab break-off (Garzanti et al., 2018). Processes such as mantle upwellings driven by the advancing trench (Strak et al., 2024) and delamination of the thickened lithosphere (Göğüş and Ueda, 2018) may also significantly influence elevation. However, quantifying these effects in our global-scale geodynamic model is challenging, thus, we did not include collisional mountains in our analysis.

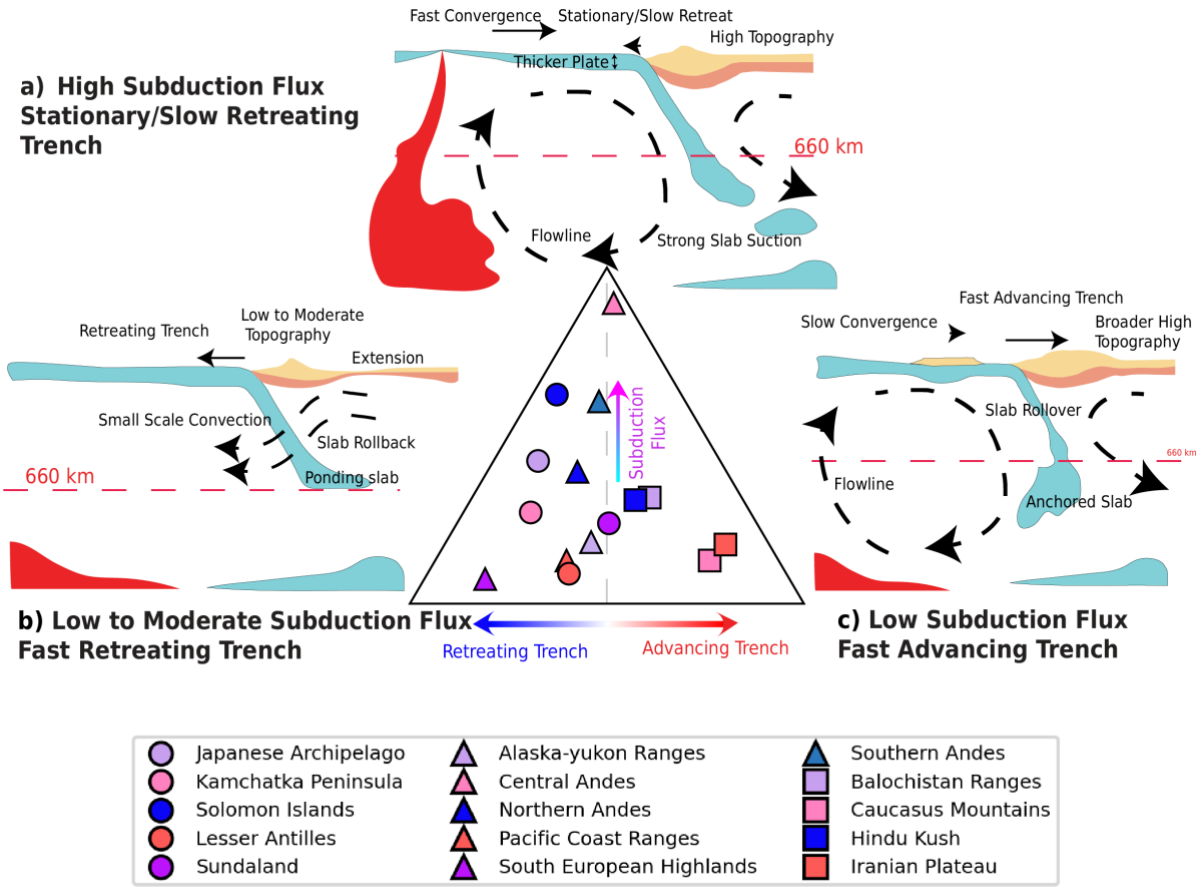

Figure 7: EBM Classification of End-Member Scenarios

Central diagram: Triangular classification diagram categorizing mountain ranges based on subduction flux and trench dynamics. The mountain-building process initiates as the downgoing slab penetrates the 660 km transition zone (Faccenna et al., 2021), with early-stage island arcs (represented by circles).**a)** High subduction flux scenario: Strong slab suction and whole-mantle convection drive significant crustal thickening, as observed in the Central Andes. **b)** Low to moderate subduction flux scenario: Fast trench retreat results in confined upper mantle flow and limited crustal thickening, as illustrated by the Japanese Arcs. **c)** Low subduction flux and trench advance scenario: episodic slab breakoff and collisional orogeny occur, which is typical of regions with a continental crust on the subducting plate. Mountains can transition between scenarios over time as they evolve. For instance, a ponding slab in the transition zone may penetrate deeper if a thick oceanic lithosphere becomes available for subduction, shifting from a fast trench retreat (scenario b) to a high subduction flux (scenario a). Conversely, reduced convergence, especially with the continental crust on the subducting plate, may lead to a transition from a high subduction flux (a) to trench advance (c), accommodating compression through trench migration and resulting in collisional orogens. This dynamic interplay between slab dynamics and subduction flux shapes the topography and tectonic evolution, producing a high, thick crust in high subduction flux settings and more moderate elevations in lower flux scenarios.

7. Model Limitations

Although our model provides valuable insights into present-day mountain topography along active margins, several limitations must be acknowledged. First, the shape function illustrates correlations between individual parameters and topography rather than causation. These parameters are interdependent to some extent (Fig. S2); for instance, high subduction flux often accompanies the subduction of thicker, colder plates that absorb less heat from the surrounding mantle, resulting in a colder mantle associated with higher topography.

Various processes have been studied to explain these topographic variations (Capitanio et al., 2011; Schellart, 2017; Wolf et al., 2022; Xue et al., 2022). For example, the rheology of the subducting-overriding plate interface significantly influences the topography (Behr et al., 2022). In northern Colombia, a transition to flat-slab subduction coincided with uplift and rapid exhumation over the past 7.5 million years, underscoring the importance of slab geometry and mantle wedge properties (Siravo et al., 2019). Additionally, factors such as mantle composition and water content affect viscosity, which, in turn, influences temperature distribution and topography. Arc volcanism also contributes to mountain elevation through smaller-scale edifices built atop the underlying orogen, although our model does not explicitly quantify this effect.

Although these parameters are important, they are not explicitly accounted for in our model; however, some of these are implicitly incorporated owing to the tree-based structure of the EBM. For instance, trench migration variability related to slab width (Schellart, 2017) is captured in our model without explicit parameterization (Fig. 4b), as this variability is already integrated into the EBM inputs—thus, directly including it would be redundant. Future studies may include these parameters to improve the accuracy of the model.

8. Conclusion and Future Directions

Our study advances the understanding of the complex geodynamic, tectonic, and climatic processes that shape active margin mountain topography. By leveraging the predictive and interpretable capabilities of EBM, we demonstrated a novel framework for linking key parameters, such as subduction flux, trench migration rate, mantle dynamics, and climate, to present-day topography.

Our study shows that the topography at active margins is best represented as a continuum of classes due to the variable nature of tectonic and mantle dynamics, where one end-member can transition into another. For instance, in regions with low-to-moderate subduction flux and fast trench retreat, the slab may initially pond at the mantle transition zone, causing trench rollback and moderate crustal thickening. This results in low-topography mountains (<1000 m) with extensional back-arc basins. However, if the slab penetrates deeper into the mantle, transitioning the region to a high subduction flux scenario, it resembles the present-day Central Andes region. Here, strong slab suction and whole-mantle convection lead to substantial crustal thickening and high elevations (>3000 m). Conversely, a decrease in convergence rates, especially with an older and stronger subducting plate, may cause the system to evolve from a high subduction flux to a trench advance scenario, forming a broader, high topography (>1500 m).

The explainable nature of EBM offers profound implications for deciphering past geodynamic and climatic conditions, enabling deeper insights into processes such as slab dynamics, mantle convection, and climate. Future research could use our framework to investigate the temporal and spatial evolution of mountain belts over deeper time scales. By

reconstructing historical topographic changes and predicting future scenarios, this study underscores the potential of integrative, data-driven models to illuminate the interplay between the Earth's surface and interior processes. It also opens new avenues for understanding the role of these dynamic landscapes in shaping past and future ecosystems and their biodiversity. Furthermore, the model provides a foundation for exploring metallogenesis at convergent margins, where topographic evolution often controls ore precipitation and preservation.

Acknowledgements

SPS was supported by the BHP STELLAR Industry Collaboration. MS acknowledges support from the Australian Research Council grant DP200100966; SZ was supported by the Australian Research Council grant DE210100084 and a University of Sydney Robinson Fellowship, while NMW was supported by the BHP STELLAR industry collaboration and Australian Research Council grant IE230100098. The development of pyGPlates and GPlates was funded by the AuScope National Collaborative Research Infrastructure System (NCRIS) program. We also thank the developers of Kalpa (https://kalpa.bighistory.in/) for providing us with tools to render and plot 3D visualizations.

Open Research

The EBM model for mountain elevations was developed using the open-source software InterpretML (Nori et al., 2019), GPlately (Mather et al., 2024), and Python-based workflows developed for this study, referred to as Python Deep Time Data Mining (pyDTDM). All figures were generated using the Matplotlib library (Caswell et al., 2024), and the 3D models were rendered and plotted using Kalpa (https://kalpa.bighistory.in/). To facilitate the replication of our work, we have made the following resources available at the following link: link to code and data.

A GPlates project containing loaded reconstruction model files (gpml and rotation models).

1. PyDTDM workflows for data preprocessing, modelling, visualization, and saving.
2. The extracted parameters were provided as raster (NetCDFs) and vector files (ESRI Shapefiles).
3. Geospatial explanations are available as raster (NetCDFs) and vector files (ESRI Shapefiles).

The workflows are also available via github link: https://github.com/singhsatyampratap/pyDTDM.

All the workflows and datasets are also available via zenodo link: DOI: 10.5281/zenodo.16806728

References

Amante, C., Eakins, B.W., 2009. ETOPO1 arc-minute global relief model : procedures, data sources and analysis.

Beck, S.L., Zandt, G., Myers, S.C., Wallace, T.C., Silver, P.G., Drake, L., 1996. Crustal-thickness variations in the central Andes. Geology 24, 407–410. https://doi.org/10.1130/0091-7613(1996)024%253C0407:CTVITC%253E2.3.CO;2

Behr, W.M., Holt, A.F., Becker, T.W., Faccenna, C., 2022. The effects of plate interface rheology on subduction kinematics and dynamics. Geophysical Journal International 230, 796–812. https://doi.org/10.1093/gji/ggac075

Bower, D.J., Gurnis, M., Flament, N., 2015. Assimilating lithosphere and slab history in 4-D Earth models. Physics of the Earth and Planetary Interiors 238, 8–22. https://doi.org/10.1016/j.pepi.2014.10.013

Braun, J., 2010. The many surface expressions of mantle dynamics. Nature Geosci 3, 825–833. https://doi.org/10.1038/ngeo1020

Capitanio, F.A., Faccenna, C., Zlotnik, S., Stegman, D.R., 2011. Subduction dynamics and the origin of Andean orogeny and the Bolivian orocline. Nature 480, 83–86.

Caruana, R., Lou, Y., Gehrke, J., Koch, P., Sturm, M., Elhadad, N., 2015. Intelligible Models for HealthCare: Predicting Pneumonia Risk and Hospital 30-day Readmission. Proceedings of the 21th ACM SIGKDD International Conference on Knowledge Discovery and Data Mining 1721–1730. https://doi.org/10.1145/2783258.2788613

Caswell, T.A., Andrade, E.S. de, Lee, A., Droettboom, M., Hoffmann, T., Klymak, J., Hunter, J., Firing, E., Stansby, D., Varoquaux, N., Nielsen, J.H., Gustafsson, O., Sunden, K., Root, B., May, R., hannah, Elson, P., Seppänen, J.K., Lee, J.-J., Dale, D., McDougall, D., Straw, A., Lucas, G., Hobson, P., Comer, R., Gohlke, C., Vincent, A.F., Yu, T.S., Ma, E., Silvester, S., 2024. matplotlib/matplotlib: REL: v3.7.5. https://doi.org/10.5281/zenodo.10669804

Cawood, P.A., Kröner, A., Collins, W.J., Kusky, T.M., Mooney, W.D., Windley, B.F., 2009. Accretionary orogens through Earth history. Geological Society, London, Special Publications 318, 1–36. https://doi.org/10.1144/SP318.1

Champagnac, J.-D., Molnar, P., Sue, C., Herman, F., 2012. Tectonics, climate, and mountain topography. Journal of Geophysical Research: Solid Earth 117. https://doi.org/10.1029/2011JB008348

Chen, F., Davies, D.R., Goes, S., Suchoy, L., Kramer, S.C., 2022. How Slab Age and Width Combine to Dictate the Dynamics and Evolution of Subduction Systems: A 3-D Spherical Study. Geochemistry, Geophysics, Geosystems 23, e2022GC010597. https://doi.org/10.1029/2022GC010597

Dewey, J.F., Bird, J.M., 1970. Mountain belts and the new global tectonics. Journal of Geophysical Research (1896-1977) 75, 2625–2647. https://doi.org/10.1029/JB075i014p02625

Di Giuseppe, E., Faccenna, C., Funiciello, F., Van Hunen, J., Giardini, D., 2009. On the relation between trench migration, seafloor age, and the strength of the subducting lithosphere. Lithosphere 1, 121–128. https://doi.org/10.1130/L26.1

Faccenna, C., Becker, T.W., 2020. Topographic expressions of mantle dynamics in the Mediterranean. Earth-Science Reviews 209, 103327. https://doi.org/10.1016/j.earscirev.2020.103327

Faccenna, C., Becker, T.W., Conrad, C.P., Husson, L., 2013. Mountain building and mantle dynamics. Tectonics 32, 80–93. https://doi.org/10.1029/2012TC003176

Faccenna, C., Becker, T.W., Holt, A.F., Brun, J.P., 2021. Mountain building, mantle convection, and supercontinents: Holmes (1931) revisited. Earth and Planetary Science Letters 564, 116905. https://doi.org/10.1016/j.epsl.2021.116905

Faccenna, C., Oncken, O., Holt, A.F., Becker, T.W., 2017. Initiation of the Andean orogeny by lower mantle subduction. Earth and Planetary Science Letters 463, 189–201. https://doi.org/10.1016/j.epsl.2017.01.041

Ferrier, K.L., Huppert, K.L., Perron, J.T., 2013. Climatic control of bedrock river incision. Nature 496, 206–209. https://doi.org/10.1038/nature11982

Flament, N., Gurnis, M., Müller, R.D., 2013. A review of observations and models of dynamic topography. Lithosphere 5, 189–210. https://doi.org/10.1130/L245.1

Garfunkel, Z., Anderson, C.A., Schubert, G., 1986. Mantle circulation and the lateral migration of subducted slabs. Journal of Geophysical Research: Solid Earth 91, 7205–7223. https://doi.org/10.1029/JB091iB07p07205

Garzanti, E., Radeff, G., Malusà, M.G., 2018. Slab breakoff: A critical appraisal of a geological theory as applied in space and time. Earth Science Reviews 177, 303–319. https://doi.org/10.1016/j.earscirev.2017.11.012

Göğüş, O.H., Ueda, K., 2018. Peeling back the lithosphere: Controlling parameters, surface expressions and the future directions in delamination modeling. Journal of Geodynamics 117, 21–40. https://doi.org/10.1016/j.jog.2018.03.003

Hayes, G.P., Moore, G.L., Portner, D.E., Hearne, M., Flamme, H., Furtney, M., Smoczyk, G.M., 2018. Slab2, a comprehensive subduction zone geometry model. Science 362, 58–61. https://doi.org/10.1126/science.aat4723

Karlstrom, K.E., Coblentz, D., Dueker, K., Ouimet, W., Kirby, E., Van Wijk, J., Schmandt, B., Kelley, S., Lazear, G., Crossey, L.J., Crow, R., Aslan, A., Darling, A., Aster, R., MacCarthy, J., Hansen, S.M., Stachnik, J., Stockli, D.F., Garcia, R.V., Hoffman, M., McKeon, R., Feldman, J., Heizler, M., Donahue, M.S., and the CREST Working Group, 2012. Mantle-driven dynamic uplift of the Rocky Mountains and Colorado Plateau and its surface response: Toward a unified hypothesis. Lithosphere 4, 3–22. https://doi.org/10.1130/L150.1

Konstantinov, A.V., Utkin, L.V., 2021. Interpretable machine learning with an ensemble of gradient boosting machines. Knowledge-Based Systems 222, 106993. https://doi.org/10.1016/j.knosys.2021.106993

Koppers, A.A.P., Becker, T.W., Jackson, M.G., Konrad, K., Müller, R.D., Romanowicz, B., Steinberger, B., Whittaker, J.M., 2021. Mantle plumes and their role in Earth processes. Nat Rev Earth Environ 2, 382–401. https://doi.org/10.1038/s43017-021-00168-6

Leonard, J.S., Whipple, K.X., Heimsath, A.M., 2023. Isolating climatic, tectonic, and lithologic controls on mountain landscape evolution. Science Advances 9, eadd8915. https://doi.org/10.1126/sciadv.add8915

Li, X., Hu, Y., Guo, J., Lan, J., Lin, Q., Bao, X., Yuan, S., Wei, M., Li, Z., Man, K., Yin, Z., Han, J., Zhang, J., Zhu, C., Zhao, Z., Liu, Y., Yang, J., Nie, J., 2022. A high-resolution climate simulation dataset for the past 540 million years. Sci Data 9, 371. https://doi.org/10.1038/s41597-022-01490-4

Lou, Y., Caruana, R., Gehrke, J., Hooker, G., 2013. Accurate intelligible models with pairwise interactions, in: Proceedings of the 19th ACM SIGKDD International Conference on Knowledge Discovery and Data Mining, KDD '13. Association for Computing Machinery, New York, NY, USA, pp. 623–631. https://doi.org/10.1145/2487575.2487579

Lu, C., Grand, S.P., Lai, H., Garnero, E.J., 2019. TX2019slab: A New P and S Tomography Model Incorporating Subducting Slabs. Journal of Geophysical Research: Solid Earth 124, 11549–11567. https://doi.org/10.1029/2019JB017448

Lu, X., Lai, J., Wang, L., Ji, J., Zhong, D., 2024. Numerical modelling of coupled climate, tectonics, and surface processes on the eastern Himalayan syntaxis. Earth-Science Reviews 258, 104964. https://doi.org/10.1016/j.earscirev.2024.104964

Mather, B.R., Müller, R.D., Zahirovic, S., Cannon, J., Chin, M., Ilano, L., Wright, N.M., Alfonso, C., Williams, S., Tetley, M., Merdith, A., 2024. Deep time spatio-temporal

data analysis using pyGPlates with PlateTectonicTools and GPlately. Geoscience Data Journal 11, 3–10. https://doi.org/10.1002/gdj3.185

McNamara, A.K., Zhong, S., 2004. Thermochemical structures within a spherical mantle: Superplumes or piles? Journal of Geophysical Research: Solid Earth 109. https://doi.org/10.1029/2003JB002847

Moresi, L., Zhong, S., Han, L., Conrad, C., Tan, E., Gurnis, M., Choi, E., Thoutireddy, P., Manea, V., McNamara, A., Becker, T., Leng, W., Armendariz, L., 2014. CitcomS v3.3.1. https://doi.org/10.5281/zenodo.7271920

Müller, R.D., Cannon, J., Qin, X., Watson, R.J., Gurnis, M., Williams, S., Pfaffelmoser, T., Seton, M., Russell, S.H.J., Zahirovic, S., 2018. GPlates: Building a Virtual Earth Through Deep Time. Geochemistry, Geophysics, Geosystems 19, 2243–2261. https://doi.org/10.1029/2018GC007584

Nieto-Samaniego, A.F., Alaniz-Alvarez, S.A., Silva-Romo, G., Eguiza-Castro, M.H., Mendoza-Rosales, C.C., 2006. Latest Cretaceous to Miocene deformation events in the eastern Sierra Madre del Sur, Mexico, inferred from the geometry and age of major structures. GSA Bulletin 118, 238–252. https://doi.org/10.1130/B25730.1

Nori, H., Jenkins, S., Koch, P., Caruana, R., 2019. InterpretML: A Unified Framework for Machine Learning Interpretability [WWW Document]. arXiv.org. URL https://arxiv.org/abs/1909.09223v1 (accessed 10.8.24).

Parsons, B., Sclater, J.G., 1977. An analysis of the variation of ocean floor bathymetry and heat flow with age. Journal of Geophysical Research (1896-1977) 82, 803–827. https://doi.org/10.1029/JB082i005p00803

Royden, L.H., 1993. The tectonic expression slab pull at continental convergent boundaries. Tectonics 12, 303–325. https://doi.org/10.1029/92TC02248

Schellart, W.P., 2017. Andean mountain building and magmatic arc migration driven by subduction-induced whole mantle flow. Nat Commun 8, 2010. https://doi.org/10.1038/s41467-017-01847-z

Schellart, W.P., 2008. Overriding plate shortening and extension above subduction zones: A parametric study to explain formation of the Andes Mountains. GSA Bulletin 120, 1441–1454. https://doi.org/10.1130/B26360.1

Schellart, W.P., Moresi, L., 2013. A new driving mechanism for backarc extension and backarc shortening through slab sinking induced toroidal and poloidal mantle flow: Results from dynamic subduction models with an overriding plate. Journal of Geophysical Research: Solid Earth 118, 3221–3248. https://doi.org/10.1002/jgrb.50173

Scotese, C., 2016. Phanerozoic Global Temperature Curve. Scotese, C.R., 2016. Figure 15 in Some Thoughts on Global Climate Change: The transition from Icehouse to Hothouse, in the Earth History: The evolution of the Earth System (in preparation), PALEOMAP Project, Evanston, IL.

Siravo, G., Faccenna, C., Gérault, M., Becker, T.W., Fellin, M.G., Herman, F., Molin, P., 2019. Slab flattening and the rise of the Eastern Cordillera, Colombia. Earth and Planetary Science Letters 512, 100–110. https://doi.org/10.1016/j.epsl.2019.02.002

Snethlage, M.A., Geschke, J., Ranipeta, A., Jetz, W., Yoccoz, N.G., Körner, C., Spehn, E.M., Fischer, M., Urbach, D., 2022. A hierarchical inventory of the world's mountains for global comparative mountain science. Sci Data 9, 149. https://doi.org/10.1038/s41597-022-01256-y

Strak, V., Xue, K., Schellart, W.P., 2024. Mantle upwelling induced by slab rollover subduction could explain widespread intraplate volcanism in Tibet. Commun Earth Environ 5, 1–13. https://doi.org/10.1038/s43247-024-01581-7

Tan, E., Choi, E., Thoutireddy, P., Gurnis, M., Aivazis, M., 2006. GeoFramework: Coupling multiple models of mantle convection within a computational framework. Geochemistry, Geophysics, Geosystems 7. https://doi.org/10.1029/2005GC001155

Torsvik, T.H., Steinberger, B., Gurnis, M., Gaina, C., 2010. Plate tectonics and net lithosphere rotation over the past 150 My. Earth and Planetary Science Letters 291, 106–112. https://doi.org/10.1016/j.epsl.2009.12.055

van Hinsbergen, D.J.J., 2022. Indian plate paleogeography, subduction and horizontal underthrusting below Tibet: paradoxes, controversies and opportunities. National Science Review 9, nwac074. https://doi.org/10.1093/nsr/nwac074

Whipple, K.X., 2009. The influence of climate on the tectonic evolution of mountain belts. Nature Geosci 2, 97–104. https://doi.org/10.1038/ngeo413

Whipple, K.X., Meade, B.J., 2006. Orogen response to changes in climatic and tectonic forcing. Earth and Planetary Science Letters 243, 218–228. https://doi.org/10.1016/j.epsl.2005.12.022

Willett, S.D., Slingerland, R., Hovius, N., 2001. Uplift, Shortening, and Steady State Topography in Active Mountain Belts. American Journal of Science 301, 455–485. https://doi.org/10.2475/ajs.301.4-5.455

Wolf, S.G., Huismans, R.S., Braun, J., Yuan, X., 2022. Topography of mountain belts controlled by rheology and surface processes | Nature [WWW Document]. URL https://www.nature.com/articles/s41586-022-04700-6 (accessed 12.17.22).

Xue, K., Schellart, W.P., Strak, V., 2022. Overriding Plate Deformation and Topography During Slab Rollback and Slab Rollover: Insights From Subduction Experiments. Tectonics 41, e2021TC007089. https://doi.org/10.1029/2021TC007089

Yang, T., Gurnis, M., Zahirovic, S., 2016. Mantle-induced subsidence and compression in SE Asia since the early Miocene. Geophysical Research Letters 43, 1901–1909. https://doi.org/10.1002/2016GL068050

Yin, A., Harrison, T.M., 2000. Geologic Evolution of the Himalayan-Tibetan Orogen. Annual Review of Earth and Planetary Sciences 28, 211–280. https://doi.org/10.1146/annurev.earth.28.1.211

Yuan, Q., 2024. Numerical Modeling of Melting Processes During Slab Break-off: Insights Into Tectonic Setting for Massif-Type Anorthosites. Lithosphere 2024, lithosphere_2023_344. https://doi.org/10.2113/2024/lithosphere_2023_344

Yuan, X., Li, Y., Brune, S., Li, K., Pons, M., Wolf, S.G., 2024. Coordination between deformation, precipitation, and erosion during orogenic growth. Nat Commun 15, 10362. https://doi.org/10.1038/s41467-024-54690-4

Zahirovic, S., Eleish, A., Doss, S., Pall, J., Cannon, J., Pistone, M., Tetley, M.G., Young, A., Fox, P., 2022. Subduction and carbonate platform interactions. Geoscience Data Journal 9, 371–383. https://doi.org/10.1002/gdj3.146

Zhong, S., Gurnis, M., 1995. Mantle Convection with Plates and Mobile, Faulted Plate Margins. Science 267, 838–843. https://doi.org/10.1126/science.267.5199.838

Zhong, S., Zuber, M.T., Moresi, L., Gurnis, M., 2000. Role of temperature-dependent viscosity and surface plates in spherical shell models of mantle convection. Journal of Geophysical Research: Solid Earth 105, 11063–11082. https://doi.org/10.1029/2000JB900003

Chapter 4

Article 3: Deep Learning Reconstructs Global Active Margin Paleotopography Since the Mesozoic from Plate Kinematics and Mantle Dynamics

Deep Learning Reconstructs Global Active Margin Paleotopography Since the Mesozoic from Plate Kinematics and Mantle Dynamics

Satyam Pratap Singh[1,2*], Maria Seton[1], Sabin Zahirovic[1], Nicky M. Wright[1], Simon Williams[3], Jianping Zhou[1,4]

[1]EarthByte Group, School of Geosciences, The University of Sydney, NSW 2006, Australia
[2]Now at Geonome Pty Ltd, NSW 2010, Australia
[3]Institute for Marine and Antarctic Studies, University of Tasmania, Hobart, TAS 7001, Australia
[4] Frontiers Science Centre for Deep Ocean Multispheres and Earth System, Key Lab of Submarine Geosciences and Prospecting Techniques, MOE and College of Marine Geosciences, Ocean University of China, Qingdao, China

Correspondence: Satyam Pratap Singh, EarthByte Group, School of Geosciences, The University of Sydney, Sydney, NSW 2006, Australia Email: ssingh@es.iitr.ac.in

Abstract

Topography at active margins exerts a fundamental control on Earth's climate, biodiversity, and natural resource distribution. Reconstructing its evolution through geological time remains challenging because paleoelevation proxies are sparse, unevenly distributed, and subject to large uncertainties. Here, we present a deep-learning model built on physically grounded variables, including plate kinematics, mantle convection, and a paleoclimate-informed parameter, to reconstruct paleotopography along active margins. Our model explains 92% of the variance in modern elevations, with a root mean squared error of 576 m relative to ETOPO1. To evaluate its applicability through time, we compare model predictions with global geochemical-based paleoelevation proxies since the Mesozoic (~200 Ma) and benchmark them against a regional paleotopographic reconstruction for the Cenozoic Andes, where paleoelevation constraints are abundant. Our model successfully predicts ~4 km of Central Andean uplift since the Oligocene, associated with an approximately threefold increase in subduction flux (0.03–0.08 km³/yr), consistent with paleoelevation estimates. Building on this data–model agreement in a well-constrained region, we apply our methodology to a case study of East Asia. The model reveals a multiphase mountain-building history comprising a Late Jurassic high plateau, subsequent Early Cretaceous extension and plateau collapse, and a mid-Cretaceous rejuvenation that produced a narrow coastal mountain belt. The reconstructed elevation history agrees with independent geochemical paleoelevation proxies, crustal-thickness estimates, and zircon records of magmatic and metamorphic flare-ups, demonstrating that a combined geological

modelling and artificial-intelligence framework can recover lost mountain belts and illuminate the coupled evolution of topography, climate, and the biosphere over geological time.

Significance statement

Topography along subduction margins strongly influences climate, biodiversity, and natural resources, yet ancient mountain belts are difficult to reconstruct because paleoelevation indicators are sparse and unevenly distributed. By integrating plate kinematics, mantle convection, climate proxies, and deep learning, this study recovers the uplift histories of both well-documented (Central Andes) and previously unresolved (multiphase Jurassic–Cretaceous orogen in East Asia) mountain systems. The results show how artificial intelligence can fuse geological datasets and models into quantitative maps of past topography, providing a powerful new framework for testing how tectonics, climate, ecosystems, and resources have co-evolved through deep time.

1. Introduction

Topography along active margins shapes atmospheric circulation, ecological gradients, and the localization of mineral systems, thereby modulating Earth's climate, ecosystems, and the distribution of natural resources (1–3). Mountains formed at subduction zones act as climate modulators, generating rain shadows, steering atmospheric circulation, and shaping large-scale precipitation patterns (4–6). These high-relief terrains also promote ecological diversification by introducing environmental gradients and physical barriers, leading to elevated biodiversity in many active margin mountain belts. Moreover, the rise and evolution of topography at active margins are intimately linked to the formation and preservation of mineral systems, including porphyry copper deposits critical for global metal supply and the energy transition (2, 7).

Despite its importance, reconstructing the paleotopography of active margins through deep time remains a major challenge in part due to the limited spatial and temporal coverage of paleoelevation proxies. Methods such as stable isotope paleoaltimetry, fossil flora analysis, and low-temperature thermochronology provide important insights but are inherently localised, episodic, and sensitive to climatic or erosional overprints (8–13). Many of these techniques assume modern isotopic lapse rates and atmospheric structures, which may not be valid over deep time, contributing to large uncertainties (often >1–2 km) in elevation estimates (9, 14–16). Furthermore, erosion more readily removes the high-elevation record in active settings, limiting preservation to sedimentary archives that only indirectly reflect landscape morphology. As a result, existing reconstructions rely on spatial and temporal interpolation across large gaps, leaving major uncertainties in the evolution of many active margins.

These challenges are particularly acute along the Mesozoic East Asian Margin (EAM), where the topographic history remains debated. One hypothesis proposes a broad, high-elevation plateau during the Late Jurassic, analogous to the modern Altiplano, supported by sedimentary and geochemical records indicating significant crustal thickening (17–19). Alternatively, other studies emphasize a complex, multiphase evolution with distinct episodes of mountain building and collapse; geochemical proxies (Sr/Y, Ce/Y ratios) and climate

modelling indicate that crustal thickening between 120 and 105 Ma produced a narrow coastal mountain range exceeding 2,500 m in elevation, which altered atmospheric circulation, increased inland aridity, and drove the expansion of desert belts across Asia (20–22). Structural and stratigraphic data further document repeated cycles of contraction, extension, and topographic inversion across NE China, associated with the transition from an Andean-type margin to widespread back-arc extension by the Late Cretaceous (23–25). Recent tectonomagmatic syntheses and mantle-flow models add further complexity, suggesting alternating episodes of flat-slab subduction, lithospheric delamination, and back-arc extension, and implying an episodic, heterogeneous topographic evolution rather than sustained Andean-style uplift (26, 27).

Whether a continuous, high-elevation "East Asian Cordillera" existed during the Jurassic–Cretaceous has major implications for global climate, atmospheric circulation, and trans-Asian biotic dispersal. Yet existing, localised proxies cannot unambiguously distinguish between plateau-like and narrow, transient mountain-belt scenarios. The erosional loss of high-standing landscapes, the indirect nature of most sedimentary archives, and the strong spatial heterogeneity of available proxies leave large gaps in our paleotopographic reconstructions. These limitations highlight the need for approaches that do not depend solely on sparse paleoelevation indicators.

Long-term elevation at active margins is tightly linked to plate kinematics, mantle flow, and climate. As such, forward models and global reconstructions of these processes provide a largely continuous, physically based context for estimating past topography (28–32). Leveraging these model-derived fields within a reproducible modelling framework enables quantitative, spatially continuous paleotopographic reconstructions that complement and test fragmentary proxy records.

Here, we develop a physics-grounded deep learning framework that predicts active margin paleotopography from global plate kinematic reconstructions (32), mantle convection outputs (31, 33–35), and paleoclimate-informed variables (Supplementary Section 1.3). We refer to this deep learning model as the Subduction Topography Network (STN). We train this model on present-day topography along all subduction margins and validate its performance against withheld present-day regions, a global compilation of geochemical crustal thickness–based paleoelevation proxies from Mesozoic–Cenozoic arc magmatic rocks, and benchmark against an independent Cenozoic paleotopographic reconstruction for the South American Andes. We then apply the framework to the Jurassic–Cretaceous EAM to evaluate whether subduction-driven processes could have generated and sustained high topography and test competing scenarios for broad plateau versus narrow coastal orogen configurations through time. More broadly, this framework establishes a quantitative and reproducible pathway for recovering the topographic evolution of active margins and for linking long-term tectonic forcing with past climate and surface environments.

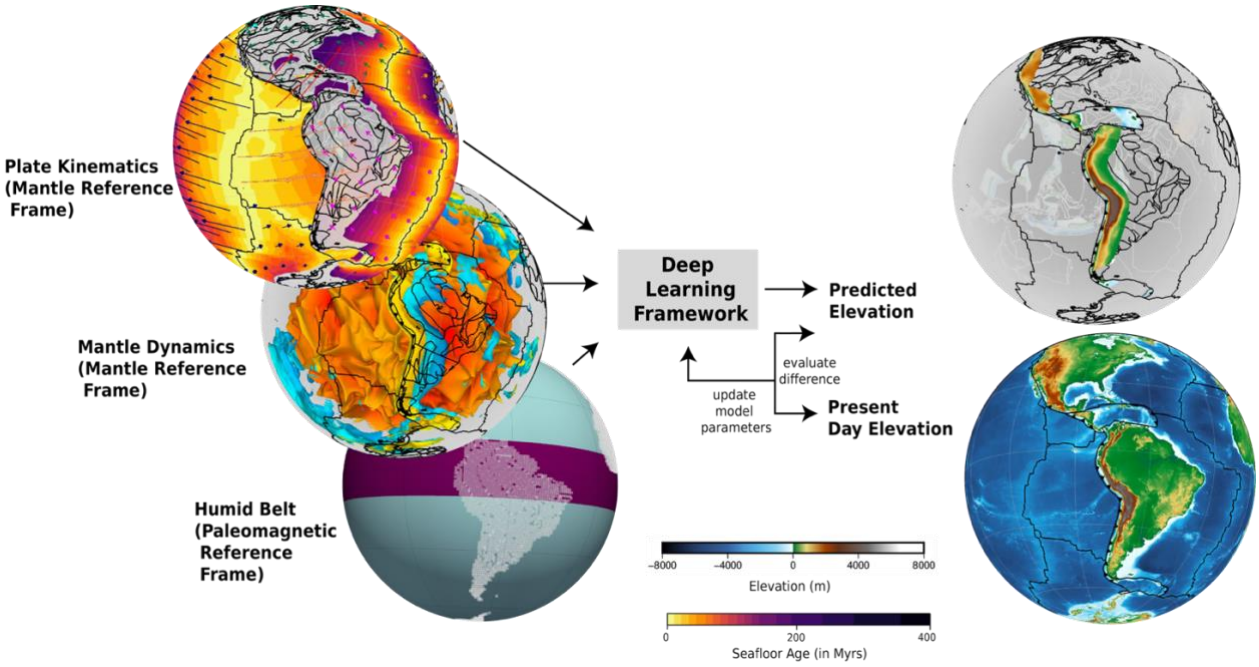

Figure 1 | Deep learning framework for reconstructing paleotopography.
a) We develop a deep neural network model to reconstruct ancient topography along active margins by learning from present-day global topography (ETOPO1) and three categories of geodynamic and climatic predictors: (1) plate kinematics, (2) mantle dynamics in the mantle reference frame, and (3) the duration spent within the equatorial humid belt in the paleomagnetic reference frame. All predictor variables are detailed in Supplementary Table 1. Because these input features are reconstructable through time, the trained model enables paleotopographic predictions across geological timescales. Isosurface rendering of a mantle temperature field showing two isovalues: 1,260 °C (blue) and 1,670 °C (red). These represent cooler downgoing slabs and hotter mantle upwellings, respectively. Colours on the isosurfaces indicate the direction of scalar gradients: red shades (back side) indicate increasing scalar values, and blue shades (front side) indicate decreasing values, helping visualise whether the scalar field is increasing or decreasing along the view direction.

2. Materials and Methods

We trained a deep neural network using present-day plate kinematics and a paleoclimate-informed parameter derived from a global plate tectonic reconstruction (see Supplementary Sections 1.1, 1.2, and 1.4) and outputs of an accompanying CitcomS mantle convection model (see Supplementary Section 1.2) as input variables, with present-day topography (ETOPO1) as the target variable (Figure 1; Supplementary Table 1). Once trained, the STN learns and generalises the relationship between the input and target variables. Because the input parameters can be reconstructed back through geological time from plate reconstructions and mantle convection models, the STN can be applied to predict topography in deep time. We used the STN to generate topographic predictions from 200 Ma to the

present at 1 Ma intervals and at 0.1° spatial resolution. To quantify uncertainty, we evaluated the STN predictions against: (i) present-day topography of five geographically diverse regions withheld from training (Section 2.3.1); (ii) Cenozoic paleotopographic estimates for the Andes (Section 2.3.2); and (iii) geochemical-based paleoelevation proxies from Mesozoic–Cenozoic East Asia (Section 2.3.3).

2.1 Preparing the Dataset for STN

Polygons were delineated around all subduction zones from a global plate tectonic reconstruction (32) by generating automated buffers extending 1,000 km landward from each trench on the overriding plate. This threshold was selected because most high-elevation, arc-related, and thickened-crust domains lie within ~800 km of the trench. These polygons were constructed at 1 Myr intervals from 200 Ma to the present and used to define the spatial domain for sampling tectonic and mantle parameters. Within these polygons, we generated a uniform spherical grid with a target spacing of ~0.1° in latitude and longitude (Supplementary Section 1.1). Subduction zones were discretised on this grid, and plate-kinematic parameters were sampled from the global plate reconstruction in a mantle reference frame. The plate kinematic values were assigned to grid points using nearest-neighbour interpolation (Supplementary Section 1.2). We used the same plate reconstruction (32) in a paleomagnetic reference frame to identify whether grid points persisted within the near-equatorial humid belt (±10° latitude), characterised by high precipitation rates (3; Supplementary Section 1.4). This metric served as a proxy for surface-process influences on topography, representing the cumulative erosional potential associated with high precipitation and temperature in tropical settings. By incorporating the duration spent in the humid belt, the model accounts for the long-term coupling between climate-driven denudation and tectonic uplift (3, 52). To capture multi-Myr integration of tectonics and climate, all parameters were time-averaged over a 25 Myr moving window at each timestep. Upper mantle temperature and vertical flow fields at different depths were extracted from CitcomS mantle convection models (Supplementary Table 1), using the same plate tectonic reconstruction as boundary conditions following the model setup established in this study (31).

2.2 STN Architecture, Training and Prediction

The STN is a fully connected neural network with five hidden layers, Rectified Linear Unit (ReLU) activations, batch normalisation, and dropout regularisation to reduce overfitting (Supplementary Section 1.7 and Supplementary Figure 1). For training, we used the present-day point grid to sample elevations from ETOPO1 (36). Because ETOPO1 is provided at 1 arc-min resolution, we applied a Gaussian filter with $\sigma = 2$ grid cells (~2 arc-min) prior to sampling in order to smooth small-scale variations and retain features relevant to the scale of our analysis. The STN was trained to learn the relationship between the input parameters and present-day elevation by minimising the mean squared error (MSE) between predicted and observed values (Supplementary Section 1.8). We withheld five geographically diverse regions during the training of the STN to assess its performance on unseen data. These regions were selected to represent diverse subduction geometries: continental arcs (Northern Andes, Central America), island arcs (Kuril Islands, Sunda Arc), and transitional–collisional margins (Iranian Plateau). Once trained, the STN was used to predict elevation at every 1

Myr timestep from 200 Ma to the present. Training hyperparameters, detailed architecture, and code are provided in the Supplementary Material and GitHub repository.

2.3 STN Validation

We assessed the model's predictive performance using both modern and paleo-elevation datasets. A summary is provided below; more details on the validation framework can be found in Supplementary Section 1.10.

2.3.1 Present-Day Validation

For present-day validation, we first assessed the STN's performance using the input and target dataset held out for validation, which includes five geographically diverse regions (R1–R5; Figure 2). We also compared the global ETOPO1 (36) elevation with predicted elevation and evaluated model accuracy using standard metrics, including root mean squared error (RMSE), mean absolute error (MAE), and explained variance score (R^2), ensuring the model's generalising capabilities.

2.3.2 Global Deep-Time Validation

To evaluate the model's applicability through geological time, we compared paleotopographic predictions against independent, globally distributed paleoelevation proxies derived from arc-related magmatic rocks (37) spanning the Mesozoic (~200 Ma) to present using the framework proposed (38). These geochemical proxies (e.g., Sr/Y, La/Yb) provide crustal thickness estimates, which were converted to elevation using empirical calibrations (38–40). Geochemical data from igneous rocks are far more abundant across both space and time (37) compared to other forms of paleoelevation estimates. As a result, they offer a valuable option to quantitatively evaluate predicted paleotopographic reconstructions along active margins through Earth's history.

2.3.3 A Critical Natural Benchmark: the South American Andes

For regional validation, we focused our comparison on the Cenozoic South American Andes. We compared our model outputs with a comprehensive paleoelevation synthesis by Boschman (2021), one of the few available datasets based on independent stable isotope paleoaltimetry ($\delta^{18}O$), sedimentological, and paleobotanical data constraints across the Cenozoic. The Andes were selected for this validation because they represent a long-lived, well-studied active margin where uplift history has been constrained using a broad array of proxies without relying on the geodynamic or kinematic inputs used in our model. Equivalent paleoelevation datasets are not available for most other regions, making the Andes a critical natural benchmark.

2.3.4 Validation of Jurassic–Cretaceous EAM

To validate our modelled paleotopography in East Asia during the Jurassic–Cretaceous, we compared our results with independent geochemical-based paleoelevation estimates based on the method proposed by Zhou et al. (2025) and Li et al. (2024), hereafter referred to as Zhou++ and Li++, respectively. While these approaches carry substantial uncertainties—often in the range of 2–3 km (20, 38, 40, 41)– they offer valuable, spatially extensive first-

order constraints for model benchmarking. In addition to crustal-thickness-based estimates, we incorporated zircon-based records as qualitative constraints on tectonic activity and surface environments. We compiled U-Pb zircon age data from igneous, sedimentary, and metamorphic rocks across East Asia, sourced from a global database (42). These zircon datasets were used to generate kernel density estimates of age distributions, with a bandwidth of 5 Myr, to identify peaks in magmatic activity (igneous zircons; 43–45), erosion and sediment transport (sedimentary zircons; 46), and metamorphic events (metamorphic zircons; 44, 47). Such patterns help infer relative elevation trends, orogenic phases, and crustal evolution over time, as magmatic flareups commonly coincide with episodes of enhanced crustal thickening and/or arc widening driven by changes in subduction dynamics (43, 44, 47, 48), while increased sedimentary zircon input signals enhanced erosion and sediment recycling from elevated terrains (46, 49). Together, these independent lines of evidence strengthen validation of Jurassic–Cretaceous topography along East Asia.

3 Results

3.1 Present-day Topography Validation

Our model demonstrates high accuracy metrics in reproducing present-day topography along active margins, achieving an RMSE of 576 m relative to the ETOPO1 dataset (36), while explaining 92% of the spatial variance (i.e., the geographic distribution of elevation changes across the Earth's surface; $R^2 = 0.92$) (Figure 2). To evaluate the model’s generalisability, we assessed its performance across five tectonically diverse regions, including both continental mountains and island arcs, that were withheld from training (R1–R5; Figure 2; Supplementary Figure 2). In the northern Andes (R1), the model reproduces the broad elevation gradients with a regional MAE of 513 m. Given that total relief in the Andes exceeds 6,000 m, an MAE of ~500 m represents an error of less than 10% of the topographic signal, confirming the model’s ability to resolve continental orogenic scales. In the Kuril Island Arc (R2), the model reproduces both the arc topography and the bathymetry of the back-arc basin with an MAE of 1,352 m. While numerically higher than the continental regions, this error is small relative to the extreme 10,000 m of total elevational characteristic of trench-arc systems, which span from deep-sea trenches to subaerial volcanic peaks. Along the Central American Cordillera (R3), the model predicts a slightly broader, elevated topography than observed, with an MAE of 559 m, whereas in the Sunda Arc (R4) and the West Asia–Iranian Plateau (R5) it resolves both arc system topography and plateau topography, with MAEs of 1,045 m and 666 m, respectively. This consistent performance across regions with contrasting tectonic settings highlights the robustness and predictive capability of our model.

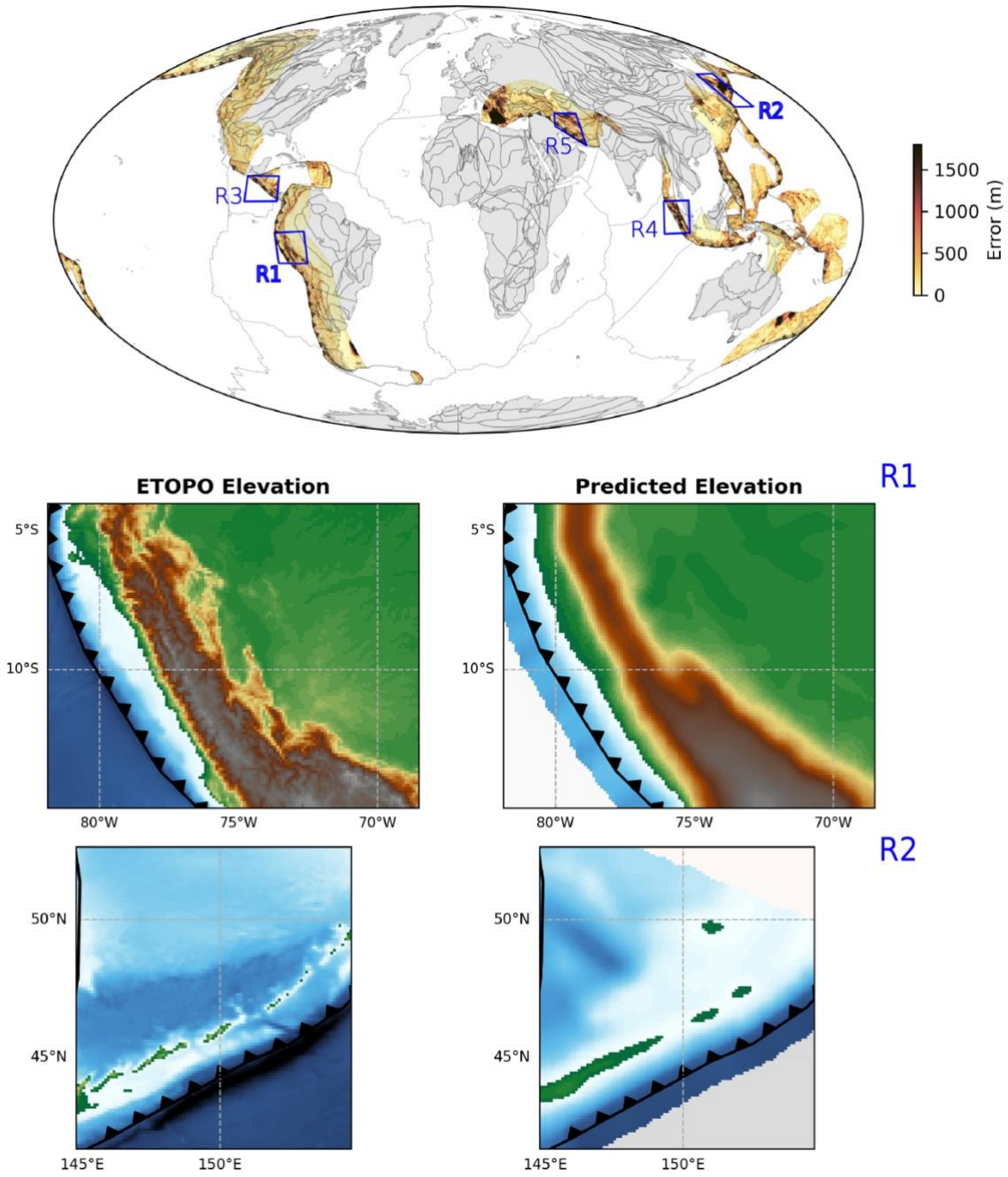

Figure 2 | Validation of model predictions against smoothed present-day topography.
a) Spatial misfit between predicted and smoothed present-day elevations (ETOPO1; Amante & Eakins, 2009) using the trained deep learning model and present-day inputs (see Supplementary Table 1). Blue polygons (R1–R5) indicate independent validation regions that were excluded from training.
b) Predicted versus actual ETOPO1 elevation for R1 (Northern Andes) and R2 (Kuril Islands), highlighting the model's performance on unseen data. For regions R3–R5, refer to Supplementary Figure 2.

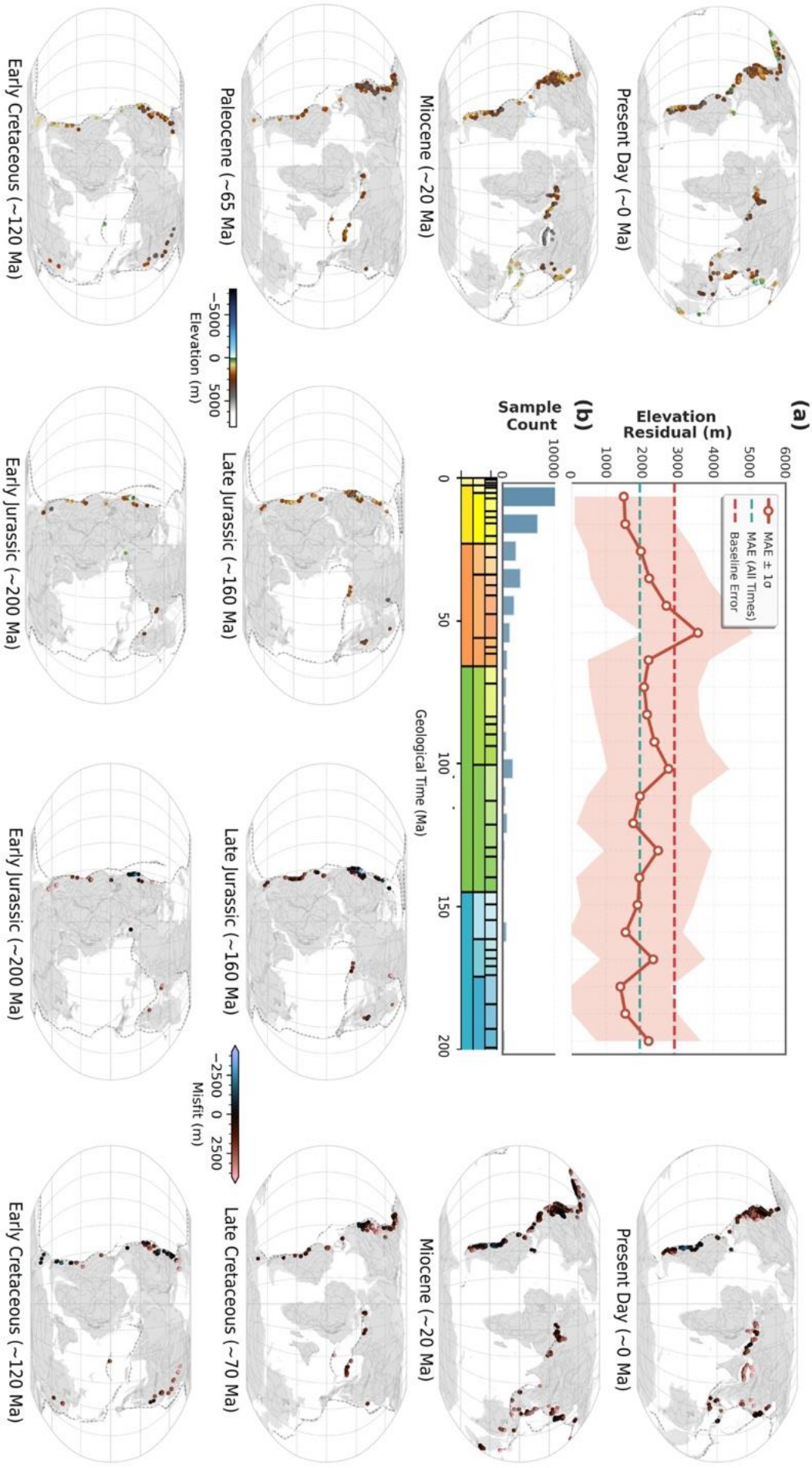
(a)
Elevation Residual (m)
MAE ± 1σ
MAE (All Times)
Baseline Error
(b)
Sample Count
Geological Time (Ma)
Present Day (~0 Ma)
Miocene (~20 Ma)
Paleocene (~65 Ma)
Early Cretaceous (~120 Ma)
Late Jurassic (~160 Ma)
Early Jurassic (~200 Ma)
Late Cretaceous (~70 Ma)
Elevation (m)
Misfit (m)

Figure 3 | Validation of global active margin paleotopography through deep time.
(a) Mean absolute error (MAE) between predicted and proxy-derived paleoelevations, binned into 10 Myr temporal intervals at 0.5° spatial resolution. The standard deviation represents the uncertainty associated with the proxy-derived elevation estimates and reflects observational uncertainties within the dataset. The *baseline error* refers to the misfit between the predicted paleoelevation and a reference scenario in which all active-margin points across all time slices are assigned a constant value equal to the mean elevation of present-day active margins.
(b) Bar plot showing the number of proxy samples within each 10 Myr interval.
Left: Geochemically derived paleoelevation estimates for selected time intervals. A time-continuous reconstruction is provided in Supplementary Animation 2.
Right: Point-wise misfit between predicted paleoelevation and geochemical proxy estimates, illustrating the spatial distribution of residuals across all time slices.

3.2 Global Validation in Deep Time

Across deep time, the model reproduces first-order elevation patterns recorded by geochemical paleoelevation proxies from arc magmatic rocks since the Mesozoic (~200 Ma; Supplementary Section 1.10). Predicted elevations were compared with 0.5 by 0.5 geochemical paleoelevation proxy grid estimates at each time slice, and misfits were mapped globally and summarised as a time-dependent mean absolute error (MAE; Figure 3; Supplementary Animations 2–3). Over the full 200 Myr interval, the model attains an average MAE of 1,930 m relative to the geochemical proxies, with MAE remaining broadly stable through time despite large variations in sample density (Figure 3a–b). To quantify the predictive skill of the STN, we compared its performance against a null baseline—a 'naive' model in which all active margin points at all times are assigned a constant elevation equal to the present-day mean active margin elevation (–732 m). This constant-elevation baseline assumes no topographic evolution through time and yields a significantly higher MAE of ~2,950 m relative to the same proxy dataset (Figure 3a). The ~1,000 m reduction in error achieved by the STN demonstrates that the model effectively captures the dynamic topographic signals driven by evolving plate kinematics and mantle flow, providing a robust improvement over static reconstructions.
Despite the intrinsic uncertainties in the proxies themselves (typical 1σ of ±1,515 m and occasionally up to ±4,000 m; (38), 60% of predicted elevations fall within the reported uncertainty bounds of the geochemical estimates. In the context of deep-time reconstructions, where the ground truth itself carries kilometre-scale uncertainty, this level of agreement represents a robust alignment with the geological record. Most misfits (~50%) lie within ±1,000, i.e. half of the model's predictions are more precise than the standard 1σ uncertainty of the geochemical calibration used for validation. Error maps show that large discrepancies (>2,500 m) are spatially restricted, occurring primarily in western North America during the Late Cretaceous–Paleogene Laramide orogeny where flat-slab subduction of an oceanic plateau and related geodynamic complexities are not fully captured by our model (50), and in a few other isolated segments where proxy coverage is sparse or highly uncertain (Figure 3).

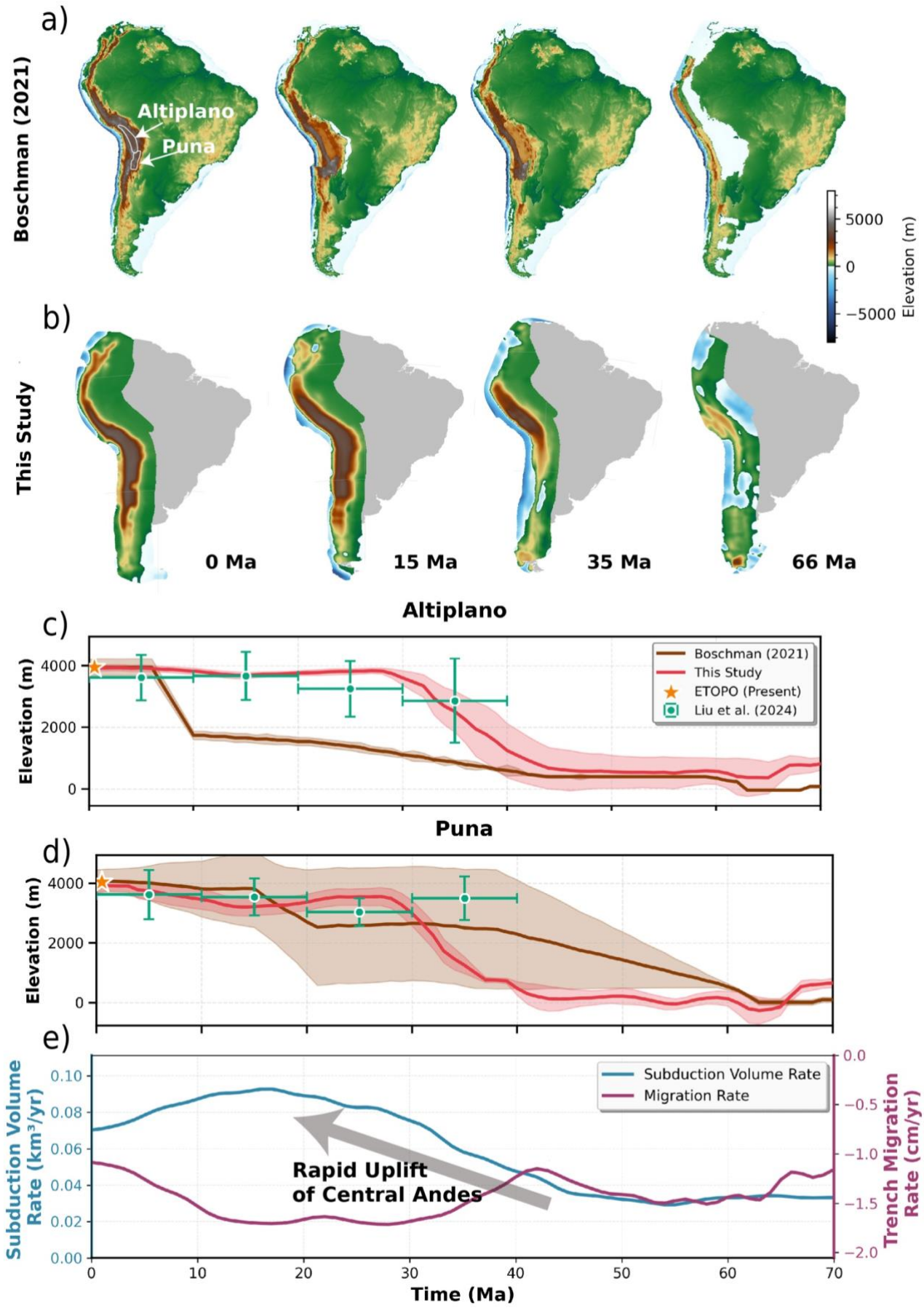
a)
Boschman (2021)
Altiplano
Puna
5000
0
−5000
Elevation (m)
b)
This Study
0 Ma
15 Ma
35 Ma
66 Ma
Altiplano
c)
Elevation (m)
4000
2000
0
Boschman (2021)
This Study
ETOPO (Present)
Liu et al. (2024)
Puna
d)
Elevation (m)
4000
2000
0
e)
Subduction Volume Rate (km³/yr)
0.10
0.08
0.06
0.04
0.02
0.00
Subduction Volume Rate
Migration Rate
Rapid Uplift of Central Andes
0.0
−0.5
−1.0
−1.5
−2.0
Trench Migration Rate (cm/yr)
0
10
20
30
40
50
60
70
Time (Ma)

Figure 4 | Integrated comparison of Cenozoic Andean paleotopography and driving parameters.
a) Spatiotemporal evolution of Andean surface uplift from 66 Ma to the present, showing model predictions compared with Boschman (2021).
b) Comparison of Altiplano paleotopography between our model, Boschman (2021), and geochemical proxy-based estimates from Liu et al. (2024).
c) Comparison of Puna paleotopography between our model, Boschman (2021), and geochemical proxy-based estimates from Liu et al. (2024).
d) Input drivers of topographic change in the Central Andes (Altiplano and Puna). The subduction flux increased from 0.03 km^3/yr during the Eocene to >0.08 km^3/yr by the Miocene, driving rapid uplift of the Central Andes.

3.3 Comparison with Regional Paleotopography: The Andes

We compared our Cenozoic paleoelevation reconstruction of the Central Andes with the independently derived paleotopography model (51) to assess the timing and magnitude of surface uplift along this convergent margin (Figure 4a–b). Although the two approaches differ fundamentally—our model integrates continuously evolving subduction parameters constrained by plate kinematics, whereas Boschman (2021) interpolates discrete geological proxy data—both reconstructions agree on low elevations across the Northern and Central Andes at 66 Ma, with most back-arc regions near sea level. Both models also converge on the development of high modern topography along the full Andean margin at the present day. The key differences arise in the timing and progression of the main uplift phase. Our model indicates a major uplift of the Altiplano and Puna plateaus beginning around 40 Ma, accelerating between 30–15 Ma, and stabilising near ~4,000 m by the Middle Miocene (Figure 4c–d). This trajectory aligns well with independent geochemical paleoelevation estimates. In contrast, Boschman (2021) reconstructs generally lower Paleogene elevations in the Western Cordillera and infers a delayed, more abrupt uplift after ~10 Ma for much of the Central Andes. Importantly, the onset of rapid uplift in our model at ~35–40 Ma coincides with a major shift in subduction-zone dynamics (Figure 4e). The peak in subduction-volume rate at 15 Ma (~0.08 km^3/yr) marks the transition into a regime capable of sustaining high elevations (Figure 4b), underscoring the coupling between tectonic forcing and surface uplift.

3.4 Evolution of the Jurassic-Cretaceous EAM

The modelled paleoelevation history of the EAM reveals episodic mountain building characterised by three distinct phases of elevated topography (Figure 5b). The Late Jurassic phase (~160–140 Ma) shows a broad, extensive plateau spanning ~500–800 km in width with mean elevations reaching 3,000–4,000 m across all three reconstruction methods (STN, Zhou++, Li++; Figure 5a, bottom-right panel). This wide, high plateau is defined by a major peak in sedimentary zircons at ~150 Ma that coincides with a dominant metamorphic zircon peak (Figure 5c), indicating synchronous rapid erosion, sediment recycling, and deep-crustal metamorphism during significant crustal-thickening events—consistent with the elevated paleotopography modelled for this interval.

The Early Cretaceous phase (~140–110 Ma) records a pronounced collapse of the Late Jurassic plateau. Modelled elevations decline to ~1,000–2,000 m mean elevation (Figure 5a–b). Paleotopographic maps show low-elevation zones characteristic of extensional systems (Figure 5a, bottom left panel), with basin development across the continental margin. Zircon populations display elevated igneous zircon densities and a strong metamorphic zircon maximum at ~120 Ma (Figure 5c), indicating ongoing thermal flux and magmatic activity despite the overall extensional regime associated with Paleo-Pacific Plate rollback.

The mid-Cretaceous phase (~110–80 Ma) shows renewed high elevations reaching ~2,500 m between 105 and 95 Ma (Figure 5b), but this phase displays a distinct topographic architecture compared to the Late Jurassic. Rather than a broad, wide plateau, the mid-Cretaceous phase forms a narrow, linear coastal mountain range extending >1,000 km along the continental margin (Figure 5a, lower left panel), with a width of ~200–400 km as shown in the paleotopographic reconstruction. This coastal range is characterised by steeper relief and a more restricted spatial extent than the Jurassic plateau. The zircon record shows sustained igneous zircon densities and elevated metamorphic zircon activity (Figure 5c), reflecting the renewal of crustal thickening and magmatic flux.

A final Late Cretaceous phase (~80–60 Ma) culminates in a major magmatic flare-up, recorded by the highest igneous zircon density peak at ~75 Ma (Figure 5c)—the most voluminous magmatic episode along the margin. This interval corresponds to the last period of high elevations visible in all three reconstructions (Figure 5b). Immediately after ~75 Ma, all zircon populations—igneous, metamorphic, and sedimentary—decline sharply (Figure 5c), paralleling the modelled decrease in mean elevation to ~1,500–2,000 m after ~60 Ma and the downward trends in the Zhou++ and Li++ crustal-thickness reconstructions. By the Early Cenozoic, the paleotopographic maps show collapse of the coastal mountains to low-elevation configurations (Figure 5a), with mean elevations declining to ~500–1,000 m or lower.

4. Discussion

4.1 A Physics-driven Framework for Active Margin Paleotopography Reconstruction

The STN presented here provides a generalisable, physics-driven framework for reconstructing the paleotopography of active margins over geological timescales. It leverages the established principle that long-term surface elevation at active margins is strongly influenced by the interplay between plate kinematics (e.g., trench migration, subduction flux),

mantle dynamics (e.g., upper mantle temperature, flow fields), and climate-driven surface processes (e.g., time spent in humid belt) (29, 52).

The model's ability to explain 92% of modern elevation variance (with an RMSE of 576 m) and its consistent performance across geographically and tectonically diverse withheld regions (Figure 2) demonstrates its high predictive skill. Crucially, its application to the Cenozoic Central Andes—a well-studied, long-lived orogen—yields an uplift history consistent with independent geochemical proxies and geological syntheses (Figure 4). The model successfully predicts the 4 km uplift since the Oligocene, temporally correlating the onset of rapid elevation gain with a major transition in subduction dynamics, specifically the shift from low subduction volume rate (0.03 km^3/yr) to peak subduction flux (0.08 km^3/yr at 15 Ma) (Figure 4c-e). This strong correlation underscores that changes in subduction zone parameters are primary drivers of active margin topography.

The STN approach moves beyond traditional lithofacies-based methods (53), which are often qualitative and difficult to reproduce, by providing a quantifiable, spatially continuous, and time-dependent reconstruction informed by fundamental geodynamic processes and geological models. The results show that deep learning, when constrained by Earth science principles, can effectively convert disparate and heterogeneous data (plate motion, mantle models) into high-resolution paleotopographic maps, offering a powerful new route for hypothesis testing in deep-time Earth system science.

4.2 Sources of Deep–Time Uncertainty

4.2.1 Uncertainties in Input Parameters

Plate kinematics remain imperfectly constrained even for the present day, with absolute reference frame choices affecting plate velocities by several centimetres per year and hence influencing derived quantities such as trench migration rate (54). While the STN uses normalised inputs to reduce sensitivity to absolute values and prevent issues like exploding and vanishing gradients (55), it cannot eliminate the impact of underlying uncertainties in tectonic trends. In deep time, plate reconstructions may diverge markedly in their estimates of trench migration and subduction histories. For instance, some models depict a westward-migrating Farallon trench during the Early Cretaceous (28), whereas others, like (56), suggest a more slow-to-stationary configuration when compared in the same mantle reference frame. Model-based sensitivity analyses show that plausible differences in trench migration rate and subduction flux between reconstructions can propagate into kilometre-scale differences in predicted elevation in flux-dominated systems such as the Andes (57). Additional uncertainty arises because convergence rates and slab thickness for now-subducted oceanic plates must be inferred from synthetic age grids and incomplete seafloor records. Consequently, some regional misfits between model and proxies reflect uncertainties in the underlying reconstructions rather than limitations of the learned topography–tectonics relationship itself.

Additionally, our results are based on a single global plate reconstruction model, and alternative reconstructions may yield somewhat different uplift histories. Ensemble approaches (using multiple plate reconstructions and mantle models) would quantify this uncertainty range and should be taken into consideration for future studies. However, the general stability of the global MAE over time, despite large fluctuations in proxy data density

(Figure 3b), strengthens the argument for the model's consistency. The STN therefore offers a valuable, high-resolution baseline against which local proxy-based estimates can be compared and refined, while recognising that its reconstructions represent one internally consistent scenario among several plausible alternatives.

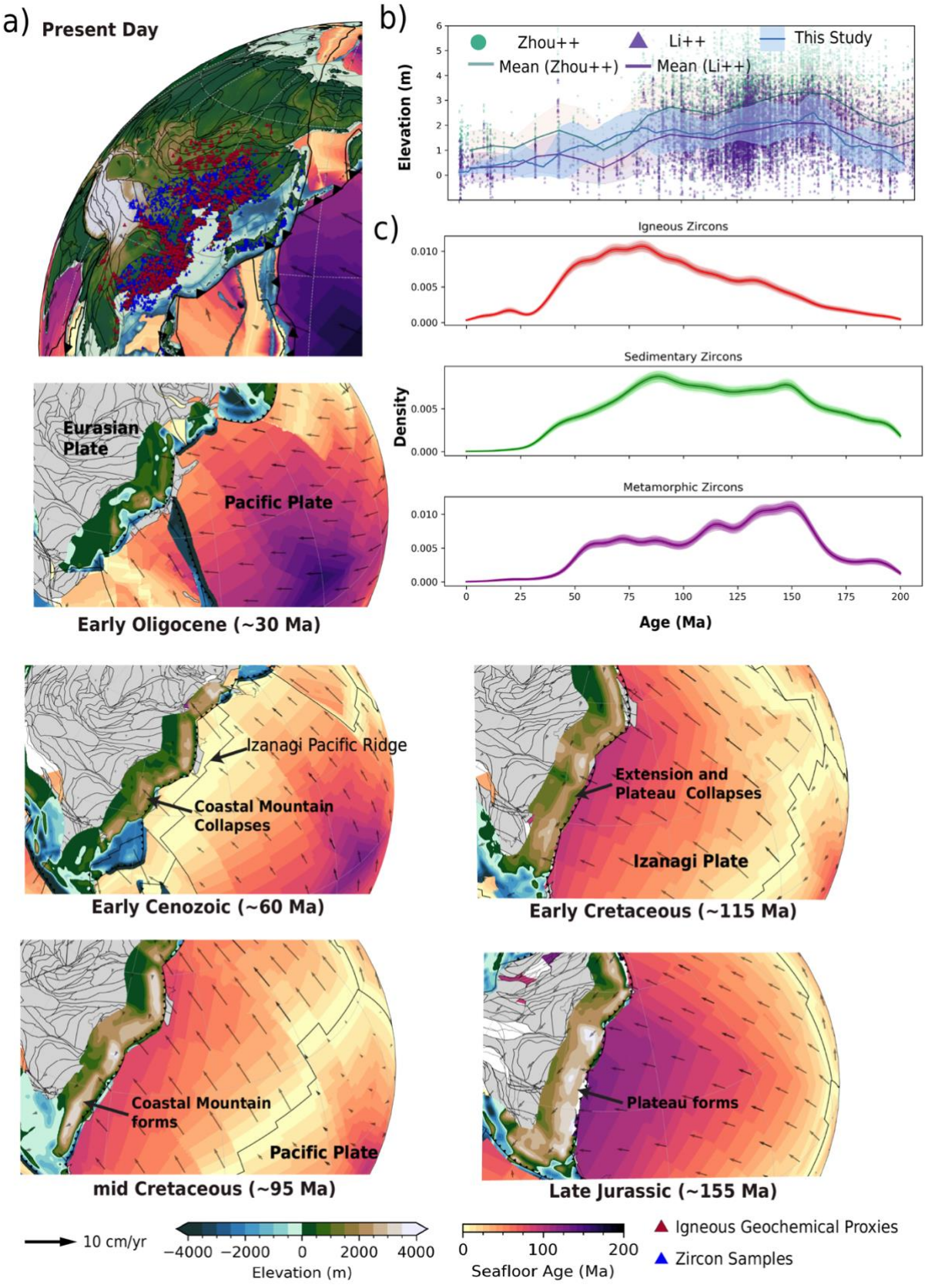

Fig. 5. Paleotopographic and Geodynamic Evolution of the Lost East Asian Margin (EAM).

(a) Present-day topography and paleogeographic reconstructions showing the episodic evolution of the EAM from the Late Jurassic to Present. The top panel shows the present-day configuration with plate boundaries and major tectonic features. Lower panels show reconstructed paleotopography at key time slices: Late Jurassic (~155 Ma) showing plateau formation, Early Cretaceous (~115 Ma) showing extension and plateau collapse, mid-Cretaceous (~95 Ma) showing renewed coastal mountain formation and Early Cenozoic (~60 Ma) showing coastal mountain collapse and the Izanagi Plate.

(b) Reconstructed Mean Elevation. Modelled mean elevation (This Study) is compared with geochemical ratio-based paleoelevation estimates (Zhou++, Li++). All three methods converge on a similar first-order pattern: high elevations (commonly >2,500 m) during the Late Jurassic (~160–140 Ma), a pronounced decline during the Early Cretaceous rifting phase (~140–110 Ma) marking plateau collapse, renewed high elevations during the mid-Cretaceous (~110–80 Ma) coastal mountain phase reaching ~2,500 m, and a final collapse after ~60 Ma. This episodic pattern reflects discontinuous orogenesis rather than sustained Andean-style Mountain building, emphasising that the EAM experienced alternating phases of uplift and extensional collapse.

(c) Kernel density estimates of zircon U–Pb ages from the EAM, providing temporal constraints on magmatic, metamorphic, and erosional processes.

4.2.2 Uncertainties from Paleoelevation Proxies

Geochemical proxies used to infer paleoelevation are typically calibrated in modern subduction settings, and applying these relationships to times or regions lacking clear evidence of similar tectonic regimes may violate key assumptions and generate discrepancies with model predictions. Despite these challenges, the relatively high spatial density of arc-related geochemical datasets (37) enables meaningful, first-order model validation along Mesozoic active margins. For most active margins, model–proxy mismatches fall within ±1,515 m, indicating that the framework captures the primary patterns of paleotopographic change despite proxy and reconstruction uncertainties. Residual mismatches may also reflect paleogeographic uncertainties, including the location and polarity of ancient subduction zones and unresolved plate boundaries (58).

For the EAM specifically, the Zhou++ and Li++ reconstructions differ in absolute elevation estimates due to variations in empirical calibration and underlying assumptions, yet both replicate the same first-order uplift and collapse trends recovered by the STN. This convergence across two independent proxy-based methods increases confidence in the reconstructed paleotopography, while the ~1–2 km spread between them provides a realistic uncertainty envelope for elevation magnitude. Part of this spread likely reflects regional complexities: geochemical ratios calibrated in modern arcs may conflate crustal thickness changes with variations in mantle source or slab processes such as breakoff (39, 59), and the age and thickness of the now subducted Izanagi plate are synthetically reconstructed, so differences in plate age directly affect inferred subduction flux and thus predicted elevation.

4.3 Reconstructing the Topographic Evolution of the EAM

Our reconstructions reveal that the EAM underwent three major phases of orogenic growth and collapse during the Late Jurassic–Cretaceous, each driven by distinct plate kinematics and mantle dynamics processes and expressed in zircon geochronology, crustal-thickness proxies, and topographic evolution.

Late Jurassic (~160–145 Ma): Growth of a Broad, High-Elevation Plateau
Our reconstruction shows that the EAM developed a broad, extensive plateau during the Late Jurassic, with a lateral width of ~500–800 km and mean elevations reaching ~3,000–4,000 m (Figure 5a–b). This time corresponds to the largest sedimentary zircon peak at ~150 Ma, synchronous with a major metamorphic zircon peak (Figure 5c), indicating rapid erosion, sediment recycling, and deep-crustal metamorphism associated with significant crustal thickening (43, 44, 47, 48). This phase of plateau construction is recorded by voluminous monzogranite magmatism derived from partial melting of thickened lower crust and by strongly negative εHf(t) values in zircons, indicating reworking of ancient continental basement (18, 19, 60). The plateau formed under an oblique or low-angle subduction regime of the Izanagi (Paleo-Pacific) Plate, which transmitted compressive stresses far inland and generated a wide orogenic system analogous to the modern Altiplano (19, 27). Sedimentary provenance and paleocurrent data indicate predominantly westward sediment transport, consistent with erosion from an elevated coastal source region (61–63). Together, the geochemical, structural, and sedimentary evidence support the existence of a continent-scale "Jurassic East Asian Plateau."

Early Cretaceous (~145–110 Ma): Plateau Collapse and Widespread Extension
The Early Cretaceous marks a profound tectonic transition, with the collapse of the Jurassic plateau and the onset of regionally extensive extension. All reconstructions show a sharp decline in mean elevation to ~1,000–2,000 m, accompanied by the development of low-elevation zones (Figure 5a, bottom left panel). This period is characterised by emplacement of A-type granites, widespread bimodal volcanism, and the formation of major rift basins, including the Songliao Basin (19, 64, 65). Zircon U–Pb ages and thermochronology document rapid exhumation of metamorphic core complexes, crustal thinning, and kilometre-scale accumulation of syn-rift sediments, including alluvial fans and evaporites (18, 64). This extensional regime reflects rollback of the subducting Izanagi Plate, gravitational collapse of previously overthickened lithosphere, and potential lithospheric delamination (27, 65, 66). Although paleoelevation reconstructions retain a "high" signal during this interval, the structural reality was a Basin-and-Range-style landscape comprising fault-bounded basins and diminished mean elevations. The Early Cretaceous, therefore, represents a transition from plateau stability to dynamic extensional collapse.

Mid-Cretaceous (~110–80 Ma): Rejuvenation of Coastal Orogeny
Following this collapse, the mid-Cretaceous (~110–80 Ma) marks a renewed phase of orogeny, albeit with a fundamentally different topographic architecture from the Late Jurassic. Mean elevations rise to ~2,500 m between ~105 and 95 Ma, but instead of forming a broad plateau, the margin developed a narrow, linear coastal mountain range extending more than 1,000 km along strike and only ~200–400 km across. Independent geological and geochemical constraints corroborate this topographic reorganisation: crustal thicknesses of 50–55 km imply paleoelevations >2.5 km (20); clumped-isotope paleoaltimetry from the eastern North China Craton indicates elevations >2 km by ~80 Ma and up to 2.8–4.1 km during the Early–mid Cretaceous (41, 67); and foreland molasse accumulation suggests elevations of 3.5–4.0 km spanning several hundred kilometres along the margin (68). Sustained igneous and metamorphic zircon activity during this interval reflects renewed

crustal thickening and magmatic flux. This coastal orogeny was driven by high subduction flux (~0.13 km³/yr) and fast convergence rates (>10 cm/yr), producing an Andean-style mountain belt with steep relief.

Late Cretaceous–Early Cenozoic (~80–60 Ma): Magmatic Flare-Up and Terminal Collapse of the Orogen

The final tectonic phase occurs in the Late Cretaceous (~80–60 Ma), culminating in a major magmatic flare-up at ~75 Ma that represents the most voluminous magmatic event along the margin during the Mesozoic. This interval corresponds to the last expression of high elevations across all reconstruction methods, after which all zircon populations—igneous, metamorphic, and sedimentary—decline sharply. Mean elevations fall to ~1,500–2,000 m after ~60 Ma and drop to <1,000 m by the Early Cenozoic. Paleotopographic maps show the collapse of the coastal mountains into a low-relief passive-margin configuration. This decline reflects the subduction of very young (<30 Myr), thermally weak Izanagi lithosphere, rapid trench retreat (up to –2 cm/yr), and widespread backarc extension that initiated the opening of marginal basins such as the Japan Sea. By the Early Cenozoic, the tectonic regime shifted from compressional shortening to pervasive extension, marking the end of Mesozoic orogenic activity and the establishment of the modern low-relief EAM.

The East Asian orogen differs from better-known systems like the Andes or Himalaya not only in timing and morphology, but in preservation state. Much of its original topography has since collapsed or been reworked, making it "lost" in the geological record, yet recoverable through integrated modelling and proxy synthesis. The STN results demonstrate that, where the plate boundary record is sufficiently well constrained to define a subduction zone and its kinematic history, physics-grounded machine learning can recover plausible paleoelevation histories even in regions where direct paleotopographic proxies are sparse or absent. More generally, the EAM example illustrates how the geological record of plate boundary processes—subduction, ridge interaction, slab rollback—extends far beyond the traditional paleoelevation proxy record, and how integrating these kinematic constraints with data driven paleotopography provides a powerful route to identifying other "lost" orogens in Earth's tectonic past.

4.4 Model Limitations: Caveats, and Future Directions

Although the STN provides a robust framework for reconstructing paleotopography across subduction-dominated margins, several limitations arise from the scale, nature, and availability of its inputs. The model is designed primarily for active margin systems, where long-term surface elevation is governed by subduction processes. It does not explicitly incorporate the physics of intracontinental deformation (e.g., the Laramide orogeny) or large-scale continental collision (e.g., Himalaya–Tibet), even though such topographies are present in the modern training data. As a result, predictive skill is maximised in subduction settings—the intended scope of this study—while performance in collisional or intracontinental regions remains less certain. Dynamic mantle forces, variations in viscosity structure, slab behaviour, and hydration state introduce additional uncertainty (29, 69–71), with potential time lags between crustal thickening and surface uplift (72–74). While the STN may implicitly encode some of these effects, resolving their mechanistic contributions requires integration with forward geodynamic modelling. Trained on modern topography, the model is well-suited for Phanerozoic reconstructions but less accurate for Proterozoic settings, where tectonic regimes, lithospheric strength, and plate interactions differed fundamentally (75, 76). Finally,

while deep learning provides strong predictive performance, it offers limited mechanistic interpretability compared with more transparent models such as explainable boosting machines (57). Future efforts should explore hybrid, physics-informed architectures that couple deep learning with geodynamic forward models and explainable AI approaches. Expanding geological and geophysical datasets—particularly from tectonically complex or under-sampled regions—will further constrain the model and enhance its physical realism.

The STN framework establishes a scalable, open-source foundation for integrating diverse Earth science datasets to reconstruct paleotopography. Future developments that incorporate continental-collision inputs, multi-model ensembles, higher-resolution data, and hybrid explainable architectures will significantly extend its applicability and allow quantitative testing of hypotheses linking tectonics, crustal evolution, climate, and the biosphere across deep time.

5. Conclusion

The STN demonstrates that a physically ground set of plate-kinematic, mantle-flow, and paleoclimate-informed variables is sufficient to reconstruct active-margin paleotopography over the past 200 Myr. Trained only on present-day topography, the STN explains 92% of modern elevation variance and reproduces first-order relief patterns across tectonically diverse margins, indicating that long-term surface elevation is tightly coupled to subduction flux, trench migration, and upper-mantle structure. Applied through time, the model captures the ~ 4 km Cenozoic uplift of the Central Andes and ties its main acceleration to a transition to high subduction flux, consistent with independent paleoelevation and geochemical constraints. In East Asia, the STN recovers a Jurassic–Cretaceous Cordilleran-style orogen with mean elevations commonly exceeding 2.5–3 km, whose multiphase uplift and subsequent Cenozoic collapse align with crustal-thickness-based reconstructions and zircon records of magmatic flare-ups and crustal thickening. These results show that physics-grounded machine learning can recover "lost" mountain belts and deliver reproducible, quantitative paleotopographic histories, providing a foundation for future work linking subduction dynamics to past climate, biodiversity, and mineral systems.

Data Availability

All code, hyperparameters, and training scripts are available at https://github.com/singhsatyampratap/pyDTDM/tree/main/Workflows/ActiveMarginPaleotopography. Present-day elevation data (ETOPO1) are publicly available from NOAA (https://www.ncei.noaa.gov/products/etopo-global-relief-model). Plate kinematic reconstructions are from Merdith et al. (2021) and CitcomS mantle convection model outputs will be archived at Zenodo. Processed input datasets, trained model weights, and all paleotopographic predictions will be archived at Zenodo (https://zenodo.org) with a persistent DOI upon publication.

Acknowledgement

SPS, MS, SZ and NMW gratefully acknowledge funding from the BHP STELLAR Industry Collaboration. Additional support was received from the Australian Research Council through DP200100966 (MS), DE210100084 (SZ) and IE230100098 (NMW). JPZ received support from the Deep Earth Probe and Mineral Resources Exploration-National Science and Technology Major Project (No.2025ZD1004904). Development of pyGPlates and GPlates was enabled by AuScope, funded under the Australian National Collaborative Research Infrastructure System (NCRIS). The authors also thank the Kalpa development team (**https://kalpa.bighistory.in/**) for providing tools used to render and visualise 3D datasets.

Author Competing Interest

The authors declare that they have no known competing financial interests or personal relationships that could have appeared to influence the work reported in this paper.

References

1. A. Antonelli, *et al.*, Geological and climatic influences on mountain biodiversity. *Nature Geosci* **11**, 718–725 (2018).

2. B. H. Boggiani, T. Salles, C. Mallard, N. Atwood, The roles of surface processes on porphyry copper deposits preservation. *EGUsphere* 1–31 (2024). https://doi.org/10.5194/egusphere-2024-1868.

3. F. A. Macdonald, N. L. Swanson-Hysell, Y. Park, L. Lisiecki, O. Jagoutz, Arc-continent collisions in the tropics set Earth's climate state. *Science* **364**, 181–184 (2019).

4. B. Bookhagen, M. R. Strecker, Orographic barriers, high-resolution TRMM rainfall, and relief variations along the eastern Andes. *Geophysical Research Letters* **35** (2008).

5. R. Garreaud, M. Vuille, A. C. Clement, The climate of the Altiplano: observed current conditions and mechanisms of past changes. *Palaeogeography, Palaeoclimatology, Palaeoecology* **194**, 5–22 (2003).

6. J. Houston, A. J. Hartley, The central Andean west-slope rainshadow and its potential contribution to the origin of hyper-aridity in the Atacama Desert. *International Journal of Climatology* **23**, 1453–1464 (2003).

7. J.-W. Park, I. H. Campbell, M. Chiaradia, H. Hao, C.-T. Lee, Crustal magmatic controls on the formation of porphyry copper deposits. *Nat Rev Earth Environ* **2**, 542–557 (2021).

8. S. Botsyun, *et al.*, Opportunities and Challenges for Paleoaltimetry in "Small" Orogens: Insights From the European Alps. *Geophysical Research Letters* **47**, e2019GL086046 (2020).

9. T. A. Ehlers, C. J. Poulsen, Influence of Andean uplift on climate and paleoaltimetry estimates. *Earth and Planetary Science Letters* **281**, 238–248 (2009).

10. C. Garzione, J. Quade, P. Decelles, N. English, Predicting paleoelevation of Tibet and the Himalaya from N 18 O vs. altitude gradients in meteoric water across the Nepal Himalaya. *Earth and Planetary Science Letters* **183**, 215–229 (2000).

11. F. Poblete, *et al.*, Towards interactive global paleogeographic maps, new reconstructions at 60, 40 and 20 Ma. *Earth-Science Reviews* **214**, 103508 (2021).

12. D. B. Rowley, C. N. Garzione, Stable Isotope-Based Paleoaltimetry. (2007).

13. D. B. Rowley, R. T. Pierrehumbert, B. S. Currie, A new approach to stable isotope-based paleoaltimetry: implications for paleoaltimetry and paleohypsometry of the High Himalaya since the Late Miocene. *Earth and Planetary Science Letters* **188**, 253–268 (2001).

14. J. A. Badgeley, E. J. Steig, M. Dütsch, Uncertainty in Reconstructing Paleo-Elevation of the Antarctic Ice Sheet From Temperature-Sensitive Ice Core Records. *Geophysical Research Letters* **49**, e2022GL100334 (2022).

15. A. J. Hartley, T. Sempere, G. Wörner, A comment on "Rapid late Miocene rise of the Bolivian Altiplano: Evidence for removal of mantle lithosphere" by C.N. Garzione et al. [Earth Planet. Sci. Lett. 241 (2006) 543–556]. *Earth and Planetary Science Letters* **259**, 625–629 (2007).

16. A. Mulch, Stable isotope paleoaltimetry and the evolution of landscapes and life. *Earth and Planetary Science Letters* **433**, 180–191 (2016).

17. Y. Suo, *et al.*, Eastward tectonic migration and transition of the Jurassic-Cretaceous Andean-type continental margin along Southeast China. *Earth-Science Reviews* (2019). https://doi.org/10.1016/j.earscirev.2019.102884.

18. H. Qiu, W. Lin, Y. Chen, M. Faure, Jurassic–Early Cretaceous tectonic evolution of the North China Craton and Yanshanian intracontinental orogeny in East Asia: New insights from a general review of stratigraphy, structures, and magmatism. *Earth-Science Reviews* (2023). https://doi.org/10.1016/j.earscirev.2023.104320.

19. X. Zhang, W. Xu, C.-Y. Sun, F. Wang, Y. Li, Tectonic nature of the NE Asian continental margin during the Late Jurassic–Early Cretaceous: constraints from the geochronology and geochemistry of igneous rocks in the NE North China Craton. *International Geology Review* **62**, 1949–1970 (2019).

20. J. Li, *et al.*, Cretaceous coastal mountain building and potential impacts on climate change in East Asia. *Sci Adv* **10**, eads0587 (2024).

21. C. Wu, *et al.*, Cretaceous mountain building processes triggered the aridification and drainage evolution in east Asia. *Geological Society of America Bulletin* (2023). https://doi.org/10.1130/b36763.1.

22. C. Wu, J. P. Rodríguez-López, M. Santosh, Plateau archives of lithosphere dynamics, cryosphere and paleoclimate: The formation of Cretaceous desert basins in east Asia. *Geoscience Frontiers* (2022). https://doi.org/10.1016/j.gsf.2022.101454.

23. F. Zhang, Y. Dilek, H. Chen, S. Yang, Q. Meng, Structural architecture and stratigraphic record of Late Mesozoic sedimentary basins in NE China: Tectonic archives of the Late Cretaceous continental margin evolution in East Asia. *Earth-Science Reviews* **171**, 598–620 (2017).

24. Y. Tian, Y. Qin, Z. Zhang, P. Zhang, Cretaceous-Cenozoic Landscape Evolution of Southern East Asia: New Constraints From Sediment Provenances. *Tectonics* **44** (2025).

25. L. Dmitrienko, *et al.*, Meso-Cenozoic Evolution of Earth Surface System under the East Asian Tectonic Superconvergence. *Acta Geologica Sinica - English Edition* **92** (2018).

26. Z.-H. Li, *et al.*, Dynamics of convergent plate margins: Progress and challenge. *Sci. China Earth Sci.* (2025). https://doi.org/10.1007/s11430-024-1513-5.

27. L. Liu, *et al.*, East Asian lithospheric evolution dictated by multistage Mesozoic flat-slab subduction. *Earth-Science Reviews* **217**, 103621 (2021).

28. R. D. Müller, *et al.*, A Global Plate Model Including Lithospheric Deformation Along Major Rifts and Orogens Since the Triassic. *Tectonics* **38**, 1884–1907 (2019).

29. S. G. Wolf, R. S. Huismans, J. Braun, X. Yuan, Topography of mountain belts controlled by rheology and surface processes | Nature. (2022). Available at: https://www.nature.com/articles/s41586-022-04700-6 [Accessed 17 December 2022].

30. Q. Yuan, Numerical Modeling of Melting Processes During Slab Break-off: Insights Into Tectonic Setting for Massif-Type Anorthosites. *Lithosphere* **2024**, lithosphere_2023_344 (2024).

31. D. J. Bower, M. Gurnis, N. Flament, Assimilating lithosphere and slab history in 4-D Earth models. *Physics of the Earth and Planetary Interiors* **238**, 8–22 (2015).

32. A. S. Merdith, *et al.*, Extending full-plate tectonic models into deep time: Linking the Neoproterozoic and the Phanerozoic. *Earth-Science Reviews* **214**, 103477 (2021).

33. S. Zhong, M. T. Zuber, L. Moresi, M. Gurnis, Role of temperature-dependent viscosity and surface plates in spherical shell models of mantle convection. *Journal of Geophysical Research: Solid Earth* **105**, 11063–11082 (2000).

34. E. Tan, E. Choi, P. Thoutireddy, M. Gurnis, M. Aivazis, GeoFramework: Coupling multiple models of mantle convection within a computational framework. *Geochemistry, Geophysics, Geosystems* **7** (2006).

35. S. Zhong, M. Gurnis, Mantle Convection with Plates and Mobile, Faulted Plate Margins. *Science* **267**, 838–843 (1995).

36. C. Amante, B. W. Eakins, ETOPO1 arc-minute global relief model : procedures, data sources and analysis. (2009).

37. M. Gard, D. Hasterok, J. A. Halpin, Global whole-rock geochemical database compilation. *Earth System Science Data* **11**, 1553–1566 (2019).

38. B. Liu, S. Williams, M. Seton, G. Zhao, Mapping paleoelevations along active continental margins with igneous geochemistry: A case study from South America. *Gondwana Research* **134**, 285–297 (2024).

39. P. Luffi, M. N. Ducea, Chemical Mohometry: Assessing Crustal Thickness of Ancient Orogens Using Geochemical and Isotopic Data. *Reviews of Geophysics* **60**, e2021RG000753 (2022).

40. J. Zhou, *et al.*, Machine Learning and Big Data Mining Reveal Earth's Deep Time Crustal Thickness and Tectonic Evolution: A New Chemical Mohometry Approach. *Journal of Geophysical Research: Solid Earth* **130**, e2024JB030404 (2025).

41. L. Zhang, Y. Yin, C. Wang, High-Altitude and Cold Habitat for the Early Cretaceous Feathered Dinosaurs at Sihetun, Western Liaoning, China. *Geophysical Research Letters* **48**, e2021GL094370 (2021).

42. Y. Wu, X. Fang, J. Ji, A global zircon U–Th–Pb geochronological database. *Earth System Science Data* **15**, 5171–5181 (2023).

43. K. Condie, R. Aster, Episodic zircon age spectra of orogenic granitoids: The supercontinent connection and continental growth. *Precambrian Research* **180**, 227–236 (2010).

44. A. Fornelli, V. Festa, F. Micheletti, R. Spiess, F. Tursi, Building an Orogen: Review of U-Pb Zircon Ages from the Calabria–Peloritani Terrane to Constrain the Timing of the Southern Variscan Belt. *Minerals* (2020). https://doi.org/10.3390/min10110944.

45. P. Vermeesch, On the visualisation of detrital age distributions. *Chemical Geology* **312**, 190–194 (2012).

46. M. Pereira, C. Gama, Revisiting the Intermediate Sediment Repository Concept Applied to the Provenance of Zircon. *Minerals* (2021). https://doi.org/10.3390/min11030233.

47. Q. Gu, *et al.*, Using detrital zircon to reconstruct Neoproterozoic crustal thickness variation in the northwestern margin of the Yangtze Block. *Scientific Reports* **15** (2025).

48. M. Tang, W. Ji, X. Chu, A. Wu, C. Chen, Reconstructing crustal thickness evolution from europium anomalies in detrital zircons. *Geology* (2020). https://doi.org/10.1130/geol.s.12869660.

49. J. Richter-Krautz, M. Hofmann, J. Zieger, U. Linnemann, A. Kleber, Zircon provenance of Quaternary cover beds using U–Pb dating: Regional differences in the Southwestern USA. *Earth Surface Processes and Landforms* **46**, 968–989 (2021).

50. L. Liu, *et al.*, The role of oceanic plateau subduction in the Laramide orogeny. *Nature Geoscience* **3**, 353–357 (2010).

51. L. M. Boschman, Andean mountain building since the Late Cretaceous: A paleoelevation reconstruction. *Earth-Science Reviews* **220**, 103640 (2021).

52. J.-D. Champagnac, P. Molnar, C. Sue, F. Herman, Tectonics, climate, and mountain topography. *Journal of Geophysical Research: Solid Earth* **117** (2012).

53. C. R. Scotese, An Atlas of Phanerozoic Paleogeographic Maps: The Seas Come In and the Seas Go Out | Annual Review of Earth and Planetary Sciences. (2021). Available at: https://www.annualreviews.org/doi/abs/10.1146/annurev-earth-081320-064052 [Accessed 17 December 2022].

54. W. P. Schellart, Overriding plate shortening and extension above subduction zones: A parametric study to explain formation of the Andes Mountains. *GSA Bulletin* **120**, 1441–1454 (2008).

55. I. Goodfellow, Y. Bengio, A. Courville, *Deep Learning* (MIT Press, 2016).

56. S. Zahirovic, *et al.*, Subduction and carbonate platform interactions. *Geoscience Data Journal* **9**, 371–383 (2022).

57. S. P. Singh, M. Seton, S. Zahirovic, N. Wright, *Reconstructing the Topographic Evolution of Active Margins Since the Devonian Using Artificial Intelligence* (2025).

58. M. Seton, S. E. Williams, M. Domeier, A. S. Collins, K. Sigloch, Deconstructing plate tectonic reconstructions. *Nat Rev Earth Environ* **4**, 185–204 (2023).

59. M. J. Farner, C.-T. A. Lee, Effects of crustal thickness on magmatic differentiation in subduction zone volcanism: A global study. *Earth and Planetary Science Letters* **470**, 96–107 (2017).

60. S. Dong, *et al.*, Late Jurassic–Early Cretaceous continental convergence and intracontinental orogenesis in East Asia: A synthesis of the Yanshan Revolution. *Journal of Asian Earth Sciences* **114**, 750–770 (2015).

61. J. Yuan, *et al.*, Mesozoic tectonic evolution of the northeastern margin of the North China Craton: Insight from the mountain-basin system. *Geological Society of America Bulletin* (2025). https://doi.org/10.1130/b38348.1.

62. Z. Li, S. Dong, H. Qu, Timing of the initiation of the Jurassic Yanshan movement on the North China Craton: evidence from sedimentary cycles, heavy minerals, geochemistry, and zircon U–Pb geochronology. *International Geology Review* **56**, 288–312 (2014).

63. H. Huang, *et al.*, Triassic-Jurassic evolution of the Dabashan Foreland Basin: Detrital zircon perspectives on the tectonic amalgamation of the South China and North China blocks. *Palaeogeography, Palaeoclimatology, Palaeoecology* (2024). https://doi.org/10.1016/j.palaeo.2024.112300.

64. K. Qi, Z. Ren, J. Cui, Qian, G. Xing, Zircon U–Pb Geochronology and Hf Isotope, Whole-Rock Geochemistry and Sr–Nd Isotopes of the Late Jurassic–Early Cretaceous Intrusive Rocks From North Shanxi Province: Insight on Petrogenesis and Magmatic Process in the Central North China Craton. *Geological Journal* (2025). https://doi.org/10.1002/gj.5145.

65. Z. Guo, Y. Yang, Late Mesozoic basin evolution in NE China and its surrounding areas, mechanisms of the continental-scale extensional regime in East Asia during the Late

Jurassic–Early Cretaceous. *Earth-Science Reviews* (2023). https://doi.org/10.1016/j.earscirev.2023.104418.

66. Y. Zhang, E. Qiu, S. Dong, J. Li, W. Shi, Late Mesozoic intracontinental deformation and magmatism in North and NE China in response to multi-plate convergence in NE Asia: An overview and new view. *Tectonophysics* (2022). https://doi.org/10.1016/j.tecto.2022.229377.

67. L. Zhang, *et al.*, High elevation of Jiaolai Basin during the Late Cretaceous: Implication for the coastal mountains along the East Asian margin. *Earth and Planetary Science Letters* **456**, 112–123 (2016).

68. P. Chen, "Paleoenvironmental changes during the Cretaceous in eastern China" in *Developments in Palaeontology and Stratigraphy*, Cretaceous Environments of Asia., H. Okada, N. J. Mateer, Eds. (Elsevier, 2000), pp. 81–90.

69. F. Chen, D. R. Davies, S. Goes, L. Suchoy, S. C. Kramer, How Slab Age and Width Combine to Dictate the Dynamics and Evolution of Subduction Systems: A 3-D Spherical Study. *Geochemistry, Geophysics, Geosystems* **23**, e2022GC010597 (2022).

70. W. P. Schellart, Andean mountain building and magmatic arc migration driven by subduction-induced whole mantle flow. *Nat Commun* **8**, 2010 (2017).

71. K. Xue, W. P. Schellart, V. Strak, Effect of Plate Length on Subduction Kinematics and Slab Geometry: Insights From Buoyancy-Driven Analog Subduction Models. *Journal of Geophysical Research: Solid Earth* **125**, e2020JB020514 (2020).

72. N. Flament, M. Gurnis, R. D. Müller, A review of observations and models of dynamic topography. *Lithosphere* **5**, 189–210 (2013).

73. R. F. Livaccari, Role of crustal thickening and extensional collapse in the tectonic evolution of the Sevier-Laramide orogeny, western United States. *Geology* **19**, 1104–1107 (1991).

74. M. Mamani, A. Tassara, G. Wörner, Composition and structural control of crustal domains in the central Andes. *Geochemistry, Geophysics, Geosystems* **9** (2008).

75. N. Flament, N. Coltice, P. F. Rey, A case for late-Archaean continental emergence from thermal evolution models and hypsometry. *Earth and Planetary Science Letters* **275**, 326–336 (2008).

76. P. F. Rey, N. Coltice, Neoarchean lithospheric strengthening and the coupling of Earth's geochemical reservoirs. *Geology* **36**, 635–638 (2008).

Chapter 5

Discussion

Deep-time reconstruction of the Earth's surface is an interdisciplinary challenge that necessitates the integration of geological data and the intricate physics of geodynamic processes over vast spatial expanses and multi-Myr timescales. To overcome the restrictions of proxy-constrained models, this thesis proposes a set of computational procedures and machine learning frameworks built with reproducibility, scalability, and physically grounded drivers at their core. The following discussion critically synthesizes the key innovations and examines their larger implications for understanding Earth's history, along with the inherent limitations of the approaches presented.

5.1 Keys Innovations and Broader Implications

The conceptual and computational advancements provided in this thesis substantially alter the field of deep-time paleotopography reconstruction. Central to this progress is the creation of an integrated ecosystem of software and computational frameworks that combine the three key pillars of solid Earth system science: quantitative plate tectonic reconstructions, physically grounded geodynamic simulations, and integrated data analysis. By combining these various methodologies, the work addresses the limitations of previous models that relied on qualitative heuristics or fragmentary proxies. The newly created frameworks are scalable and capable of identifying correlations within heterogeneous, multi-gigabyte datasets. These tools provide a quantitative route for paleotopographic reconstruction where qualitative approaches may fail, while reducing the computational burdens associated with process-driven numerical simulations. Within this context, the following subsections describe specific advances in deformable plate tectonic modelling, deep-time geoscience data mining, open-source machine learning platforms, and physics-integrated deep learning. Each component works towards improving the reproducibility and spatial scope of deep-time surface reconstruction.

5.1.1 Passive Rift Evolution Through Deformable Plate Reconstruction

The deformable plate reconstruction methodology presented in Chapter 2 represents a significant step forward in modelling the early evolution of rift and the underlying dynamics of passive margins. Unlike traditional deformable plate models (Müller et al., 2019; King

and Welford, 2022), which typically impose uniform stretching factors and thus obscure the spatial intricacies of deformation in rifted margins, this approach uses pyGPlates[a] to resolve time-dependent strain rates and crustal thinning. The methodological focus is on directing the strain towards the rift axes by employing exponentially varying stretching factors. This approach results in subsidence and thinning patterns that are both physically plausible and empirically validated, as observed in basins such as the GoM. Calibration against present-day crustal thickness models, such as GEMMA (Reguzzoni and Sampietro, 2015), results in a significant reduction in RMSE with predicted crustal thickness, from values typical of 14.8 km uniform deformation model (Müller et al., 2019) to much lower errors (5.6 km). In the GoM basin, evolving focused deformation emerges as the primary determinant of crustal thickness, subsidence rates, and arrangement of accommodation space. These factors directly influence the depositional partitioning and architectural evolution of sedimentary ecosystems. The workflow not only refines tectonic subsidence histories of GoM but also elucidates depositional patterns, such as the 40 Myr hiatus in red bed strata attributed to rapid subsidence shifting sedimentation southward beneath Jurassic salt formations. The deformable plate reconstruction workflow shows transferability to various passive margin scenarios, particularly where early extension histories are poorly understood. These refined subsidence models also provide improved constraints for petroleum system analysis, reservoir prediction, and paleogeographic mapping. Importantly, they highlight how early rift evolution can influence the distribution and deposition of red-bed in passive margins that may host sedimentary copper deposits (Hitzman et al., 2010, 2005)—resources of increasing global importance. Importantly, the workflow and related datasets are distributed under an open GPL licence, which promotes reproducibility and collaborative knowledge building within the geoscience community. Future developments include applying these methodologies to global passive margins, combining deformable plate results with landscape evolution models for comprehensive source-to-sink evaluations, and improving basin-stratigraphic models. The use of auxiliary data streams, such as well logs and sediment thickness records, allows for the quantitative reconstruction of paleobathymetry, broadening the breadth and resolution of basin development models globally using this computational framework.

5.1.2 XAI for Present-Day Topographic Diversity

By applying XAI to global active margins, this study identifies the primary drivers of mountain topography. This technique utilizes an interpretable, data-driven approach to quantify the interplay of tectonic and geodynamic processes that support current surface diversity. The XAI model, which was trained on a wide range of plate kinematic variables, mantle temperature, vertical flow, and paleoprecipitation, reveals that elevation at modern active margins is primarily controlled by a combination of subduction flux, trench migration rate, and mantle-driven dynamics, with precipitation having a minor but significant regional influence. This multi-process framework has good explanatory ability for spatial elevation patterns, as indicated by high correlation (R value: 0.77) and low RMSE (444 m) when compared to observed topography. The study revealed three archetypal geodynamic regimes: (a) High subduction flux and thick, old oceanic plates support plateau-like altitudes (e.g., the Central Andes), where convergent plate movement and deep mantle circulation accelerate crustal thickening and uplift. (b) Rapid trench retreat is associated with large, low-relief regions, such as the Japanese Archipelago, highlighting the importance

[a] https://www.gplates.org/docs/pygplates/

of rollback and overriding plate deformation. (c) Significant trench advance results in large, compressional uplift zones (such as Central Makran), where collisional tectonics predominate over slab pull.

These results demonstrate the capacity of the XAI framework to provide a quantitative basis for linking tectonic forcing with surface expression. This methodology provides a foundation for exploring the primary controls on crustal and lithospheric thickening, the geometry of subducting slabs, and the potential relationships between topographic gradients and biodiversity. By integrating mantle dynamics and surface processes, this approach offers a versatile toolkit for investigating Earth system evolution at active margins.

5.1.3 A Deep Learning Framework for Reconstructing Paleotopography of Active Margins

The deep learning approach presented in chapter 4 represents a quantitative method for reconstructing the paleotopographic development of active margins from the Mesozoic to the Cenozoic. This methodology explains 92% of the variance ($R^2 = 0.92$) in modern global elevations using a neural network trained on global plate kinematics, mantle dynamic parameters, and paleoclimate-informed proxies, with a global root mean squared error (RMSE) of 576 m relative to ETOPO1. The retrospective application of this model allows for the recovery of topographic features that are often fragmentary in the geological record. One prominent example is the reconstruction of East Asia's Jurassic-Cretaceous Cordillera, which has been identified in regional proxy records but has been largely overlooked in previous global reconstructions. The model's outputs emphasise the interplay between episodes of increased subduction flux, rapidly changing trench kinematics, and suddenly diminishing topography caused by slab rollback and tectonic extension. Critically, these reconstructed surface histories are highly consistent with independent validation datasets such as geochemical proxies, crustal thickness estimates, and lithological records, demonstrating the utility of physics-integrated deep learning for systematic hypothesis testing and tectonic benchmarking. In the Central Andes, the framework reconstructs the timing and magnitude of late Oligocene-Miocene uplift, matching empirical paleoelevation curves and linking uplift pulses to surges in subduction flow and trench retreat attenuation. By integrating multiple geochemical datasets into the validation pipeline, the model provides reproducible reconstructions in areas where traditional proxy coverage is limited or discontinuous. The resolved temporal evolution of active margins establishes a framework for investigating mineral systems. Because porphyry copper formation is linked to the interplay among magmatic flux, crustal thickening, and surface uplift, resolving these variables provides a basis for predicting regions favorable for mineralization and assessing the preservation potential of ore systems. Similarly, these reconstructions offer refined boundary conditions for paleoclimate models. By providing more detailed topographic inputs compared to oversimplified elevation models, this work facilitates more realistic future simulations of monsoonal systems, orographic rainfall, and ocean–atmosphere interactions. Through these refined elevation histories, the thesis supports the integration of tectonics, climate, and the evolution of life.

5.1.4 pyDTDM: A Python Library for Deep-Time Data Mining

One of the primary challenges in deep-time Earth system studies is the multi-gigabyte scale and fragmented organization of datasets, which span geological, geophysical, and

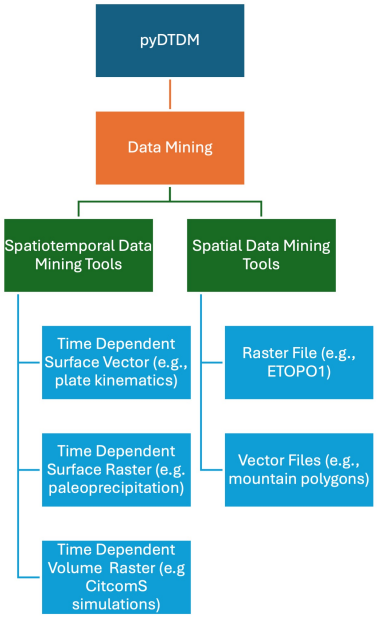

Figure 5.1: Schematic overview of the pyDTDM library architecture, illustrating its modular design for spatiotemporal and spatial data mining in deep-time geoscience applications. The library's components facilitate efficient extraction and processing of diverse geological datasets, enabling seamless integration with machine learning workflows.

paleoclimatic domains. Researchers navigating this ecosystem must acquire records from a variety of sources, including multiple software platforms and inconsistent file formats, which require manual data harmonization to begin computational analysis. When these diverse datasets are combined for machine learning, data management complexity increases. Scaling from raw data to model-ready inputs can be computationally intensive, frequently requiring specialized programming knowledge that can limit accessibility and reproducibility for the broader research community. Addressing this challenge, the pyDTDM library[b] library (created for Chapters 3 and 4 and visually summarized in the Figure 5.1) serves as a modular Python framework designed to unify deep-time data mining in geoscience. Its architecture consists of a data mining hub that is divided into various spatiotemporal and spatial mining suites, each configured to handle the fundamental data types critical to deep-time modelling operations. The spatiotemporal mining capabilities of pyDTDM are structured for dynamic datasets. Extensions such as GPlately and pyGPlates automate the extraction of complex spatiotemporal surface vectors, including parameters such as subduction flux, trench migration velocities, kinematic histories, time-dependent surface rasters (paleoprecipitation, seafloor ages), and volumetric outputs from high-resolution CitcomS simulations. This library not only speeds up the quantification of geological factors regulating topographic change, but also significantly decreases manual and computational overhead compared to traditional methods. In addition, the spatial mining suite makes it easier to import and use modern static data, ranging from topographic raster grids (ETOPO1) to sophisticated vector files outlining current geological formations, such as mountain polygons. This dual channel ensures that pyDTDM allows researchers to seamlessly transition between deep-time reconstructions and investigations of present spatial events, encouraging the rigorous integration of physical and statistical

[b] https://github.com/BigHistory-IN/pyDTDM

methodologies within a coherent computational framework.

Beyond fast data wrangling, pyDTDM is specifically built for interoperability and smooth export: users can quickly convert mining outputs into tabular forms (CSV, Excel) and easily interface findings with various mapping and visualization tools, such as GPlates and QGIS. Such adaptability solidifies its position as a critical foundation for open, repeatable research practices, coinciding with the Earth science community's growing use of AI-driven discovery and transparent data analytics. Its distribution under the GPL licence ensures not just open access but also democratization, allowing academics worldwide to engage in and broaden the scope of deep-time data science without barriers to entrance.

5.1.5 Kalpa: An Open-Source Software Platform for Machine Learning, Data Analytics, and Visualization in Geosciences

Kalpa was developed as part of this thesis as an open-source platform that addresses methodological challenges in Earth science by integrating computational analytics, machine learning, and geospatial visualization within a single environment. The platform's role extends beyond data management to support specific methodological implementations. In Chapter 3, Kalpa demonstrates how to build interpretability-driven machine learning models using frameworks like EBM to dissect the factors that influence current topography. Kalpa uses plate kinematic data, mantle parameters, and climate proxies to perform quantitative assessments of the tectonic, mantle, and climatic constraints on active margin diversification, showing nonlinearities that traditional "black box" models frequently obscure. Its integrated visualisation suite converts analytical results into immersive, high-fidelity maps and 3D figures, making complicated spatial linkages and time-varying characteristics understandable and scientifically actionable. In Chapter 4, Kalpa facilitates deep learning pipelines, training neural networks on evolving geoscience data to reconstruct paleotopography of active margins since the Mesozoic. The platform's strict versioning and pipeline tracking guarantee reproducibility—every model and analytic procedure is recorded, supporting effortless collaboration and portable sharing as reusable modules.

This thesis illustrates how the combination of open-source data mining and machine learning modeling provides a framework for deep-time Earth system studies. Kalpa facilitates the transition of modeling workflow outputs into interpretable, reproducible data, supporting scientific analysis and the integration of physical models with data-driven inference. By providing these tools, the platform supports transparent and collaborative research within the Earth science community.

5.2 Limitations

Despite the computational advances made in this thesis, numerous fundamental limitations remain, reflecting the unavoidable abstraction involved in digitally reconstructing the deep-time paleotopography. While each chapter has addressed specific challenges, several limitations persist across the methodologies presented. These include uncertainties in plate tectonic reconstructions, simplifications in numerical models, and challenges in validating predictions against incomplete proxy records. Each of these limitations is discussed in detail below.

5.2.1 Uncertainty in Plate Tectonic Reconstruction

No plate reconstruction, no matter how advanced, can claim to be objectively correct. Each "best-fit" kinematic or deformable plate reconstruction is ultimately one of many possible interpretations, with different scenarios resulting in varied tectonic histories. Reconstructions grow increasingly speculative as geological age increases—particularly for plates lost to subduction, where histories must be inferred from cryptic onshore accreted terranes or feeble indications in mantle tomography. As a result, large-scale interpolation and extrapolation are inescapable, for e.g. the location of active margins within the plate reconstruction can have spatial errors ranging from 500 to 1000 km even during the last 100 to 200 million years (Seton et al., 2023). Deformable plate models exacerbate this ambiguity at the boundaries of rigid plates and deforming domains, frequently leaving transitions less than rigidly controlled (King and Welford, 2022). Decisions about the timing and position of plate boundary initiations, jumps, or polarity reversals are influenced as much by analogies and geodynamic plausibility as by direct data, resulting in model-dependent artefacts that spread to all future projections (Seton et al., 2023; Clennett et al., 2020). Any investigation of paleoelevation, active margin dynamics, or rift history must be interpreted within a broad range of positional and kinematic uncertainty, which will only decrease as new data and analytical approaches become available.

5.2.2 Numerical Model Constraints

Geodynamic and numerical models are fundamentally deliberate simplifications of nature's deeply layered reality, guided by a set of partial differential equations that can only approximate the underlying physics (Bower et al., 2015; McKenzie, 1978). The CitcomS-based simulations used to feed the XAI and deep learning frameworks capture first-order buoyancy-driven events, but they do not resolve complicated processes like slab breakoff, delamination, hydration-induced mantle weakening, or the dynamic involvement of arc volcanism. Nuanced elements like as regional and temporal fluctuations in mantle viscosity, transitory rheological shifts and magmatic intrusions are systematically excluded. As a result, the models occasionally fail to reproduce rapid or unusual uplift and subsidence events observed in regional stratigraphic and thermochronological records. In passive margin contexts, crustal thickness and tectonic subsidence models include assumptions, such as constant lithospheric and crustal densities, and the absence of depth-dependent stretching, salt mobilisation, or brittle faulting. This modelling regime, while practical, can provide significant mismatches in real-world situations, particularly when thick evaporite layers, sediment loading, or magmatic overprints complicate the crustal structure. Choices in deformative mesh parameters, boundary and initial conditions, and the physical plausibility of input densities all have a significant impact on these models' predictive capacity, bringing difficult-to-quantify levels of uncertainty.

5.2.3 Uncertainty in Validation

The patchy, uneven, and usually unclear nature of accessible proxies complicates the validation of all deep-time predictions, including paleoelevation, crustal thickness, and tectonic boundary geometries. Geochemical markers of crustal thickness, for example, usually have uncertainties of more than 1-2 km, and their precision is further compromised by lithological heterogeneity or the faint signature of salt and sedimentary cover. Model reconstructions rely heavily on the dependability of such proxies, as well as the quality of

kinematic reconstructions that are limited by the inadequate preservation of disappeared plates, slabs, or orogenic belts. Ground-truthing is especially difficult in areas with lost or eroded orogens, subducted oceanic crust, or fragmented metamorphic and paleoclimatic indicators. These incomplete records produce large, overlapping uncertainty envelopes, confounding the assignment of topographic characteristics to specific tectonic causes.

5.2.4 Methodological and Architectural Limitations

Beyond the uncertainties inherent in the input data, several technical limitations related to the modeling methodology must be acknowledged. First, the spatial scope of STN and the XAI framework is primarily optimized for subduction-dominated active margins. Because the input feature set focuses on subduction flux and trench kinematics, the current architecture may not accurately generalize to intracontinental deformation (such as the Laramide orogeny) or large-scale continental collisions (such as the Himalaya-Tibet system) without the inclusion of additional mechanical variables. The underlying neural network architecture also presents specific constraints. The STN utilizes a feed-forward design, which lacks a recurrent "memory" component to explicitly solve time-dependent geodynamic equations. While temporal consistency in the resulting reconstructions is achieved through the data preprocessing stage—specifically via a 25 Myr moving window used to smooth kinematic and geodynamic drivers—the model does not natively account for the physical evolution of the lithosphere over time. Consequently, the 25 Myr time-averaging necessary for smooth topographic evolution may inadvertently smooth out short-term (1–5 Myr) topographic pulses or high-frequency tectonic events, potentially masking rapid orogenic fluctuations. Finally, while the modeling approach is "physics-grounded" by utilizing geodynamic simulations as inputs, it does not constitute a Physics-Informed Neural Network (PINN). In its current form, the network learns statistical relationships between geodynamic drivers and elevation but does not explicitly encode governing physical laws, such as conservation of mass or momentum, into its loss function. Future iterations of this work could improve predictive realism and interpretability by migrating toward a PINN architecture, ensuring that all reconstructed paleotopographies strictly adhere to known geodynamic governing equations.

a)

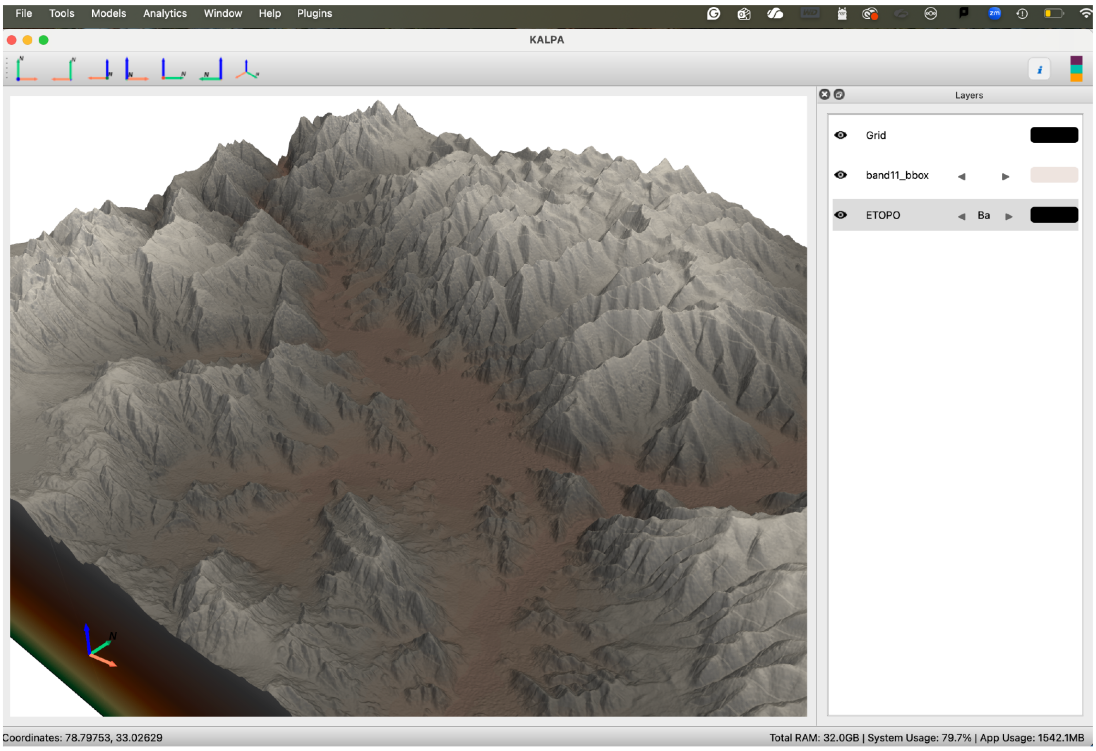

b)

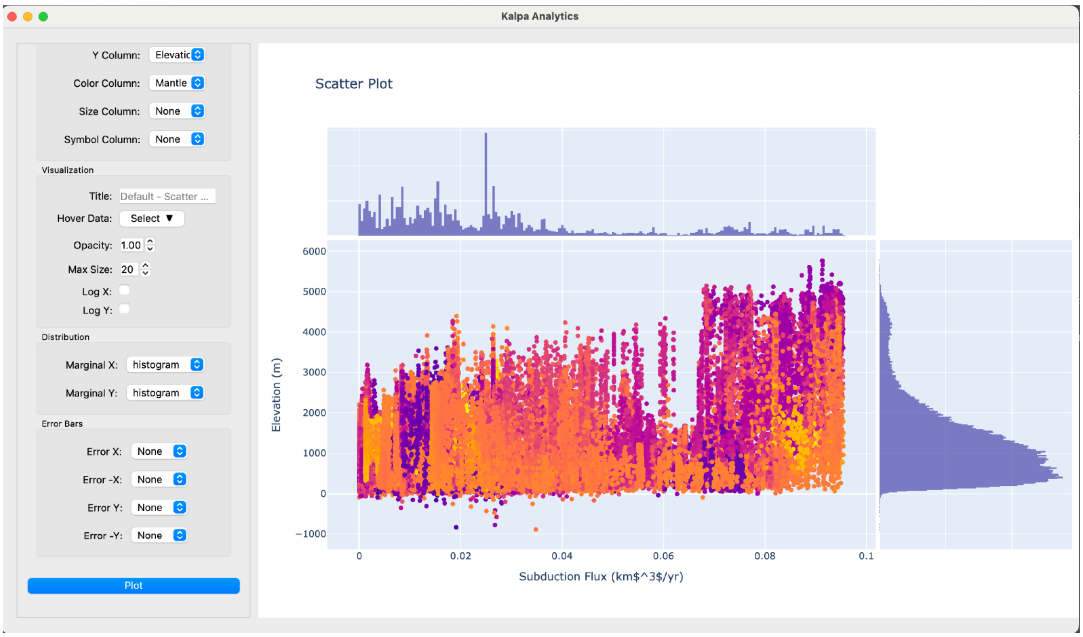

Figure 5.2: Kalpa's Integrated Visualization and Exploratory Data Analysis Suite. a) High-fidelity 3D visualization of topography generated by Kalpa, demonstrating its ability to ingest and render complex 3D data volumes (e.g., raster and vector formats) for geoscientific interpretation. b) The Kalpa Analytics window, featuring an interactive scatter plot and marginal histograms. This tool enables users to conduct advanced exploratory analysis of spatiotemporal datasets, such as visualizing the relationship between elevation and Subduction Flux, facilitating the identification of complex nonlinearities necessary for building robust machine learning models.

a)

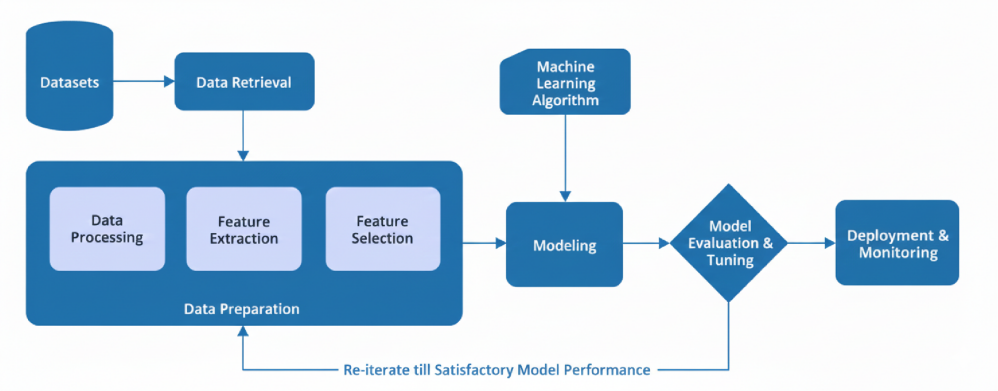

b)

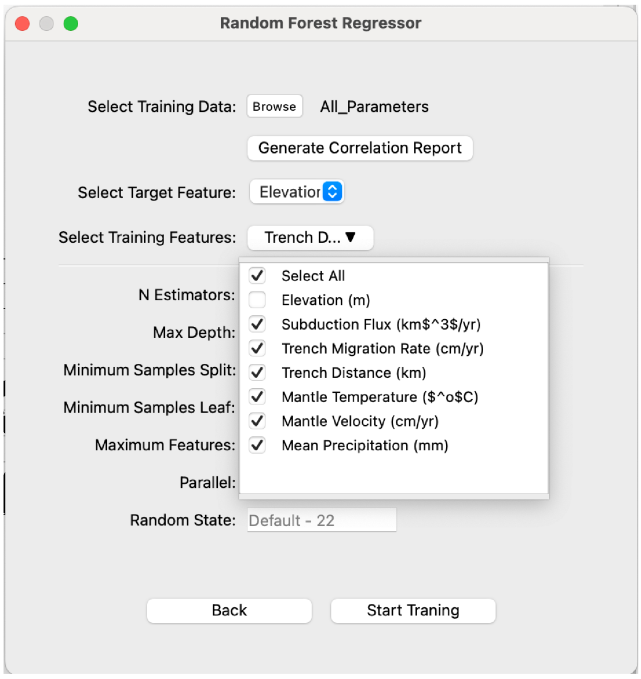

Figure 5.3: Kalpa's End-to-End Machine Learning Workflow and Training Interface. a) The comprehensive workflow of the Kalpa platform, illustrating the integrated stages of machine learning for deep-time Earth system studies. The pipeline runs from Data Preparation (Processing, Feature Extraction, Selection) to Modeling and iterative Evaluation & Tuning, ensuring a robust transition to Deployment & Monitoring. b) Screenshot of the Random Forest Regressor training module within Kalpa. This interface demonstrates the platform's user-focused design for model training, allowing users to easily select a Target Feature (e.g., Elevation) and relevant Training Features (e.g., Subduction Flux, Mantle Velocity, Precipitation) from transdisciplinary data sources to direct rigorous assessments and build predictive models.

Chapter 6

Conclusion

This thesis presents a quantitative framework for reconstructing Earth's paleotopography by integrating plate tectonic kinematics, geodynamic simulations, and machine learning methodologies. The work addresses the methodological gap between process-driven numerical models and data-driven empirical reconstructions by establishing a reproducible computational architecture.

The three research questions posed at the outset have been addressed as follows: For passive rift margins, the thesis develops deformable plate tectonic reconstructions that utilize focused, exponentially varying strain localization to improve the prediction of crustal architecture and tectonic subsidence. By resolving the stratigraphic architecture in the GoM, the work provides a method for quantifying how lithospheric stretching influences basin geometry and accommodation space. Similarly, for active margins, the thesis identifies subduction flux and trench dynamics as the primary orchestrators of active margin topography, demonstrates that geological data and physics-integrated computational frameworks enable global-scale paleotopographic reconstructions that align with independent geological datasets. These refined elevation models provide the necessary boundary conditions for future studies of paleoenvironmental features, such as atmospheric circulation and precipitation patterns.

The development of the pyDTDM library, the Kalpa geospatial platform, and open-source deformable plate frameworks supports reproducible and scalable Earth system science. These tools facilitate accessible research practices and encourage community-driven advancement in deep-time surface modeling.

Several avenues for future investigation remain: First, the integration of hybrid frameworks that synthesize XAI with predictive deep learning will substantially enhance mechanistic interpretability without sacrificing predictive capacity. Second, expansion of paleoelevation proxy networks—particularly through augmentation of geochemical, thermochronological, and paleobotanical datasets from presently undersampled regions—will tighten validation constraints and reduce uncertainty envelopes. Third, coupling XAI with paleotopographic reconstructions will illuminate the physical causality underlying orogenic episodicity and enable refined hypothesis testing regarding slab dynamics, mantle circulation, and lithospheric architecture. Fourth, integration with coupled paleoclimate-paleobiogeographic modelling platforms will amplify utility for paleoclimatological and paleobiological studies, enabling quantitative exploration of how tectonic-modulated to-

pography has shaped atmospheric circulation, precipitation patterns, biodiversity dispersal corridors, and evolutionary trajectories. The paleotopographic maps and temporal histories recovered—from the Mesozoic GoM basin to the East Asian Margin—provide quantitative representations of ancient landscapes. This work demonstrates that deep-time surfaces are recoverable through the application of physical principles and computational modeling. By providing refined elevation histories, this thesis offers a foundation for the broader Earth system science community to investigate how surface elevation has modulated climate and influenced biological and mineral systems over geological time.

Bibliography

Christopher Amante and Barry W. Eakins. ETOPO1 arc-minute global relief model : Procedures, data sources and analysis. 2009.

Jovid Aminov, Guillaume Dupont-Nivet, Diego Ruiz, and Boris Gailleton. Paleogeographic reconstructions using QGIS: Introducing Terra Antiqua plugin and its application to 30 and 50 Ma maps. *Earth-Science Reviews*, 240:104401, May 2023. ISSN 0012-8252. doi: 10.1016/j.earscirev.2023.104401.

J. A. Badgeley, E. J. Steig, and M. Dütsch. Uncertainty in Reconstructing Paleo-Elevation of the Antarctic Ice Sheet From Temperature-Sensitive Ice Core Records. *Geophysical Research Letters*, 49(23):e2022GL100334, 2022. ISSN 1944-8007. doi: 10.1029/2022GL100334.

Lydian M. Boschman. Andean mountain building since the Late Cretaceous: A paleoelevation reconstruction. *Earth-Science Reviews*, 220:103640, September 2021. ISSN 0012-8252. doi: 10.1016/j.earscirev.2021.103640.

Lydian M. Boschman and Fabien L. Condamine. Mountain radiations are not only rapid and recent: Ancient diversification of South American frog and lizard families related to Paleogene Andean orogeny and Cenozoic climate variations. *Global and Planetary Change*, 208:103704, January 2022. ISSN 0921-8181. doi: 10.1016/j.gloplacha.2021.103704.

S. Botsyun, T. A. Ehlers, S. G. Mutz, K. Methner, E. Krsnik, and A. Mulch. Opportunities and Challenges for Paleoaltimetry in "Small" Orogens: Insights From the European Alps. *Geophysical Research Letters*, 47(4):e2019GL086046, 2020. ISSN 1944-8007. doi: 10.1029/2019GL086046.

Martin H. P. Bott. The stress regime associated with continental break-up. *Geological Society, London, Special Publications*, 68(1):125–136, January 1992. doi: 10.1144/GSL.SP.1992.068.01.08.

Dan J. Bower, Michael Gurnis, and Nicolas Flament. Assimilating lithosphere and slab history in 4-D Earth models. *Physics of the Earth and Planetary Interiors*, 238:8–22, January 2015. ISSN 0031-9201. doi: 10.1016/j.pepi.2014.10.013.

Sascha Brune, Christian Heine, Peter D. Clift, and Marta Pérez-Gussinyé. Rifted margin architecture and crustal rheology: Reviewing Iberia-Newfoundland, Central South Atlantic, and South China Sea. *Marine and Petroleum Geology*, 79:257–281, January 2017. ISSN 0264-8172. doi: 10.1016/j.marpetgeo.2016.10.018.

Jean-Daniel Champagnac, Peter Molnar, Christian Sue, and Frédéric Herman. Tectonics,

climate, and mountain topography. *Journal of Geophysical Research: Solid Earth*, 117 (B2), 2012. ISSN 2156-2202. doi: 10.1029/2011JB008348.

Marin K. Clark. The significance of paleotopography. *Reviews in Mineralogy and Geochemistry*, 66(1):1–21, October 2007. ISSN 1529-6466. doi: 10.2138/rmg.2007.66.1.

Edward J. Clennett, Karin Sigloch, Mitchell G. Mihalynuk, Maria Seton, Martha A. Henderson, Kasra Hosseini, Afsaneh Mohammadzaheri, Stephen T. Johnston, and R. Dietmar Müller. A Quantitative Tomotectonic Plate Reconstruction of Western North America and the Eastern Pacific Basin. *Geochemistry, Geophysics, Geosystems*, 21(8): e2020GC009117, 2020. ISSN 1525-2027. doi: 10.1029/2020GC009117.

C. J. Ebinger, D. Keir, I. D. Bastow, K. Whaler, J. O. S. Hammond, A. Ayele, M. S. Miller, C. Tiberi, and S. Hautot. Crustal Structure of Active Deformation Zones in Africa: Implications for Global Crustal Processes. *Tectonics*, 36(12):3298–3332, 2017. ISSN 1944-9194. doi: 10.1002/2017TC004526.

Todd A. Ehlers and Christopher J. Poulsen. Influence of Andean uplift on climate and paleoaltimetry estimates. *Earth and Planetary Science Letters*, 281(3):238–248, May 2009. ISSN 0012-821X. doi: 10.1016/j.epsl.2009.02.026.

L. A. Evenstar, A. J. Hartley, and A. E. Mather. Orogenic-orographic feedback and the rise of the Central Andes. *Earth and Planetary Science Letters*, 602:117931, January 2023. ISSN 0012-821X. doi: 10.1016/j.epsl.2022.117931.

Carmala Garzione, Jay Quade, Peter Decelles, and Nathan English. Predicting paleoelevation of Tibet and the Himalaya from N 18 O vs. altitude gradients in meteoric water across the Nepal Himalaya. *Earth and Planetary Science Letters*, 183:215–229, November 2000. doi: 10.1016/S0012-821X(00)00252-1.

A. J. Hartley, T. Sempere, and G. Wörner. A comment on "Rapid late Miocene rise of the Bolivian Altiplano: Evidence for removal of mantle lithosphere" by C.N. Garzione et al. [Earth Planet. Sci. Lett. 241 (2006) 543–556]. *Earth and Planetary Science Letters*, 259(3):625–629, July 2007. ISSN 0012-821X. doi: 10.1016/j.epsl.2007.04.012.

Kinga Hips. Sedimentary aspects of the onset of Middle Triassic continental rifting in the western end of Neotethys; inferences from the Silica and Torna Nappes, NE Hungary: A review. *Facies*, 68(3):8, April 2022. ISSN 1612-4820. doi: 10.1007/s10347-022-00646-3.

Murray Hitzman, Rodney Kirkham, David Broughton, Jon Thorson, and David Selley. The Sediment-Hosted Stratiform Copper Ore System. In Jeffrey W. Hedenquist, John F. H. Thompson, Richard J. Goldfarb, and Jeremy P. Richards, editors, *One Hundredth Anniversary Volume*, page 0. Society of Economic Geologists, January 2005. ISBN 978-1-887483-01-8. doi: 10.5382/AV100.19.

Murray W. Hitzman, David Selley, and Stuart Bull. Formation of Sedimentary Rock-Hosted Stratiform Copper Deposits through Earth History. *Economic Geology*, 105(3): 627–639, May 2010. ISSN 0361-0128. doi: 10.2113/gsecongeo.105.3.627.

Javier Igea and Andrew J. Tanentzap. Global topographic uplift has elevated speciation in mammals and birds over the last 3 million years. *Nature Ecology & Evolution*, 5(11): 1530–1535, November 2021. ISSN 2397-334X. doi: 10.1038/s41559-021-01545-6.

Michael T. King and J. Kim Welford. Advances in Deformable Plate Tectonic Models: 1. Reconstructing Deformable Continental Blocks and Crustal Thicknesses Back Through Time. *Geochemistry, Geophysics, Geosystems*, 23(6):e2022GC010372, 2022. ISSN 1525-2027. doi: 10.1029/2022GC010372.

Andrei V. Konstantinov and Lev V. Utkin. Interpretable machine learning with an ensemble of gradient boosting machines. *Knowledge-Based Systems*, 222:106993, June 2021. ISSN 0950-7051. doi: 10.1016/j.knosys.2021.106993.

Christian Körner. Mountain Biodiversity, Its Causes and Function. *AMBIO: A Journal of the Human Environment*, 33(sp13):11–17, November 2004. ISSN 0044-7447, 1654-7209. doi: 10.1007/0044-7447-33.sp13.11.

Joachim Kuhlemann. Paleogeographic and paleotopographic evolution of the Swiss and Eastern Alps since the Oligocene. *Global and Planetary Change*, 58(1):224–236, July 2007. ISSN 0921-8181. doi: 10.1016/j.gloplacha.2007.03.007.

Karl A. Lang, Christoph Glotzbach, Uwe Ring, Peter J. J. Kamp, and Todd A. Ehlers. Linking orogeny and orography in the Southern Alps of New Zealand: New observations from detrital fission-track thermochronology of the Waiho-1 borehole. *Earth and Planetary Science Letters*, 552:116586, December 2020. ISSN 0012-821X. doi: 10.1016/j.epsl.2020.116586.

Gabi Laske, Guy Masters, Zhitu Ma, and Mike Pasyanos. Update on CRUST1.0 - A 1-degree Global Model of Earth's Crust. pages EGU2013–2658, April 2013.

Xavier Le Pichon and Jean-Claude Sibuet. Passive margins: A model of formation. *Journal of Geophysical Research: Solid Earth*, 86(B5):3708–3720, 1981. ISSN 2156-2202. doi: 10.1029/JB086iB05p03708.

Sophie Leleu, Adrian J. Hartley, Cees van Oosterhout, Lorcan Kennan, Katrin Ruckwied, and Keith Gerdes. Structural, stratigraphic and sedimentological characterisation of a wide rift system: The Triassic rift system of the Central Atlantic Domain. *Earth-Science Reviews*, 158:89–124, July 2016. ISSN 0012-8252. doi: 10.1016/j.earscirev.2016.03.008.

Lin Li and Carmala N. Garzione. Spatial distribution and controlling factors of stable isotopes in meteoric waters on the Tibetan Plateau: Implications for paleoelevation reconstruction. *Earth and Planetary Science Letters*, 460:302–314, February 2017. ISSN 0012-821X. doi: 10.1016/j.epsl.2016.11.046.

Xiang Li, Yongyun Hu, Jiaqi Guo, Jiawenjing Lan, Qifan Lin, Xiujuan Bao, Shuai Yuan, Mengyu Wei, Zhibo Li, Kai Man, Zihan Yin, Jing Han, Jian Zhang, Chenguang Zhu, Zhouqiao Zhao, Yonggang Liu, Jun Yang, and Ji Nie. A high-resolution climate simulation dataset for the past 540 million years. *Scientific Data*, 9(1):371, June 2022. ISSN 2052-4463. doi: 10.1038/s41597-022-01490-4.

Xiaobo Li. Preliminary analysis on the paleogeography and paleoenvironment in the eastern Yanliao area during the Jurassic-Cretaceous tectonic transition. 28:391–411, March 2021. doi: 10.13745/j.esf.sf.2020.6.29.

Bingxi Liu, Simon Williams, Maria Seton, and Guochun Zhao. Mapping paleoelevations along active continental margins with igneous geochemistry: A case study from South

America. *Gondwana Research*, 134:285–297, October 2024. ISSN 1342-937X. doi: 10.1016/j.gr.2024.07.010.

Yin Lou, Rich Caruana, Johannes Gehrke, and Giles Hooker. Accurate intelligible models with pairwise interactions. In *Proceedings of the 19th ACM SIGKDD International Conference on Knowledge Discovery and Data Mining*, KDD '13, pages 623–631, New York, NY, USA, August 2013. Association for Computing Machinery. ISBN 978-1-4503-2174-7. doi: 10.1145/2487575.2487579.

Xueyun Lu, Jingtao Lai, Lining Wang, Jianqing Ji, and Dalai Zhong. Numerical modelling of coupled climate, tectonics, and surface processes on the eastern Himalayan syntaxis. *Earth-Science Reviews*, 258:104964, November 2024. ISSN 0012-8252. doi: 10.1016/j.earscirev.2024.104964.

Francis A. Macdonald, Nicholas L. Swanson-Hysell, Yuem Park, Lorraine Lisiecki, and Oliver Jagoutz. Arc-continent collisions in the tropics set Earth's climate state. *Science*, 364(6436):181–184, April 2019. doi: 10.1126/science.aav5300.

Dan McKenzie. Some remarks on the development of sedimentary basins. *Earth and Planetary Science Letters*, 40(1):25–32, June 1978. ISSN 0012-821X. doi: 10.1016/0012-821X(78)90071-7.

Benjamin J. W. Mills, Alexander J. Krause, Christopher R. Scotese, Daniel J. Hill, Graham A. Shields, and Timothy M. Lenton. Modelling the long-term carbon cycle, atmospheric CO2, and Earth surface temperature from late Neoproterozoic to present day. *Gondwana Research*, 67:172–186, March 2019. ISSN 1342-937X. doi: 10.1016/j.gr.2018.12.001.

Andreas Mulch. Stable isotope paleoaltimetry and the evolution of landscapes and life. *Earth and Planetary Science Letters*, 433:180–191, January 2016. ISSN 0012-821X. doi: 10.1016/j.epsl.2015.10.034.

R. Dietmar Müller, Sabin Zahirovic, Simon E. Williams, John Cannon, Maria Seton, Dan J. Bower, Michael G. Tetley, Christian Heine, Eline Le Breton, Shaofeng Liu, Samuel H. J. Russell, Ting Yang, Jonathon Leonard, and Michael Gurnis. A Global Plate Model Including Lithospheric Deformation Along Major Rifts and Orogens Since the Triassic. *Tectonics*, 38(6):1884–1907, 2019. ISSN 1944-9194. doi: 10.1029/2018TC005462.

Barry Parsons and John G. Sclater. An analysis of the variation of ocean floor bathymetry and heat flow with age. *Journal of Geophysical Research (1896-1977)*, 82(5):803–827, 1977. ISSN 2156-2202. doi: 10.1029/JB082i005p00803.

F. Poblete, G. Dupont-Nivet, A. Licht, D. J. J. van Hinsbergen, P. Roperch, M. G. Mihalynuk, S. T. Johnston, F. Guillocheau, G. Baby, F. Fluteau, C. Robin, T. J. M. van der Linden, D. Ruiz, and M. L. J. Baatsen. Towards interactive global paleogeographic maps, new reconstructions at 60, 40 and 20 Ma. *Earth-Science Reviews*, 214:103508, March 2021. ISSN 0012-8252. doi: 10.1016/j.earscirev.2021.103508.

Carsten Rahbek, Michael K. Borregaard, Alexandre Antonelli, Robert K. Colwell, Ben G. Holt, David Nogues-Bravo, Christian M. Ø. Rasmussen, Katherine Richardson, Minik T. Rosing, Robert J. Whittaker, and Jon Fjeldså. Building mountain biodiver-

sity: Geological and evolutionary processes. *Science*, 365(6458):1114–1119, September 2019. doi: 10.1126/science.aax0151.

M. Reguzzoni and D. Sampietro. GEMMA: An Earth crustal model based on GOCE satellite data. *International Journal of Applied Earth Observation and Geoinformation*, 35:31–43, March 2015. ISSN 1569-8432. doi: 10.1016/j.jag.2014.04.002.

David B. Rowley and Carmala N. Garzione. Stable Isotope-Based Paleoaltimetry. 2007.

David B Rowley, Raymond T Pierrehumbert, and Brian S Currie. A new approach to stable isotope-based paleoaltimetry: Implications for paleoaltimetry and paleohypsometry of the High Himalaya since the Late Miocene. *Earth and Planetary Science Letters*, 188 (1):253–268, May 2001. ISSN 0012-821X. doi: 10.1016/S0012-821X(01)00324-7.

W. P. Schellart. Andean mountain building and magmatic arc migration driven by subduction-induced whole mantle flow. *Nature Communications*, 8(1):2010, December 2017. ISSN 2041-1723. doi: 10.1038/s41467-017-01847-z.

Christopher R. Scotese. An Atlas of Phanerozoic Paleogeographic Maps: The Seas Come In and the Seas Go Out | Annual Review of Earth and Planetary Sciences. https://www.annualreviews.org/doi/abs/10.1146/annurev-earth-081320-064052, March 2021.

M. Seton, R. D. Müller, S. Zahirovic, C. Gaina, T. Torsvik, G. Shephard, A. Talsma, M. Gurnis, M. Turner, S. Maus, and M. Chandler. Global continental and ocean basin reconstructions since 200Ma. *Earth-Science Reviews*, 113(3):212–270, July 2012. ISSN 0012-8252. doi: 10.1016/j.earscirev.2012.03.002.

Maria Seton, Simon E. Williams, Mathew Domeier, Alan S. Collins, and Karin Sigloch. Deconstructing plate tectonic reconstructions. *Nature Reviews Earth & Environment*, 4(3):185–204, March 2023. ISSN 2662-138X. doi: 10.1038/s43017-022-00384-8.

Robert A. Spicer. Tibet, the Himalaya, Asian monsoons and biodiversity – In what ways are they related? *Plant Diversity*, 39(5):233–244, October 2017. ISSN 2468-2659. doi: 10.1016/j.pld.2017.09.001.

E. Tan, E. Choi, P. Thoutireddy, M. Gurnis, and M. Aivazis. GeoFramework: Coupling multiple models of mantle convection within a computational framework. *Geochemistry, Geophysics, Geosystems*, 7(6), 2006. ISSN 1525-2027. doi: 10.1029/2005GC001155.

Christian Vérard, Cyril Hochard, Peter Baumgartner, and Gérard Stampfli. Geodynamic evolution of the Earth over the Phanerozoic: Plate tectonic activity and palaeoclimatic indicators. *Journal of Palaeogeography*, 4:167–188, April 2015. doi: 10.3724/SP.J.1261.2015.00072.

Sean D. Willett. Orogeny and orography: The effects of erosion on the structure of mountain belts. *Journal of Geophysical Research: Solid Earth*, 104(B12):28957–28981, 1999. ISSN 2156-2202. doi: 10.1029/1999JB900248.

Sebastian G. Wolf, Ritske S. Huismans, Jean Braun, and Xiaoping Yuan. Topography of mountain belts controlled by rheology and surface processes | Nature. https://www.nature.com/articles/s41586-022-04700-6, June 2022.

Nicky M. Wright, Maria Seton, Simon E. Williams, Joanne M. Whittaker, and R. Dietmar Müller. Sea-level fluctuations driven by changes in global ocean basin volume following supercontinent break-up. *Earth-Science Reviews*, 208:103293, September 2020. ISSN 0012-8252. doi: 10.1016/j.earscirev.2020.103293.

Xiaoping Yuan, Yuqiang Li, Sascha Brune, Kai Li, Michaël Pons, and Sebastian G. Wolf. Coordination between deformation, precipitation, and erosion during orogenic growth. *Nature Communications*, 15(1):10362, November 2024. ISSN 2041-1723. doi: 10.1038/s41467-024-54690-4.

Sabin Zahirovic, Ahmed Eleish, Sebastiano Doss, Jodie Pall, John Cannon, Mattia Pistone, Michael G. Tetley, Alex Young, and Peter Fox. Subduction and carbonate platform interactions. *Geoscience Data Journal*, 9(2):371–383, 2022. ISSN 2049-6060. doi: 10.1002/gdj3.146.

Deng Zeng, Lin Ding, Zhongyu Xiong, Liyun Zhang, Chao Wang, Junyi Wang, Xiaodong Wang, Yahui Yue, Jing Xie, and Xudong Guo. Insights into paleoelevation and paleodrainage change in northern Tibet from the Late Cretaceous to late Oligocene. *GSA Bulletin*, 137(11-12):5112–5130, June 2025. ISSN 0016-7606. doi: 10.1130/B38115.1.

Shijie Zhong and Michael Gurnis. Mantle Convection with Plates and Mobile, Faulted Plate Margins. *Science*, 267(5199):838–843, February 1995. doi: 10.1126/science.267.5199.838.

Jianping Zhou, Ehsan Farahbakhsh, Simon Williams, Xiaohui Li, Yongjiang Liu, Sanzhong Li, and R. Dietmar Müller. Machine Learning and Big Data Mining Reveal Earth's Deep Time Crustal Thickness and Tectonic Evolution: A New Chemical Mohometry Approach. *Journal of Geophysical Research: Solid Earth*, 130(5):e2024JB030404, 2025. ISSN 2169-9356. doi: 10.1029/2024JB030404.

A Ziengler, David Rowley, A Lottes, D Sahagian, M Hulver, and T Gierlowski. Paleogeographic Interpretation: With an Example From the Mid-Cretaceous. *Ann. Rev. Earth Planet. Sci.*, 13:385–423, May 1985. doi: 10.1146/annurev.ea.13.050185.002125.

Appendix A

Supporting Information for A Crustal Thickness Evolution Model for the Mesozoic Central Gulf of Mexico

Supporting Information for

A Crustal Thickness Evolution Model for the Mesozoic Central Gulf of Mexico

Satyam Pratap Singh[1], Sabin Zahirovic[1], Maria Seton[1], Nicky M. Wright[1], Nicholas Atwood[2], Catherine Belgarde[2], Claire Mallard[1], Christopher Alphonso[1], Youseph Ibrahim[1, 3]

[1]EarthByte Group, School of Geosciences, The University of Sydney, NSW 2006, Australia

[2]BHP Minerals Service Co, Tucson, Arizona 85704, USA

[3] Now at Department of Geology and Geophysics, Texas A&M University, TX 77840, United States

Contents of this file

Supplementary Information

Appendix

A. Uniform Deformation Model

Traditional numerical approaches in plate tectonic reconstructions primarily focus on rigid plate motions, and only account for deformation implicitly through overlapping of present day plates (e.g. Pindell and Kennan 2009; Seton et al. 2012; Boschman et al. 2014; Müller et

al. 2016; Pindell et al. 2021). However, a more recent global plate tectonic reconstruction model has emerged, introducing a novel methodology that incorporates deforming regions at plate boundaries through the establishment of deforming topology networks over rigid tectonic plates at the plate boundaries (Müller et al. 2018; Müller et al. 2019). To implement this approach, the deforming network is discretised into constant strain rate spherical triangular elements, using the Delaunay triangulation technique (Gurnis et al. 2018). By expressing the relative motion and velocities of the triangulation nodes within the deforming areas as finite rotations it becomes possible to calculate the strain rate associated with deformation at plate boundaries (Müller et al. 2019) as defined in equation 1.

$$\dot{S} = \nabla . \vec{u} = \dot{\varepsilon}_D \tag{1}$$

$\dot{S}$ is the strain rate; $\vec{u}$ is the velocity of points and $\dot{\varepsilon}_D$ is the dilatation strain rate.

Furthermore, this methodology allows for the estimation of the finite strain history of points within these deformation zones, enabling the calculation of crustal thickness over time. By employing the governing equations, the temporal variations in crustal thickness can be used to derive the tectonic subsidence of passive rift margins. This integrated approach provides a more comprehensive understanding of the dynamic passive rift evolution.

B. Modelling Crustal Thickness

The evolution of passive rift margins hinges upon the process of crustal thinning. By considering the incompressibility of the lithospheric block, the mass conservation equation can be employed to depict the time-dependent evolution of crustal thickness. This assumes that there is no net mass generation or loss during the deformation process, with horizontal divergence or convergence governing the vertical thinning or thickening (Gurnis et al. 2018; Müller et al. 2019). Hence, the crustal thickness at any time *t* can be calculated using equation 2.

$$\frac{DH}{Dt} = -H . \dot{S} \tag{2}$$

where H is the crustal thickness and $\dot{S}$ is the strain rate.

C. Modelling Tectonic Subsidence

Basin formation arises from the stretching of the continental lithosphere and is part of a broader continuum encompassing continental rifting, passive margin development, and the emergence of a new oceanic crust (e.g. Brune et al. 2023; Şengör & Natal'in, 2001). Over geological timescales, the process of rifting culminates in the thinning and formation of passive margins, with seafloor spreading commonly commencing when the stretching factor (β) surpasses a critical threshold (Le Pichon & Sibuet, 1981). The β can be expressed as:

$$\beta = \frac{H_i}{H}$$

(3)

where H_i and H are the initial crustal thickness and crustal thickness at time t, respectively.

The isostatic adjustments stemming from lithospheric processes triggered by such stretching are reflected in subsidence histories, which offer insights into the mechanisms driving basin formation. Backstripped tectonic subsidence data, which represents subsidence after removing the isostatic effect of sediment loading, have indicated that such lithospheric processes primarily contribute to total subsidence in passive rift settings and drive overall basin formation (Xie & Heller, 2009). However, the GoM contains several regional subsidence anomalies related to salt tectonics and other processes, making it challenging to "correct" the backstripped tectonic subsidence curves for these effects (Li 2006).

Under the assumption of local isostatic equilibrium, the evolution of passive continental margins can be elucidated by McKenzie's (1978) stretching model. According to this model, the present-day depth of the seafloor at any point within a rift is contingent upon the timing and duration of rifting, the elapsed time since rifting cessation, and the stretching factor (β). Nevertheless, stretching alone does not govern tectonic subsidence (McKenzie 1978). Subsidence analysis of most passive rift margins worldwide reveals that subsidence occurs through a combination of mechanisms. Initially, subsidence arises from rifting and extension of the continental crust and also due thermal anomaly from upwelling of asthenosphere. After the stretching ceases subsidence is characterized by a slower diffusive decay of thermal anomaly which will further produce a thermal subsidence attributable to the gradual cooling and rethickening of the stretched lithosphere (Jarvis and McKenzie 1980).

For our model, the tectonic subsidence due to the extension (TS_1; equation 4) can be calculated using the thinning factor.

$$\mathrm{TS}_1 = A\left(1 - \frac{1}{\beta}\right) \tag{4}$$

In most models for subsidence calculation, tectonic subsidence from crustal stretching is modeled separately, followed by post-rift thermal subsidence for simplification(McKenzie 1978). However, we simultaneously solve for both thermal subsidence and subsidence due to stretching within pyGPlates. However, the loss of heat and thermal subsidence actually commences during the extension phase and needs to be considered simultaneously to obtain a realistic estimate of syn-rift extension. Therefore, slow thermal subsidence (TS_2; equation 5) can be calculated by estimating temperature evolution using the advection-diffusion equation 6.

$$TS_2 = B\int_0^L (T'(z) - T(\mathrm{z})) \tag{5}$$

where *T'* and *T* are steady state (equation 6) and initial temperature, *L* is the thickness of the lithosphere, and *z* is the depth from the surface.

$$\frac{dT}{dt} = \kappa \frac{d^2T}{dz^2} - v(z)\frac{dT}{dz} \tag{6}$$

The thermal diffusivity κ represents how heat spreads in a material. The vertical velocity, denoted as $v(z)$, arises from stretching effects. At the top surface (where z=0), the vertical velocity is zero. At the bottom surface (where z=L), it is represented as -V_0 and varies linearly with depth (z).
A and B are constant ratios that depend on the density of crust (ρ_c), mantle(ρ_m), asthenosphere (ρ_a), and thermal expansion coefficient (α) and calculated as follows

$$A = \frac{(\rho_m - \rho_c)}{(\rho_a - \rho_w)} H_i \tag{7}$$

$$B = \frac{\alpha \rho_m}{(\rho_a - \rho_m)} \tag{8}$$

D. Modeling Sediment Loading

We estimated the net effect of sediment loading by calculating the contribution of sediment deposition to subsidence at different periods (Figure S1). This allows us to assess the accommodation space created by sedimentation. Using isostatic equilibrium, the total water depth can be calculated as:

$$W(t) = S_I + S_t - \frac{(\rho_a - {\rho_s}^i)}{(\rho_a - \rho_w)} \mathrm{T(t)} + \frac{\rho_a}{(\rho_a - \rho_w)} \Delta SL(t)$$

where S_I and S_t are the subsidence due to stretching and thermal subsidence respectively, W(t) is water depth, T(t) is sediment thickness through time, ${\rho_s}^i$ is density of sediment , ρ_a is asthenosphere density, ρ_w is the density of water and ΔSL is sea level variations. The uplift from sedimentary loading at any time can be then estimated from the term $\frac{(\rho_a - {\rho_s}^i)}{(\rho_a - \rho_w)} \mathrm{T(t)}$.
The sediment density estimate is based on MacRae, (1994). Sediment thickness estimate from Xie et al. (2019).
* Maximum presalt sediment thickness is assumed (Filina and Beutel, 2022).
+ Jurassic salt thickness is assumed to 600 m.

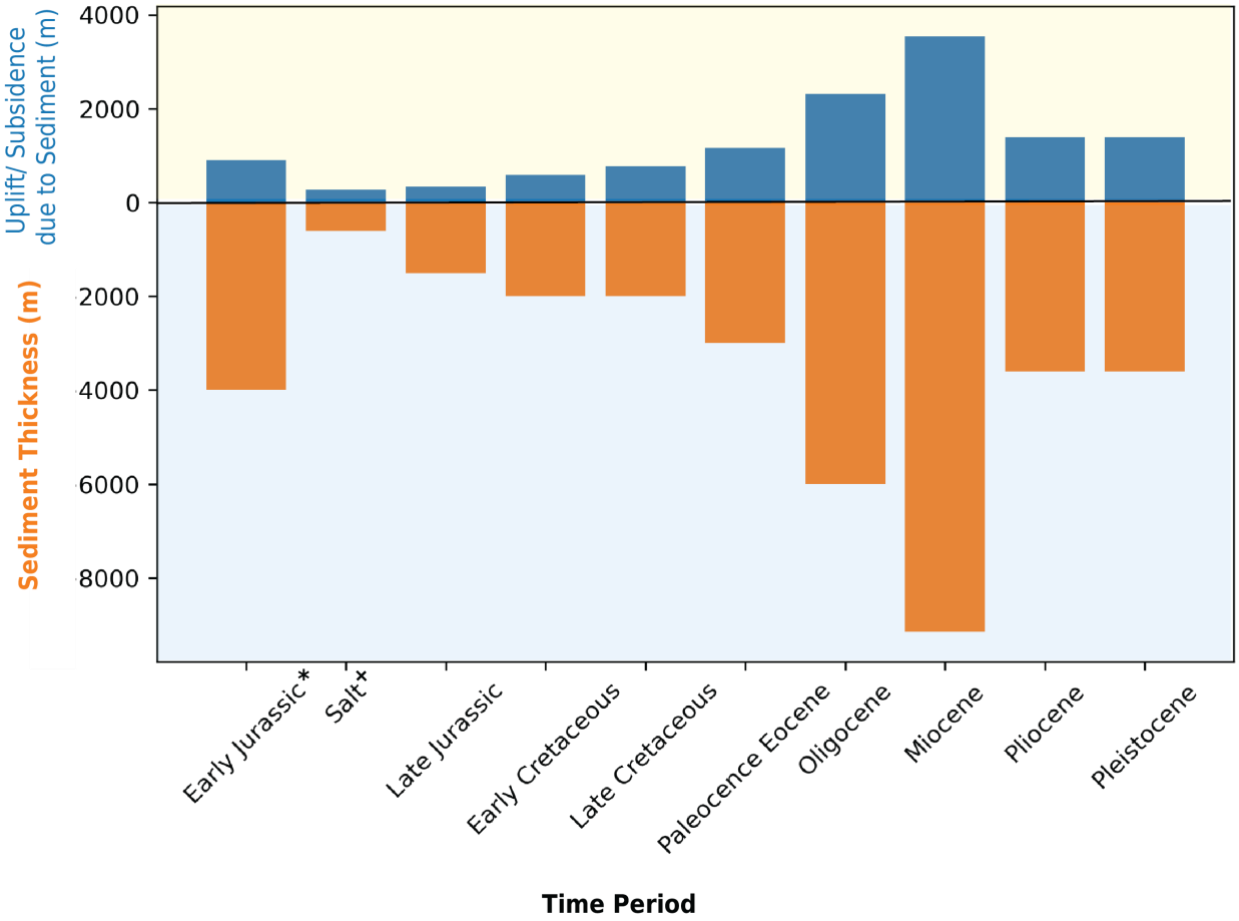

Figure S1 Contribution of sediment deposition to paleowater depth at different periods. This information can be utilized to understand the amount of accommodation space created by sedimentation at the end of each period. Sediment loading, due to its weight, causes the crustal basement to subside. However, due to its overall thickness, it increases the bathymetry, thereby decreasing accommodation space for further sedimentation. It's important to note that in the early period of basin formation, tectonic subsidence primarily dominates, resulting in significant accommodation space creation.

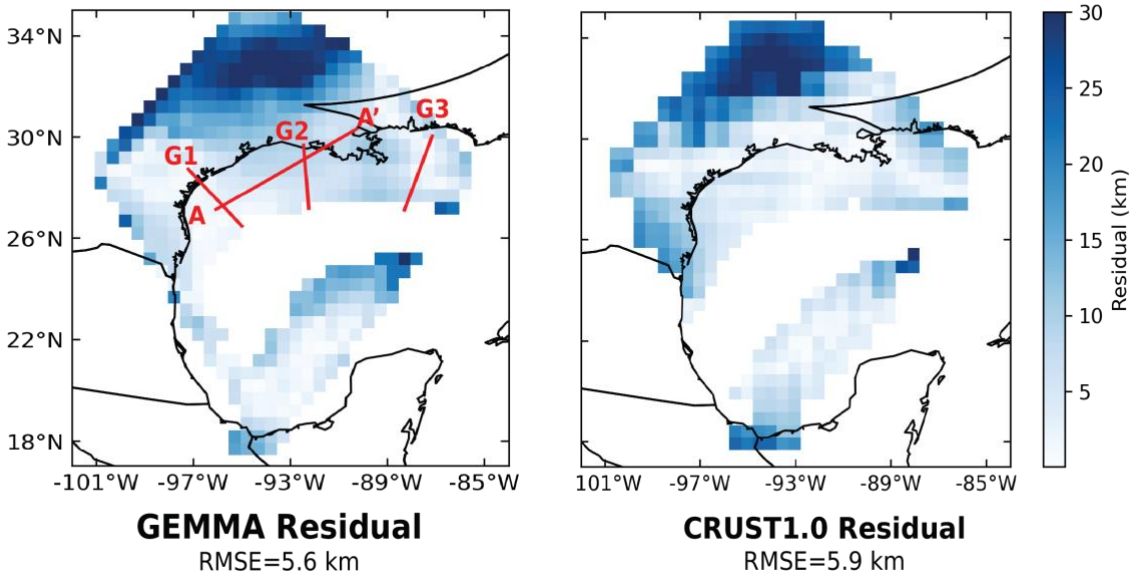

Figure S2: Absolute difference between GEMMA crustal thickness model (Reguzzoni and Sampietro 2015) and calculated crustal thickness at 0 Ma optimised with GEMMA model (Left) and absolute difference between Crust1.0 crustal thickness model (Laske et al. 2013) and calculated crustal thickness at 0 Ma optimised with Crust1.0 crustal thickness model (right). Note, Crust1.0 is at resolution 1° x 1° while GEMMA is at 0.5 ° x 0.5 °.

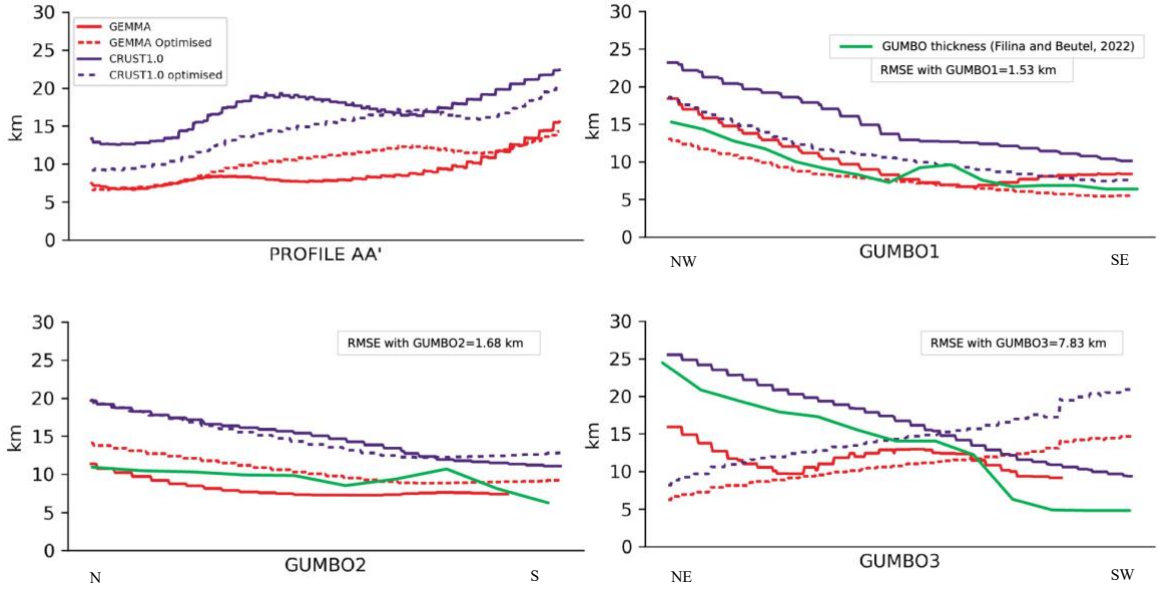

Figure S3: Profile section showing comparison between present-day crustal thickness model (GEMMA, Crust1.0 and GUMBO line crustal thickness from Filina and Beutel, 2022) and calculated crustal thickness at 0 Ma optimised by GEMMA and Crust1.0 crustal thickness model. The RMSE with GUMBO model are produced by comparing GEMMA optimised model. The profile section is in Supplementary Figure S2.

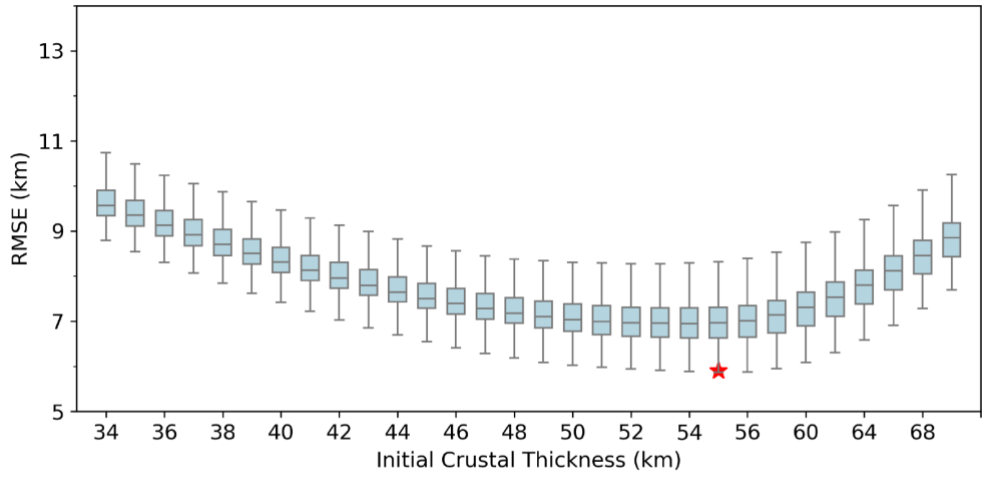
RMSE (km)
13
11
9
7
5
34 36 38 40 42 44 46 48 50 52 54 56 60 64 68
Initial Crustal Thickness (km)

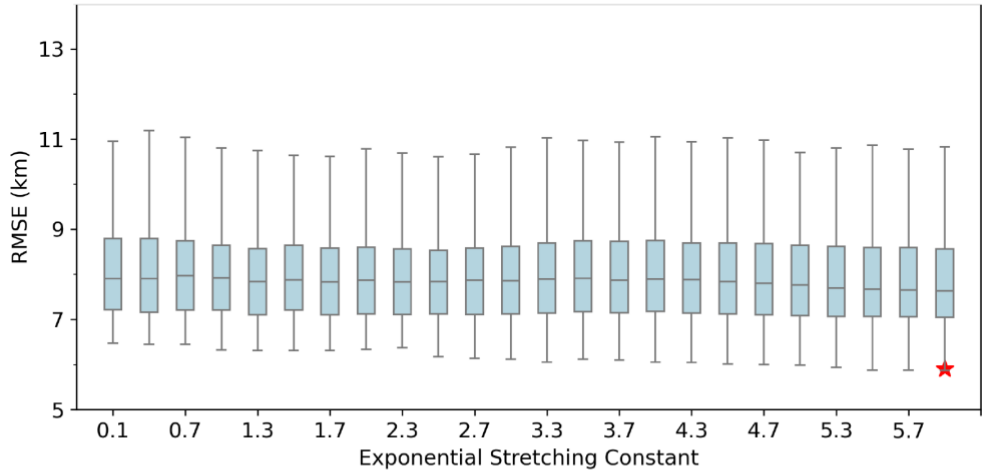
RMSE (km)
13
11
9
7
5
0.1 0.7 1.3 1.7 2.3 2.7 3.3 3.7 4.3 4.7 5.3 5.7
Exponential Stretching Constant

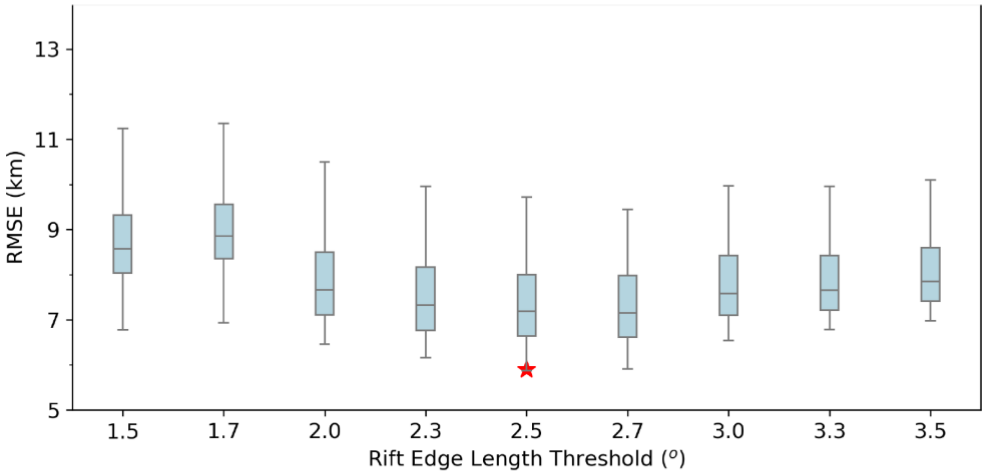
RMSE (km)
13
11
9
7
5
1.5 1.7 2.0 2.3 2.5 2.7 3.0 3.3 3.5
Rift Edge Length Threshold (°)

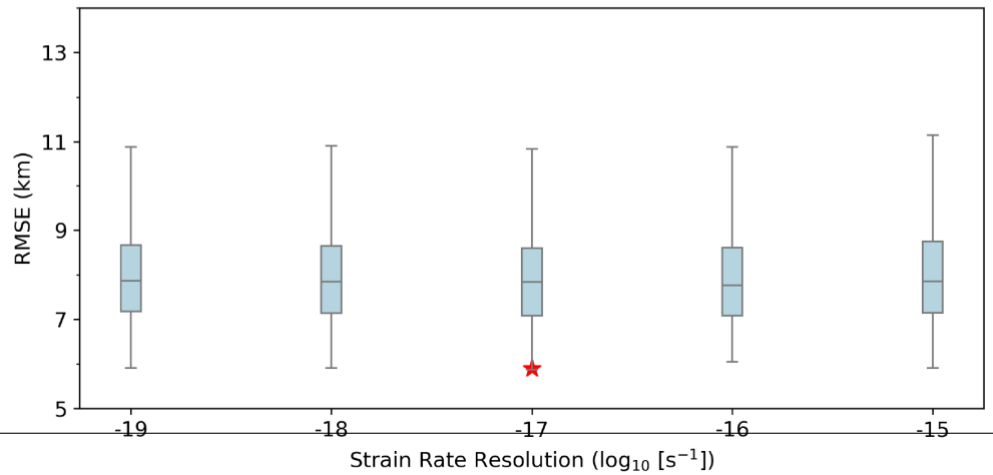
RMSE (km)
13
11
9
7
5
-19 -18 -17 -16 -15
Strain Rate Resolution (log10 [s−1])

Figure S4: Results from our optimisation using Crust1.0 crustal model. The red star marks the minimum RMSE value found during the simultaneous optimisation of the initial crustal thickness and focused deformation mesh parameters defined in Section 3.3.

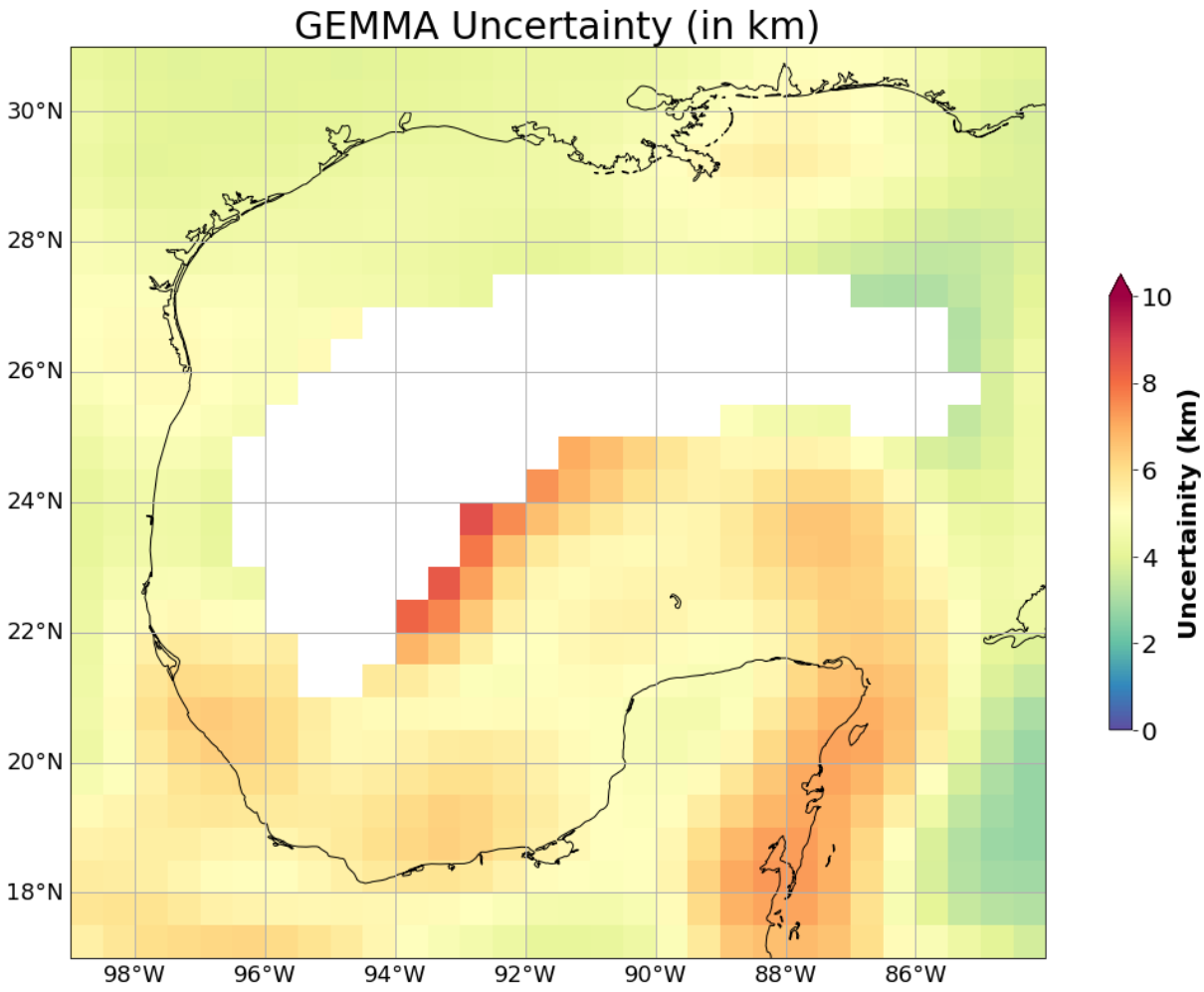

Figure S5: Moho Depth uncertainity for GEMMA model for the study area.

References

Boschman LM, van Hinsbergen DJJ, Torsvik TH, Spakman W, Pindell JL. 2014. Kinematic reconstruction of the Caribbean region since the Early Jurassic. Earth-Science Reviews [Internet]. [accessed 2022 Aug 24] 138:102–136. https://doi.org/10.1016/j.earscirev.2014.08.007

Brune S, Kolawole F, Olive J-A, Stamps DS, Buck WR, Buiter SJH, Furman T, Shillington DJ. 2023. Geodynamics of continental rift initiation and evolution. Nat Rev Earth Environ [Internet]. [accessed 2023 Apr 11]:1–19. https://doi.org/10.1038/s43017-023-00391-3

Gurnis M, Yang T, Cannon J, Turner M, Williams S, Flament N, Müller RD. 2018. Global tectonic reconstructions with continuously deforming and evolving rigid plates. Computers & Geosciences [Internet]. [accessed 2022 Dec 18] 116:32–41. https://doi.org/10.1016/j.cageo.2018.04.007

Jarvis GT, McKenzie DP. 1980. Sedimentary basin formation with finite extension rates. Earth and Planetary Science Letters [Internet]. [accessed 2023 Jun 20] 48(1):42–52. https://doi.org/10.1016/0012-821X(80)90168-5

Laske G, Masters G, Ma Z, Pasyanos M. 2013. Update on CRUST1.0 - A 1-degree Global Model of Earth's Crust [Internet]. [accessed 2023 Sep 29]:EGU2013-2658. https://ui.adsabs.harvard.edu/abs/2013EGUGA..15.2658L

Li P. 2006. Reconstruction of Burial History of Strata in the North Louisiana Salt Basin Area. GCAGS Transactions. 56:455–471.

MacRae G. 1994. Mesozoic development of the DeSoto Canyon Salt Basin in the framework of the early evolution of the Gulf of Mexico [Thesis] [Internet]. [place unknown]: Texas A&M University. Libraries; [accessed 2024 Jan 30]. https://oaktrust.library.tamu.edu/handle/1969.1/DISSERTATIONS-1489401

McKenzie D. 1978. Some remarks on the development of sedimentary basins. Earth and Planetary Science Letters [Internet]. [accessed 2022 Jul 29] 40(1):25–32. https://doi.org/10.1016/0012-821X(78)90071-7

Müller RD, Cannon J, Qin X, Watson RJ, Gurnis M, Williams S, Pfaffelmoser T, Seton M, Russell SHJ, Zahirovic S. 2018. GPlates: Building a Virtual Earth Through Deep Time. Geochemistry, Geophysics, Geosystems [Internet]. [accessed 2024 Mar 9] 19(7):2243–2261. https://doi.org/10.1029/2018GC007584

Müller RD, Seton M, Zahirovic S, Williams SE, Matthews KJ, Wright NM, Shephard GE, Maloney KT, Barnett-Moore N, Hosseinpour M. 2016. Ocean basin evolution and global-scale plate reorganization events since Pangea breakup. Annual Review of Earth and Planetary Sciences. 44(1):107–138.

Müller RD, Zahirovic S, Williams SE, Cannon J, Seton M, Bower DJ, Tetley MG, Heine C, Le Breton E, Liu S, et al. 2019. A Global Plate Model Including Lithospheric Deformation Along Major Rifts and Orogens Since the Triassic. Tectonics [Internet]. [accessed 2022 Aug 24] 38(6):1884–1907. https://doi.org/10.1029/2018TC005462

Pindell J, Kennan L. 2009. Tectonic evolution of the Gulf of Mexico, Caribbean and northern South America in the mantle reference frame: An update. Geological Society, London, Special Publications. 328:1–55. https://doi.org/10.1144/SP328.1

Pindell J, Villagómez D, Molina-Garza R, Graham R, Weber B. 2021. A revised synthesis of the rift and drift history of the Gulf of Mexico and surrounding regions in the light of improved age dating of the Middle Jurassic salt. Geological Society, London, Special Publications [Internet]. [accessed 2022 Aug 24] 504(1):29–76. https://doi.org/10.1144/SP504-2020-43

Reguzzoni M, Sampietro D. 2015. GEMMA: An Earth crustal model based on GOCE satellite data. International Journal of Applied Earth Observation and Geoinformation [Internet]. [accessed 2022 Sep 12] 35:31–43. https://doi.org/10.1016/j.jag.2014.04.002

Şengör AMC, Natal'in BA. 2001. Rifts of the world. In: Ernst RE, Buchan KL, editors. Mantle plumes: their identification through time [Internet]. Vol. 352. [place unknown]: Geological Society of America; [accessed 2023 Jan 10]; p. 0. https://doi.org/10.1130/0-8137-2352-3.389

Seton M, Müller RD, Zahirovic S, Gaina C, Torsvik T, Shephard G, Talsma A, Gurnis M, Turner M, Maus S, Chandler M. 2012. Global continental and ocean basin reconstructions since 200Ma. Earth-Science Reviews [Internet]. [accessed 2022 Dec 18] 113(3):212–270. https://doi.org/10.1016/j.earscirev.2012.03.002

Xie F, Wu Q, Wang L, Shi Z, Zhang C, Liu B, Wang C, Shu Z, Di H. 2019. Passive continental margin basins and the controls on the formation of evaporites: a case study of the Gulf of Mexico Basin. Carbonates and Evaporites. 34. https://doi.org/10.1007/s13146-017-0404-z

Xie X, Heller PL. 2009. Plate tectonics and basin subsidence history. GSA Bulletin [Internet]. [accessed 2022 Dec 18] 121(1–2):55–64. https://doi.org/10.1130/B26398.1

Appendix B

Supporting Information for Topographic Diversity in Subduction-Related Mountains Driven by Plate Tectonics and Mantle Dynamics

Topographic Diversity in Subduction-Related Mountains Driven by Plate Tectonics and Mantle Dynamics

Satyam Pratap Singh[1], Maria Seton[1], Sabin Zahirovic[1], Nicky M. Wright[1], Nicholas Atwood[2], Clement Fay[3]

[1]*EarthByte Group, School of Geosciences, The University of Sydney, NSW 2006, Australia*
[2]*BHP Minerals Service Co, Tucson, Arizona 85704, USA*
[3]*BHP Minerals Service Co, Victoria Street, London SW1E 5LB, UK*

Corresponding Author: Satyam Pratap Singh (satyampratap.singh@sydney.edu.au)

Contents of this file

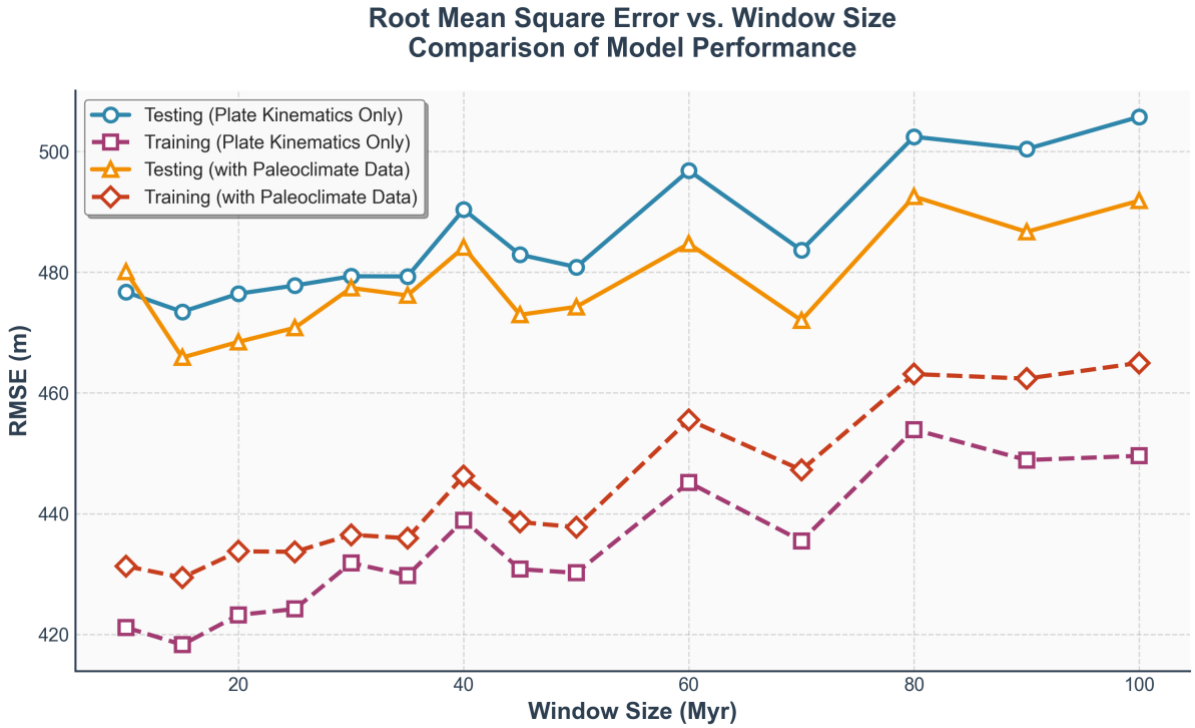

Supplementary Figure S1: Root Mean Square Error (RMSE) as a function of window size used for temporal averaging of plate kinematic and precipitation variables. Four model configurations are compared: plate kinematics only (training: purple dashed, testing: blue solid) and with climate variables (training: red dashed, testing: orange solid). Optimal window sizes minimize overfitting while maintaining predictive accuracy.

a)

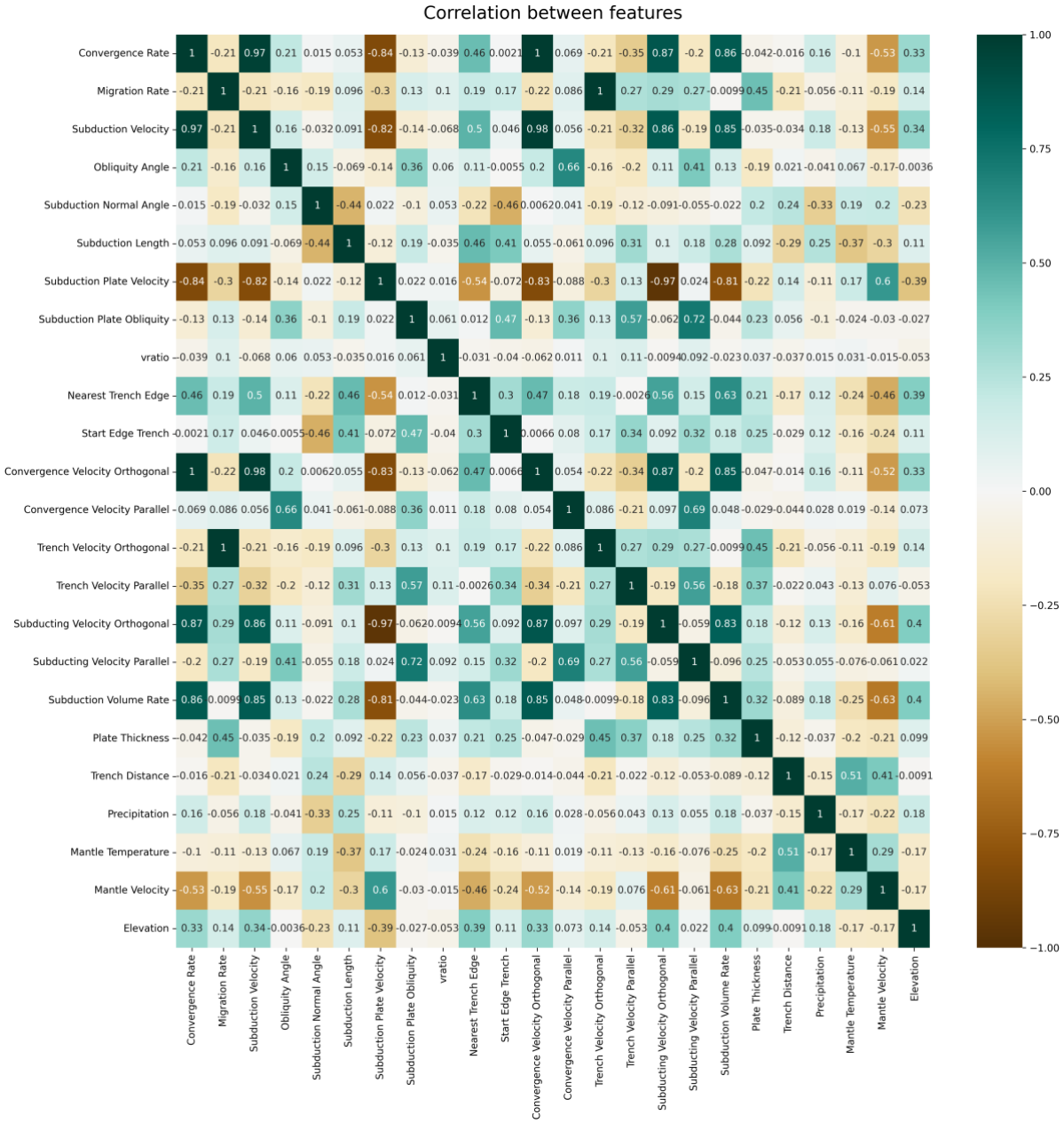
Correlation between features
Convergence Rate
Migration Rate
Subduction Velocity
Obliquity Angle
Subduction Normal Angle
Subduction Length
Subduction Plate Velocity
Subduction Plate Obliquity
vratio
Nearest Trench Edge
Start Edge Trench
Convergence Velocity Orthogonal
Convergence Velocity Parallel
Trench Velocity Orthogonal
Trench Velocity Parallel
Subducting Velocity Orthogonal
Subducting Velocity Parallel
Subduction Volume Rate
Plate Thickness
Trench Distance
Precipitation
Mantle Temperature
Mantle Velocity
Elevation
1.00
0.75
0.50
0.25
0.00
−0.25
−0.50
−0.75
−1.00

b)

Supplementary Figure S2: a) Pearson correlation between all the extracted parameters b) Pearson correlation between parameters used to build the final XAI model.

Supplementary Table 1: Summary of Predictive Features in the preferred EBM model.

Category	Parameters	Brief Explanation
Plate Kinematics	Subduction Flux	Volume rate of lithosphere being subducted; proxy for tectonic forcing on the overriding plate
Plate Kinematics	Trench Migration Rate	Rate of advancement or retreat of the trench, reflecting slab dynamics and overriding plate motion

Plate Kinematics	Trench Distance	Minimum distance from mountain location to the nearest trench; captures tectonic influence and continent/leeward dynamics.
Mantle Dynamics	Upper Mantle Temperature	Mean temperature at 200–440 km depth; colder regions support higher topography
Mantle Dynamics	Upper Vertical Flow Velocity	Mean vertical velocity in upper mantle; upwellings elevate, downwellings lower elevation
Long-term Climate	Paleoprecipitation	Mean annual precipitation over the relevant geologic window; regulates erosion and isostatic uplift

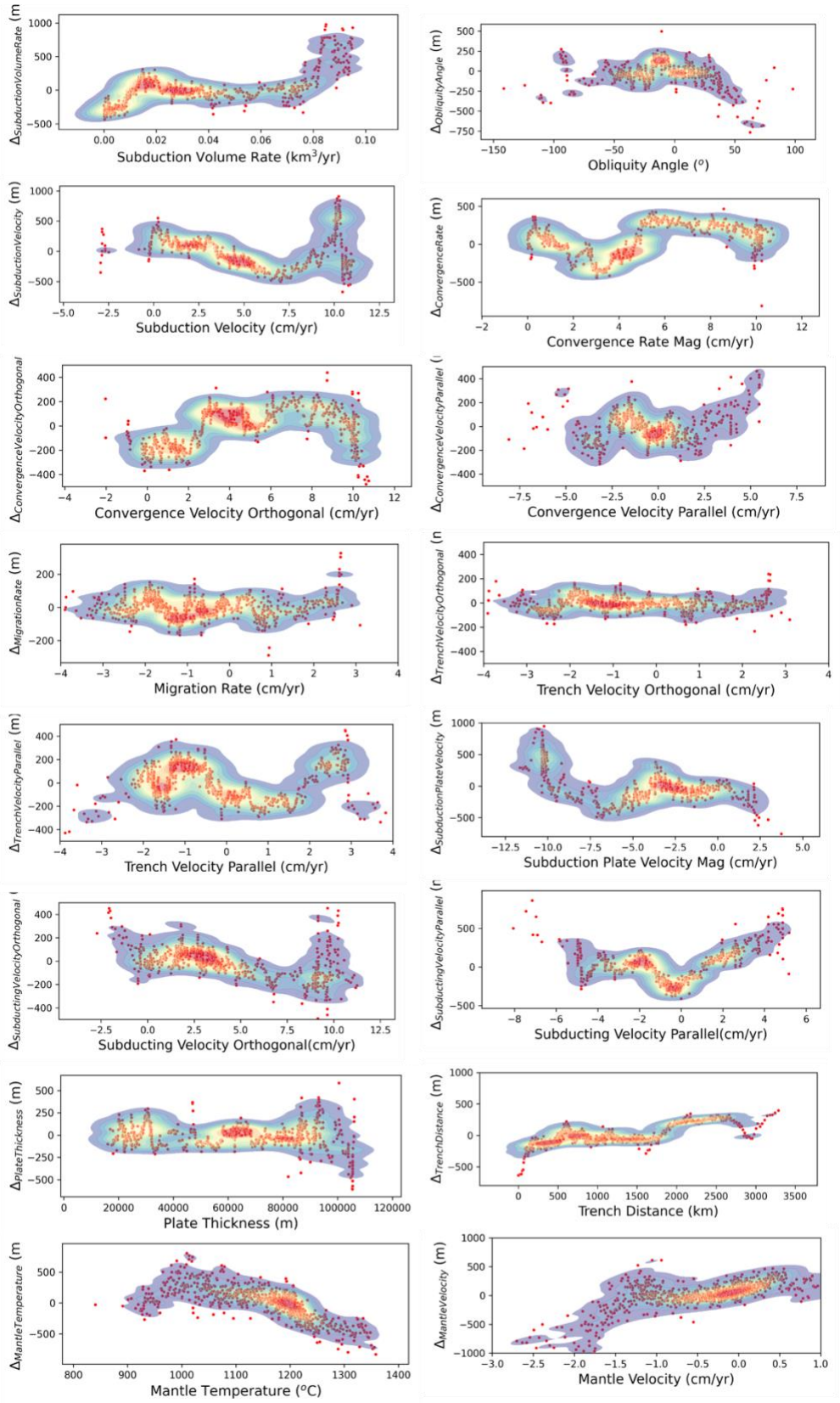

Supplementary Figure S3: Shape function for an XAI model incorporating all extracted parameters. The figure illustrates that increasing model complexity hinders interpretability. While adding more parameters slightly improved accuracy (from 444 m to 410 m), it also reduced the model's explanatory clarity.

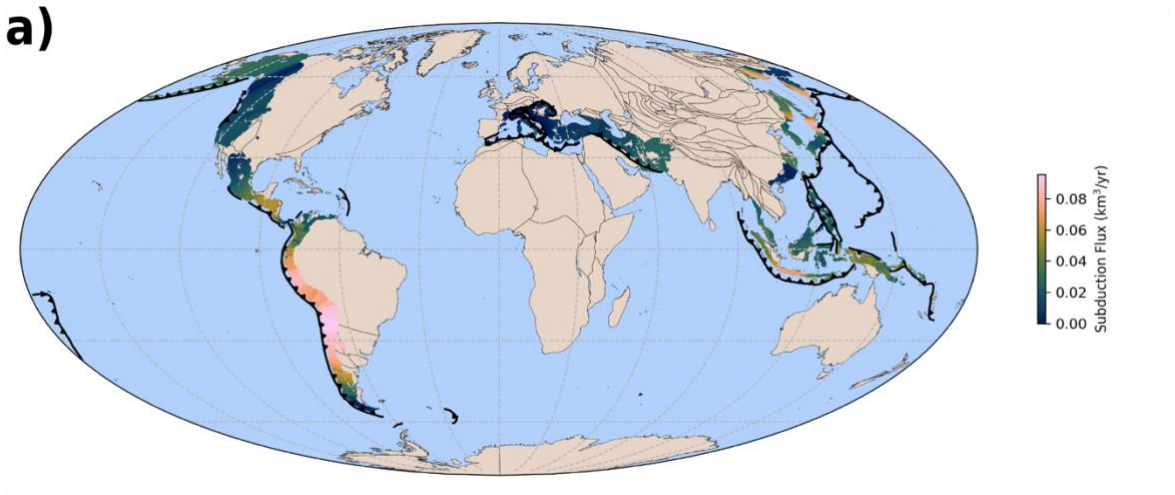
a)
0.08
0.06
0.04
0.02
0.00
Subduction Flux (km³/yr)

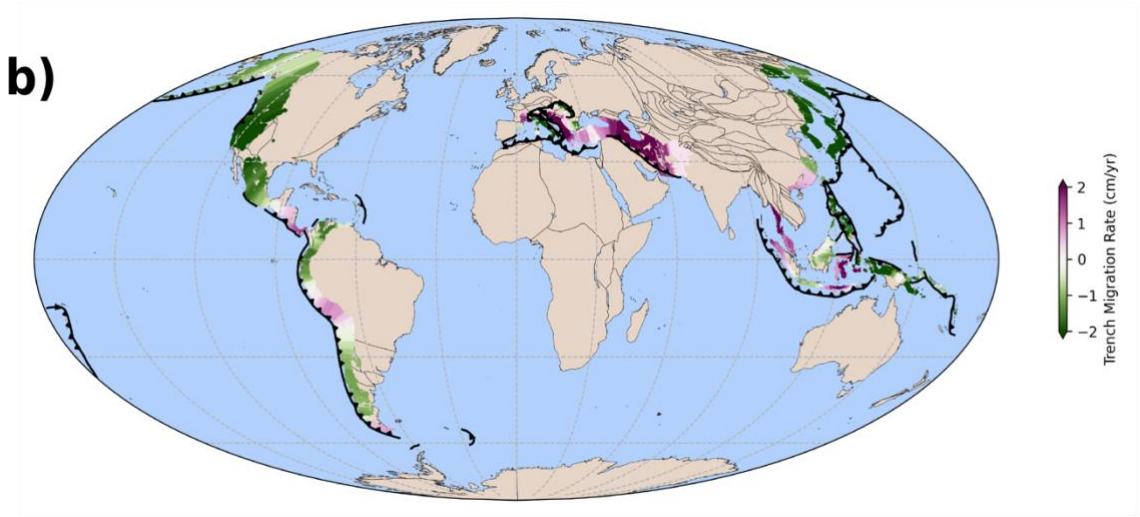
b)
2
1
0
−1
−2
Trench Migration Rate (cm/yr)

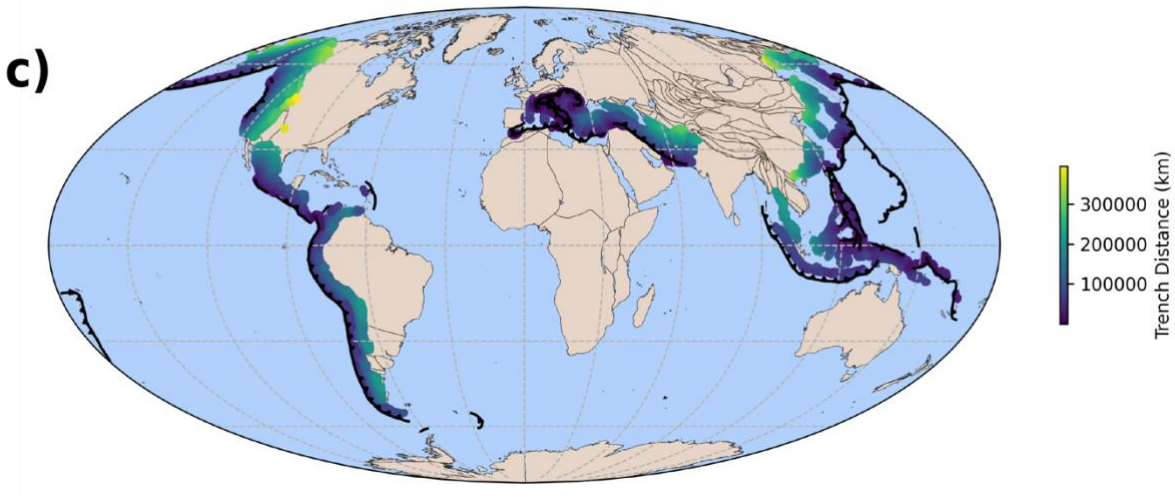
c)
300000
200000
100000
Trench Distance (km)

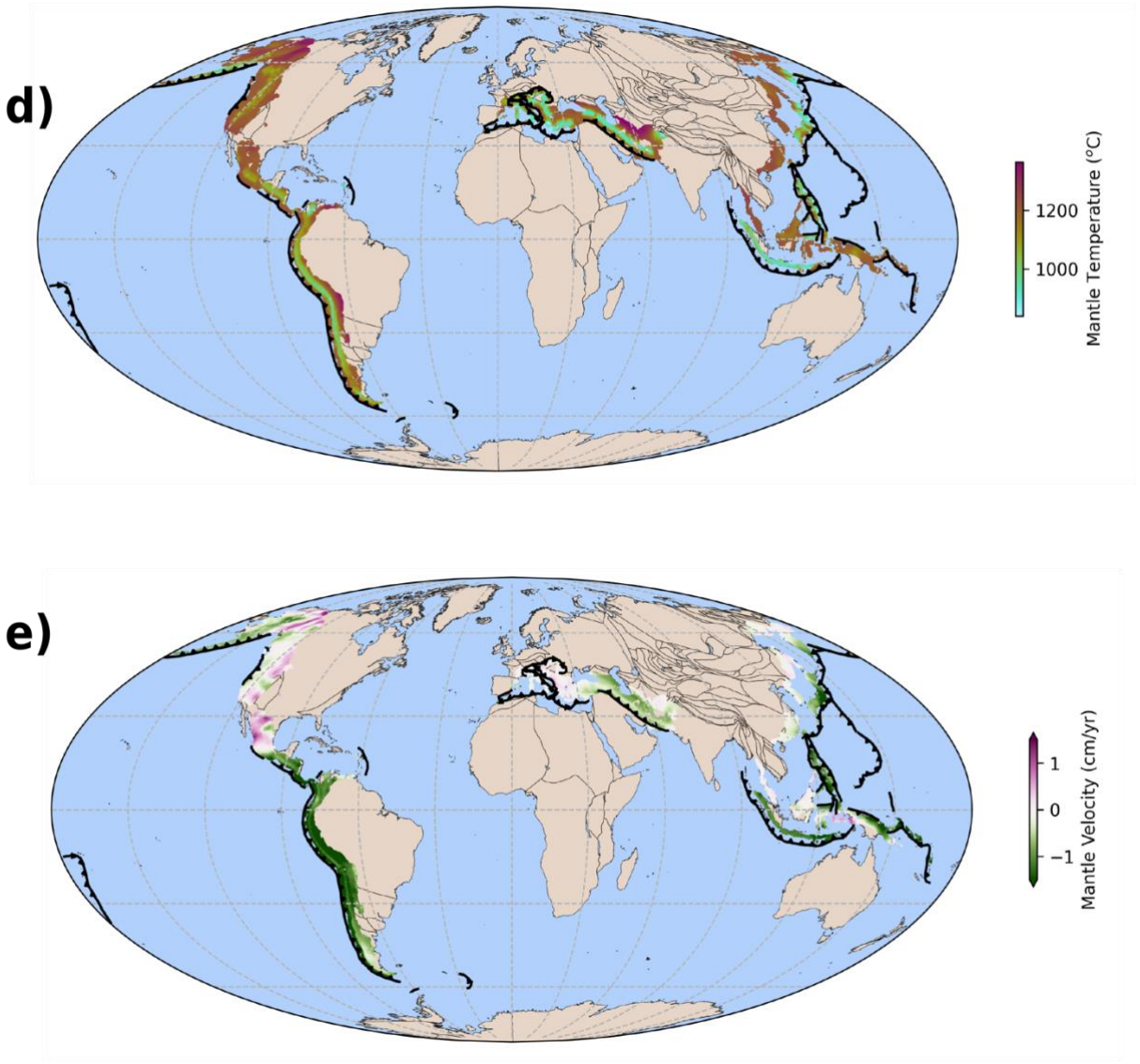

Supplementary Figure S4: Geospatial distribution of different parameters used for training our model. a) mean subduction flux rate, b) mean trench migration rate, c) distance from trench d) upper mantle temperature, e) vertical mantle flow velocity

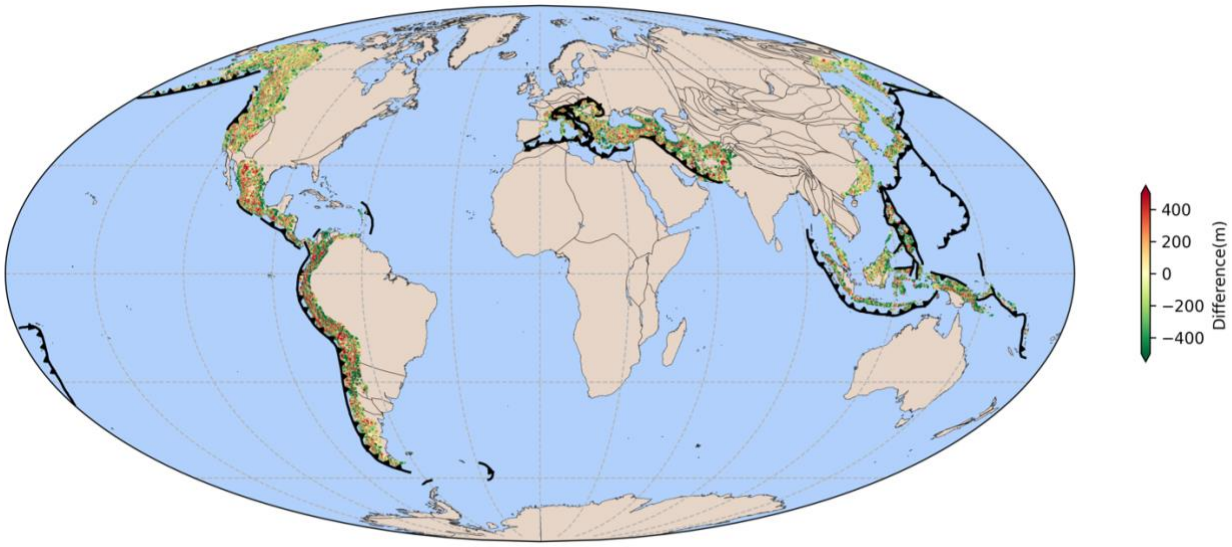

Supplementary Figure S5: The absolute difference between actual and predicted elevations.

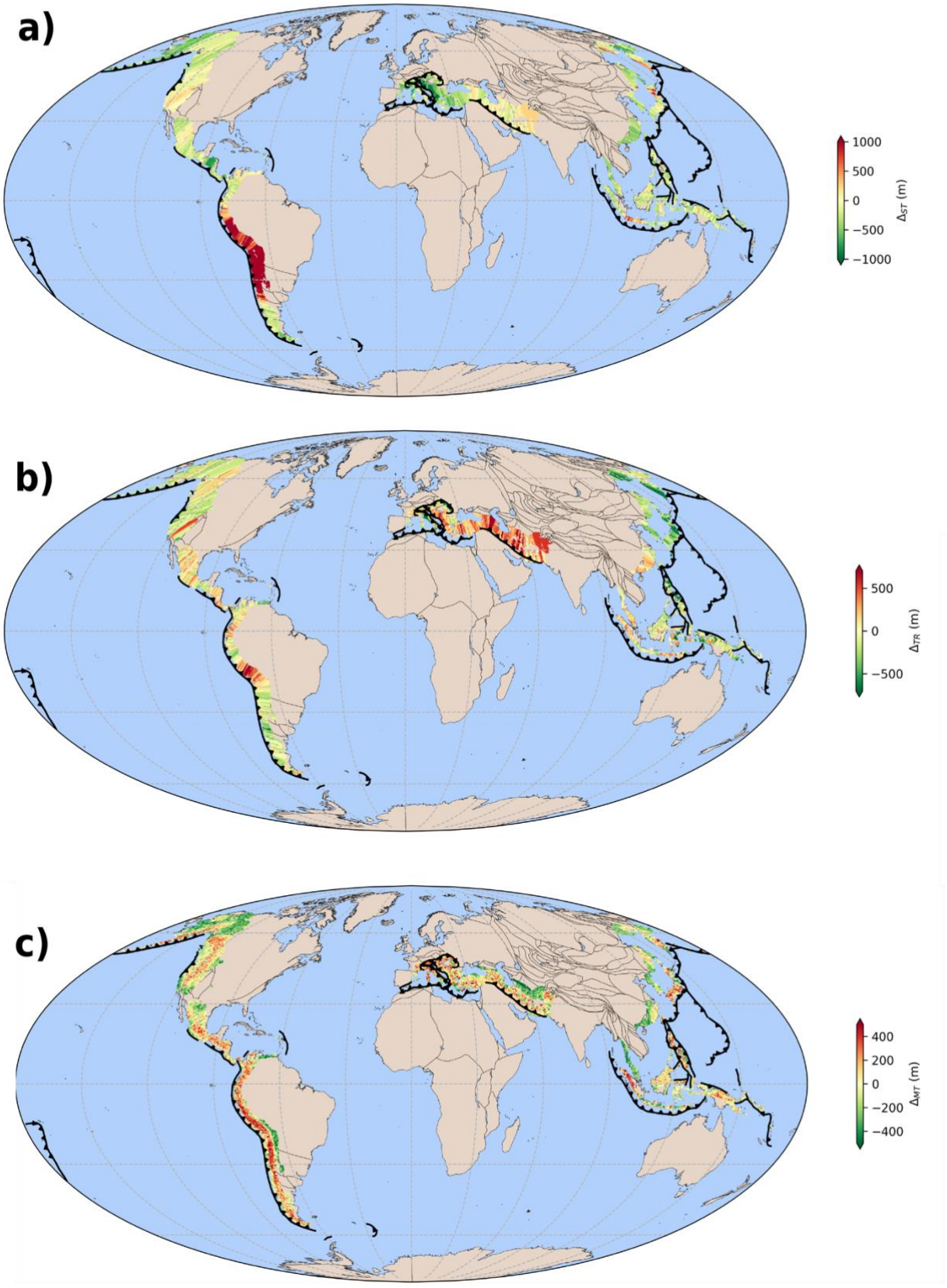
a)
1000
500
0
−500
−1000
Δ_{ST} (m)
b)
500
0
−500
Δ_{TR} (m)
c)
400
200
0
−200
−400
Δ_{MT} (m)

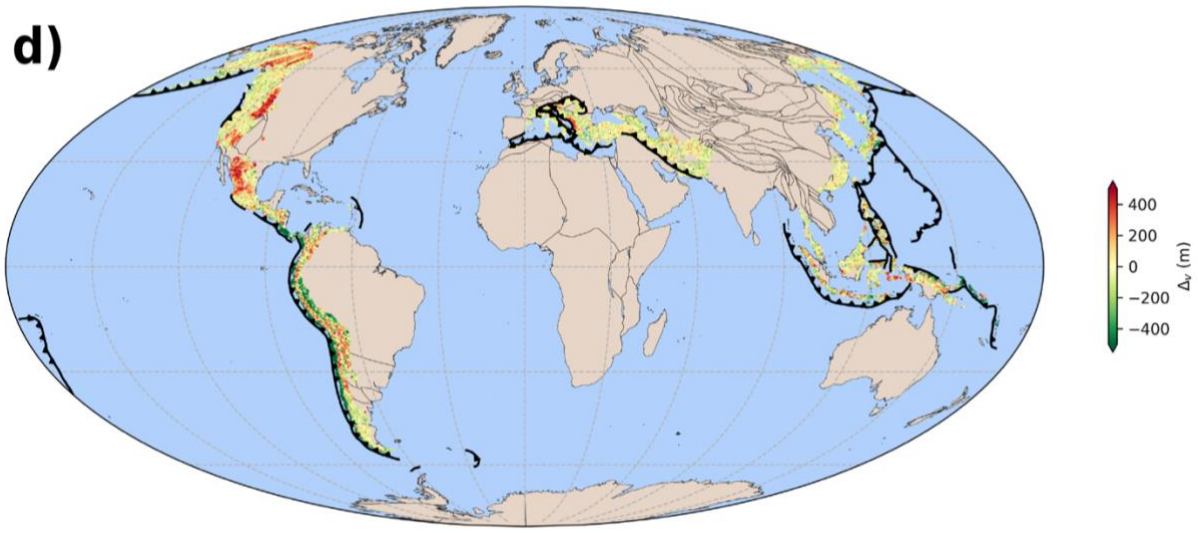

Supplementary Figure S6: Geospatial Explanation: Spatial distribution of contribution factor corresponding to different parameters used in our model. a) mean subduction flux rate, b) mean trench migration rate, c) upper mantle temperature, d) vertical mantle flow velocity

Appendix C

Supporting Information for Deep Learning Reconstructs Global Active Margin Paleotopography Since the Mesozoic from Plate Kinematics and Mantle Dynamics

Supporting Information for

Deep Learning Reconstructs Global Active Margin Paleotopography Since the Mesozoic from Plate Kinematics and Mantle Dynamics

Satyam Pratap Singh[1,2*], Maria Seton[1], Sabin Zahirovic[1], Nicky M. Wright[1], Simon Williams[3], Jianping Zhou[1,4]

[1]EarthByte Group, School of Geosciences, The University of Sydney, NSW 2006, Australia
[2]Now at Geonome Pty Ltd, NSW 2010, Australia
[3]Institute for Marine and Antarctic Studies, University of Tasmania, Hobart, TAS 7001, Australia
[4] Frontiers Science Centre for Deep Ocean Multispheres and Earth System, Key Lab of Submarine Geosciences and Prospecting Techniques, MOE and College of Marine Geosciences, Ocean University of China, Qingdao, China

Content

1 Methods

To model the paleotopography along active margins, we employ a deep feed-forward neural network capable of learning non-linear relationships between tectonic, geodynamic, and paleoclimate-informed constraints and surface elevation. Our workflow integrates global plate kinematics, a mantle convection model, and climate proxies to reconstruct topography through deep time.

1.1 Spherical Grid Generation and Sampling Strategy

We delineated polygons surrounding all subduction zones on the overriding plate using a global plate tectonic reconstruction (Merdith et al., 2021) at 1 Myr intervals from 200 Ma to the present. Within these polygons, we generated an approximately uniform spherical grid with a target spacing of ~0.1° in latitude and longitude. This provides consistent global coverage while avoiding the geometric distortions inherent in planar projections, ensuring mathematically rigorous sampling across all latitudes and hemispheres. Subduction zones were discretised directly on this spherical grid, enabling the capture of spatial variations in kinematics along entire trench lengths. Sampling points at 0.1° spacing were assigned to convergent boundaries and projected orthogonally toward the overriding plate to define the domain from which neural-network training samples were extracted.

1.2 Plate-Kinematic History

Plate kinematic parameters were reconstructed using the global plate tectonic model of Merdith et al., (2021) with plate motions referenced to an optimised mantle-fixed reference frame. Present-day and past trench geometries were discretised at 0.1° intervals and filtered to include only segments associated with subducting slabs in the Slab2 model (Hayes et al., 2018). For each trench point and each 1 Myr timestep, we extracted a suite of kinematic variables, including convergence velocity (magnitude and trench-normal/trench-parallel components), trench migration velocity (magnitude and vector components relative to the mantle frame), obliquity angle, lithospheric age and thickness of the subducting plate, lithospheric age of the overriding plate (if oceanic; otherwise assigned as not a number), and subduction flux.

Subduction flux(Q) was computed as:

$$Q = h\,L\,v_c,$$

where h is the thickness of the subducting oceanic lithosphere, L is the local arc length of the trench segment, and v_c is the convergence rate (trench-normal component of convergence velocity with respect to trench). Lithospheric thickness was estimated using the half-space cooling model of Parsons & Sclater, (1977), with seafloor ages derived from the reconstruction model (Merdith et al., 2021). Because present-day and paleo-elevation reflect

the cumulative effects of tectonic processes operating over multimillion-year timescales, we evaluated multiple averaging intervals for plate-kinematic forcing. To ensure the robustness of the STN, we conducted a systematic sensitivity analysis of the kinematic averaging window (10–100 Myr). As detailed in Supplementary Table 2, the STN displays stable and consistently high performance across all evaluated windows, with R^2 scores ranging from 0.73 to 0.77. The negligible variation in predictive accuracy indicates that the model is robust to the choice of time-averaging. This mathematical stability allowed us to select the 25 Myr window based on primary geodynamic considerations: Balancing the multi-million-year response time of the lithosphere with the need to filter high-frequency noise from plate reconstruction artifacts. This 25 Myr integration period is physically consistent with the timescales of crustal thickening and the thermal-mechanical response of the overriding plate to subduction forcing (Candioti et al., 2020; Knight et al., 2020; Sobouti & Arkani-Hamed, 2002). For each sampling point, mean plate-kinematic parameters were therefore computed over this 25 Myr window, ensuring that the forcing reflects the tectonic context most relevant to surface elevation at each timestep. This approach captures long-term tectonic context while emphasising the processes most relevant to surface topography at each timestep.

1.3 Mantle Dynamics

Deep mantle circulation exerts a first-order control on long-wavelength topography and complements the upper-plate forcing captured by plate kinematics (Braun, 2010; Flament et al., 2013). To incorporate these deeper processes, we used global, time-dependent mantle convection simulations generated with *CitcomS*, a finite-element spherical model that solves the conservation equations for mass, momentum, and energy under a pseudo-compressible formulation (Tan et al., 2006; Zhong et al., 2000; Zhong & Gurnis, 1995). The simulations are driven by the Merdith et al. (2021) plate tectonic reconstruction and impose constraints on lithospheric thermal structure and slab geometry, following the approach of Bower et al., (2015). As a result, downwellings at active margins reflect both convergence rate and the negative buoyancy of subducting slabs, enabling a physically consistent representation of plate–mantle coupling through geological time. To incorporate mantle contributions to surface elevation, we sampled the reconstructed mantle temperature and vertical flow velocity beneath each surface grid point across a series of depth horizons. We extracted values at seventeen depth levels between 200 km and 660 km, spanning the base of the lithosphere to the uppermost lower mantle (Supplementary Table 2). Shallower levels primarily record the influence of recent slab descent, whereas deeper slices capture older subduction signals that modulate longer-term dynamic topography. The resulting 26 mantle parameters (temperature and vertical velocity at each depth) provide the neural network with a dynamically coherent description of mantle forcing that complements, and extends beyond, plate kinematic information alone

1.4 Equatorial Humid-Belt Residency

Surface elevation is also influenced by long-term climatic conditions, particularly orographic precipitation, chemical weathering, and erosion (Clark et al., 2004; Whipple, 2009). Rather than using paleoclimate models—which typically require paleotopography as an input—we adopt a heuristic but robust proxy for long-term moisture availability: the cumulative time a location has resided within the equatorial humid belt. Defined as the paleolatitudinal zone between ±10° (Macdonald et al., 2019), this belt has persistently exhibited high rainfall over

geological time (e.g. Li et al., 2022) and therefore provides a meaningful predictor of erosional potential at convergent margins. To assess the sensitivity of this choice, we additionally tested humid-belt half-widths of 15° and 20°; across these experiments, the misfit (Supplementary Section 1.7) varied by less than 50 m, with the ±10° definition yielding the lowest error.

For each reconstruction point, we track its paleolatitude through time in a paleomagnetic reference frame (Merdith et al., 2021) and compute the total time spent inside the humid belt within the same temporal window used for plate-kinematic averaging**.** This produces a single climatic parameter that quantifies long-term moisture exposure relevant to surface processes. To capture additional topographic–climatic interactions, we also include the present-day distance to the nearest subduction trench, which approximates windward–leeward gradients in orographic precipitation (Singh et al., 2025).

1.5 Subduction Topography Network (STN)

STN is trained on present-day ETOPO1 elevations (Amante & Eakins, 2009), allowing it to learn relationships between inputs and observed topography (Figure 1). We selected deep neural networks over simpler models (random forest, gradient boosting) because preliminary testing showed that deep architectures better capture non-linear interactions between plate kinematics and mantle dynamics, particularly in regions with competing forces (e.g., trench retreat vs. high subduction flux). The architecture is illustrated in Supplementary Figure 1, which shows how geological data and geodynamic models are transformed into predicted elevation values through multiple processing layers. The input layer receives data points, each characterised by several different parameters, including subduction flux, trench migration rate, mantle temperature and vertical velocity at multiple depths, and climatic proxies (Supplementary Table 2). These features represent both time-averaged tectonic and climatic histories, as well as the deep mantle dynamics underlying each point. The input is passed through five fully connected (dense) hidden layers labelled FC1 through FC5. We tested 4, 6, and 8-layer architectures via our validation framework (Section 1.9); 6 layers showed the best validation performance while maintaining training stability. These layers contain a progressively smaller number of neurons—from 1,024 down to 32—mimicking the way geologists extract dominant signals from complex data. Layer widths were halved at each step to create a bottleneck effect, concentrating learned features. Each hidden layer acts as a feature extractor (Goodfellow et al., 2016; LeCun et al., 2015; Singh & Silwal, 2023): initial layers might detect broad subduction patterns, while deeper layers recognise more subtle combinations, such as interactions between subduction kinematics and mantle flow. For instance, the network may learn that high subduction flux combined with an advancing trench and cold mantle temperatures is associated with overriding plate uplift. The final layer is a single-node output that predicts elevation at each input point. Because our input grid covers tectonically active regions at high spatial resolution. In this configuration, the deep learning model functions as a meta-modeler—synthesizing plate kinematics, mantle convection, and climate across both space and time. It learns which combinations of these factors best explain present-day elevation and uses that knowledge to infer paleo-elevation throughout Earth's history.

1.6 STN Dataset Preparation and Feature Standardisation

The compiled dataset was partitioned into training and validation sets using a spatially informed 80/20 split to avoid spatial leakage artefacts (Venkateswaran et al., 2016). Eighty per cent of sampling points located within discrete, geographically distinct arc segments were assigned to the training set for fitting model weights, while the remaining 20%—drawn from spatially separated arc segments not present in the training set—was reserved as an independent test set for validation and model selection (Figure 2). This spatially stratified partitioning ensures that the model is evaluated on truly held-out regions with different tectonic characteristics, providing a rigorous assessment of generalisation performance rather than inflated validation metrics from spatial autocorrelation (Roberts et al., 2017; Valavi et al., 2019). All input features were standardised using RobustScaler (https://scikit-learn.org/stable/modules/preprocessing.html), computed on the training set only to prevent data leakage. RobustScaler is preferred over standard scaling methods because it is robust to outliers, using median and interquartile range rather than mean and standard deviation (Huber & Ronchetti, 2009). Standardisation was applied independently to each input parameter to ensure numerical stability and facilitate more efficient gradient-based optimisation during neural network training.

1.7 STN Architecture and Regularisation

The network was implemented as a deep feed-forward architecture with five fully connected layers, batch normalisation, dropout regularisation, and L2 weight decay to limit overfitting (Goodfellow et al., 2016; Kingma & Ba, 2017). Progressive halving of neuron counts (1024→512→256→128→64→32) creates a bottleneck that forces compression of learned features, reducing model complexity. All hidden layers use Rectified Linear Unit (ReLU) activations; output uses linear activation for continuous elevation prediction (Glorot et al., 2011). Batch normalisation is applied after each hidden layer to reduce internal covariate shift and stabilise training (Santurkar et al., 2019). Dropout regularisation (0.1–0.3) randomly deactivates a fraction of neurons during training to prevent co-adaptation and overfitting (Srivastava et al., 2014). L2 weight decay ($\lambda = 10^{-4}$) adds a penalty term to the loss function proportional to the magnitude of model weights, encouraging smaller weights and reducing model complexity (Goodfellow et al., 2016).

1.8 Loss Function and Performance Metrics

We minimised the mean-squared error (MSE) between observed present-day elevation

(ETOPO1; Amante & Eakins, 2009) and model-predicted elevation (Hastie et al., 2009):

$$\mathrm{MSE} = \frac{1}{N}\sum_{i=1}^{N} w_i\left(y_i^{\mathrm{obs}} - y_i^{\mathrm{pred}}\right)^2$$

where $y_i^{\text{obs}}$is the observed elevation, $y_i^{\text{pred}}$is the predicted elevation, $w_i$is an optional sample weight (defaulting to 1), and N is the number of training samples.

We report root-mean-square error (RMSE) and mean absolute error (MAE) as primary performance metrics (Chai & Draxler, 2014):

$$\text{RMSE} = \sqrt{\frac{1}{N}\sum_{i=1}^{N}\left(y_i^{\text{obs}} - y_i^{\text{pred}}\right)^2}$$

$$\text{MAE} = \frac{1}{N}\sum_{i=1}^{N}\left|y_i^{\text{obs}} - y_i^{\text{pred}}\right|$$

These metrics provide complementary information: RMSE penalises larger errors more heavily and is sensitive to outliers, while MAE provides a robust measure of average prediction error (Willmott & Matsuura, 2005).

1.9 Model Optimisation and Training Procedure

Model optimisation used the Adam optimiser (Kingma & Ba, 2017) with an initial learning rate of 0.005 (Supplementary Table 3). Training proceeded in mini-batches with a batch size of 1024 samples. Regularisation and training-stability measures included dropout (0.1–0.3), L2 weight decay ($\lambda = 10^{-4}$), and batch normalisation (Goodfellow et al., 2016; Srivastava et al., 2014). We applied an adaptive learning-rate schedule (ReduceLROnPlateau: factor =0.5, patience = 2 epochs) to reduce learning rate when validation loss plateaued (Smith, 2017), and implemented early stopping: training halted when the validation loss failed to improve for 20 consecutive epochs (minimum delta = 10^{-4}) to avoid overfitting (Prechelt, 1998).

Hyperparameter choices (network depth and width, dropout rates, weight decay magnitude, batch size, learning-rate schedule) were selected via spatially stratified cross-validation across distinct trench segments, ensuring that hyperparameter optimisation did not introduce spatial bias. Final model performance was assessed on the held-out test set and by inspecting spatial error patterns across different tectonic settings (R1-R5, Figure 2). Representative hyperparameter values for the final model are provided in Supplementary Table 3.

1.10 Validation and Comparison Framework

To rigorously assess the performance of our trained neural network, we implemented a multi-tiered validation framework incorporating both present-day and paleoelevation datasets.

1.10.1 Present-Day Topography Validation

To evaluate the predictive skill and generalisability of the trained neural network, we implemented a validation strategy based on geographically independent test regions. Instead of using a random global split, we withheld approximately 20% of the present-day dataset by

selecting five tectonically diverse arc segments (R1–R5) that span a range of convergent margin settings, including continental arcs, island arcs, and collisional orogens. These regions were entirely excluded from model training to ensure that validation reflects true extrapolative performance rather than spatial autocorrelation.

Model predictions within these withheld regions were compared against present-day elevation from ETOPO1 at matching spatial resolution (0.1°). Evaluation metrics included RMSE, (MAE, and R^2. In addition to these quantitative metrics, we assessed spatial patterns of prediction error to examine whether systematic biases occur under specific combinations of plate kinematics, slab dynamics, or climatic conditions. By validating exclusively on tectonically contrasting margin segments that were never seen during training, this approach provides a robust test of the model's ability to reconstruct topographic structure from geodynamic and climatic inputs alone.

1.10.2 Paleoelevation Validation Using Independent Geological Constraints

Beyond present-day validation, we tested the model's paleoelevation predictions against independent proxy datasets across key tectonic regions and timescales.

Global Active Margin Validation (Mesozoic to Present)

We extended validation to a global scale by comparing predicted paleoelevations with a compilation of 39 geochemical proxies from arc-related magmatic rocks spanning ~200 Ma to present uisng the framework proposed by Liu et al, (2024). These proxies (e.g., Sr/Y, La/Yb, Gd/Yb ratios) serve as paleo-crustal thickness indicators, which are first-order controls on surface elevation in convergent margins. Data were sourced from GEOROC and EarthChem databases and binned temporally at 10 Myr intervals and spatially at 0.5° resolution to accommodate dating uncertainties. We translated crustal thickness into elevation using empirical relationships developed by Luffi & Ducea (2022). Median elevation estimates derived from this geochemical dataset carry an uncertainty range of approximately 2000–3000 m. Several challenges complicate this comparison. Plate reconstructions used to spatially back-project proxies assume rigid continental fragments, yet active margins frequently experience crustal shortening, extension, and distributed deformation (King & Welford, 2022; Müller et al., 2019). Consequently, geological markers may be displaced or eroded, limiting precise spatial correlation. Additionally, some geochemical proxies may be influenced by mantle-derived contamination from non-magmatic arc sources, potentially decoupling geochemical signals from crustal thickness (Luffi & Ducea, 2022). Despite these caveats, the comparison provides valuable large-scale validation where direct paleoelevation proxies are sparse.

Andean Paleotopography (Late Cretaceous to Present)

We compared model predictions for the Andes with a regional paleotopographic synthesis compiled by Boschman (2021). Boschman integrated multiple proxy datasets—including stable isotope paleoaltimetry ($\delta^{18}O$), sedimentological, and paleobotanical records—spanning 80 Ma to present and generated time-sliced paleoelevation grids covering the entire Andean margin. This comparison allows us to evaluate both spatial and temporal fidelity of our predictions relative to well-constrained geological reconstructions of orogenic growth.

East Asia (Jurassic to Present)

In East Asia, we evaluated predicted Jurassic to present elevations against crustal thickness estimates derived from trace-element geochemical ratios (e.g., Sr/Y, La/Yb) measured in arc magmatic rocks. These geochemical proxies were translated into paleoelevation using two complementary approaches. Li et al. (2024) employed a conventional empirical calibration based on present-day crustal thickness–elevation relationships. In contrast, Zhou et al. (2025) utilized a CatBoost machine learning regression model that captures potentially complex, non-linear relationships between geochemical signatures (including SiO_2, MgO, Sr/Y, La/Yb) and crustal thickness, achieving high cross-validated accuracy. They converted crustal thickness (H) to surface elevation (h) using an empirical linear relation valid for H > 20 km:

$$H = 6.79\ (\pm 0.95) \times h + 26.40\ (\pm 1.45)\ ,$$

While this conversion assumes a uniform elevation–Moho correlation across tectonic settings, it may not fully capture complexities such as mantle-derived contamination, crustal compositional heterogeneity, or local tectonic variations. Additionally, the spatial distribution and quality of geochemical samples influence the robustness of the paleoelevation estimates.

Though these two methods produce notably different absolute elevation values, both consistently constrain the timing and geographic distribution of major orogenic phases across East Asia. Their inclusion thus provides a robust, multi-method benchmark for evaluating the fidelity of our model predictions and offers critical insights into the spatiotemporal evolution of paleotopography under varying methodological assumptions.

1.11 Reproducibility and Code Availability

All random seeds and implementation details to reproduce training runs—including the full hyperparameter search and evaluation scripts—are available in the project repository: https://github.com/singhsatyampratap/pyDTDM

Supplementary Table 1: STN Training Performance Sensitivity to plate kinematics parameters

Kinematic Window (Myr)	**MAE (m)**	**RMSE (m)**	**R2**
10	457.45	744.00	0.77
15	489.91	798.90	0.73
25	488.50	803.25	0.73
35	497.12	807.20	0.73
45	458.71	757.99	0.76
60	464.25	760.66	0.76
80	481.99	782.25	0.75

Kinematic Window (Myr)	MAE (m)	RMSE (m)	R2
100	464.60	762.23	0.76

Supplementary Table 2: List of input variables used to train the deep learning model for predicting active margin topography from the Mid-Cambrian to present. The model architecture enables automated feature extraction and hierarchical learning, allowing it to infer the most influential parameters driving topographic variation.

Categories	Input Parameters
Plate Kinematics	Convergence Velocity (Orthogonal and Parallel), Trench Migration Rate (Orthogonal and Parallel), Subduction Volume Rate, Subduction Length (Spatial), Distance from Nearest Slab Edge (Slab Width), Lithospheric Age of Overriding Plate (if oceanic)
Mantle Dynamics	Upper-mantle temperature and slab-sinking velocity were extracted at 13 depths: 202, 217, 233, 268, 293, 323, 357, 396, 439, 487, 540, 597, and 660 km.
Climate	Distance from Trench, Time spent in equatorial humid belts

Supplementary Table 3: These hyperparameters were selected through cross-validation and resulted in optimal validation performance while preventing overfitting.

Hyperparameter	Value	Rationale
Optimiser	Adam	Adaptive learning rates for efficient convergence (Kingma & Ba, 2017)
Initial Learning Rate	0.005	Sufficiently small to permit fine-tuning; combined with adaptive schedule for stability (Smith, 2017)
Batch Size	1024	Balances computational efficiency with gradient estimate stability (Prechelt, 1998)
Loss Function	Mean Squared Error (MSE)	Standard for regression (Hastie et al., 2009)
Dropout Rate	0.1–0.3	Reduces co-adaptation of neurons and prevents overfitting (Srivastava et al., 2014)
L2 Weight Decay	10^{-4}	Regularisation strength balancing model complexity and fit quality (Goodfellow et al., 2016)
Learning Rate Schedule	ReduceLROnPlateau (factor = 0.5, patience = 2)	Reduces learning rate when validation loss plateaus, enabling convergence to better minima (Smith, 2017)
Early Stopping	Patience = 20 epochs; Min Delta = 10^{-4}	Prevents overfitting by halting when validation performance stagnates (Prechelt, 1998)
Feature Standardisation	RobustScaler	Robust to outliers; ensures numerical stability during gradient descend (Huber & Ronchetti, 2009)

Supplementary Figures

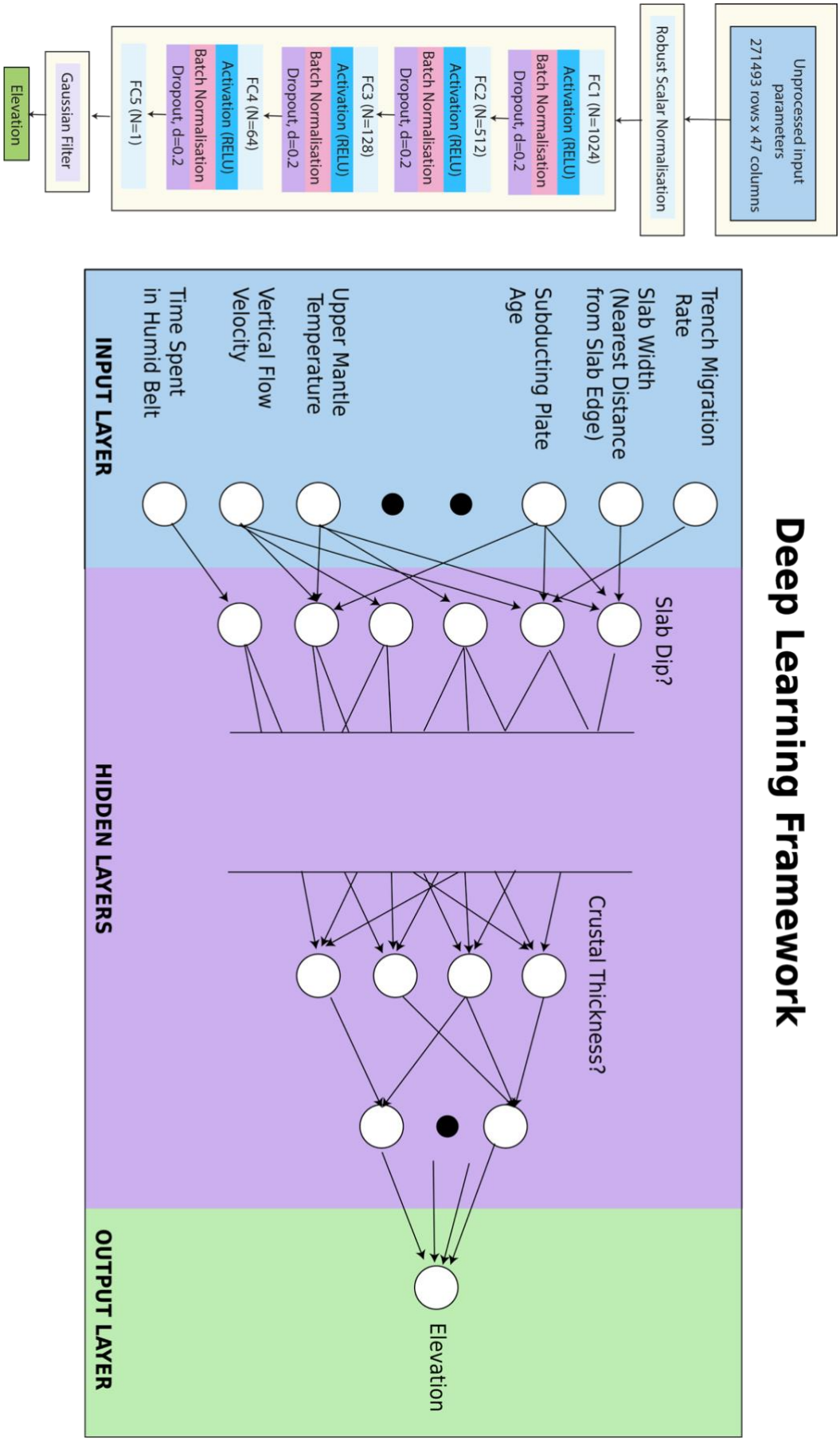
Unprocessed input parameters
271493 rows x 47 columns
Robust Scalar Normalisation
FC1 (N=1024)
Activation (RELU)
Batch Normalisation
Dropout, d=0.2
FC2 (N=512)
Activation (RELU)
Batch Normalisation
Dropout, d=0.2
FC3 (N=128)
Activation (RELU)
Batch Normalisation
Dropout, d=0.2
FC4 (N=64)
Activation (RELU)
Batch Normalisation
Dropout, d=0.2
FC5 (N=1)
Gaussian Filter
Elevation
Deep Learning Framework
Trench Migration Rate
Slab Width (Nearest Distance from Slab Edge)
Subducting Plate Age
Upper Mantle Temperature
Vertical Flow Velocity
Time Spent in Humid Belt
INPUT LAYER
Slab Dip?
Crustal Thickness?
HIDDEN LAYERS
Elevation
OUTPUT LAYER

Supplementary Figure 1 | Deep learning architecture used for elevation prediction. This figure illustrates the neural network architecture used to model present-day topography from a suite of tectonic, geodynamic, and climatic input parameters (see Supplementary Table 1 for the full list). The network is trained on ETOPO1 elevation data (Amante & Eakins, 2009) and learns complex, non-linear relationships between inputs and surface elevation. The input layer processes 37 features, including subduction flux, trench migration rates, mantle temperature and vertical velocity profiles, and paleoclimate constraint, representing the integrated surface–deep Earth system. These features are passed through five fully connected hidden layers (FC1–FC5), with neuron counts decreasing from 1,024 to 32, mimicking a hierarchical feature extraction process. Early layers capture broad geodynamic signals, while deeper layers resolve subtle interactions, such as the role of slab flux coupled with trench behaviour and mantle flow in driving surface uplift. Batch normalisation and dropout are applied at each layer to enhance generalisation. The output node predicts elevation at each location, enabling the model to act as a meta-model linking different processes to surface topography (see Singh et al., 2025 for interpretability analysis).

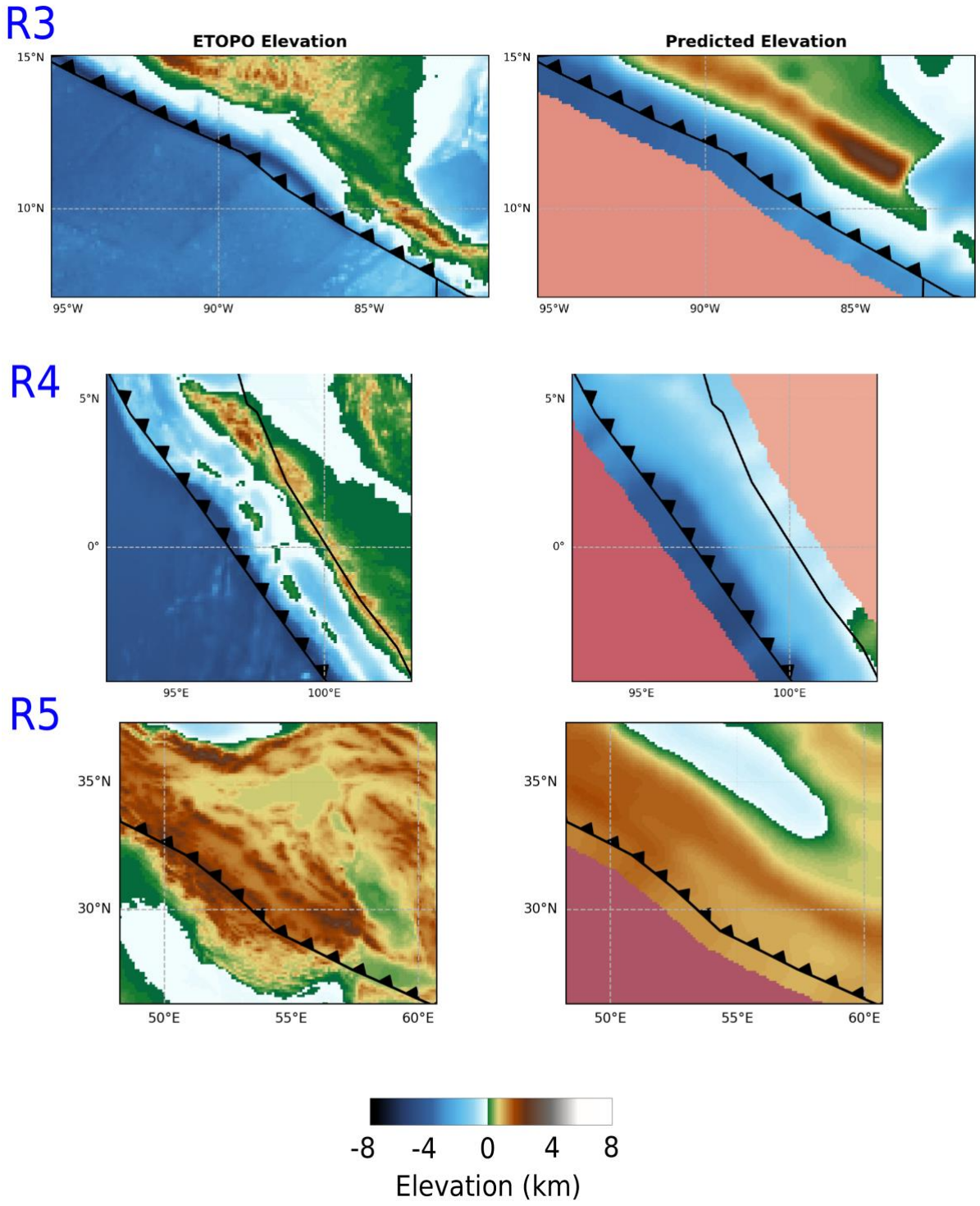

Supplementary Figure 2 | Model validation in independent regions R3–R5.
Comparison of predicted and observed present-day elevations for three additional validation regions excluded from training (R3–R5). The model captures major topographic features and spatial gradients, demonstrating robust generalisation across diverse tectonic settings.

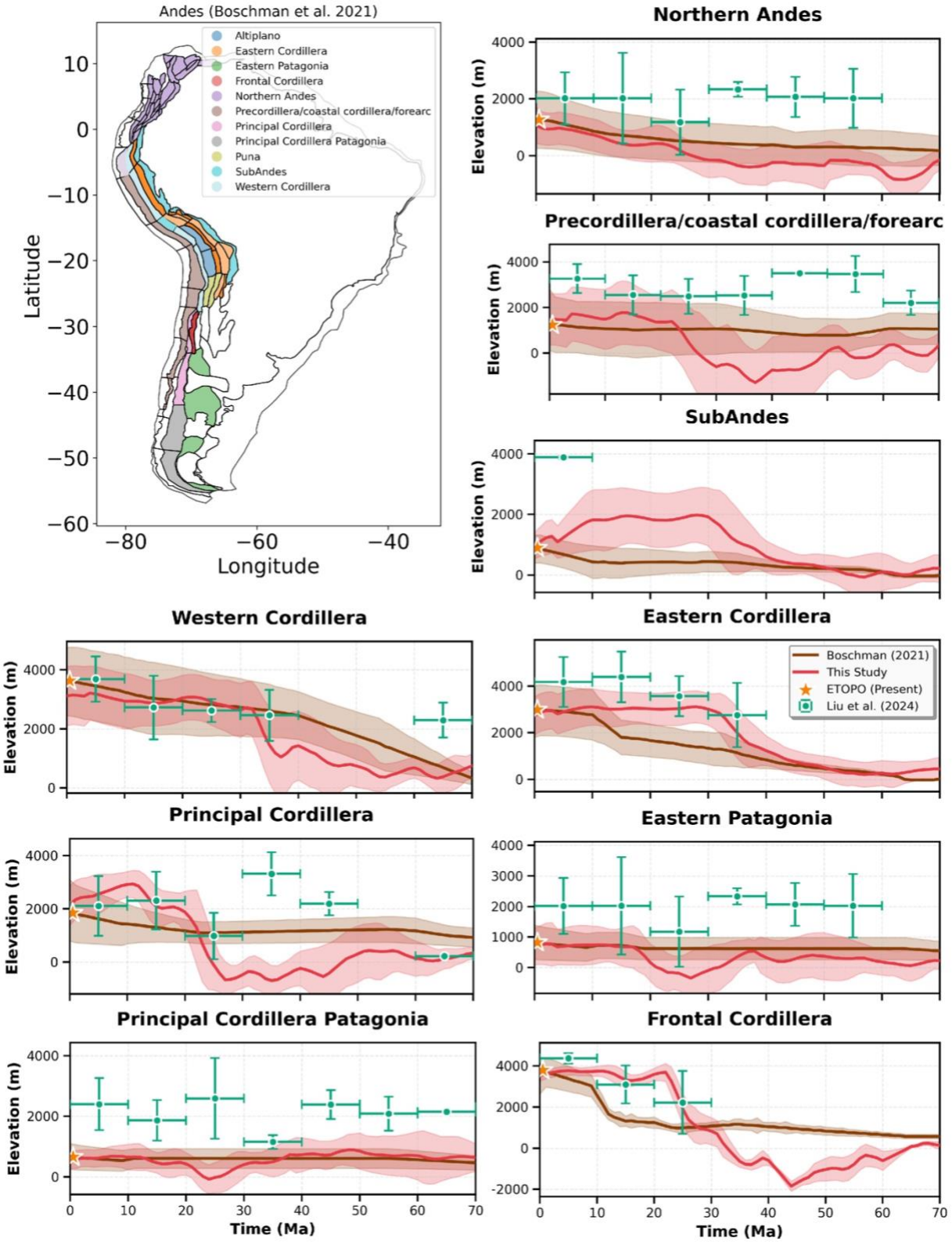

Supplementary Figure 3 | Comparison of model-predicted paleoelevation with Boschman (2021) across defined domains.
This figure compares the paleoelevation trajectories predicted by our model with those reported by Boschman (2021) across key tectonic domains. Each dark line represents the mean elevation for a given domain, while the shaded envelope indicates ±1 standard deviation, capturing intra-domain variability. Our model broadly reproduces the regional

elevation patterns and trends reported in Boschman (2021), while offering enhanced spatial and temporal resolution.

Supplementary Animation

Supplementary Animation 1 | Spatiotemporal evolution of surface topography along the active margin since the Mesozoic (~200 Ma), as predicted by the STN.

Supplementary Animation 2 | Temporal evolution of elevation estimates derived from independent igneous geochemical proxies following the methodology of Luffi & Ducea (2022), from the Mesozoic (~200 Ma) to present.

Supplementary Animation 3 | Misfit between predicted paleotopography and geochemically derived elevation estimates, highlighting spatial and temporal discrepancies across the active margin.

Reference

Amante, C., & Eakins, B. W. (2009). ETOPO1 arc-minute global relief model : procedures, data sources and analysis. Retrieved from https://repository.library.noaa.gov/view/noaa/1163

Bower, D. J., Gurnis, M., & Flament, N. (2015). Assimilating lithosphere and slab history in 4-D Earth models. *Physics of the Earth and Planetary Interiors*, *238*, 8–22. https://doi.org/10.1016/j.pepi.2014.10.013

Braun, J. (2010). The many surface expressions of mantle dynamics. *Nature Geoscience*, *3*(12), 825–833. https://doi.org/10.1038/ngeo1020

Candioti, L., Schmalholz, S., & Duretz, T. (2020). Impact of upper mantle convection on lithosphere hyperextension and subsequent horizontally forced subduction initiation. *Solid Earth*, *11*, 2327–2357. https://doi.org/10.5194/se-11-2327-2020

Chai, T., & Draxler, R. R. (2014). Root mean square error (RMSE) or mean absolute error (MAE)? – Arguments against avoiding RMSE in the literature. *Geoscientific Model Development*, *7*(3), 1247–1250. https://doi.org/10.5194/gmd-7-1247-2014

Clark, M. K., Schoenbohm, L. M., Royden, L. H., Whipple, K. X., Burchfiel, B. C., Zhang, X., et al. (2004). Surface uplift, tectonics, and erosion of eastern Tibet from large-scale drainage patterns. *Tectonics*, *23*(1). https://doi.org/10.1029/2002TC001402

Flament, N., Gurnis, M., & Müller, R. D. (2013). A review of observations and models of dynamic topography. *Lithosphere*, *5*(2), 189–210. https://doi.org/10.1130/L245.1

Glorot, X., Bordes, A., & Bengio, Y. (2011). Deep Sparse Rectifier Neural Networks. Presented at the International Conference on Artificial Intelligence and Statistics. Retrieved from https://www.semanticscholar.org/paper/Deep-Sparse-Rectifier-Neural-Networks-Glorot-Bordes/67107f78a84bdb2411053cb54e94fa226eea6d8e

Goodfellow, I., Bengio, Y., & Courville, A. (2016). *Deep Learning*. MIT Press.

Hastie, T., Tibshirani, R., & Friedman, J. (2009). *The Elements of Statistical Learning*. New York, NY: Springer. https://doi.org/10.1007/978-0-387-84858-7

Hayes, G. P., Moore, G. L., Portner, D. E., Hearne, M., Flamme, H., Furtney, M., & Smoczyk, G. M. (2018). Slab2, a comprehensive subduction zone geometry model. *Science*, *362*(6410), 58–61. https://doi.org/10.1126/science.aat4723

Huber, P., & Ronchetti, E. (2009). Robust Statistics. In *Journal of the American Statistical Association* (Vol. 78, p. xvi+354 pp. + loose erratum). https://doi.org/10.2307/2287149

King, M. T., & Welford, J. K. (2022). Advances in Deformable Plate Tectonic Models: 1. Reconstructing Deformable Continental Blocks and Crustal Thicknesses Back Through Time. *Geochemistry, Geophysics, Geosystems*, *23*(6), e2022GC010372. https://doi.org/10.1029/2022GC010372

Kingma, D. P., & Ba, J. (2017, January 30). Adam: A Method for Stochastic Optimization. arXiv. https://doi.org/10.48550/arXiv.1412.6980

Knight, B., Davies, J., & Capitanio, F. (2020). Timescales of successful and failed subduction: insights from numerical modelling. *Geophysical Journal International*. https://doi.org/10.1093/gji/ggaa410

LeCun, Y., Bengio, Y., & Hinton, G. (2015). Deep learning. *Nature*, *521*(7553), 436–444. https://doi.org/10.1038/nature14539

Li, X., Hu, Y., Guo, J., Lan, J., Lin, Q., Bao, X., et al. (2022). A high-resolution climate simulation dataset for the past 540 million years. *Scientific Data*, *9*(1), 371. https://doi.org/10.1038/s41597-022-01490-4

Luffi, P., & Ducea, M. N. (2022). Chemical Mohometry: Assessing Crustal Thickness of Ancient Orogens Using Geochemical and Isotopic Data. *Reviews of Geophysics*, *60*(2), e2021RG000753. https://doi.org/10.1029/2021RG000753

Macdonald, F. A., Swanson-Hysell, N. L., Park, Y., Lisiecki, L., & Jagoutz, O. (2019). Arc-continent collisions in the tropics set Earth's climate state. *Science*, *364*(6436), 181–184. https://doi.org/10.1126/science.aav5300

Merdith, A. S., Williams, S. E., Collins, A. S., Tetley, M. G., Mulder, J. A., Blades, M. L., et al. (2021). Extending full-plate tectonic models into deep time: Linking the Neoproterozoic and the Phanerozoic. *Earth-Science Reviews*, *214*, 103477. https://doi.org/10.1016/j.earscirev.2020.103477

Müller, R. D., Zahirovic, S., Williams, S. E., Cannon, J., Seton, M., Bower, D. J., et al. (2019). A Global Plate Model Including Lithospheric Deformation Along Major Rifts and Orogens Since the Triassic. *Tectonics*, *38*(6), 1884–1907. https://doi.org/10.1029/2018TC005462

Parsons, B., & Sclater, J. G. (1977). An analysis of the variation of ocean floor bathymetry and heat flow with age. *Journal of Geophysical Research (1896-1977)*, *82*(5), 803–827. https://doi.org/10.1029/JB082i005p00803

Prechelt, L. (1998). Early Stopping - But When? In G. B. Orr & K.-R. Müller (Eds.), *Neural Networks: Tricks of the Trade* (pp. 55–69). Berlin, Heidelberg: Springer. https://doi.org/10.1007/3-540-49430-8_3

Roberts, D. R., Bahn, V., Ciuti, S., Boyce, M. S., Elith, J., Guillera-Arroita, G., et al. (2017). Cross-validation strategies for data with temporal, spatial, hierarchical, or phylogenetic structure. *Ecography*, *40*(8), 913–929. https://doi.org/10.1111/ecog.02881

Santurkar, S., Tsipras, D., Ilyas, A., & Madry, A. (2019, April 14). How Does Batch Normalization Help Optimization? arXiv. Retrieved from http://arxiv.org/abs/1805.11604

Singh, S. P., & Silwal, V. (2023). Enhanced crustal and intermediate seismicity in the Hindu Kush-Pamir region revealed by attentive deep learning model. *Artificial Intelligence in Geosciences*. https://doi.org/10.1016/j.aiig.2023.10.002

Smith, L. N. (2017). Cyclical Learning Rates for Training Neural Networks. In *2017 IEEE Winter Conference on Applications of Computer Vision (WACV)* (pp. 464–472). https://doi.org/10.1109/WACV.2017.58

Sobouti, F., & Arkani-Hamed, J. (2002). Thermo-mechanical modeling of subduction of continental lithosphere. *Physics of the Earth and Planetary Interiors*, *131*, 185–203. https://doi.org/10.1016/s0031-9201(02)00064-x

Srivastava, N., Hinton, G., Krizhevsky, A., Sutskever, I., & Salakhutdinov, R. (2014). Dropout: A Simple Way to Prevent Neural Networks from Overfitting. *Journal of Machine Learning Research*, *15*(56), 1929–1958. Retrieved from http://jmlr.org/papers/v15/srivastava14a.html

Tan, E., Choi, E., Thoutireddy, P., Gurnis, M., & Aivazis, M. (2006). GeoFramework: Coupling multiple models of mantle convection within a computational framework. *Geochemistry, Geophysics, Geosystems*, *7*(6). https://doi.org/10.1029/2005GC001155

Valavi, R., Elith, J., Lahoz-Monfort, J. J., & Guillera-Arroita, G. (2019). blockCV: An r package for generating spatially or environmentally separated folds for k-fold cross-validation of species distribution models. *Methods in Ecology and Evolution*, *10*(2), 225–232. https://doi.org/10.1111/2041-210X.13107

Venkateswaran, P., Shimpi, V., Natu, M., & Sadaphal, V. (2016). Domain Driven Forecasting: Applying Theory Into Practice. In *2016 IEEE 16th International Conference on Data Mining Workshops (ICDMW)* (pp. 584–591). https://doi.org/10.1109/ICDMW.2016.0089

Whipple, K. X. (2009). The influence of climate on the tectonic evolution of mountain belts. *Nature Geoscience*, *2*(2), 97–104. https://doi.org/10.1038/ngeo413

Willmott, C. J., & Matsuura, K. (2005). Advantages of the mean absolute error (MAE) over the root mean square error (RMSE) in assessing average model performance. *Climate Research*, *30*, 79–82. https://doi.org/10.3354/cr030079

Zhong, S., & Gurnis, M. (1995). Mantle Convection with Plates and Mobile, Faulted Plate Margins. *Science*, *267*(5199), 838–843. https://doi.org/10.1126/science.267.5199.838

Zhong, S., Zuber, M. T., Moresi, L., & Gurnis, M. (2000). Role of temperature-dependent viscosity and surface plates in spherical shell models of mantle convection. *Journal of Geophysical Research: Solid Earth*, *105*(B5), 11063–11082. https://doi.org/10.1029/2000JB900003